The Fate of Formamide in the Outer Solar System:

G-Value Analysis and Spectral Evolution Under Simulated Europan Radiation

by

Allie H. Corrigan



A Thesis submitted to the Division of Natural Sciences, University of Kent, in fulfilment of the degree of Doctorate of Philosophy

Division of Natural Sciences

School of Physics and Astronomy

University of Kent

December 2025

Professor Nigel Mason

Page Count: 217

Word Count: 65294

Abstract

Europa is one of the most promising locations for life beyond Earth, with a global subsurface ocean, active geology, a reservoir of volatiles, and a surface continually processed by energetic radiation from Jupiter's magnetosphere. Understanding how prebiotic molecules evolve in such an environment is essential for interpreting observations from upcoming missions such as JUICE and Europa Clipper. This thesis investigates the radiation-driven chemistry of formamide (NH_2CHO) - a key prebiotic precursor capable of generating nucleobases, amino acids, and other bioessential molecules - embedded within water-rich ices under Europa-like conditions. Using ion, electron, and vacuum-UV (VUV) irradiation at 90 K for charged particles and across 10-130 K for VUV, on substrates representing saline and mineralogical diversity, the work provides the first systematic multi-regime analysis of formamide-water ices relevant to icy moons.

Ion irradiation experiments, performed at Atomki (15 keV H^+, 30 keV O^{2+}, 60 keV S^{5+}), show that high linear-energy-transfer (LET) particles drive efficient bulk radiolysis. Formamide undergoes rapid early destruction followed by fluence-dependent plateaus controlled by matrix trapping, water-mediated reformation, and shielding by accumulated products. CO, OCN^-, and CO_2 emerge as dominant radiolysis products, with CO_2 being particularly stable. G-values scale primarily with LET and substrate, revealing that salt-rich NaCl enhances both destruction and product formation, whereas ZnSe is comparatively inert. Electron irradiation, performed at the NSRRC, at 2 keV produces diffuse, low-LET energy deposition and is markedly less efficient: fragmentation and desorption dominate, and the formation of stable condensed residues is minimal. Nonetheless, the high flux of magnetospheric electrons at Europa means their cumulative contribution to near-surface turnover is significant. VUV irradiation, performed at the NSRRC, at 9 eV probes the upper tens of nanometres of the ice. It exhibits a strong temperature-dependent behaviour: compaction and enhanced high-energy absorption at 10 K, band broadening at 50 K, and annealing-dominated spectra above 90 K. Across all temperatures, formamide's W-band remains intact, with photoproducts manifesting only as subtle high-energy shoulders.

When combined, these experiments show that Europa's surface chemistry is vertically stratified: high-LET ions dominate dense-track radiolysis in the near-surface bulk, electrons provide more diffuse, depth-extended processing while controlling near-surface volatile loss and desorption, and VUV photons restructure only the uppermost tens of nanometres of the surface. Formamide is found to be resilient, with a Europa-like ion-induced lifetime of $\sim 10^5$ years, short relative to resurfacing but long enough to remain detectable if freshly supplied by plumes, impact gardening, or oceanic upwelling. Substrate effects indicate that chloride- and sulphate-rich terrains will be chemically active but poor at preserving organics, whereas purer water-ice regions may act as organic reservoirs. These findings provide a mechanistic basis for interpreting spectral and mass-spectrometric data returned by JUICE and Europa Clipper, offer constraints on the survival and transformation of prebiotic molecules on icy worlds, and highlight the need for future studies involving aqueous brines, mixed-irradiation environments, and mass-spectrometric product identification. In doing so, this thesis contributes to our understanding of Europa as a chemically dynamic system capable of both destroying and generating molecular precursors relevant to the origins of life.

Acknowledgements

It is universally acknowledged that a PhD is not the easiest degree to attain. Being the overzealous and easily stressed person that I am, I took on this challenge anyway - and was still not prepared for the four years that followed. I am profoundly grateful to everyone who has helped, encouraged, and kept me (mostly) sane along the way.

I gratefully acknowledge funding from the University of Kent Alumni Scholarship, which supported my tuition fees and stipend for the first three years of my PhD. I also acknowledge partial support from Europlanet 2024 RI, which contributed to laboratory equipment and consumables, and supported travel to conferences and to experimental facilities.

I owe special thanks to my supervisor, Professor Nigel J. Mason, who has been a steadfast source of support throughout these four years. I have always known that I could go to him with anything, academic or otherwise, and I am deeply grateful for his calm guidance, good humour and patience. Travelling to conferences together (and occasionally sharing one too many drinks) and feeling his confidence in me, even when I lacked it myself, helped convince me that I belonged here.

I am also profoundly grateful to the colleagues who have supported this work. My secondary supervisor, Jon Tandy, has been an excellent sounding board, offering thoughtful feedback and clear-headed advice. I want to thank the team at Atomki, in particular Richárd Rácz and Duncan V. Mifsud, as well as Sándor Biri, Péter Herczku, Béla Sulik, K. K. Rahu and Gergő Lakatos, for their help, kindness and many invaluable discussions during my visits. I would further like to thank the team at the NSRRC in Taiwan, especially Wei-Yuan Chiang and Sheng-Lung Chou, for their warm welcome and accommodation, and my collaborators from PRL in India - Bhala Sivaraman, Wafikul Khan and Ragav Ramachandran - for the insightful conversations about both concepts and experiments.

I also owe an enormous thank you to my friends and colleagues, from undergrad through to the end of this PhD. To my physics cohort and fast friends - Matt, Iv, Dan, Owen, Ethan and Amber - thank you for keeping me sane, letting me complain (at length) and tolerating my grumpy office moods; the laughter, lab chaos, coffee runs and

general nonsense made the daily grind genuinely enjoyable. I am equally grateful to the friends outside physics who have been a constant source of support, guidance and entertainment. In particular, my two besties Olivia and Lily (collectively, "Olilyia") have been fantastic housemates and incredible friends, and I have loved our theatre trips, gossiping-on-the-couch sessions, late-night heart-to-hearts and early-evening cosy "I'm a Celeb" nights.

I thank my mum, whose steady, loving support has run through every stage of this PhD, from check-in messages and Percy Pig care packages to a perfectly timed escape to Canterbury with sparkling wine, gossip and pancakes. I am equally grateful to my dad, whose dry humour, steadiness and ex-Army level of calm under pressure, along with his quiet encouragement and occasional liquid moral support, kept me grounded when things were hardest.

Thank you to my siblings, Madeline and Seamus, for their quiet support, light bullying and shared TikTok memes that made everything feel normal again. I am so proud of Madeline for finishing her Law degree and starting her first proper job, and inspired by Seamus's drive and ambition in all his projects. A heartfelt thank you also goes to my godparents, Debi and Clive, for their blend of affection and comedy, their relentless joking about this "woman in STEM" and their open invitations and encouragement, which always arrived exactly when I needed them. Since I was a child, I have dreamed of becoming an astrophysicist and earning a doctorate, and throughout every phase of that ambition, my family never once doubted me; their belief in me has meant more than words can express.

Thank you to Dougal "The Dog" Bradley for contributing "plkiuujygf" to the thesis, and Shadow "The Cat" for contributing "yttttttttttttttttttttttttth7". These edits did not make it into the final version, but their efforts - both on the keyboard and as quiet company on the longer days - were invaluable. I would also like to thank the global video-game lo-fi remix community; I am convinced I have now listened to every 8-bit, 16-bit and vaguely Nintendo-adjacent "bink-bonk" beat on the internet. Their commitment to producing music that is somehow both soothing and deranging kept me writing when all rational thought suggested I should stop. My office mate and partner,

Ben, probably suffered the collateral damage of these soundtracks, and for that, I am only partially sorry.

Before I get to Ben properly, I want to thank Ben's parents, Karen and Neil, for welcoming me into their home this past year and letting me live with them rent-free. More importantly, thank you for the emotional support, the home-cooked meals most nights, and the much-needed spa days and chats when I really needed to unwind.

A very special thank you goes to Ben, who has been my rock throughout this PhD. He stood by me through the long nights, stress cycles, failed experiments and "why am I doing a PhD?" spirals, took on the small tasks when everything felt too much, and even proofread this entire thesis. I am endlessly grateful for his patience, humour and unwavering belief in me. I love you to the moon and back - or more accurately, to Europa and back - and this thesis exists because you helped me survive it.

Contents

1 Thesis Scope and Objectives **1**

1.1 Research Aims and Objectives 2

1.2 Design and Methodology 3

1.3 Expected Outcomes 4

1.4 Thesis Overview 5

2 Introduction to Prebiotic Chemistry and the Role of Formamide **7**

2.1 Prebiotic Chemistry 8

2.1.1 The Miller-Urey Experiment 8

2.1.2 Key Concepts and Mechanisms 11

2.1.3 Current Theories and Models 13

2.2 The Outer Solar System and the ISM as a Laboratory for Prebiotic Chemistry 15

2.2.1 Prebiotic Chemistry in the ISM 16

2.2.2 Prebiotic Chemistry in Comets 19

2.2.3 Prebiotic Chemistry on Planetary and Icy Bodies 23

2.3 Europa as a Prebiotic Environment 26

2.3.1 Europa's Environmental Conditions 27

2.3.2 Spacecraft Missions to Europa: JUICE and Europa Clipper . . 29

2.3.2.1 The JUICE Mission 30

2.3.2.2 Europa Clipper Mission 32

2.4 Formamide as a Key Prebiotic Molecule 35

2.4.1 Detection of Formamide in Extraterrestrial Environments . . . 37

2.4.1.1 Comet 67P 42

2.5 Laboratory Studies of Irradiated Ices Relevant to the Jovian System . . 44

2.5.1 Early Irradiation Studies of Water Ice 44
2.5.2 Mixed Ice Analogues and the Evolution of Experimental Complexity 47
2.5.3 Salt-Rich Analogues and Galileo-Era Observations 50
2.5.4 Experimental Studies Directly Relevant to Formamide 55
2.5.5 Summary Table 58
2.6 Research Gap and Objectives of the Thesis 61

3 Physical Chemistry & Spectroscopy Fundamentals 88
3.1 Basics of IR and VUV Spectroscopy 89
3.1.1 Infrared Spectroscopy 89
3.1.1.1 Principles 89
3.1.1.2 Applications to Astrochemistry 92
3.1.1.3 Formamide in the IR 94
3.1.1.4 Challenges and Limitations of IR Spectroscopy 95
3.1.2 Vacuum Ultraviolet Spectroscopy 96
3.1.2.1 Principles 96
3.1.2.2 Applications to Astrochemistry 99
3.1.2.3 Formamide in the VUV 101
3.1.2.4 Challenges and Limitations of VUV Spectroscopy . . . 102
3.1.3 Formamide Ice Structure and Phase Behaviour 102
3.2 Fundamentals of Radiation Chemistry 110
3.2.1 Energy Sources and Radiation Fields in the ISM and Jovian System 111
3.2.1.1 Heavy Ion Irradiation: H^+, O^{2+}, S^{5+} 112
3.2.1.2 Low-Energy Electrons 115
3.2.1.3 VUV Photons and Electronic Excitation 116
3.2.2 Molecular Effects of Radiation 119
3.2.3 Radiation Processing of Astrophysical Ices 121
3.2.4 Environmental Influences 122
3.3 G-Values: Definition and Interpretation 123

3.3.1 What is a G-Value? . . . 124
3.3.2 Why Use G-Values? . . . 125
3.3.3 Determining G-Values . . . 127
3.3.4 Limitations and Considerations for the Derived G-Values . . . 130
3.3.5 Survivability Under Europan Radiation . . . 131

4 Methodology and Experimental Apparatus 148

4.1 Experimental Apparatus and Irradiation Facilities . . . 149
4.2 ECRIS at AQUILA . . . 151
4.2.1 FTIR Spectroscopy and Ice Thickness Determination . . . 157
4.2.2 Experimental Methodology . . . 160
4.3 NSRRC Synchrotron (TLS) . . . 165
4.3.1 U90 Endstation (Electron Irradiation) . . . 166
4.3.2 FTIR and Ice Thickness Determination . . . 167
4.3.3 BL03 Endstation (VUV Irradiation) . . . 169
4.3.4 Ice Preparation and Thickness Estimation at BL03 . . . 172
4.3.5 Experimental Methodology . . . 173
4.3.6 Effects of Temperature . . . 174
4.4 Data Acquisition and Processing . . . 175
4.4.1 FTIR Spectroscopy . . . 175
4.4.2 Summary of Film Thickness Estimates . . . 176
4.4.3 Fluence Calculations . . . 176
4.4.4 Temperature-Programmed Desorption (TPD) . . . 178

5 Ion Irradiation of Formamide and Water Ice Mixture 184

5.1 Experimental Overview and Irradiation Parameters . . . 185
5.2 Evolution of IR Spectra and Radiolysis Products . . . 188
5.2.1 Proton Irradiation . . . 190
5.2.1.1 NaCl Window Experiments . . . 191
5.2.1.2 ZnSe Window Experiments . . . 198
5.2.2 Oxygen Ion Irradiation . . . 204
5.2.2.1 NaCl Window Experiments . . . 204

5.2.2.2 ZnSe Window Experiments . . . 208
5.2.3 Sulphur Ion Irradiation . . . 210
5.2.3.1 NaCl Window Experiments . . . 212
5.2.3.2 ZnSe Window Experiments . . . 214
5.3 Radiation Chemical Yields (G-values) for Destruction and Formation . 217
5.4 Estimation of Mean Survival Times under Europa-like Irradiation . . . 222
5.5 Comparative Analysis and Implications for Europa's Surface Chemistry 225
5.5.1 Local Implications for Ion-Driven Chemistry . . . 227

6 Electron Irradiation of Formamide and Water Ice Mixture 237
6.1 Experimental Overview and Irradiation Parameters . . . 238
6.2 Evolution of IR Spectra and Radiolysis Products . . . 241
6.2.1 NaCl Window . . . 242
6.2.2 ZnSe Window . . . 246
6.3 Determination of ice composition and thickness . . . 249
6.3.1 Assumptions and Uncertainties . . . 250
6.4 Destruction Efficiency . . . 251
6.5 Electrons vs Ions: A Comparative Analysis . . . 254
6.6 Implications for Europa's Near-Surface Chemistry . . . 257

7 VUV Irradiation of Formamide and Water Ice Mixture 265
7.1 Introduction . . . 266
7.2 Experimental Parameters and Methodology . . . 269
7.2.1 Ice Thickness Determination . . . 269
7.3 Electronic Spectra and Spectral Evolution . . . 272
7.3.1 Experimental Run 1: Spectral Evolution from 10-90 K . . . 272
7.3.1.1 TPD Heating Trends . . . 278
7.3.2 Experimental Run 2: Spectral Evolution from 10-130 K . . . 280
7.3.2.1 TPD Heating Trends . . . 289
7.4 Temperature Dependence of Photochemistry . . . 291
7.5 Conclusions and Implications for Europa's Surface Chemistry . . . 294
7.5.1 Implications for Europa's Surface Chemistry . . . 296

8 Conclusions and Solar System Relevance 300

8.1 Thesis Summary . . . 301

8.2 Summary of Results Using Different Types of Radiation . . . 303

8.3 Implications for Detectability on Europa . . . 306

8.3.1 Assumptions and Limitations . . . 307

8.4 Future Work . . . 308

8.4.1 Aqueous Formamide-Salt Irradiation Experiments . . . 309

8.4.2 Mass-Spectrometric Identification of Radiolysis Products . . . 309

8.4.3 Time- and Fluence-Dependent Reaction Network Modelling . . . 310

8.4.4 Mission-Aligned Analogue Experiments . . . 310

8.4.5 Mixed and Sequential Radiation Experiments . . . 311

8.5 Final Conclusions . . . 312

A Determination of G-Values from Exponential Dose–Response Fits 314

A.1 Overview . . . 314

A.2 Determination of Column Density . . . 314

A.3 Construction of Dose–Response Curves . . . 315

A.4 Analytical Fitting of Dose-Response Curves . . . 315

A.5 Determination of the Initial Destruction Rate . . . 316

A.6 Calculation of G-Values . . . 317

List of Figures

1.1 This illustration shows NASA's Europa Clipper mission doing a flyby of Europa. **Credit:** NASA/JPL-Caltech. 5

2.1 Schematic depicting the set-up of the original Miller-Urey experiment. **Credit:** By courtesy of Encyclopædia Britannica, Inc., copyright 2023; used with permission, [4]. 10

2.2 Overview of the Strecker synthesis. An aldehyde reacts with ammonia (from NH_4Cl) and cyanide (KCN) to form an α-aminonitrile, which is subsequently hydrolysed under acidic conditions to yield the corresponding α-amino acid. Key bond-forming steps include C-N and C-C formation, while hydrolysis breaks the C=O π-bond and C-O σ-bond of the nitrile intermediate. **Credit:** Reproduced with permission from J. Ashenhurst, Master Organic Chemistry, [9]. 12

2.3 Simplified illustration of the "primordial soup" concept. Simple organic molecules such as sugars, fatty acids, amino acids, and nucleotides accumulate in early Earth's surface waters and assemble into more complex structures, such as polymers, membranes, and eventually primitive cells. **Credit:** Reproduced from 'The Brain from Top to Bottom' by Bruno Dubuc, McGill University, under copyleft ©, [16]. 14

2.4 Simplified view of a hydrothermal vent system on the early Earth. Water circulates through hot rock, producing hydrogen and methane through reactions with iron- and magnesium-rich minerals. These fluids rise and mix with the ocean, where heat and minerals can help form simple organic molecules. **Credit:** Reprinted from The Archean Earth (Second Edition), C. K. Jones, M. Leung, C. Tu, S. Ebadirad, N. L. Marshall, L. Tan, T. W. Lyons, Setting the stage: Building and maintaining a habitable world and the early conditions that could favor life's beginnings on Earth and beyond, Pages 25–40, Copyright (2026), with permission from Elsevier, [20]. 15

2.5 JWST image of the Pillars of Creation, illustrating dense molecular clouds within the interstellar medium. These cold, dust-rich regions host ice-coated grains where low-temperature surface chemistry produces complex organic molecules relevant to prebiotic chemistry. **Credit:** NASA, ESA, CSA, STScI, J. DePasquale (STScI), A. Pagan (STScI), A. M. Koekemoer (STScI). CC BY 4.0. 17

2.6 Comet C/2014 Q2 (Lovejoy), showing its bright coma and dust tail generated as volatile ices are released from the nucleus. Lovejoy is chemically significant, with radio and submillimetre observations revealing a range of complex organic molecules, making it an important example of prebiotic chemistry in cometary comae. **Credit:** NASA/MSFC/MEO/Aaron Kingery. 20

2.7 Conceptual cross-section of Jupiter's moon Europa, showing key features including the icy surface, subsurface ocean, the hypothesised hydrothermal activity at the seafloor, and the irradiation incident on the moon. These processes may support chemical energy gradients that can sustain life. **Credit:** K. Hand et al./NASA/JPL, [81]. 24

2.8 Schematic of electrical currents in Jupiter's magnetosphere and their interactions with the Galilean moons. **Credit:** Ruslik0, via Wikimedia Commons, CC BY-SA 3.0, [82]. 25

2.9 An image taken of Europa by NASA's Galileo spacecraft, showing the diversity of Europa's geology. **Credit:** NASA/JPL-Caltech/SETI Institute. 26

2.10 Schematic representation of Europa's interaction with Jupiter's magnetosphere. Left: Europa's orbit within Jupiter's tilted magnetic field. Right: energetic electrons and keV ions (H^+, O^+, S^+) spiral along magnetic field lines and bombard the surface, driving radiolysis, sputtering, and production of volatile species such as O_2 and H_2, which contribute to Europa's tenuous exosphere. **Credit:** Figure 1 on page 508 from Europa. © 2009 The Arizona Board of Regents. Reprinted by permission of the University of Arizona Press, [101]. 29

2.11 Artist's impression of ESA's JUICE spacecraft conducting a close flyby of Europa, with Jupiter visible in the background. **Credit:** ESA (acknowledgement: ATG Medialab), ESA Standard Licence. 30

2.12 Overview of the scientific instruments aboard ESA's JUICE spacecraft. The payload includes ten state-of-the-art instruments covering remote sensing, geophysical, and in-situ measurements, designed to investigate the surfaces, atmospheres, and interiors of Jupiter's icy moons. **Credit:** ESA (acknowledgement: ATG Europe), ESA Standard Licence. 31

2.13 Artist's impression of NASA's Europa Clipper spacecraft conducting a close flyby of Jupiter's moon Europa. Jupiter can be seen in the background. **Credit:** NASA/JPL-Caltech. 33

2.14 Spitzer Space Telescope infrared image of the massive star-forming region DR21 in the Cygnus X complex. This molecular cloud hosts several dense clumps, including DR21(OH), where recent millimetre and submillimetre surveys have detected complex organic molecules such as formamide (NH_2CHO) in the gas phase, [134]. **Credit:** NASA/JPL-Caltech. 36

2.15 A colour composite image of the Galactic Centre and Sagittarius B2 as seen by the ATLASGAL survey. **Credit:** ESO/APEX & MSX/IPAC/NASA. 38

2.16 Schematic representation of the hierarchical structure and evolutionary stages of a massive molecular cloud, from extended diffuse material to dense, ice-rich cores and active star-forming regions. The cold, dense phases (infrared-dark clouds and massive dense cores) provide the low temperatures (10-20 K), high densities, and dust-grain ice mantles under which complex organic molecules such as formamide are expected to form and persist. **Credit:** Used with permission of Annual Reviews, Inc., from High-Mass Star and Massive Cluster Formation in the Milky Way, F. Motte, S. Bontemps and F. Louvet, *Annual Review of Astronomy and Astrophysics*, vol. 56, 2018; permission conveyed through Copyright Clearance Center, Inc., [152]. 39

2.17 Hubble Space Telescope image of Herbig-Haro object HH 47, a young stellar outflow emerging from a Bok globule at the edge of the Gum Nebula, in the southern constellation of Vela. Protostellar environments of this kind - characterised by shocks, warm irradiated gas, and chemically enriched jets - are known sites where complex organic molecules such as formamide (NH_2CHO) have been detected in recent spectral surveys. **Credit:** NASA, ESA; P. Hartigan (Rice University). 41

2.18 An image of comet 67P/Churyumov-Gerasimenko taken by the Rosetta NAVCAM. **Credit:** ESA/Rosetta/NAVCAM - CC BY-SA IGO 3.0. . . 43

2.19 Schematic representation of the principal radiation-induced processes occurring within water ice. Ionisation and excitation lead to molecular dissociation, radiolysis product formation, trapping of species within the ice matrix, and sputtering of material from the surface. **Credit:** Reproduced from B. D. Teolis et al., Water ice radiolytic O_2, H_2, and H_2O_2 yields for any projectile species, energy, or temperature: A model for icy astrophysical bodies, *Journal of Geophysical Research: Planets*, 122, 1996–2012 (2017), with permission from John Wiley and Sons. © 2026. American Geophysical Union, [183]. 46

2.20 Incremental ion irradiation of a 1:1 formamide-water ice mixture deposited on a NaCl substrate at 90 K. The sample was irradiated with S^{5+} ions at 60 keV. Infrared absorbance spectra are shown across ten irradiation intervals, from pre-irradiation (spectrum 1, yellow) to post-final irradiation (spectrum 10, dark purple). The two featured absorption bands at ∼1385 cm^{-1} and ∼1328 cm^{-1} correspond to vibrational modes of formamide. The systematic decrease in absorbance intensity indicates the progressive destruction of formamide under irradiation with sulphur ions. 63

3.1 Types of molecular vibrations include: (a) stretching vibrations and (b) bending vibrations. The "+" and "−" symbols represent atomic motion directed out of and into the plane of the page, respectively. **Credit:** Reproduced with permission from Springer Nature: J. J. Ojeda and M. Dittrich, Fourier Transform Infrared Spectroscopy for Molecular Analysis of Microbial Cells, *Microbial Systems Biology*, Methods in Molecular Biology, vol. 881, pp. 187–211, Humana Press, 2012, Springer Nature, [1]. 90

3.2 The Horsehead Nebula (Barnard 33) and NGC 2023, captured in visible light. NGC 2023 is visible in the lower left of the image. **Credit:** Jonathan Lodge, Telescope Live, [6]. 92

3.3 IR spectrum of pure formamide deposited at 105 K. Annotated with vibrational band assignments typically observed for formamide [11, 12]. **Credit:** Plot reproduced from the Leiden Ice Database for Astrochemistry (LIDA; Rocha et al. 2022) [13]; data from Slavicinska et al. (2023) [11]. Band assignment annotations added by the author. 94

3.4 An ALMA image of the protoplanetary disc surrounding the nearby young star TW Hydrae, revealing the classic rings and gaps that signify planets are in formation in this system. **Credit:** S. Andrews (Harvard-Smithsonian CfA); B. Saxton (NRAO/AUI/NSF); ALMA (ESO/NAOJ/NRAO), CC BY 4.0. 99

3.5 VUV spectrum of pure formamide deposited at 10 K on a LiF window. Annotated with transitional modes typically observed for formamide [36, 37]. 101

3.6 Mid-IR spectra of solid formamide at 30, 160, and 200 K, showing the evolution from broad bands in the low-temperature amorphous solid to sharper features in the crystalline/aggregated phase. Schematics on the left indicate representative hydrogen-bonded dimers and their association into larger motifs. **Credit:** Reprinted from Spectrochimica Acta Part A: Molecular and Biomolecular Spectroscopy, Vol. 105, B. Sivaraman, B. N. Raja Sekhar, B. G. Nair, V. Hatode, N. J. Mason, Infrared spectrum of formamide in the solid phase, Pages 238–244, Copyright (2013), with permission from Elsevier, [12]. 105

3.7 Illustration of how formamide (blue) plasticises a hydrogen-bonded polymer network more strongly than water (purple). The storage modulus G' drops at lower temperatures in the presence of formamide, reflecting a lower glass-transition temperature T_g and stabilisation of liquid/glassy states. **Credit:** Used with permission of the American Chemical Society, from Formamide as a Robust Alternative to Water for Plasticizing Polyelectrolyte Complexes, S. Hassoun, Z. A. Digby, N. Abou Hamad and J. B. Schlenoff, *Macromolecules*, vol. 57, 2024; permission conveyed through Copyright Clearance Center, Inc., [48]. 108

3.8 An artist's rendition of the surface of Europa being bombarded by radiation from Jupiter's magnetosphere. **Credit:** NASA/JPL-Caltech. . 110

3.9 Estimated penetration depths of various forms of ionising radiation into bulk H_2O ice, shown as a function of wavelength and energy. Coloured bars represent the dominant stopping ranges for S^+, O^+, H^+ ions, electrons, Bremsstrahlung X-rays, and micrometeoroid impacts in the icy surface of Europa. These depths are relevant to both surface processing and the chemistry probed by laboratory analogues. **Credit:** Reproduced from Becker et al. (2024), Fig. 18 [55], CC BY 4.0. Underlying data from Warren and Brandt [56], the NIST PSTAR/ESTAR databases, and Costello et al. [57]. 112

3.10 Schematic of Jupiter's magnetosphere illustrating key structural features: Io's plasma torus in red, the orbits of the Galilean moons (Io, Europa, Ganymede, Callisto) in orange, and magnetic field lines in blue. This diagram visually represents the sources and trapping regions of charged radiation, ions and electrons that irradiate Europa's surface. Adapted from [75]. 115

4.1 Image of the ECRIS system in the AQUILA laboratory. 151

4.2 A drawing of the cross-section of the Atomki-ECRIS. **Credit:** Reproduced from Biri et al. (2021), Fig. 3 [3], CC BY 4.0. 152

4.3 A drawing depicting the top-down view of the beamlines from the Atomki ECR ion source. **Credit:** Reprinted from R. Rácz et al., AQUILA: A laboratory facility for the irradiation of astrochemical ice analogs by keV ions, *Rev. Sci. Instrum.* 95, 095105 (2024), with the permission of AIP Publishing, [4]. 153

4.4 Schematic of the ion beam transport line from the 55° bending magnet to the AQUILA chamber. **Credit:** Reprinted from R. Rácz et al., AQUILA: A laboratory facility for the irradiation of astrochemical ice analogs by keV ions, *Rev. Sci. Instrum.* 95, 095105 (2024), with the permission of AIP Publishing, [4]. 153

4.5 A top-down schematic of the AQUILA chamber, arranged for transmission absorption mid-infrared spectroscopy. Its rotatable sample holder and heat shielding facilitate ion beam irradiation, with the infrared beam aligned orthogonally to the deposition surface. When rotated, the sample holder also allows for laser interferometry[1] to measure ice thickness by reflecting the incident laser beam into the photodiode. **Credit:** Reprinted from R. Rácz et al., AQUILA: A laboratory facility for the irradiation of astrochemical ice analogs by keV ions, *Rev. Sci. Instrum.* 95, 095105 (2024), with the permission of AIP Publishing, [4]. 155

4.6 Images of the sample holder with a NaCl window mounted. **(a)** is the sample holder outside of the cryogenic chamber, and **(b)** is the sample holder outside of the cryogenic chamber with its heat shield cover. . . . 157

4.7 Schematic illustration of two-beam optical interferometry. A reference surface and a sample surface form an interferometer, and the superposition of the reflected beams produces interference fringes whose spacing encodes differences in optical path length. **Credit:** Reproduced with permission from OptoSigma, 'Principle of Interferometer', [8] 160

4.8 Post-irradiation photographs of the substrates, showing residual deposits on (**a**) a NaCl window and (**b**) a ZnSe window. Each substrate was replaced between experiments to avoid contamination from prior runs. 161

4.9 Cold finger and substrate inside the cryogenic chamber. **(a)** shows the cold finger with mounted substrate as viewed through a window; **(b)** shows the cold finger with deposition needle aligned for background dosing of the formamide-water ice. 163

4.10 Images of the U90 station where **(a)** is the sample holder inside the chamber, and **(b)** is an image taken through a window of the deposition needle pointed at the sample holder. 167

4.11 Images of the BL03 station where **(a)** is the BL03 endstation, and **(b)** is the sample holder. 169

4.12 Schematic layout of the BL03 (03A1) beamline at the Taiwan Light Source. The synchrotron source (S) is followed by a series of optical components: horizontal and vertical focusing mirrors (HFM, VFM), slits (S1, S2), a cylindrical grating monochromator (G), and vertical/horizontal refocusing mirrors (VRFM, HRFM), leading to two possible detector paths (D1 and D2). All distances are in mm. **Credit:** Reprinted from Nuclear Instruments and Methods in Physics Research Section A: Accelerators, Spectrometers, Detectors and Associated Equipment, Vol. 467, Y. F. Song et al., Performance of a novel VUV bending magnet beamline, Pages 569–572, Copyright (2001), with permission from Elsevier, [25] 170

5.1 Infrared spectra of a cryogenic 50:50 (molar) formamide-water ice mixture deposited onto an NaCl window and maintained at 90 K, from pre-irradiation (spectrum 1, yellow) to post-final irradiation (spectrum 10, dark purple), with each number in between representing the fluence increment number, with 15 keV H^+ ions. Key vibrational modes of formamide are labelled, including CH stretch ($\sim$2730 cm^{-1}), C=O stretch ($\sim$1690 cm^{-1}), NH_2 scissoring ($\sim$1630 cm^{-1}), CH bending ($\sim$1388 cm^{-1}), CN stretching ($\sim$1328 cm^{-1}), and a broad region near 3200-3400 cm^{-1} representing the overlapping N-H/O-H stretches of formamide and water. The post-irradiation spectrum shows significant changes in peak intensity and the appearance of new features, including CO (C$\equiv$O stretching; $\sim$2135 cm^{-1}), OCN^- (C$\equiv$N stretching; $\sim$2165 cm^{-1}), and CO_2 (asymmetric stretching; $\sim$2340 cm^{-1}), marked with asterisks. Spectra have been vertically offset for clarity. 189

5.2 Evolution of infrared spectral features for a 50:50 formamide-water ice mixture deposited on a NaCl window and irradiated with 15 keV H^+ ions at 90 K. (a) Full mid-infrared spectrum across all fluences. (b) Formamide degradation tracked via CH and NH_2 bending modes. (c) Emergence of CO and OCN^- features post-irradiation. (d) Progressive formation of CO_2 with fluence. All spectra are colour-coded by increasing ion fluence, from pre-irradiation (spectrum 1, yellow) to post-final irradiation (spectrum 13, dark purple), with each number in between representing the fluence increment number. 192

5.3 Comparison of infrared spectra of formamide-water ice deposited on NaCl (dashed line) and ZnSe (dash-dot line) substrates under equivalent deposition conditions at 90 K, before proton irradiation. The close agreement in band positions and relative intensities of the key formamide features (CH bend at ∼1388 cm^{-1}, CN stretch at ∼1328 cm^{-1}, C=O stretch at ∼1690 cm^{-1}) supports that the two ices are chemically equivalent prior to irradiation, and that any subsequent differences in spectral evolution can be attributed to substrate effects rather than differences in initial ice composition. 198

5.4 Evolution of infrared spectral features for a 50:50 formamide-water ice mixture deposited on a ZnSe window and irradiated with 15 keV H^+ ions at 90 K. (a) Full mid-infrared spectrum across all fluences. (b) Formamide degradation tracked via CH and NH_2 bending modes. (c) Emergence of CO and OCN^- features post-irradiation. (d) Progressive formation of CO_2 with fluence. All spectra are colour-coded by increasing ion fluence, from pre-irradiation (spectrum 1, yellow) to post-final irradiation (spectrum 14, dark purple), with each number in between representing the fluence increment number. 199

5.5 Schematic illustration of how interfacial water structure depends on surface charge. Increasing the surface charge draws counterions and water molecules into the interface, forming tightly bound hydration layers and a pronounced potential drop across the Stern and diffuse regions. In the context of this work, an ionic substrate such as NaCl behaves similarly to panels (b-d), forming a compact, ordered interfacial region that can retain volatile radiolysis products more effectively. A weakly interacting surface, such as ZnSe, resembles panel (a), showing minimal hydration layering. **Credit:** Reproduced with permission from Springer Nature: G. Gonella et al., Water at charged interfaces, *Nature Reviews Chemistry*, vol. 5, pp. 466–485, 2021, Springer Nature, [43]. 203

5.6 Evolution of infrared spectral features for a 50:50 formamide-water ice mixture deposited on a NaCl window and irradiated with 30 keV O^{2+} ions at 90 K. (a) Full mid-infrared spectrum across all fluences. (b) Formamide degradation tracked via CH and NH_2 bending modes. (c) Emergence of CO and OCN^- features post-irradiation. (d) Progressive evolution and subsequent decay of CO_2 with fluence. All spectra are colour-coded by increasing ion fluence, from pre-irradiation (spectrum 1, yellow) to post-final irradiation (spectrum 8, dark purple), with each number in between representing the fluence increment number. 206

5.7 Comparison of the O-H/N-H stretching region (∼3000–3600 cm^{-1}) for formamide-water ice irradiated with 15 keV H^+ ions (dashed line) and 30 keV O^{2+} ions (dash-dot line), shown at the final spectrum of each run (H^+: 1.10×10^{16} cm^{-2}; O^{2+}: 1.92×10^{15} cm^{-2}). 207

5.8 Comparison of the infrared spectra of formamide-water ice deposited on NaCl (dashed line) and ZnSe (dash-dot line) substrates under equivalent deposition conditions at 90 K, before oxygen irradiation. The close agreement in band positions and relative intensities of the key formamide features (CH bend at ∼1388 cm^{-1}, CN stretch at ∼1328 cm^{-1}, C=O stretch at ∼1690 cm^{-1}) supports that the two ices are chemically equivalent prior to irradiation, and that any subsequent differences in spectral evolution can be attributed to substrate effects rather than differences in initial ice composition. 208

5.9 Evolution of infrared spectral features for a 50:50 formamide-water ice mixture deposited on a ZnSe window and irradiated with 30 keV O^{2+} ions at 90 K. (a) Full mid-infrared spectrum across all fluences. (b) Formamide degradation tracked via CH and NH_2 bending modes. (c) Emergence of CO and OCN^- features post-irradiation. (d) Progressive evolution and subsequent decay of CO_2 with fluence. All spectra are colour-coded by increasing ion fluence, from pre-irradiation (spectrum 1, yellow) to post-final irradiation (spectrum 10, dark purple), with each number in between representing the fluence increment number. 209

5.10 Evolution of infrared spectral features for a 50:50 formamide-water ice mixture deposited on a NaCl window and irradiated with 60 keV S^{5+} ions at 90 K. (a) Full mid-infrared spectrum across all fluences. (b) Formamide degradation tracked via CH and NH_2 bending modes. (c) Emergence of CO and OCN^- features post-irradiation. (d) Progressive formation of CO_2 with fluence. All spectra are colour-coded by increasing ion fluence, from pre-irradiation (spectrum 1, yellow) to post-final irradiation (spectrum 10, dark purple), with each number in between representing the fluence increment number. 212

5.11 Comparison of the infrared spectra of formamide-water ice deposited on NaCl (dashed line) and ZnSe (dash-dot line) substrates under equivalent deposition conditions at 90 K, before sulphur irradiation. The close agreement in band positions and relative intensities of the key formamide features (CH bend at ∼1388 cm^{-1}, CN stretch at ∼1328 cm^{-1}, C=O stretch at ∼1690 cm^{-1}) supports that the two ices are chemically equivalent prior to irradiation, and that any subsequent differences in spectral evolution can be attributed to substrate effects rather than differences in initial ice composition. 214

5.12 Evolution of infrared spectral features for a 50:50 formamide-water ice mixture deposited on a ZnSe window and irradiated with 60 keV S^{5+} ions at 90 K. (a) Full mid-infrared spectrum across all fluences. (b) Formamide degradation tracked via CH and NH_2 bending modes. (c) Emergence of CO and OCN^- features post-irradiation. (d) Progressive formation of CO_2 with fluence. All spectra are colour-coded by increasing ion fluence, from pre-irradiation (spectrum 1, yellow) to post-final irradiation (spectrum 8, dark purple), with each number in between representing the fluence increment number. 215

5.13 Near-infrared observations of Europa's surface from Galileo/NIMS, showing the distribution of non-ice components interpreted as hydrated salts. Panel (A) presents a near-hemispheric albedo map, while (B) and (D) highlight concentrations of non-ice material (red shading) associated with darker terrains, including chaos regions and lineae. The association of salts with these geologic units supports their identification as evaporite-like deposits, likely formed by briny fluids reaching the surface. **Credit:** Reproduced from T. B. McCord et al., *Science*, doi:10.1126/science.280.5367.1 (1998), AAAS, [64]. 225

6.1 Evolution of infrared spectral features for a 50:50 formamide-water ice mixture deposited onto a NaCl window, at 90 K, and irradiated with 2 keV electrons. These spectra display the pre-irradiation spectrum (yellow) and the post-irradiation spectrum (dark purple). 242

6.2 Evolution of infrared spectral features for a 50:50 formamide-water ice mixture deposited onto a ZnSe window, at 90 K, and irradiated with 2 keV electrons. These spectra display the pre-irradiation spectrum (yellow) and the post-irradiation spectrum (dark purple). 246

6.3 Enhanced colour image of Europa where the reddish linear features show cracks and ridges, the "chaos terrain". The red material at the ridges and chaos terrains is a non-ice contaminant, likely salts brought to the surface from the ocean. Sourced: NASA/JPL/University of Arizona. . 257

7.1 An image acquired by the LASCO C2 coronagraph instrument on the ESA-NASA SOHO spacecraft showing a widely spreading coronal mass ejection (CME), taken in January 2002. Such eruptions contribute strongly to the Sun's vacuum-ultraviolet (VUV) output, which in turn irradiates the surfaces of outer Solar System bodies, including Europa [1]. **Credit:** ESA/NASA/Soho. 267

7.2 Schematic of the experimental geometry for VUV irradiation of formamide-water ices on NaCl substrates. The VUV beam is incident from the vacuum side, ensuring that absorption arises only from the condensed film and not from the NaCl substrate. 268

7.3 VUV absorption spectra of formamide-water ices collected pre- and post-irradiation at 10, 50, and 90 K for **Experimental Run 1**. All experiments used NaCl substrates and 9 eV photon irradiation. Sharp vertical features ('spikes') that appear at fixed energies are instrumental artefacts (e.g. detector noise or residual lamp structure) and do not correspond to molecular absorption bands. 273

7.4 Subtraction spectra (post- subtract pre-irradiation) of formamide-water ices deposited on NaCl substrates at 10, 50, and 90 K for **Experimental Run 1**. The differential absorbance isolates photochemically induced changes. 273

7.5 Full width at half maximum (FWHM) of the formamide W-band as a function of temperature for Experimental Run 1, fitted over a common 210-280 nm window. Pre-irradiation values are shown as filled circles and post-irradiation values as filled squares; the hollow marker denotes a low-confidence fit (see discussion on p. 277). 278

7.6 TPD spectra for **Experimental Run 1** experiments showing the thermal evolution of irradiated formamide-water ices from initial deposition temperatures to 200 K. 279

7.7 VUV absorption spectra of formamide-water ices collected pre- and post-irradiation at 10, 50, and 90 K for **Experimental Run 2**. Sharp vertical features ('spikes') that appear at fixed energies are instrumental artefacts (e.g. detector noise or residual lamp structure) and do not correspond to molecular absorption bands. 281

7.8 Subtraction spectra (post- subtract pre-irradiation) of formamide-water ices deposited on NaCl substrates at 10, 50, and 90 K for **Experimental Run 2**. 281

7.9 VUV absorption spectra of formamide-water ices collected pre- and post-irradiation at 110 and 130 K for '**Experimental Run 2**. Sharp vertical features ('spikes') that appear at fixed energies are instrumental artefacts (e.g. detector noise or residual lamp structure) and do not correspond to molecular absorption bands. 286

7.10 Subtraction spectra (post- subtract pre-irradiation) of formamide-water ices deposited on NaCl substrates at 110 and 130 K for **Experimental Run 2**. 286

7.11 Full width at half maximum (FWHM) of the formamide W-band as a function of temperature for Experimental Run 2, fitted over 230–300 nm (50 K, 90 K) and 210-280 nm (110 K, 130 K). Pre-irradiation values are shown as filled circles and post-irradiation values as filled squares; hollow markers denote low-confidence fits (see discussion on p. 287). The 10 K spectrum is excluded (see discussion on p. 287). 288

7.12 TPD spectra for Experimental Run 2 experiments, showing the thermal evolution of irradiated formamide-water ices from initial temperatures to 300 K. 289

A.1 Representative dose-response curve illustrating the G-value extraction procedure described in this appendix, shown here for the 1328 cm^{-1} formamide band under S^{5+} ion irradiation on a ZnSe substrate. Black squares represent experimental data points; the red curve shows the fitted double-exponential decay function (Equation A.2). This procedure was applied identically to all ion irradiation datasets. 316

List of Tables

2.1 Representative laboratory analogue experiments performed relevant to the icy moons of Jupiter and the study of ice-mineral interfaces. 58

3.1 Common electronic transitions observed in the VUV region, including typical origin and destination orbitals [19, 20]. 97

3.2 Ion properties and energy deposition characteristics for H^+, O^{2+}, and S^{5+} irradiating a 50:50 H_2O/formamide ice mixture at 90 K. Deposited energy and linear energy transfer (LET) values are based on SRIM simulations, assuming ice thicknesses between 237-278 nm [77]. For protons, only partial energy deposition occurs, while oxygen and sulfur ions deposit their full energy within the ice. 115

3.3 Energy deposition characteristics of electrons and VUV photons used to irradiate cryogenic formamide-water ices. Penetration depth and LET for electrons are approximate, based on ESTAR simulations in H_2O. Values reflect expected behaviour in H_2O-rich ices at 90 K and may vary slightly with composition. 117

4.1 Combined experimental irradiation conditions for formamide-water ices across ion, electron, and photon experiments. Energies are listed with native units (keV for ions/electrons, eV for photons). Dashes indicate not applicable or not reported. 150

4.2 Experimental parameters for ion irradiation of cryogenic formamide-water ices on NaCl and ZnSe windows at 90 K. Ice composition is given as the molar ratio of formamide to water. Energies correspond to the incident ion kinetic energy delivered by the Atomki-ECRIS. 164

4.3 Summary of electron irradiation experiments (2 keV) through NaCl and ZnSe windows. All runs were performed at 90 K. Total fluence and ice thickness values are also provided. 168

4.4 Summary of experimental irradiation conditions for Sets 1 and 2. Both sets used photon irradiation (9 eV) through a NaCl window; the only variable was the sample temperature, as listed. 171

5.1 Experimental conditions for ion irradiation of formamide–water ices at 90 K on NaCl and ZnSe substrates. 185

5.2 Cumulative ion fluences corresponding to the spectrum indices used in Figures 5.2-5.12. 190

5.3 Radiolysis yields (G-values) for formamide on NaCl and ZnSe windows under ion irradiation. Listed are destruction yields $G(-M)$ and product formation yields $G(+P)$ (molecules per 100 eV) for the main infrared absorption bands. Uncertainties are quoted with two significant figures; central values are rounded consistently. A dash indicates not applicable. 219

5.4 Mean survival times of formamide under irradiation, averaged across H^+, O^{2+}, and S^{5+} projectiles, for the 1388 and 1328 cm^{-1} bands on NaCl and ZnSe windows. Values are reported as mean ± uncertainty ($CL = 95\%$), in years. 223

6.1 Summary of experimental irradiation conditions for electron irradiation experiments, and the transmission range of the windows. Samples were irradiated at 2 keV through different windows, with varied ice compositions and thicknesses. 249

6.2 Summary of fluence, $G(-M)$ values, and destruction efficiency for electron irradiation experiments at 2 keV through different windows. 252

7.1 Summary of experimental irradiation conditions for Experimental Runs 1 and 2. Both runs used photon irradiation (9 eV); the VUV beam impinged from the vacuum side. Ice thicknesses here are displayed as estimates only. The same fluence applies to all temperatures. 268

7.2 Summary of dominant physical and spectral processes observed during VUV irradiation of formamide-water ices across the investigated temperature range. 291

Chapter 1

Thesis Scope and Objectives

1.1 Research Aims and Objectives

Prebiotic chemistry refers to the set of chemical processes that occur in the absence of life but contribute to the formation of biologically relevant molecules, such as amino acids, nucleobases, sugars, and other complex organic compounds. These reactions are considered precursors to life and are driven by various environmental factors, including radiation, temperature, and the presence of key molecular building blocks. In the context of this thesis, prebiotic chemistry is explored under simulated outer Solar System conditions, where the focus is on the survivability and transformation of organic molecules such as formamide. Understanding the potential for prebiotic chemistry to occur in the outer Solar System and on icy moons such as Europa requires a detailed examination of the destruction of prebiotically relevant molecules, those that either act as precursors to biologically important compounds or contribute to pathways leading to their formation, and the subsequent generation of complex organic molecules (COMs), which contain carbon and hydrogen and are crucial for life.

In this thesis, the research aims to assess the survivability, destruction pathways, and spectral evolution of formamide (NH_2CHO) - a molecule central to prebiotic chemistry - when embedded in water-rich ices and exposed to various types of ionising radiation under cryogenic conditions relevant to the outer Solar System.

The research described in this thesis had the following objectives:

- To simulate radiation processing of formamide-water ices at temperatures relevant to the mean annual surface temperature of Europa (90 K) under ion, electron, and VUV irradiation.
- To investigate the temperature dependence of the ice response to VUV irradiation.
- To monitor the degradation of formamide and track the appearance of new IR/VUV spectral features indicating the formation of new species, using in-situ spectroscopy.
- To quantify molecular destruction and product formation using radiation chem-

ical yields (G-values).

- To assess the influence of irradiation type, fluence, and substrate material (NaCl versus ZnSe) on the observed chemistry.

- To contribute experimental data relevant to icy body environments such as Europa, Ganymede, and Enceladus, and contextualise results with upcoming missions (e.g., JUICE, Europa Clipper).

1.2 Design and Methodology

The studies presented in this thesis employed a series of experimental designs aimed at simulating the radiation-driven chemistry experienced by formamide in different astrophysical/astrochemical environments. These include comets, trans-Neptunian objects, and icy moons like Europa and Ganymede, as well as extraplanetary environments such as protoplanetary discs. These environments are of particular interest due to their low temperatures, high radiation exposure, and potential for hosting prebiotic molecules.

The experimental methodology centres around the preparation of formamide-water ice mixtures, which are cryogenically deposited onto sodium chloride (NaCl) or zinc selenide (ZnSe) substrates at 90 K - chosen to reflect the temperatures of such environments. NaCl was selected as a geochemically relevant analogue for Europa's chloride-rich surface, whilst ZnSe served as a chemically inert reference substrate, allowing substrate-driven effects to be isolated. These ices were then subjected to controlled irradiation using a range of astrophysically relevant radiation sources. Ion irradiation with H^+, O^{2+}, and S^{5+} ions was carried out at the Atomki ECRIS facility in Hungary, simulating high-energy cosmic-ray particles. Experiments involving electron and vacuum ultraviolet (VUV) photon irradiation were conducted at the National Synchrotron Radiation Research Centre (NSRRC) in Taiwan, aiming to replicate the solar wind.

In-situ Fourier Transform Infrared (FTIR) spectroscopy and vacuum ultraviolet (VUV) absorption spectroscopy were used to monitor the changes in molecular features. These techniques can identify degradation patterns and the formation of new chemical species. Tracking key vibrational and electronic transitions associated with

formamide and its radiolysis products provided key insights into the effects of irradiation. Where possible, radiation chemical yields (G-values - defined as the number of molecules formed or destroyed per 100 eV of absorbed energy) were calculated from the spectral data to quantify the efficiency of molecular destruction and product formation. Furthermore, the calculated results were used to determine the survivability of formamide, and subsequently, how long formamide could survive on Europa's surface under its local radiation environment. In addition, preliminary residue analysis was attempted using LC-MS and spectrophotometry, but these techniques did not produce interpretable results and were therefore not pursued further.

1.3 Expected Outcomes

The experiments described in this thesis provide insights into the destruction patterns of formamide when embedded in cryogenic water ice and subjected to a range of ionising radiation types. By monitoring the evolution of key vibrational and electronic signatures throughout irradiation, this work aims to characterise the pathways and efficiencies of radiation-driven molecular degradation under outer Solar System-like conditions.

The calculation of G-values is a critical aspect of this study, offering quantitative measures of formamide destruction and product formation across different irradiation types, fluences, and substrate materials. This approach allows for a more precise definition of the threshold conditions under which formamide becomes unstable or undergoes chemical transformation. The presented results, therefore, may provide some constraints on the fate of formamide in a range of astrochemical settings.

These findings contribute to broader efforts to model radiation chemistry in both planetary and interstellar ices, and establish comparative data for interpreting infrared and VUV spectral signatures from icy bodies and the interstellar medium. In environments where molecular survivability under irradiation is crucial to assessing chemical evolution and habitability, such experimental data are indispensable. Moreover, recurring degradation products - particularly small, astrochemically significant species such as CO, HNCO, or OCN^- - may serve as indirect tracers of formamide's prior presence

in space environments, with implications for remote sensing and future observations.

This research also lays the groundwork for future residue analysis, aimed at identifying more complex or long-lived products resulting from radiation processing. While full residue characterisation is beyond the scope of this thesis, the experimental basis for such investigations has been firmly established.

The outcomes of this study are relevant to upcoming exploratory missions such as ESA's JUICE (JUpiter ICy Moons Explorer) and NASA's Europa Clipper, both of which will investigate the surface and near-subsurface chemistry of Jupiter's icy moons. An illustration of the Europa Clipper spacecraft is shown in Figure 1.1. The interpretation of returned IR and UV spectra from these missions will rely heavily on laboratory analogue studies simulating radiation-driven processes in planetary ices. While this thesis represents one contribution among many in the field, the data presented here provide valuable reference points for recognising molecular degradation patterns and identifying spectral features associated with the breakdown of organic molecules.

More broadly, the results presented in this thesis will contribute to a growing experimental framework for evaluating the survivability and spectral detectability of prebiotically relevant compounds in irradiated ices. This is essential not only for understanding the surface chemistry of icy moons and interstellar ices but also for assessing the broader astrobiological potential of these chemically active, radiation-rich environments.

1.4 Thesis Overview

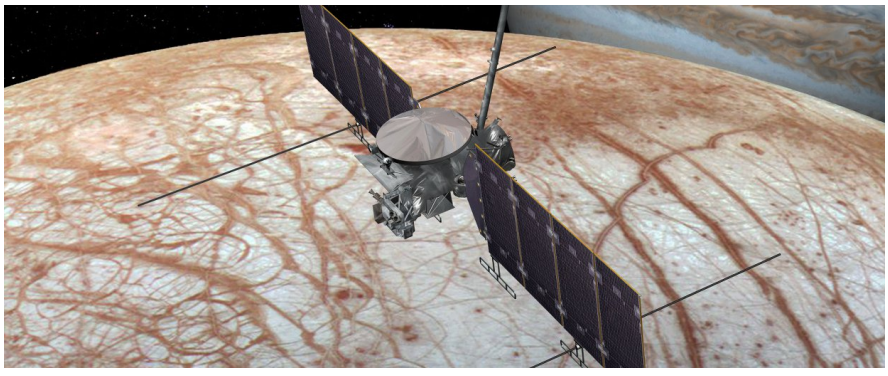


Figure 1.1: This illustration shows NASA's Europa Clipper mission doing a flyby of Europa. **Credit:** NASA/JPL-Caltech.

The remainder of this thesis describes the radiation-driven chemistry of formamide-water ice and its behaviour under outer Solar System conditions. The thesis is organised in eight chapters. Chapter 2 discusses the concept of prebiotic chemistry, the theoretical background and physical chemistry underpinning the radiolysis of formamide, the experimental methodologies employed, and the methods for analysing the results from ion, electron, and VUV irradiation.

Chapter 3 outlines the essential theoretical background relevant to this work. This includes a review of the physical chemistry of formamide, key concepts in astrochemistry, and the spectroscopic methods used to monitor radiation-induced molecular changes. Particular focus is given to in-situ infrared (IR) and vacuum ultraviolet (VUV) spectroscopy, alongside the fundamental radiation-chemistry processes that operate at cryogenic temperatures.

Chapter 4 describes the experimental methods used in this research. This includes sample preparation protocols for formamide-water ices, deposition onto cryogenically cooled substrates, and details of the irradiation conditions. The chapter also introduces the facilities where experiments were conducted: the University of Kent, Atomki (Hungary), and the National Synchrotron Radiation Research Centre (NSRRC) in Taiwan.

Chapters 5, 6, and 7 present and analyse the experimental results from ion, electron, and VUV irradiation experiments, respectively. These chapters include analyses of IR and VUV spectra, determinations of G-values for formamide degradation and product formation, and identifications of major radiolysis products. Comparisons are also made between experiments using NaCl and ZnSe substrates, offering insight into the role of the underlying substrate. The results are then discussed in the context of formamide survivability and its potential persistence on icy moons such as Europa.

Finally, Chapter 8 summarises the thesis's key findings and explores their broader implications. This includes a discussion of how the results inform the understanding of radiation chemistry in icy environments and their relevance to astrobiological targets in the outer Solar System. The Chapter also briefly considers the potential scientific impact of upcoming missions such as Europa Clipper and JUICE.

Chapter 2

Introduction to Prebiotic Chemistry and the Role of Formamide

2.1 Prebiotic Chemistry

Prebiotic chemistry is the study of the reactions and molecules that led to the emergence of life on Earth, as well as how comparable chemical pathways could operate on other planetary bodies, [1]. Prebiotic chemistry encompasses the abiotic formation and transformation of molecular species that are either building blocks of life or intermediates in plausible pathways toward life's emergence. It includes photochemical, radiolytic, thermal, and catalytic reactions occurring in early planetary or astrophysical environments. The formation of life depends heavily on several key factors: essential elements, often referred to as CHNOPS (Carbon, Hydrogen, Nitrogen, Oxygen, Phosphorus, and Sulphur), are necessary when investigating the formation of simple organics required for life to exist. A consistent energy source and liquid water are also necessary to facilitate the chemical reactions essential for the formation of these simple organic molecules. These factors, in combination with a suitable environment, are considered among the necessary prerequisites for life's emergence, though the precise conditions and pathways through which life arises remain an open question. In the primordial Earth, some processes enabled the formation of the building blocks of life, and prebiotic chemistry seeks to uncover what these processes were and how they contributed to the development of modern life. Most research in the field of prebiotic chemistry involves simulating the conditions of early Earth - such as reducing atmospheres, hydrothermal environments, or UV-irradiated aqueous solutions - and subjecting simple molecules such as water, ammonia, methane, and hydrogen cyanide to these conditions in order to assess which organic compounds can form abiotically, [2, 3].

2.1.1 The Miller-Urey Experiment

Prebiotic chemistry developed following the groundbreaking simulation experiment conducted by American chemist Stanley Miller under the guidance of his supervisor, American scientist Harold C. Urey [4]. This experiment, known as the Miller-Urey experiment, marked the inception of modern experimental research into the origins of life, [5]. Their experiment, conducted in 1953, sought to determine whether simple

organic compounds essential to life, such as amino acids, could form abiogenically under conditions relevant to Earth's early atmosphere. Their hypothesis proposed that these simple organic molecules would form through chemical reactions involving those inorganic molecules thought to have existed on early Earth. Several biologically relevant amino acids were successfully synthesised in this experiment, demonstrating that chemical evolution was possible under these conditions.

In essence, the Miller-Urey experiment is a chemical synthesis experiment that simulated Earth's early atmosphere. Synthesis was achieved by conducting a closed experiment using a mixture of simple inorganic molecules - methane, ammonia, and hydrogen - which served as an analogue of the primordial atmosphere. Two large boiling flasks were connected, allowing water to pool and gases to mix. Furthermore, in one of these boiling flasks, the water was boiled to produce a vapour and circulate the gas. Figure 2.1 shows a schematic of the original Miller-Urey experiment. Initially, boiling the water did not provide enough energy for chemical evolution; therefore, Stanley Miller added a spark discharge to mimic lightning. This closed system ran for a week, and during this time, the scientists used paper chromatography to show that the amino acids glycine, α-alanine, and beta-alanine had successfully formed, [6].

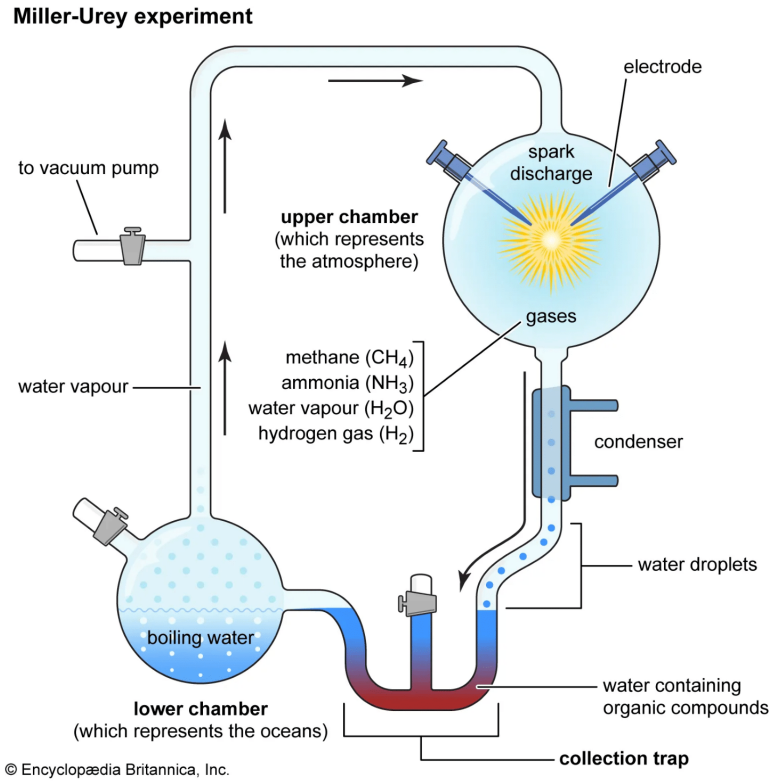


Figure 2.1: Schematic depicting the set-up of the original Miller-Urey experiment. **Credit:** By courtesy of Encyclopædia Britannica, Inc., copyright 2023; used with permission, [4].

A modern re-evaluation of the Miller-Urey experiment, performed by Criado-Reyes et al. (2021) [7], revealed that the borosilicate glass used in the apparatus, commonly chosen for its thermal stability and chemical resistance, was not as inert as previously assumed. Under the experiment's alkaline conditions, the inner glass surface partially dissolved, releasing silica and trace metal oxides while exposing new reactive sites. This behaviour mimicked the interaction between early Earth's rocky crust and alkaline waters, effectively making the glassware itself a catalytic component. Experiments comparing borosilicate to inert glass showed that borosilicate systems produced a greater diversity and yield of organic compounds, including amino acids found exclusively in its presence and even the dipeptide glycylglycine, the simplest molecule with a peptide bond. These findings highlight that not only atmospheric composition but also mineral-solution interfaces can critically influence prebiotic synthesis pathways - supporting the broader notion that surface catalysis may have been central to life's chemical origins.

The Miller-Urey experiment was a pivotal moment for prebiotic chemistry and for the study of the origins of life. Not only did the experiment show that chemical evolution is feasible from the simplest chemical ingredients, but it also provided a broader context for life's origins by suggesting which kinds of organic molecules could plausibly have been the first steps towards life on primordial Earth. This experiment has led to a massive increase in interest in prebiotic chemistry and subsequently enabled experimental research into the synthesis of various biomolecules [2].

2.1.2 Key Concepts and Mechanisms

Prebiotic chemistry focuses on producing the organic compounds necessary for creating life, but it also involves the study of the self-assembly of the first living organisms. The Strecker synthesis is a prime example of this. Adolf Strecker was a nineteenth-century chemist who was the first researcher to successfully synthesise an amino acid in the laboratory [3]. Strecker synthesis is present within the Miller-Urey experiment. In his paper, [8], Strecker discusses his experiment on the artificial formation of lactic acid and an α-aminonitrile structurally related to glycine. This intermediate is a precursor to what is now known as the Strecker synthesis, in which the α-aminonitrile hydrolyses to form amino acids. In particular, Strecker demonstrated that α-amino acids can be synthesised by reacting an aldehyde with ammonia and hydrogen cyanide. This process first forms an aminonitrile, which is then hydrolysed to form amino acids. The significance of the Strecker synthesis is that it provides a straightforward chemical pathway for synthesising amino acids from simple, prebiotically plausible precursors - an aldehyde, ammonia, and hydrogen cyanide - all of which are inorganic or simple organic molecules likely present on the early Earth (see Figure 2.2) [2, 3]. This demonstrates how complex organic molecules (COMs) central to biology could arise abiotically from a limited set of simple chemical ingredients under the conditions of the primordial environment.

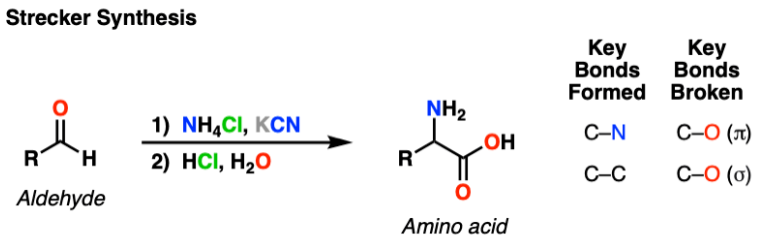


Figure 2.2: Overview of the Strecker synthesis. An aldehyde reacts with ammonia (from NH_4Cl) and cyanide (KCN) to form an α-aminonitrile, which is subsequently hydrolysed under acidic conditions to yield the corresponding α-amino acid. Key bond-forming steps include C-N and C-C formation, while hydrolysis breaks the C=O π-bond and C-O σ-bond of the nitrile intermediate. **Credit:** Reproduced with permission from J. Ashenhurst, Master Organic Chemistry, [9].

Basic organic molecules such as amino acids, sugars, and fatty acids are derived from the Krebs cycle via critical intermediates. The Krebs cycle, also known as the citric acid cycle, is an essential metabolic pathway that occurs within the mitochondria of cells [10]. However, its importance to prebiotic chemistry lies in the fact that it may have existed in primitive forms before life evolved into more complex forms, serving as a basis for the development of more complex metabolic pathways. Therefore, the Krebs cycle provides the precursor for amino acid biosynthesis. Davey et al. (2017) [11] explored how the Krebs cycle can occur without the use of enzymes, demonstrating the ability of simple organic catalysts to form essential prebiotic precursors. The paper demonstrated how some of the core reactions in the Krebs cycle could have been catalysed using inorganic species under prebiotic conditions.

There have been many instances in which prebiotic chemistry has demonstrated the ability to synthesise the building blocks of life using simple molecules under prebiotic conditions. The next step for these simple organic molecules is to develop in a biologically relevant way by polymerising into more complex organic molecules, such as nucleotides and RNA. RNA molecules are critical to the study of prebiotic chemistry, as they carry genetic information and act as catalysts in early life forms. The formation of RNA is thought to represent an early stage in the transition toward greater molecular complexity, providing a template for the eventual emergence of more sophisticated biomolecules such as DNA, proteins, and polysaccharides, and ultimately contributing to the conditions necessary for the first living systems.

Polymerisation refers to the process by which small molecules, monomers, join together to form networks, such as polymers. Under certain conditions, simple molecules can self-assemble via processes such as hydrogen bonding to form higher-order structures [12]. Polymerisation is crucial to prebiotic chemistry as it influences the availability and organisation of nucleotides and nucleosides necessary to form RNA. Self-assembly could have played a critical role in concentrating and organising reagents, thereby allowing the formation of longer RNA chains, which, as mentioned previously, is essential for investigating the origins of life.

Another key aspect of prebiotic chemistry is the critical role of energy and catalysts when discussing life's origins. Chemical energy sources, such as isonitriles (R—NC, where R is an organic group), could have been harnessed to drive the polymerisation of basic organic or even inorganic molecules, [13]. Furthermore, more basic energy sources, such as UV light or ionising radiation, are crucial for driving essential prebiotic reactions. For example, UV light is considered to have had a dual role in prebiotic reactions on the primordial Earth, initially triggering molecular synthesis but also leading to photodissociation and fragmentation [14]. Whilst the destructive effect of UV light may be seen as a negative feature, it can encourage the formation of new products, which can react with new molecules within the system.

2.1.3 Current Theories and Models

Many current theories and models have been proposed to describe the formation of basic life on early Earth. The two most highly debated theories are the 'Primordial Soup' theory and the Hydrothermal Vents theory. 'Primordial Soup', also known as 'Prebiotic Soup', refers to the idea that aqueous solutions of organic compounds existed within bodies of water on early Earth. These primordial soups would have resulted from endogenous abiotic synthesis and the delivery of interstellar medium molecules via cometary and meteoritic collisions. This theory suggests that the first living systems evolved from said aqueous solutions by gradually forming more complex structures through polymerisation and self-assembly, [15]. A simplified illustration of this concept is shown in Figure 2.3.

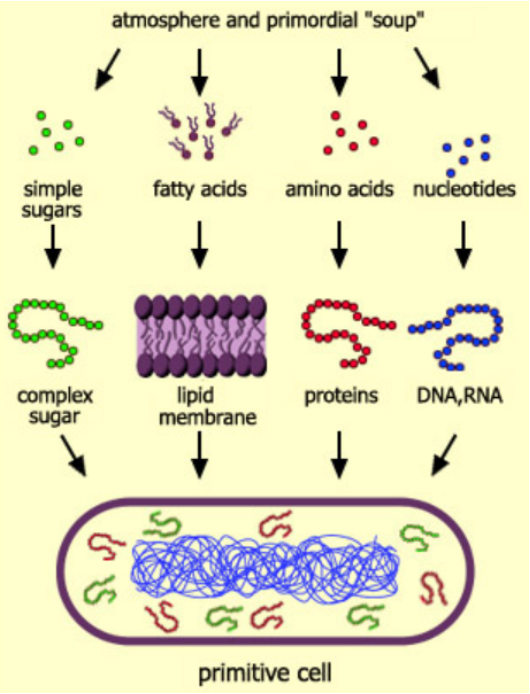


Figure 2.3: Simplified illustration of the "primordial soup" concept. Simple organic molecules such as sugars, fatty acids, amino acids, and nucleotides accumulate in early Earth's surface waters and assemble into more complex structures, such as polymers, membranes, and eventually primitive cells. **Credit:** Reproduced from 'The Brain from Top to Bottom' by Bruno Dubuc, McGill University, under copyleft ©, [16].

The hydrothermal vents theory proposes that life originated in hydrothermal vents on the ocean floor, which eject mineral-rich water heated by the Earth's core. Alkaline hydrothermal vents may have provided favourable environments for the complex chemical pathways to form basic organic molecules, [17]. Hydrothermal vents provide a constant source of heat and chemical energy, which is crucial for driving the reactions necessary to allow the formation of organic molecules from simple precursors, [18]. Additionally, the abundant minerals in these environments provide catalytic surfaces that accelerate this process. This theory and several experiments discussed in [18] suggest that hydrothermal vents could have been sites for significant prebiotic chemical processes, including the formation of simple organic molecules, [19]. A schematic of such an environment is shown in Figure 2.4.

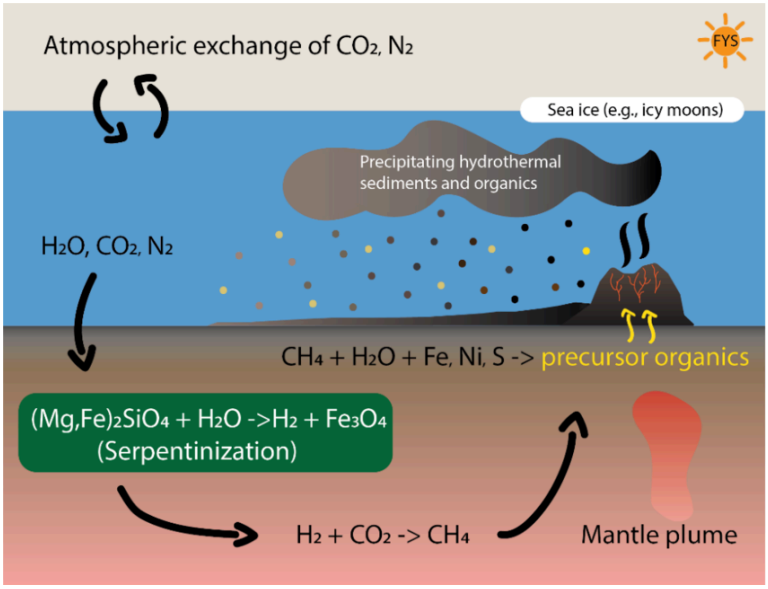


Figure 2.4: Simplified view of a hydrothermal vent system on the early Earth. Water circulates through hot rock, producing hydrogen and methane through reactions with iron- and magnesium-rich minerals. These fluids rise and mix with the ocean, where heat and minerals can help form simple organic molecules. **Credit:** Reprinted from The Archean Earth (Second Edition), C. K. Jones, M. Leung, C. Tu, S. Ebadirad, N. L. Marshall, L. Tan, T. W. Lyons, Setting the stage: Building and maintaining a habitable world and the early conditions that could favor life's beginnings on Earth and beyond, Pages 25–40, Copyright (2026), with permission from Elsevier, [20].

These are not the only two theories about how life began on Earth. Another particularly pertinent theory is that the components required to make life, or even the basic building blocks of life, may have been brought to early Earth by cometary or meteoritic bombardment. Comets and meteorites have been shown to carry organic molecules. Whilst it is unlikely that biological cells themselves formed on these comets and meteorites, it can be assumed that after bringing the necessary molecules to Earth, the reactions required to make life could occur with the addition of these molecules, [21].

2.2 The Outer Solar System and the ISM as a Laboratory for Prebiotic Chemistry

Prebiotic chemistry relevant to the origins of life does not emerge solely within planetary oceans but instead develops across a range of astrophysical environments. The low-temperature ices of the interstellar medium (ISM), the volatile-rich surfaces of comets, and the irradiated crusts of icy bodies all host chemical pathways capable of

producing and modifying organic molecules such as formamide and amino acid precursors. These settings provide essential context for understanding the chemical inputs available to Europa and the processes that may occur within its surface and subsurface environments. The purpose of this section is therefore to outline the significant stages of prebiotic chemistry across the ISM, cometary bodies, and icy planetary systems, forming the basis for the more detailed Europa discussion that follows.

2.2.1 Prebiotic Chemistry in the ISM

The interstellar medium (ISM) is a complex structure consisting of diffuse material - gas, dust, cosmic rays, and magnetic fields - that occupies the space between stars in galaxies. It is a multi-phase environment that plays a crucial role in the formation of stars, planets, and galaxies, and contributes to the long-term chemical evolution of galaxies [22, 23]. The ISM is typically divided into several phases: the hot ionised medium (HIM), the warm neutral and ionised medium (WNM/WIM), the cold neutral medium (CNM), and the dense molecular clouds [24, 25]. Of these, the dense molecular clouds are the most chemically active regions. They are cold (temperatures of 10-20 K), shielded from external ultraviolet radiation, and have sufficiently high densities for gas-phase species to freeze out onto dust grains, forming reactive ice mantles, [26, 27]. These conditions permit surface chemistry to occur on dust grains and provide the environment for low-temperature reactions driven by cosmic rays and secondary UV photons. As a result, dense molecular clouds act as “chemical factories” in which complex organic molecules can form and evolve long before planets or planetary environments exist. A famous example of such a region is shown in Figure 2.5, which depicts the Pillars of Creation, dense molecular clouds where dust-grain surface chemistry drives the formation of complex organics.



Figure 2.5: JWST image of the Pillars of Creation, illustrating dense molecular clouds within the interstellar medium. These cold, dust-rich regions host ice-coated grains where low-temperature surface chemistry produces complex organic molecules relevant to prebiotic chemistry. **Credit:** NASA, ESA, CSA, STScI, J. DePasquale (STScI), A. Pagan (STScI), A. M. Koekemoer (STScI). CC BY 4.0.

In these dense molecular clouds, gas-phase species freeze out onto sub-micron silicate or carbonaceous dust grains, forming ice mantles dominated by H_2O, CO, CO_2, NH_3, and CH_3OH, along with a range of minor species, [28, 29]. Once frozen onto the grain surfaces, these ices become sites for low-temperature chemistry driven by cosmic rays and by secondary UV photons generated within the cloud, [30, 31]. Irradiation of the ices produces reactive radicals (e.g., H, OH, NH_2, CH_3O), which can migrate across the surface and subsequently recombine, [32, 33]. This process enables reaction pathways that are inaccessible in the gas phase at such low temperatures. For example, reactions between HCO- and NH_2-bearing species can lead to the formation of formamide (NH_2CHO), while other radical-radical combinations contribute to a growing inventory of simple and complex organics, [34, 35]. Dust-grain ice mantles therefore serve as the primary chemical "substrates" of the ISM, allowing molecular complexity to emerge well before material is incorporated into comets or planetary bodies.

Recent observations have shown that dense molecular clouds are rich in organic molecules, including both simple and complex species. Many of these species are con-

sidered prebiotic and relevant to the origins of life. Simple organic molecules, such as methanol, have been detected in nearly all surveyed starless and prestellar cores [36, 37]. More complex organics, including formic acid and ketene, have also been identified in a range of star-forming environments [37, 38]. These detections demonstrate that prebiotic chemistry is active in the ISM [39]. Dense molecular cloud structures, such as the Pillars of Creation shown in Figure 2.5, visually illustrate the cold, dust-rich environments where this chemistry occurs. However, the most detailed molecular inventories come from spectroscopically rich regions such as Sgr B2, one of the most chemically complex sources in the Galaxy. Observations of Sgr B2 have revealed a wide range of prebiotic molecules, including amino acid precursors, nitriles, aldehydes, and formamide, highlighting the extent to which molecular complexity can develop before material is incorporated into comets or planetary bodies [40, 41]. Together, these detections show that many of the building blocks required for further chemical evolution originate in the ISM, where they accumulate on dust grains before being inherited by comets and other icy bodies.

During the collapse of molecular clouds, organic molecules formed in the ISM become incorporated into the material that forms protoplanetary discs, the birthplaces of planets, comets, and icy moons [42]. Observations with ALMA and JWST have revealed a range of Complex Organic Molecules (COMs) in such discs, and their presence is often interpreted as evidence of inheritance from the earlier cold-cloud phase, particularly in warm disc regions - the inner, higher-temperature zones of protoplanetary discs where ices have sublimated and in-situ formation of complex organics is thermodynamically unfavourable - where in-situ formation is unlikely [43, 44]. The enhanced D/H ratios (the deuterium-to-hydrogen ratio, a measure of isotopic enrichment that is elevated in molecules formed at low temperatures on cold grain surfaces) measured in disc organics further support this inheritance scenario, matching the isotopic signatures expected from low-temperature ISM chemistry [43]. These observations indicate that organic-rich dust and ices survive cloud collapse and are transported into the outer disc, where they serve as the raw building material for comets and other icy bodies [44]. Comets and primitive meteorites preserve organic and isotopic mixtures

that closely resemble interstellar material, implying that a significant fraction of their volatile inventory originates directly from the ISM [45, 46]. This inherited material can then be retained in comets over the lifetime of the Solar System and delivered to planetary surfaces through impacts.

Overall, these findings show that much of the organic material present in the early Solar System was inherited directly from the ISM rather than produced locally. The outer regions of protoplanetary discs, where temperatures remain low, allow this material to be preserved and incorporated into cometary nuclei. Comets, therefore, represent the next key environment for understanding how interstellar organics are stored, processed, and ultimately delivered to planetary and icy bodies, and are discussed in detail in the following section.

2.2.2 Prebiotic Chemistry in Comets

Formed in the cold outer regions of the early Solar System, comets are small, icy bodies that provide insight into the early Solar System's original building blocks. Comprised of volatile ices (such as H_2O, CO, and CO_2), organic compounds, and dust grains, comets are considered some of the most pristine and primitive objects in the Solar System [47–49]. Because most comets experience minimal thermal or aqueous alteration, the solid material they contain is well preserved, retaining components that date back to the birth of the Solar System and perhaps even earlier [50, 51]. Comets also contain a wide range of organic molecules, including simple organics, amino acid precursors, nitriles, and formamide [52–54]. This inherited material can be delivered to planetary bodies via impacts, supplying a rich assortment of organic compounds relevant to prebiotic chemistry [55, 56]. While a significant portion of this material would have been destroyed during high-velocity impacts, a substantial fraction can survive, enabling the delivery - and in some cases the synthesis - of amino acids and other prebiotic organics [55, 57].



Figure 2.6: Comet C/2014 Q2 (Lovejoy), showing its bright coma and dust tail generated as volatile ices are released from the nucleus. Lovejoy is chemically significant, with radio and submillimetre observations revealing a range of complex organic molecules, making it an important example of prebiotic chemistry in cometary comae. **Credit:** NASA/MSFC/MEO/Aaron Kingery.

Surrounding the solid nucleus of a comet is a cloud of gas and dust known as the cometary coma. The coma forms when ices in the nucleus sublimate as a result of solar heating, releasing gas and entrained dust that expands outward [58, 59]. Observations of cometary comae show that they host a chemically rich inventory of volatile organics. One well-studied example is comet C/2014 Q2 (Lovejoy)), shown in Figure 2.6, one of more than 32 comets observed by NASA's NEOWISE mission, an infrared space telescope designed to characterise near-Earth asteroids and comets [60]. Lovejoy gained significant attention as the first comet discovered to be releasing ethyl alcohol [61]. Spectroscopic observations further revealed that its coma contains H_2O, CO, CH_3OH, H_2CO, HCN, C_2H_2, C_2H_6, NH_3, CH_4, and glycolaldehyde (CH_2OHCHO) [53, 62, 63]. Many of these species (e.g. H_2O, CO, CH_3OH, H_2CO, HCN) are common "parent" molecules found in most comets [64, 65].

The detection of ethanol and glycolaldehyde - identified using the IRAM 30 m radio telescope at abundances of $\sim$0.12% and $\sim$0.02% relative to water, respectively, [52, 53] - is especially important. These two molecules are significantly more complex than the typical volatiles found in comets and represent a notable step toward biochemically relevant chemistry. At the time of their discovery (2015), they were the most chemically

complex species unambiguously confirmed in a comet. Glycolaldehyde, a simple sugar precursor involved in prebiotic reaction pathways, is particularly noteworthy because it links cometary chemistry to potential origins-of-life processes. While these detections primarily refer to volatile species released into the coma, solid-phase organics are also inferred from dust grains, returned cometary samples, and organics contained in meteorites derived from comet-like bodies.

In addition to volatile species released into the coma, comets also contain a substantial reservoir of refractory organic material embedded within their dust grains. These solid-phase organics - comprising complex hydrocarbons, polycyclic aromatic hydrocarbons (PAHs), macromolecular carbonaceous matter, and nitrogen-bearing compounds - represent a chemically richer component of cometary nuclei than the volatiles typically observed in the gas phase. Insight into this refractory inventory has come primarily from the analysis of dust grains returned by NASA's Stardust mission from comet 81P/Wild 2, which revealed the presence of PAHs, aromatic compounds, and a suite of nitrogen-containing organics [66, 67]. Interplanetary dust particles (IDPs) thought to originate from comet-like bodies similarly contain complex macromolecular organics with strong D/H and ^{15}N enrichments, consistent with an interstellar origin [67, 68]. These refractory materials are less volatile and more chemically robust than coma gases, enabling them to survive both space weathering and atmospheric entry. As a result, they constitute an essential mechanism for delivering prebiotic organics - including amino-acid precursors and other complex species - to planetary surfaces and icy bodies. This dual inventory of volatile and refractory organics highlights the chemically diverse nature of comets and reinforces their significance as carriers of inherited interstellar material throughout the Solar System.

Comets in the outer Solar System are subjected to a range of radiation sources, primarily galactic cosmic rays (GCRs), solar energetic particles, and ultraviolet (UV) photons [69, 70]. These radiation fields drive significant chemical and physical changes in cometary ices, both at the surface and to depths of several metres [69, 71]. Irradiation of these ices leads to photolysis and radiolysis, breaking apart simple molecules and producing reactive radicals such as H·, OH·, NH_2·, CH_3·, and HCO· [31, 72]. Once

formed, these radicals can migrate and recombine to create more complex organic material [70, 72]. Recombination may occur thermally - as the comet approaches perihelion and warming increases radical mobility - or non-thermally, when radicals form adjacent to one another or are produced in excited states that can overcome reaction barriers. Phase transitions within the ice can also bring radicals into contact, further promoting recombination [73–76].

Laboratory irradiation experiments in the literature strongly support these mechanisms, showing that UV, electron, and ion processing of cometary ice analogues produces a wide range of complex organic molecules, including amino acid precursors, hydrocarbons, nitriles, carbonyls, HNCO, HCN, urea, and formamide [77–79]. Although the primary focus of this thesis is Europa, the cryogenic irradiations of mixed formamide-water ices presented in this work also provide a close laboratory analogue to cometary surface processing, and therefore serve as a useful point of comparison. Specifically, the experiments described in Chapters 5 to 7, performed between 10 and 130 K, demonstrate that exposure to ultraviolet photons, electrons, and energetic heavy ions produces the same suite of radicals expected in cometary irradiation environments. These experiments consistently show radiation-driven degradation of formamide and the formation of simple formamide-derived products such as CO, CO_2, and OCN^-. The inferred reaction pathways involve intermediates like HNCO and related C-N species, which are closely linked to amino-acid precursor chemistry in other laboratory and astrochemical studies. This close agreement between low-temperature laboratory chemistry and cometary irradiation environments indicates that comets are not merely repositories of inherited interstellar material, but can also be active sites of in-situ prebiotic synthesis.

Taken together, this evidence demonstrates that comets can synthesise complex organic molecules on their irradiated surfaces. These same radiation-driven processes also operate on planetary and icy bodies, providing a natural transition to their role as chemical environments within the outer Solar System.

2.2.3 Prebiotic Chemistry on Planetary and Icy Bodies

Within astrobiology, habitability is often defined as the capability of an environment to support life, typically requiring the availability of key elements (CHNOPS), sources of chemical or physical energy, and appropriate environmental conditions such as temperature and pressure [80]. In addition to hosting liquid water, environments rich in radiation and extreme cold can also profoundly influence the chemistry of organic molecules. The icy moons of the outer Solar System - including Europa, Ganymede, Callisto, Enceladus, Titan, and Triton - provide natural laboratories for studying these processes. Their surfaces and interiors present conditions under which simple organics delivered from the ISM and comets may undergo further chemical transformation.

Many icy moons share a broadly similar internal structure: a surface ice shell, underlain by a global or regional liquid water ocean, followed by a silicate mantle and, in some cases, a metallic core. Evidence for these subsurface oceans comes from multiple lines of observation. For the Galilean moons, induced magnetic fields measured by the Galileo spacecraft indicate the presence of electrically conductive layers consistent with salty liquid water. Gravity and topography data further support internal layering, while libration measurements at bodies such as Titan and Enceladus imply decoupling between the outer ice shell and the deeper interior. The detection of water vapour plumes at Enceladus and possible plume activity at Europa provides direct evidence of subsurface reservoirs communicating with the surface. A representative schematic of the internal structure of an icy moon, including a surface ice shell, subsurface ocean, rocky mantle, and potential hydrothermal activity, is shown in Figure 2.7.

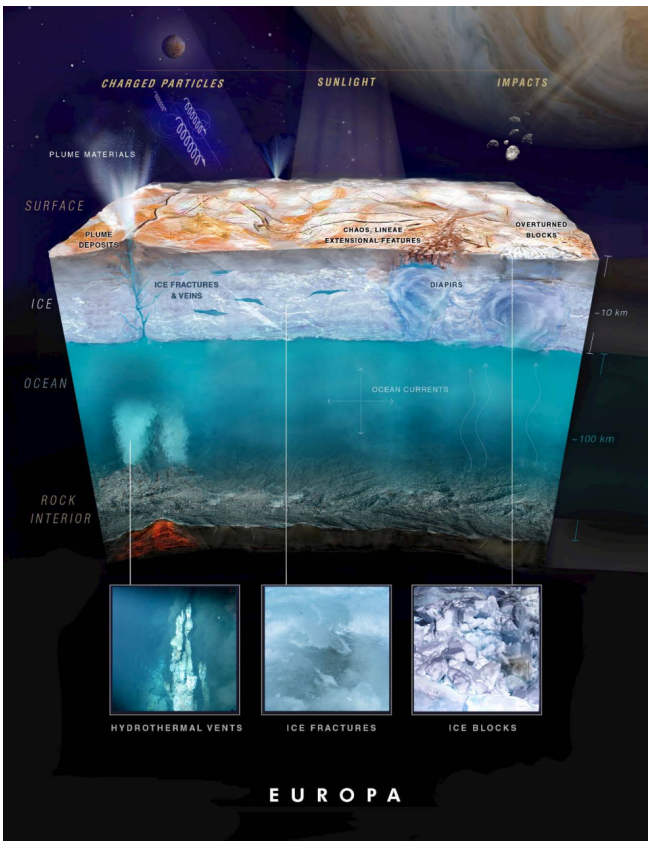


Figure 2.7: Conceptual cross-section of Jupiter's moon Europa, showing key features including the icy surface, subsurface ocean, the hypothesised hydrothermal activity at the seafloor, and the irradiation incident on the moon. These processes may support chemical energy gradients that can sustain life. **Credit:** K. Hand et al./NASA/JPL, [81].

At the base of these oceans, water-rock interactions are expected to generate hydrothermal activity similar to that of terrestrial alkaline vent systems. Serpentinisation - the hydration and alteration of ultramafic (olivine-rich) rocks - converts primary silicates into serpentine-group minerals (often with magnetite) and generates molecular hydrogen (H_2) through iron redox reactions. The resulting H_2 provides a key energy source for both abiotic and (on Earth) microbial metabolism. Such environments can drive the reduction of CO_2 and the synthesis of simple organics via Fischer Tropsch-type processes, offering a plausible mechanism for prebiotic chemical gradients within icy-moon oceans. These interior chemical systems provide a complementary pathway to the radiolytic processing that dominates at the surface.

Surface conditions on icy bodies are shaped by extremely low temperatures and varying radiation environments. Depending on their orbital configurations and magnetospheric settings, icy moons experience irradiation from solar UV photons, solar

wind ions, magnetospheric electrons and ions, and galactic cosmic rays. The interaction between Jupiter's magnetosphere and the Galilean moons, which contributes significantly to their radiation environments, is illustrated in Figure 2.8. These forms of radiation drive radiolytic processing of surface ices, breaking apart simple molecules and generating radicals that recombine to form more complex organic species. Although the intensity of irradiation varies widely, Europa experiences particularly high fluxes, Ganymede somewhat less, and Enceladus comparatively low levels, radiation-driven chemistry is a universal process across icy bodies.

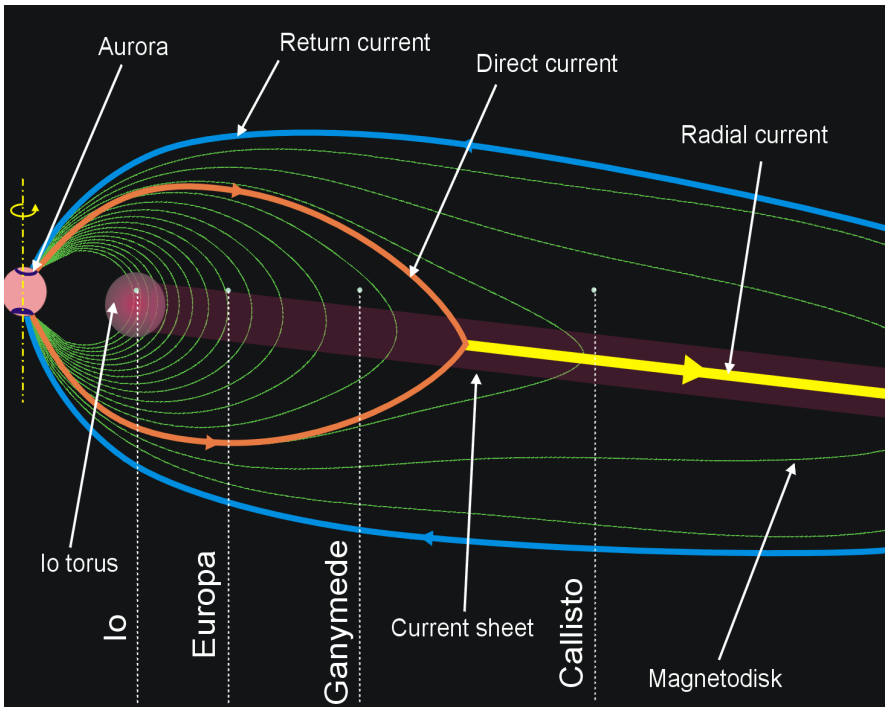


Figure 2.8: Schematic of electrical currents in Jupiter's magnetosphere and their interactions with the Galilean moons. **Credit:** Ruslik0, via Wikimedia Commons, CC BY-SA 3.0, [82].

Taken together, these factors make planetary and icy bodies critical environments for studying the stability, transformation, and potential synthesis of prebiotic molecules. Organic compounds inherited from the ISM and delivered by cometary or meteoritic infall may be altered by radiation at the surface or by hydrothermal chemistry within subsurface oceans. The experiments in this thesis investigate the behaviour of formamide-water ices under such conditions, simulating the radiation-driven chemistry relevant to the surfaces of icy bodies throughout the outer Solar System. This provides an essential foundation for the more detailed discussion of Europa that follows.

2.3 Europa as a Prebiotic Environment

Europa has long been considered one of the most promising locations for life beyond Earth. Early infrared observations revealed that its surface is dominated by water ice [83], and even before direct spacecraft exploration, several authors hypothesised that a liquid ocean might exist beneath its frozen crust [84]. Definitive evidence remained elusive until the Voyager flybys in 1979, which returned images showing a geologically young, fractured surface largely devoid of impact craters [85, 86]. The presence of widespread lineae and disrupted regions - often referred to as chaos terrains - suggested active resurfacing, potentially caused by the upwelling and refreezing of liquid water from below [87].

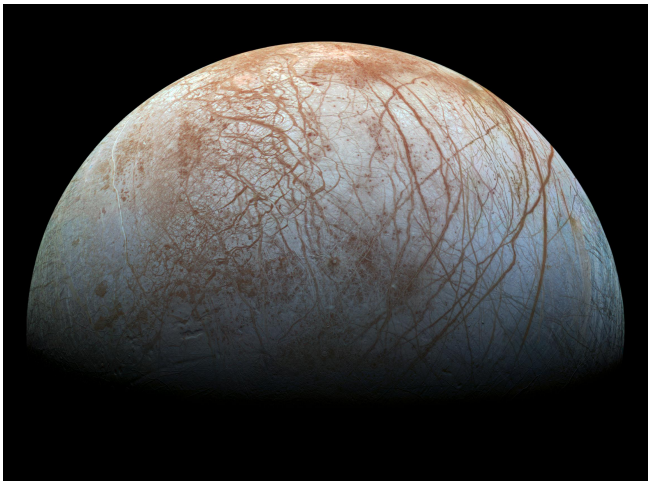


Figure 2.9: An image taken of Europa by NASA's Galileo spacecraft, showing the diversity of Europa's geology. **Credit:** NASA/JPL-Caltech/SETI Institute.

The Galileo mission, whose imagery of Europa's diverse geology is shown in Figure 2.9, provided further support for the existence of a subsurface ocean. Measurements of magnetic field perturbations indicated the presence of an electrically conductive layer capable of inducing a secondary magnetic field [86]. Given Europa's composition and thermal environment, this layer is interpreted as a global, saline liquid-water ocean beneath the ice shell. The upcoming Europa Clipper mission will refine these interpretations by measuring ice thickness, ocean properties, and potential exchange pathways between the surface and interior.

Recent observations confirm that Europa hosts several of the key chemical compo-

nents relevant to prebiotic chemistry. JWST data have revealed concentrated CO_2 in geologically young regions, suggesting an internal source [88]. Sulphur-bearing species, abundant across the trailing hemisphere, are primarily supplied by Io and implanted via Jupiter's magnetosphere [89]. Although nitrogen- and phosphorus-bearing species have not yet been definitively detected, they are expected to be present through a combination of interior processes, Io-derived material, and exogenous delivery by comets and meteorites. The inventory of essential elements on Europa remains incomplete, but evidence strongly suggests that none are uniquely absent; Europa Clipper is expected to provide the first definitive constraints [90].

With liquid water, essential elements, and plausible energy sources, Europa satisfies many of the standard criteria for habitability [91]. Hydrothermal activity at the seafloor - potentially driven by tidal heating and water-rock interactions - could generate molecular hydrogen (H_2), supporting redox gradients analogous to terrestrial alkaline vent systems [91, 92]. Such environments are considered promising sites for abiotic organic synthesis and, potentially, for sustaining microbial ecosystems. The key challenge is to determine whether these interior environments can facilitate the formation and cycling of prebiotic molecules, and whether any of this material is transported to the surface or near-surface layers that can be probed remotely.

2.3.1 Europa's Environmental Conditions

Europa's subsurface ocean is most likely maintained through a combination of tidal dissipation, radiogenic heating, and possible hydrothermal circulation. Models suggest ocean temperatures of approximately 210-270 K - below the freezing point of pure water, but consistent with a liquid state given that dissolved salts depress the freezing point and elevated pressures at depth further suppress it -, with salinities potentially comparable to or even exceeding those of terrestrial oceans, though the exact composition remains uncertain [93]. Stratification may occur within the upper ocean, with a cold, buoyant layer directly beneath the ice shell and a warmer convective region at depth [94]. Episodes of penetrative convection could account for the formation of chaos terrains by facilitating the transient ascent of warmer brines toward the surface.

Surface temperatures on Europa vary widely, from about 96 K at the equator to below 50 K near the poles, with an overall average of roughly 90 K. These temperatures change over the course of a day and with the seasons. At the equator, daytime temperatures can rise to around 130 K and fall to about 86 K at night, with the warmest point occurring a few hours after midday as the ice slowly releases stored heat [95].

Europa resides deep within Jupiter's magnetosphere and is exposed to intense fluxes of energetic electrons, protons, and heavy ions [96]. These particles drive substantial radiolysis of the surface ice, generating oxidants and reactive species that can alter surface chemistry and, potentially, be cycled into the subsurface ocean. The radiation environment is highly structured and spatially variable, as particle populations differ between the magnetic equator, plasma sheet crossings, and the leading and trailing hemispheres [97].

This variability is especially pronounced on Europa's trailing hemisphere, which is immersed in plasma originating from the Io plasma torus and therefore experiences the highest particle fluxes. Measurements from the Galileo Energetic Particle Detector (EPD) indicate that MeV electrons reach fluxes on the order of 10^{9}–$10^{10}\,\mathrm{e^{-}\,cm^{-2}\,s^{-1}}$, while energetic ions ($H^{+}$, O^{n+}, and S^{n+}) typically contribute 10^{7}–$10^{8}\,\mathrm{cm^{-2}\,s^{-1}}$ depending on longitude and hemisphere [98, 99]. These populations deliver dose rates of roughly 0.1–1 $\mathrm{Mrad\,day^{-1}}$ (10^{7}–$10^{8}\,\mathrm{Gy\,yr^{-1}}$), sufficient to drive continuous radiolysis of water ice and any embedded organics [100]. Such conditions underpin the well-known hemispheric asymmetries on Europa's surface - most notably the heavily processed, sulphur-rich trailing hemisphere - and also motivate the selection of the ion species in this study.

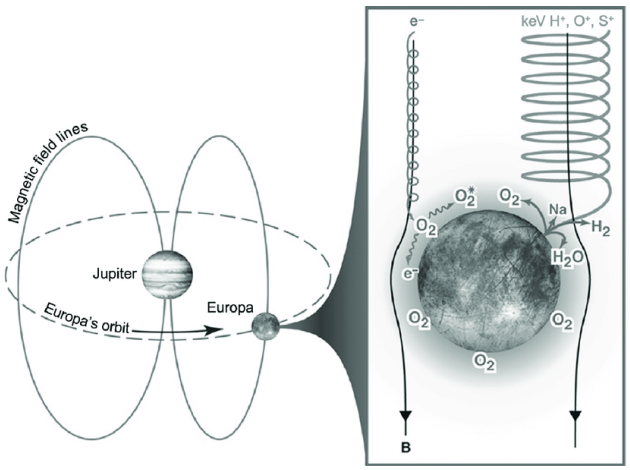


Figure 2.10: Schematic representation of Europa's interaction with Jupiter's magnetosphere. Left: Europa's orbit within Jupiter's tilted magnetic field. Right: energetic electrons and keV ions (H^+, O^+, S^+) spiral along magnetic field lines and bombard the surface, driving radiolysis, sputtering, and production of volatile species such as O_2 and H_2, which contribute to Europa's tenuous exosphere. **Credit:** Figure 1 on page 508 from Europa. © 2009 The Arizona Board of Regents. Reprinted by permission of the University of Arizona Press, [101].

Europa also possesses a tenuous, surface-bounded exosphere dominated by molecular oxygen (O_2), produced primarily through radiolysis and sputtering of surface water ice [102, 103]. Trace constituents include H_2O, Na, K, SO_2, and CO_2, some of which may be sourced from plume activity or surface-atmosphere interactions. Spatial variability in O_2 density has been observed, likely reflecting differences in surface composition, irradiation patterns, and local sputtering efficiencies [103, 104].

In summary, Europa's combination of a global subsurface ocean, potential hydrothermal activity, chemically diverse surface environment, and intense radiation processing makes it a compelling site for prebiotic chemistry. Understanding these conditions provides a foundation for evaluating whether molecules such as formamide can persist, transform, or accumulate in ways relevant to early chemical evolution.

2.3.2 Spacecraft Missions to Europa: JUICE and Europa Clipper

Europa's status as one of the most promising locations for habitability in the outer Solar System has led to the development of two primary flagship missions: ESA's JUpiter ICy moons Explorer (JUICE) and NASA's Europa Clipper. Although designed with

different primary goals, both missions share the overarching objective of investigating the composition, structure, and habitability of Jupiter's icy moons. JUICE provides a system-wide perspective through flybys of Europa and Callisto before entering orbit around Ganymede. At the same time, Europa Clipper focuses exclusively on Europa through an extensive series of low-altitude flybys. Together, these missions will deliver complementary datasets on Europa's ice shell, subsurface ocean, radiation environment, and surface chemistry. Crucially, both spacecraft carry instruments capable of detecting volatiles, salts, and organic molecules, allowing for direct assessment of Europa's prebiotic chemistry and the processes that shape its surface and near-surface ices.

2.3.2.1 The JUICE Mission

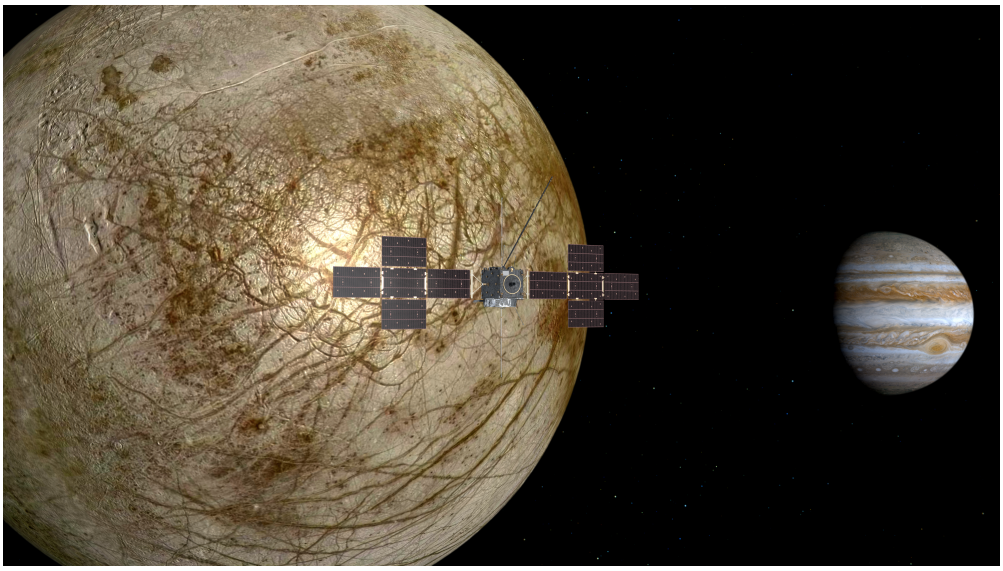


Figure 2.11: Artist's impression of ESA's JUICE spacecraft conducting a close flyby of Europa, with Jupiter visible in the background. **Credit:** ESA (acknowledgement: ATG Medialab), ESA Standard Licence.

The European Space Agency's (ESA) JUpiter ICy Moons Explorer (JUICE) mission, illustrated in Figure 2.11, was launched in 2023 to conduct detailed investigations of Jupiter and its three large icy moons: Ganymede, Callisto, and Europa [105]. After arrival in 2031, JUICE will spend several years orbiting Jupiter, performing multiple flybys of Ganymede and Callisto and two targeted flybys of Europa [106]. The mission aims to characterise the environments of these moons and assess their potential

habitability [107]. For Ganymede, JUICE will probe the structure, composition, and dynamics of its subsurface ocean; analyse its intrinsic magnetic field and surrounding plasma environment; and investigate how surface geology and chemistry relate to internal processes. During its Europa encounters, JUICE will examine the surface composition and chemistry, search for possible biosignatures, and assess how tectonics, cryovolcanism, and surface modification have shaped the moon over time. It will also probe regions that may host shallow subsurface water and investigate the structure of the ice shell. At Callisto, JUICE will study the structure of the outer ice shell and underlying ocean, map the distribution of non-water-ice materials, and examine how the moon releases material into space. These observations will also help reconstruct Callisto's past geological activity and long-term evolution [107].

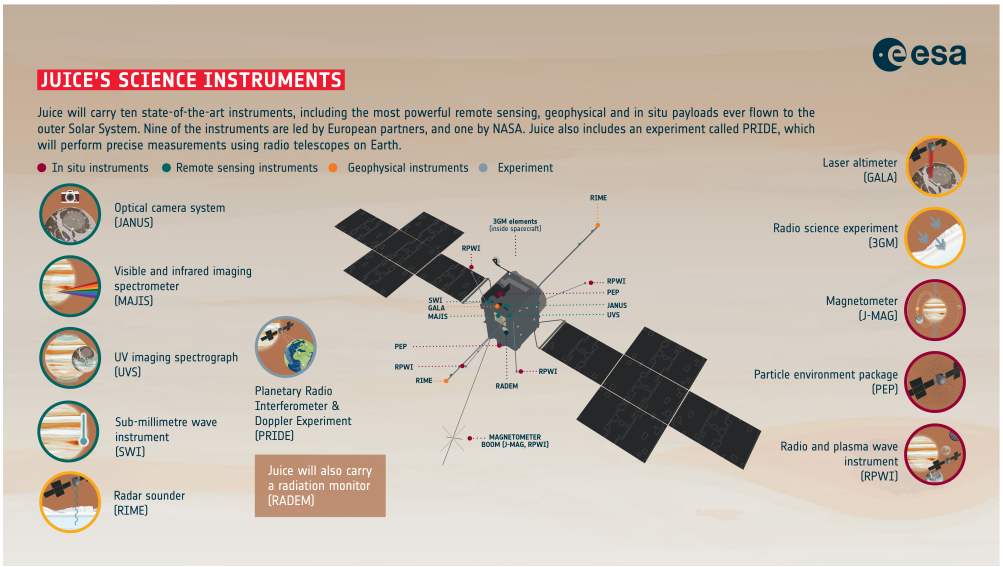


Figure 2.12: Overview of the scientific instruments aboard ESA's JUICE spacecraft. The payload includes ten state-of-the-art instruments covering remote sensing, geophysical, and in-situ measurements, designed to investigate the surfaces, atmospheres, and interiors of Jupiter's icy moons. **Credit:** ESA (acknowledgement: ATG Europe), ESA Standard Licence.

On board JUICE, ten scientific instruments work in conjunction to investigate Jupiter and its icy moons (See Figure 2.12). These include remote-sensing systems such as MAJIS, SWI, and UVS, geophysical packages like RIME and 3GM, and in-situ plasma and particle analysers such as RPWI, J-MAG, and PEP. Together, they provide a comprehensive view of each moon's surface, subsurface, and surrounding plasma environment [108]. Among these, MAJIS (Moons And Jupiter Imaging Spectrometer),

SWI (Sub-millimetre Wave Instrument), UVS (Ultraviolet imaging Spectrograph), and RIME (Radar for Icy Moons Exploration) are of particular relevance to Europa.

By combining hyperspectral surface mapping with geophysical sounding and exospheric observations, JUICE can constrain several key ingredients of prebiotic chemistry at Europa [108, 109]. MAJIS will perform hyperspectral imaging across the visible to infrared range (0.5-5.5 μm), mapping the distribution of ices, salts, CO_2/SO_2, and low-abundance organic-bearing materials, while distinguishing between radiolytic and endogenic deposits on Europa's surface at high spatial resolution [110]. SWI will measure sub-millimetre thermal emissions from the surface and exosphere, constraining near-surface temperatures and volatile abundances, and providing insight into outgassing, sputtering, and any plume-fed release that could transport material from the interior to space [111]. The UVS instrument will probe the composition and variability of Europa's tenuous exosphere, searching for signatures of plume activity and variations in atomic oxygen, hydrogen, and sulphur compounds that trace ongoing irradiation chemistry; it will also acquire ultraviolet reflectance spectra of the surface ice to help identify and map irradiation products and compositional heterogeneity [112, 113]. Meanwhile, RIME will sound the upper ice shell to depths of up to $\sim$9 km, revealing internal layering, brine inclusions, and potential shallow liquid water reservoirs - key indicators of ocean-ice exchange pathways where redox gradients and organics may concentrate [114–116]. In conjunction with contextual measurements from JANUS and the particle, field, and radiation suites (J-MAG/PEP/RPWI and RADEM), these datasets will link surface chemistry to the physical processes that drive exchange and processing, helping to evaluate whether Europa's present-day environment can preserve, transform, or mobilise prebiotic molecules [108].

2.3.2.2 Europa Clipper Mission

While JUICE will provide system-level context and targeted Europa flybys, Europa Clipper will deliver Europa-dedicated, high-sensitivity measurements (e.g., MASPEX, MISE, SUDA) to directly test the prevalence, processing, and transport of organics identified as high-value targets by JUICE.

The National Aeronautics and Space Administration (NASA) launched the Europa

Clipper mission in 2024 (Figure 2.13) with the goal of entering orbit around Jupiter and conducting 49 close flybys of Europa [117]. In contrast to JUICE, which surveys the Jovian system as a whole, Europa Clipper is a dedicated astrobiology mission focused exclusively on assessing Europa's potential habitability. Its primary science objectives are to determine whether environments exist beneath the moon's icy surface that could support life, to characterise the thickness and structure of the ice shell, and to constrain the volume, salinity, and geophysical properties of the underlying ocean [117]. The mission will investigate whether liquid water can rise toward the surface through fractures or near-surface reservoirs, examine the composition and origins of surface materials, and identify regions that may exhibit signs of recent or ongoing geological activity. By providing high-resolution, Europa-specific measurements, Europa Clipper complements JUICE's system-level context, with the two missions together offering a comprehensive understanding of Europa's interior, surface processes, and astrobiological potential.

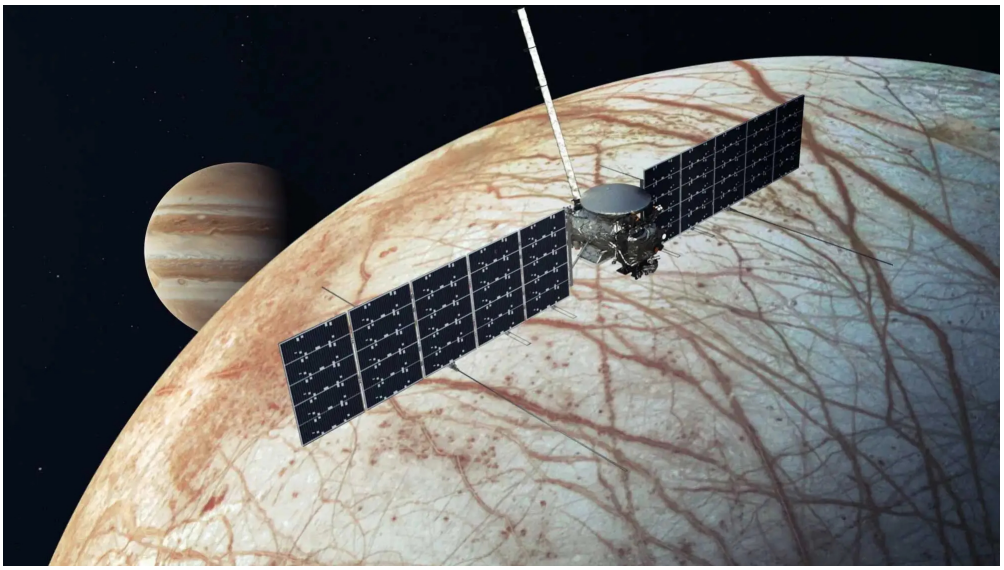


Figure 2.13: Artist's impression of NASA's Europa Clipper spacecraft conducting a close flyby of Jupiter's moon Europa. Jupiter can be seen in the background. **Credit:** NASA/JPL-Caltech.

Europa Clipper carries a suite of nine scientific instruments designed to characterise the moon's surface, subsurface, atmosphere, and plasma environment, enabling a comprehensive assessment of its habitability [118]. The payload spans high-resolution imaging, spectroscopy, geophysical sounding, and in-situ compositional analysis. The

Europa Imaging System (EIS) provides detailed colour and stereo imaging to map geological structures, identify active processes, and measure surface relief. Thermal observations from E-THEMIS (Europa Thermal Emission Imaging System) will locate warm surface anomalies and constrain textural and thermophysical properties of the ice. Europa-UVS, a far- and extreme-ultraviolet spectrograph, will analyse the composition and variability of the exosphere, search for plume activity, and detect surface frost and irradiation products.

Compositional mapping is further advanced by MISE (Mapping Imaging Spectrometer for Europa), which will survey the spatial distribution of ices, salts, organics, and thermal hotspots in the near-infrared. Subsurface characterisation is achieved through two complementary geophysical instruments: ECM (Europa Clipper Magnetometer), which will measure Europa's induced magnetic field to constrain ocean depth, salinity, and ice-shell thickness, and PIMS (Plasma Instrument for Magnetic Sounding), whose Faraday cups will characterise the surrounding plasma to correct magnetic distortions and isolate the oceanic signal. The REASON instrument (Radar for Europa Assessment and Sounding: Ocean to Near-surface) will penetrate the ice shell to reveal internal layering, potential brine pockets, and the structure of the ice-ocean boundary.

Finally, two in-situ analysers target the composition of Europa's near-surface environment. MASPEX (MAss Spectrometer for Planetary EXploration) will determine the molecular inventory of the exosphere and any plumes, offering direct insights into ocean-derived materials. SUDA (SUrface Dust Analyzer) will analyse the chemistry of dust grains ejected from Europa's surface or plumes, identifying salts, organics, and other components transported from the subsurface ocean. Together, these instruments will provide a multi-layered view of Europa's geology, composition, and internal structure, enabling robust tests of its potential habitability.

Europa Clipper's payload directly targets the detection, context, and provenance of organic molecules at Europa. MASPEX will make high-mass-resolution measurements of neutral gases in the exosphere and any active plumes, resolving key volatiles and organic compounds and constraining isotopic ratios that distinguish endogenic material from radiolytic or exogenous sources [118, 119]. MISE will map the spatial

distribution of ices, hydrated salts, organics, and thermal hotspots in the near-IR, identifying chemically distinct terrains and potential sites of recent exchange with the interior [120, 121]. SUDA will analyse the composition of dust grains lofted from the surface or plumes, detecting salts and organic-bearing particulates and linking them to their source regions [122, 123]. Thermophysical and geologic context from E-THEMIS (thermal anomalies), EIS (high-resolution colour/stereo imaging), and the geophysical pair REASON (dual-frequency ice-penetrating radar) plus ECM/PIMS (magnetometry and plasma corrections) will determine ice-shell structure, brine pockets, and ocean properties that govern redox gradients and transport pathways [118, 124–127]. In combination, these measurements will test whether Europa's present-day environment can generate, preserve, and mobilise prebiotic molecules - and whether any detected organics are surface-processed, ocean-derived, or delivered from space.

2.4 Formamide as a Key Prebiotic Molecule

Formamide (NH_2CHO) is a simple organic compound with remarkable chemical versatility, making it valuable in organic synthesis, prebiotic chemistry, and industrial applications. Its unique reactivity and ability to serve as a C1 building block[1] enables a wide range of chemical transformations and practical uses. Due to its role as a C1 feedstock, formamide is used in organic synthesis to construct more complex molecules, such as formamides, ureas, carbamates, and heterocycles, [129, 130]. With sufficient energy and environmental factors, formamide is involved in the synthesis of nucleic bases, nucleotides, amino acids and many other bioessential molecules under prebiotic conditions, [131–133]. Formamide also contains all the necessary biogenic elements: carbon, hydrogen, nitrogen, and oxygen, for such synthesis. For this, formamide is considered a central molecule in prebiotic chemistry.

[1] A C1 building block, in chemistry, refers to a simple molecule containing a single carbon atom that can be used as a starting material in chemical synthesis, [128].



Figure 2.14: Spitzer Space Telescope infrared image of the massive star-forming region DR21 in the Cygnus X complex. This molecular cloud hosts several dense clumps, including DR21(OH), where recent millimetre and submillimetre surveys have detected complex organic molecules such as formamide (NH_2CHO) in the gas phase, [134]. **Credit:** NASA/JPL-Caltech.

Formamide's stability and reactivity in both its gas and aqueous phases allow it to serve as a central feedstock and reaction medium for the formation of key biological molecules, supporting hypotheses about the origin of informational polymers and early life [135, 136]. Formamide is capable of producing complete panels of prebiotically relevant molecules, and is capable of doing so whilst also overcoming some limitations of water, such as the hydrolysis of key bonds needed for life, [133, 137].

Formamide is abundant in astrophysical environments, having been detected in star-forming regions and molecular clouds, protostellar shocks and outflows, and comets, [134, 138]. The molecule has consistently been observed in the ISM, for example, in the giant molecular cloud 'Sagittarius B2', [139–141], imaged in Figure 2.15. Equally, formamide has been observed in low-mass protostars, [142]. These detections suggest that formamide is common in star-forming regions, comets, and protostellar shocks, further discussed in Section 2.4.1. Additionally, formamide is efficiently formed in both gas and solid phases, highlighting its potential as a prebiotic precursor. Its abundance in these environments supports the idea that formamide could have been delivered to Earth (and other such planets), contributing to the emergence of life, [143, 144].

Furthermore, formamide is said to be closely related to isocyanic acid (HNCO), which is most likely formed on the icy mantles of dust grains during the cold stages of

star formation, [145]. Similarly, Frigge et al. (2018) [146] investigates the formation of N-methyl formamide ($HCONHCH_3$), a molecule related to formamide, in astrochemical ices and more specifically, in regions of space exposed to cosmic rays. These studies expand upon the fact that formamide is abundant in the ISM, underscoring its potential as a precursor to life. Additionally, these studies agree that formamide could have been brought to planetary bodies via cometary and meteoritic material, allowing for the complex chemical pathways that form life to occur.

Given formamide's prevalence in star-forming regions and its ability to generate bioessential compounds under prebiotic conditions, it is an ideal molecule to provide the necessary prebiotic components in the design of an outer Solar System analogue, helping simulate the potential chemical pathways that could occur. In this thesis, formamide is investigated not as a pure substance, but in combination with water ice, to better simulate the molecular environments expected on icy bodies in the outer Solar System. Water is the dominant volatile in these settings, and any formamide present - whether delivered by cometary impact or formed in-situ - is likely to be embedded within H_2O-dominated ices. This mixture also more accurately reflects the chemistry of interstellar and cometary ices, where formamide-water mixtures have been observed alongside water and other volatiles. Moreover, water ice plays an active chemical role under irradiation: it produces reactive species such as OH· and H· that can influence the degradation pathways of embedded molecules. Studying the radiation-driven chemistry of formamide in a water-ice matrix is therefore essential for understanding its stability and transformation under astrochemically relevant conditions.

2.4.1 Detection of Formamide in Extraterrestrial Environments

The detection of formamide in the ISM is of particular significance, as the molecule's presence in the ISM suggests that the basic chemistry required to form the building blocks of life occurs before planet formation, [147]. Additionally, the radiation experienced in the ISM, particularly of metal ions such as Fe^{2+} and Ni^{2+}, has been shown to lower the reaction barriers to facilitate the formation of formamide under interstellar conditions, [148]. Here "metals" refers to transition-metal elements capable of form-

ing divalent or trivalent cations, which can act as catalysts or coordination centres in aqueous chemistry. But where exactly has formamide been detected in the ISM?

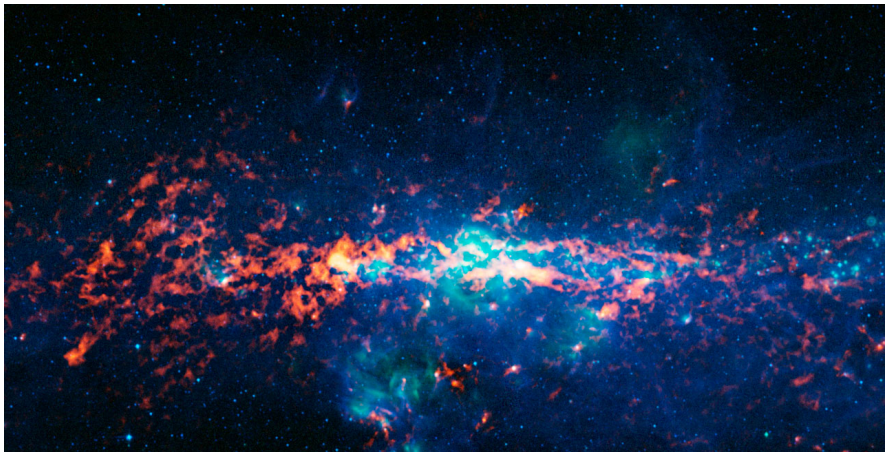


Figure 2.15: A colour composite image of the Galactic Centre and Sagittarius B2 as seen by the ATLASGAL survey. **Credit:** ESO/APEX & MSX/IPAC/NASA.

As discussed in Section 2.4, formamide has been detected in a range of extraterrestrial environments, including the ISM, the Murchison meteorite, Halley's comet, and most notably comet 67P [149]. The first interstellar detection of formamide was reported by Rubin et al. (1971), followed by its identification in comet Hale-Bopp in 1997 by Mehringer et al. [150]. Rubin et al. first conducted laboratory spectroscopy to refine the rest frequencies of key rotational transitions of formamide, and then used the NRAO (National Radio Astronomy Observatory) microwave telescope to search for these frequencies in several astronomical sources, including Sgr B2, W3, Ori A, and DR 21 (Figure 2.14), [151]. Formamide was conclusively identified in Sgr B2, while a weaker feature at the expected frequency was noted in Sgr A. The latter was considered uncertain at the time, largely because early radio instruments lacked the spectral resolution needed to distinguish faint lines from the severe line blending characteristic of the molecule-rich Galactic Centre region. Subsequent, higher-sensitivity observations have now confirmed that formamide is indeed present in Sgr A [142]. Together, these early detections established formamide as a widespread interstellar molecule and laid the foundation for understanding its role in prebiotic chemical networks across diverse astrophysical environments.

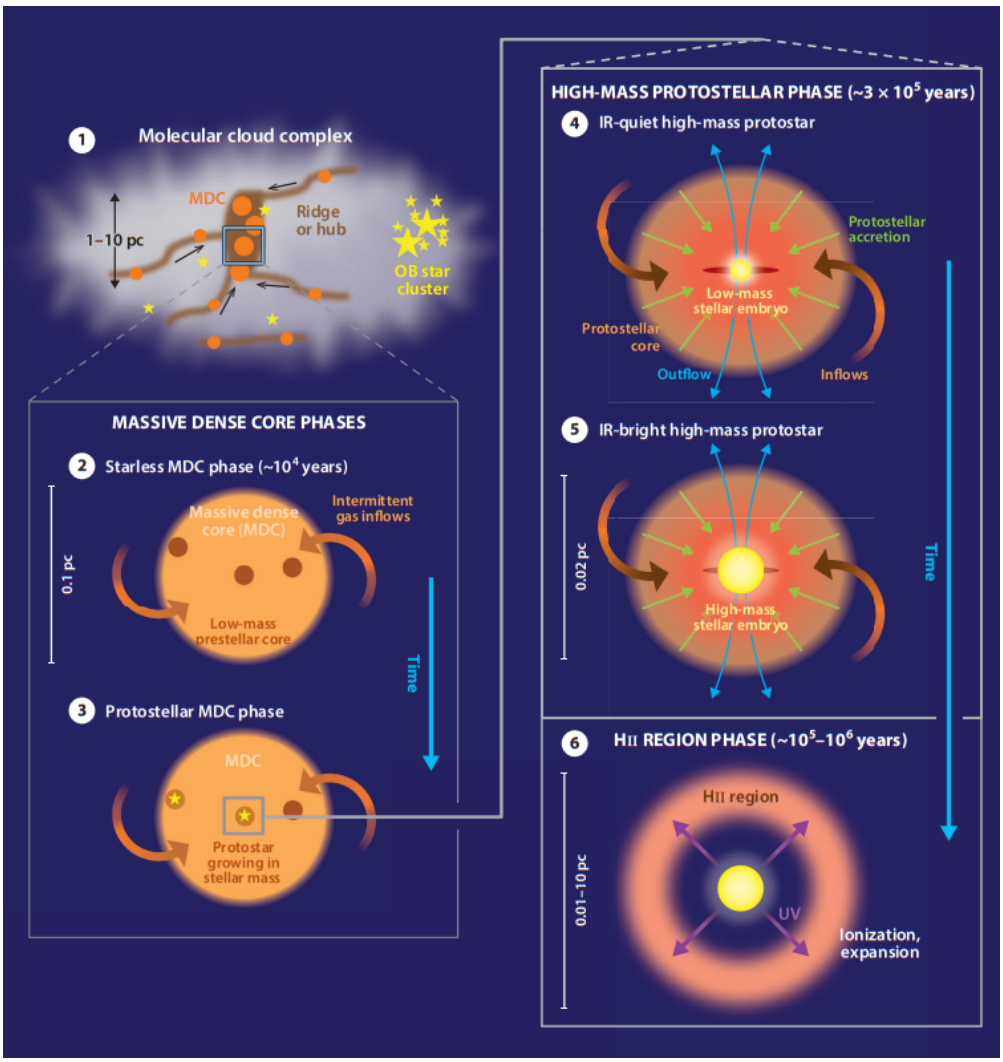


Figure 2.16: Schematic representation of the hierarchical structure and evolutionary stages of a massive molecular cloud, from extended diffuse material to dense, ice-rich cores and active star-forming regions. The cold, dense phases (infrared-dark clouds and massive dense cores) provide the low temperatures (10-20 K), high densities, and dust-grain ice mantles under which complex organic molecules such as formamide are expected to form and persist. **Credit:** Used with permission of Annual Reviews, Inc., from High-Mass Star and Massive Cluster Formation in the Milky Way, F. Motte, S. Bontemps and F. Louvet, *Annual Review of Astronomy and Astrophysics*, vol. 56, 2018; permission conveyed through Copyright Clearance Center, Inc., [152].

Since the author's initial identification, Sgr B2 has remained the archetypal source for studying interstellar formamide and related amides with increasingly sensitive and high-resolution observations, [140, 153, 154]. Modern millimetre and submillimetre spectral surveys toward Sgr B2(N) with facilities such as the IRAM 30 m telescope and ALMA now identify numerous rotational transitions of NH_2CHO, allowing its emission to be cleanly separated from the severe line confusion that affected early studies [134, 155]. These data resolve the molecule into distinct physical components

- in particular, chemically rich hot cores such as Sgr B2(N1) and Sgr B2(N2) - and yield well-constrained excitation temperatures and column densities, showing that formamide is among the more abundant complex organics in these environments [155]. Within the broader Sgr B2 complex, unbiased spectral surveys of the quiescent cloud G+0.693-0.027 have further demonstrated that formamide and other amides are already present in relatively cold, non-star-forming gas, with nearly constant abundance ratios across different evolutionary stages [156]. Together, these modern observations confirm that formamide is a robust and widespread constituent of Galactic Centre molecular clouds, present both in active hot cores and in more quiescent material, and they firmly establish Sgr B2 as a key template for understanding interstellar amide chemistry.

Beyond the Galactic Centre, formamide is now recognised as a common constituent of a wide range of star-forming environments. High-resolution ALMA surveys of nearby low-mass protostars - most notably the IRAS 16293-2422 system - have identified multiple unblended NH_2CHO transitions, revealing that its abundance in so-called "hot corinos" is comparable to that found in massive hot cores such as Sgr B2(N) [142, 157]. Similar detections in sources including B1-b, SVS13-A, and B335 indicate that formamide formation is not limited to high-mass clouds but is widespread across the early stages of low-mass star formation, [158–160]. These observations demonstrate that the chemistry leading to NH_2CHO is active in protostellar envelopes that more closely resemble the environment in which the Solar System formed.

Formamide is also efficiently produced and released in shocked gas, where energetic processes liberate ice-mantle products into the gas phase. Regions such as L1157-B1 and B2 show pronounced enhancements of NH_2CHO associated with shock-driven sputtering and grain-mantle disruption [161]. These environments provide direct evidence that energetic processing - whether from shocks, UV photons, or cosmic rays - both forms and mobilises formamide, linking the chemistry of cold prestellar ices to the warm gas detected in spectral surveys.

Formamide has now been detected in a wide range of interstellar environments, particularly in giant molecular clouds where its formation is highly efficient. Its presence

across clouds at different evolutionary stages suggests that amide chemistry is initiated early - within the cold, dense cloud phase, see Figure 2.16 - and persists throughout the subsequent steps of cloud collapse and star formation [156]. Laboratory experiments support this view: formamide can be produced at temperatures as low as 10 K in interstellar ice analogues, especially in H_2O- and CO-rich ices typical of dense cloud mantles [162, 163]. On grain surfaces, formamide forms predominantly via reactions involving CO and NH_3, and via hydrogenation of isocyanic acid (HNCO), with UV photons and cosmic rays acting as efficient drivers of this chemistry. Once formed, it can enter the gas phase through non-thermal desorption mechanisms such as chemical desorption, sputtering, and shock-driven mantle removal [156, 164]. Gas-phase routes also contribute: quantum-chemical studies show that reactions between NH_2 (amide group) and H_2CO (formaldehyde) proceed with negligible activation barriers, enabling efficient production even in the cold gas of giant molecular clouds when these precursors are available [165–167]. Together, these formation pathways make formamide a robust and persistent component of molecular-cloud chemistry, present long before star or planet formation begins. A representative example of such a protostellar outflow environment is shown in Figure 2.17.

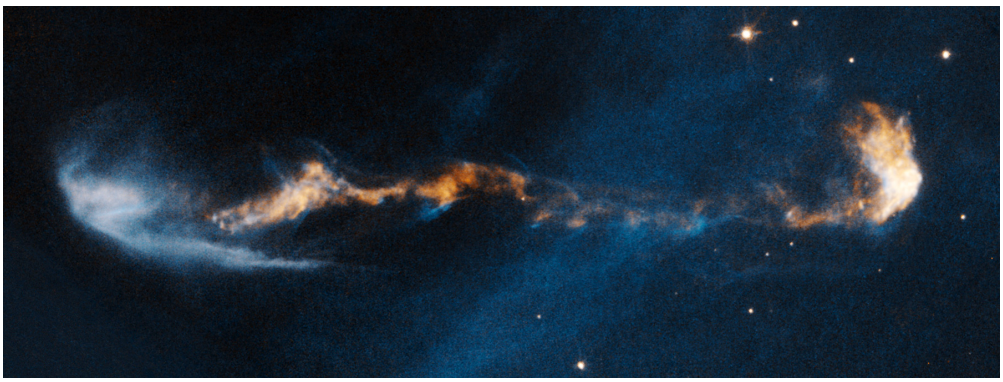


Figure 2.17: Hubble Space Telescope image of Herbig-Haro object HH 47, a young stellar outflow emerging from a Bok globule at the edge of the Gum Nebula, in the southern constellation of Vela. Protostellar environments of this kind - characterised by shocks, warm irradiated gas, and chemically enriched jets - are known sites where complex organic molecules such as formamide (NH_2CHO) have been detected in recent spectral surveys. **Credit:** NASA, ESA; P. Hartigan (Rice University).

Beyond individual detections, modern astrochemical surveys reveal consistent abundance patterns that point to shared formation pathways for formamide across a wide range of environments. Observations of sources such as IRAS 16293, Sgr B2(N), and

the quiescent Galactic Centre cloud G+0.693-0.027 show that NH_2CHO correlates tightly with HNCO, supporting the long-standing hypothesis that hydrogenation of HNCO on icy dust grains is a dominant formation route in cold phases [145, 168, 169]. Laboratory experiments using UV photons, electrons, and cosmic-ray analogues further demonstrate that formamide can be efficiently produced in H_2O-, CO-, and HNCO-rich ices at temperatures as low as 10 K, consistent with formation during the prestellar stage [162, 163]. Complementary quantum-chemical calculations and recent ALMA observations also point to a barrierless gas-phase pathway involving NH_2 + H_2CO, indicating that both solid- and gas-phase chemistry contribute to the widespread presence of NH_2CHO in molecular clouds [165, 166]. Together, these results suggest that formamide is a robust outcome of early ice chemistry that persists into later protostellar evolution.

The ubiquity of formamide in molecular clouds and protostellar envelopes has significant implications for the chemistry of planetary system formation. Observations of cometary comae show that NH_2CHO is a common volatile in Solar System comets, with detections in objects such as Hale-Bopp and 67P/Churyumov-Gerasimenko confirming that formamide survives incorporation into icy planetesimals [149, 170]. Measurements from Philae's COSAC instrument found formamide at abundances of order $\sim$400 ppm relative to water ice on 67P, demonstrating that this molecule can be preserved within primordial cometary ices [171]. The continuity between interstellar ice chemistry, protostellar environments, and cometary inventories strongly indicates that formamide and related amides are inherited rather than synthesised solely within comets. As comets are key reservoirs of volatile and organic material delivered to young planetary surfaces, the widespread detection of NH_2CHO across these evolutionary stages supports its role as a prebiotic precursor that can be transported to icy worlds such as Europa, Enceladus, and early Earth.

2.4.1.1 Comet 67P

Comet 67P/Churyumov-Gerasimenko, shown in Figure 2.18, is a comet in our Solar System that has been well studied due to its unique shape and composition, providing insights into the early Solar System. In 2004, ESA's Rosetta mission was the

first spacecraft to launch with the intention of following and documenting the comet around the Sun, [172]. In fact, 67P was the first comet to be orbited and landed on by a spacecraft, Rosetta, with the controlled impact occurring in 2016 [173]. The key findings from Rosetta's analysis suggest that the comet contains water with a D/H ratio ∼3 times that on Earth. In addition, molecular nitrogen and molecular oxygen were detected, a new finding for comets. Most interestingly, exposed water (i.e., patches of surface-exposed water ice revealed as sublimation removed the darker dust coating) was present on the comet, along with glycine and phosphorus. Furthermore, the mass spectrometry equipment aboard the Rosetta spacecraft detected formamide [171]. These measurements were obtained using two of Rosetta's mass spectrometers: Philae's COSAC GC-MS, which detected formamide at roughly 400 ppm relative to water along with other organics, and the ROSINA instrument onboard the orbiter, which analysed the volatile coma and determined that the sublimated water ice carried a D/H ratio about three times higher than that of Earth's oceans.

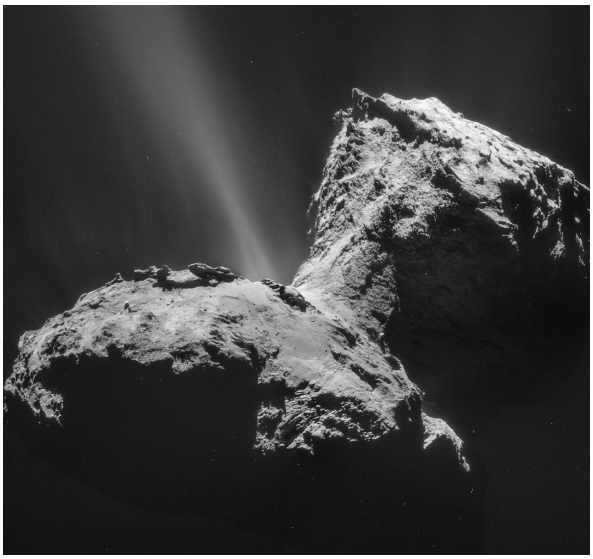


Figure 2.18: An image of comet 67P/Churyumov-Gerasimenko taken by the Rosetta NAVCAM. **Credit:** ESA/Rosetta/NAVCAM - CC BY-SA IGO 3.0.

This identification of formamide on comet 67P provided direct evidence that complex organic molecules can be present on comets, supporting the idea that molecules essential for prebiotic chemistry could have been delivered to planetary bodies via cometary and meteoritic collisions, [174]. The presence of formamide on comet 67P also connects the cometary chemistry with that of the ISM, suggesting a continuity of

organic molecule formation from space to planetary bodies, [149]. Comet 67P's unique structure, composition, and formation history make it a key object for understanding the building blocks and evolution of planetary bodies.

2.5 Laboratory Studies of Irradiated Ices Relevant to the Jovian System

The detection of formamide and other complex organic molecules in cometary environments, as discussed in the preceding sections, suggests that such species may be delivered to the surfaces of icy bodies such as Europa via cometary and meteoritic impacts. However, spacecraft observations alone are insufficient to constrain how these molecules behave once embedded within an icy surface subjected to the intense radiation environment of the Jovian system. Laboratory simulation is therefore essential, and over the past three decades, a substantial experimental literature has developed around the radiation chemistry of ices under conditions relevant to Europa and the other icy Galilean moons.

Laboratory simulation and spacecraft observation are, therefore, most powerful when used in conjunction. While missions such as JUICE and Europa Clipper provide invaluable compositional and geophysical data, they cannot replicate the controlled conditions necessary to isolate individual reaction pathways, quantify destruction and formation rates, or assess the influence of substrate composition on ice chemistry. These questions may instead be addressed through dedicated laboratory analogue experiments, which have progressively evolved to reflect the growing complexity revealed by spacecraft data.

2.5.1 Early Irradiation Studies of Water Ice

Most early experiments investigating the habitability of Europa, Ganymede, and Callisto focused on pure water ice because water ice is the dominant surface constituent on these moons [175, 176]. Additionally, understanding the response of water ice to irradiation was necessary before the effects of additional components such as salts, minerals,

and organics could be disentangled [177]. As a result, early laboratory studies sought to establish the fundamental physical and chemical response of water ice to energetic particle and photon irradiation before introducing additional chemical complexity [177].

Following the Voyager flybys of 1979, which revealed both Io's volcanic contribution to Jupiter's magnetosphere and unusual spectral and morphological features on the icy Galilean moons, interest grew in how constant charged-particle bombardment might chemically alter these icy surfaces [178–180]. One of the earliest such studies was Brown et al. (1978), [181], who irradiated thin films of pure H_2O ice with MeV He^+ and heavier ions, demonstrating stoichiometric erosion of water and providing the first quantitative evidence that 'electronic sputtering' - erosion driven by electronic excitation or ionisation - dominates over classical sputtering mechanisms. The companion paper, Lanzerotti et al. (1978), [182], applied these sputtering yields to the Jovian system establishing that Europa (like Io) is immersed in and impacted by a high flux of magnetospheric particles capable of dissociating and sputtering water ice. It was argued that the bombardment of the icy Galilean satellite surfaces is the dominant source of water-derived atmospheric products (H, O, and O_2) [182]. This pair of papers established the first direct experimental-to-observational link between laboratory ice irradiation and the physical/atmospheric environment on the Galilean icy moons.

A complementary body of work characterised the chemical products of water ice radiolysis. Johnson & Quickenden (1997), [177], reviewed nearly 40 years of laboratory data on the UV photolysis and ion/electron radiolysis of pure water ice to interpret remote sensing data from the Jovian icy satellites. The primary products of photodissociation and radiolytic ionisation are reactive species including H, OH, and O; these can diffuse through the ice matrix and recombine to yield stable products such as H_2, H_2O_2, and O_2. They also discussed trapped radiolytic species that were observable in the lab, such as trapped OH, trapped electrons, and trapped ions, all of which had characteristic temperature-dependent detrapping behaviour. Johnson & Quickenden concluded that H_2 escapes preferentially from the ice, leaving O_2 and H_2O_2 as the dominant stable products; because O_2 is more photoresistant than H_2O_2, it ultimately dominates, see Figure 2.19, accounting for Europa's O_2 atmosphere and the condensed O_2 detected on

Ganymede. They also noted that laboratory reaction and decay timescales of seconds to minutes correspond to days or years in space, owing to the much lower particle fluxes at the icy moons - a recurring caveat that laboratory analogues, while essential, require careful interpretation when extrapolated to real surfaces. This review conducted by Johnson & Quickenden provided the mechanistic and chemical-kinetics bridge between the sputtering yield measurements, [181], and the application papers, [182], explaining why O_2 specifically becomes the dominant surviving species in irradiated water ice and thus why Europa's observed atmosphere is O_2-dominated rather than a mix of H_2O, OH, H_2, etc.

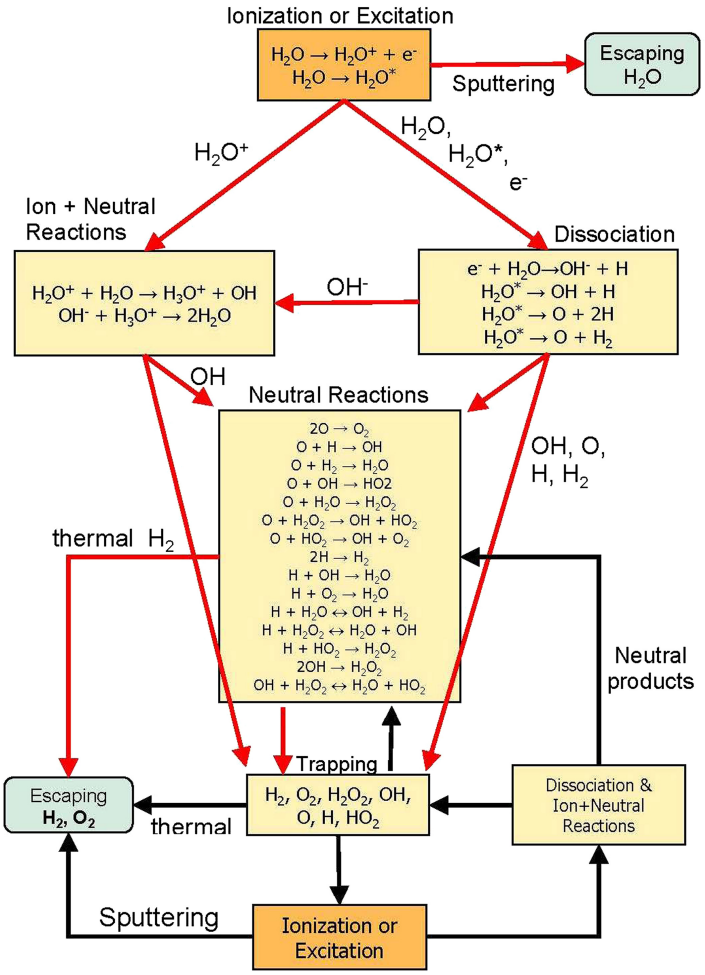


Figure 2.19: Schematic representation of the principal radiation-induced processes occurring within water ice. Ionisation and excitation lead to molecular dissociation, radiolysis product formation, trapping of species within the ice matrix, and sputtering of material from the surface. **Credit:** Reproduced from B. D. Teolis et al., Water ice radiolytic O_2, H_2, and H_2O_2 yields for any projectile species, energy, or temperature: A model for icy astrophysical bodies, *Journal of Geophysical Research: Planets*, 122, 1996–2012 (2017), with permission from John Wiley and Sons. © 2026. American Geophysical Union, [183].

Identifying these fundamental radiolysis products was essential because they subsequently become reactants in more chemically complex ice systems. Without an understanding of the baseline chemistry of irradiated water ice, it would be difficult to determine whether products observed in mixed ice experiments originated from water radiolysis, the additional molecular component, or interactions between the two.

2.5.2 Mixed Ice Analogues and the Evolution of Experimental Complexity

Once the fundamentals of how pure water behaves under icy moon-like conditions had been established, researchers were motivated to expand the research from pure water ice to more complex water ice mixtures. During the 1980s and 1990s, there had been significant advancements in infrared observations [184, 185], demonstrating that water ice was rarely found in isolation. Interstellar ices, cometary ices, and planetary ices were observed to contain quantities of CO_2, NH_3, CH_4, and CO among other volatile species [186, 187]. These observations collectively established that the chemical environment of planetary ices was far more complex than pure water ice alone, and motivated a new generation of laboratory experiments designed to replicate that complexity under controlled irradiation conditions.

The identification of volatile species in planetary ices motivated systematic laboratory investigation into how their presence would alter radiation chemistry relative to pure water ice. Moore & Hudson (2000), [188], irradiated H_2O:CO_2 and H_2O:O_2 ice mixtures with protons at 80 K, a temperature directly relevant to Europa's surface, [95], in experiments motivated explicitly by the detection of H_2O_2 on Europa by Galileo's NIMS instrument. This work demonstrated that H_2O_2 can be generated in CO_2-bearing ice mixtures under Europa-relevant conditions and that ice composition directly governs which oxidation products are chemically accessible, providing direct implications for interpreting the observed chemistry of Europa. Building on this, Moore et al. (2007), [189], undertook a more systematic study, irradiating H_2O:NH_3 ice mixtures across a range of temperatures and compositions with explicit framing around outer Solar System satellite surfaces. The dominant product was the ammo-

nium ion (NH_4^+), whose formation was found to be sensitive to both ice composition and phase, demonstrating that nitrogen-bearing reaction pathways absent from pure water or CO_2-bearing systems could be introduced through the addition of NH_3.

More recently, Mifsud et al. (2023), [190], irradiated CH_4:H_2O ices with 1 MeV protons and 2 keV electrons at 20 K on ZnSe substrates, detecting an extensive suite of daughter molecules including C_2H_6, C_3H_8, C_2H_2, CH_3OH, CO, CO_2, and tentatively H_2CO. This product diversity substantially exceeded that of either pure component irradiated in isolation, confirming that the H_2O matrix actively participates in CH_4 radiation chemistry rather than acting as a passive dilutant, and that proton irradiation produced greater daughter molecule abundances than electron irradiation despite delivering a lower radiation dose, demonstrating that radiation type and not dose alone controls product yields. These results have direct applicability to outer Solar System objects. Taken together, these experiments revealed that the radiation chemistry of icy planetary environments is strongly matrix-dependent, with each molecular addition introducing reaction pathways, products, and sensitivities that could not have been predicted from the behaviour of the individual pure components alone. Whilst the experiments described above demonstrated the importance of ice composition more broadly, sulphur-bearing ices occupied a particularly significant position within the Jovian context, warranting dedicated experimental attention for reasons specific to the magnetospheric environment.

Unlike CO_2, NH_3, or CH_4, whose presence in planetary ices reflects general volatile inventories, sulphur and oxygen ions are actively and continuously supplied to the surfaces of the Galilean moons through the volcanic outgassing of Io, which seeds Jupiter's magnetosphere with sulphur and oxygen ions that are subsequently implanted onto Europa, Ganymede, and Callisto, [191]. This makes sulphur chemistry on these surfaces not merely possible but actively driven by the magnetospheric environment in a way that has no direct parallel in other icy moon systems. The breadth of the resulting experimental landscape was surveyed by Mifsud et al. (2021) [192], in a comprehensive review of sulphur ice astrochemistry covering spectroscopy, photochemistry, radiolysis, and ion implantation of sulphur-bearing ices, which explicitly identifies sulphur ion ir-

radiation from Jupiter's magnetosphere as a key processing mechanism for the Galilean satellite surfaces. A central unresolved question underpinning much of this experimental work is whether the SO_2 detected on these surfaces, particularly on Europa's trailing hemisphere, derives from exogenic sulphur ion implantation or from endogenic sulphur compounds already present within the ice. An important experimental contribution to this question was made by Moore, Hudson & Carlson (2007) [193], who irradiated H_2O:SO_2 and H_2O:H_2S mixtures with 0.8 MeV protons at 86, 110, and 132 K, temperatures spanning the range relevant to Europa, Ganymede, and Callisto. The key products identified were H_2S_2, a direct sulphur analogue of the H_2O_2 produced from water ice radiolysis, and a suite of sulphur oxyanions including HSO_3^-, HSO_4^-, and SO_4^{2-}, with hydrated sulphuric acid forming as an ultimate oxidation product. Radiation half-lives of SO_2 and H_2S were also determined, providing quantitative constraints on surface processing rates. The sulphate species identified in these experiments, particularly SO_4^{2-}, are precisely the materials whose spectral signatures were being debated in the observational literature on Europa's non-water-ice surface composition, a debate that is taken up directly in the following section.

Across these studies, a consistent picture emerged in which the radiation chemistry of icy planetary environments is strongly governed by ice composition, with each molecular addition introducing reaction pathways and products that could not be predicted from the pure components alone. Nevertheless, a persistent limitation remained across much of this body of work, namely that the substrate upon which the ice was deposited was treated as chemically inert, contributing nothing to the observed chemistry. By the time these experiments were being conducted, however, observational evidence from the Galileo mission was painting a more complex picture of the Jovian moon surfaces, one in which hydrated salts, mineral precipitates, and ocean-derived materials appeared to play an active role in surface composition. This growing tension between experimental simplicity and observational reality motivated a further evolution in analogue methodology, leading researchers to investigate systems in which the substrate itself was no longer passive, but chemically and physically integrated into the ice being processed.

2.5.3 Salt-Rich Analogues and Galileo-Era Observations

Although the irradiation studies discussed in the preceding subsections established the fundamental mechanisms governing radiation processing in both pure and mixed icy analogues, they could not fully account for the growing body of observational evidence being returned from the Jovian system. Prior to the Galileo mission, the surfaces of the Galilean moons were generally regarded as predominantly water-ice bodies, [194–196], but data returned by NASA's Galileo spacecraft demonstrated that the surface of Europa was considerably more chemically complex than this picture suggested, [197]. Analysis of spectra returned by the Near-Infrared Mapping Spectrometer (NIMS) revealed that large regions of Europa's surface could not be explained by water ice alone; distorted absorption bands concentrated in lineae and chaos terrain instead pointed to the presence of hydrated minerals, with magnesium and sodium sulphates emerging as the leading candidates, [198, 199]. These salts were proposed to represent material delivered from Europa's subsurface ocean through geological activity, a hypothesis broadly consistent with the compositional patterns observed across geologically disrupted terrains. Subsequent ground-based and Hubble Space Telescope (HST) observations, however, began to complicate this sulphate-dominated picture, suggesting that Europa's more pristine endogenous material may instead reflect a chloride-dominated composition, [200]. Hand & Carlson (2015) [201], proposed NaCl as a probable surface constituent on the basis of radiation-induced colour changes in alkali halides that closely resembled the visible-wavelength colouration of Europa's surface. This was followed by the detection, by Trumbo et al. (2019) [200], of a 450 nm absorption feature in HST spectra of leading-hemisphere chaos terrain, consistent with irradiated NaCl and interpreted as consistent with endogenous material sourced from the interior ocean, the implications of which are discussed further in Section 2.3. Trumbo et al. (2022) [202], subsequently strengthened this identification through the detection of a previously unseen UV absorption near 230 nm, spatially co-located with the 450 nm feature and likewise well-reproduced by irradiated NaCl under Europa-relevant conditions. Taken together, these observations indicated that the chemical complexity of Europa's surface extend well beyond what the preceding generation of pure-water or mixed-ice analogues

could replicate, and that salt minerals, both sulphates and chlorides, constitute integral components of the surface. This provided a clear impetus for the development of laboratory analogue studies in which salt-bearing ices are not merely characterised spectroscopically, but actively irradiated under conditions representative of the Jovian radiation environment.

The immediate experimental response to these observations was to acquire cryogenic spectra of candidate salt minerals and test them systematically against the NIMS data. Dalton et al. (2005) [203], produced one of the first comprehensive spectral comparisons of heavily hydrated sulphate minerals, including epsomite, mirabilite, and bloedite, against Galileo NIMS observations of Europa's disrupted terrains, with spectra acquired at approximately 100 K, representative of Europa's low-latitude surface temperatures, [204]. The results demonstrated that hydrated sulphates could reproduce the key distortions in the near-infrared water absorption bands observed in lineae and chaos terrain, and established the spectral library approach as a primary tool for surface composition inference. Dalton (2007) [205], extended this by applying linear mixture modelling to the NIMS data, combining cryogenic spectra of multiple hydrated phases simultaneously, including hexahydrite, epsomite, bloedite, mirabilite, magnesium and sodium sulphate brines, and sulphuric acid hydrate at 77–130 K. Notably, sulphuric acid hydrate dominated the best-fit mixture, accounting for approximately 62% of the modelled surface, with the sulphate salt phases contributing the remainder; no single mineral phase alone was sufficient to reproduce the observations. Both studies, however, were fundamentally passive: they characterised the spectral properties of unirradiated minerals and used these as templates for spectral modelling. Neither addressed how radiation processing would alter those minerals, nor how the presence of salt might modify the radiation chemistry of ice deposited upon it. The substrate was, in effect, treated as a spectroscopic target rather than a chemically active participant, and the question of how irradiated salt-bearing ices would evolve under the persistent particle bombardment of the Jovian radiation environment remained open.

Cerubini et al. (2022) [206], began to address this by actively irradiating NaCl:H_2O ice analogues with 1 and 5 keV electrons at 100 K under high vacuum, testing two phys-

ically distinct sample types. Compact slabs, produced by controlled cooling of NaCl solutions and representative of well-crystallised, hydrohalite-dominated ice, and granular particles of two size fractions (5 and 70 μm), produced by flash-freezing, were irradiated at salt concentrations of 5, 10, and 30 wt%. These morphologies are broadly interpretable as analogues for surface materials formed through contrasting processes, such as gradual brine refreezing versus more rapid emplacement through fracture infilling or cryovolcanic activity, though the paper itself does not make this geological claim explicitly. The primary finding was the formation of F-centres[2] in every sample type upon irradiation; this is significant because the 450 nm absorption detected in HST spectra of Europa's leading-hemisphere chaos terrain by Trumbo et al. (2019) [200], is attributed to precisely this defect in irradiated NaCl, providing laboratory confirmation that electron bombardment of NaCl-bearing ices can produce the spectral signature observed from orbit. M-centres were detected at or near the detection limit in compact slabs only, consistent with their non-detection in Europa observations, where the dose rates and sample geometries accessible to remote sensing would render such features difficult to resolve even if present, [207]. A further and previously unreported feature near 580 nm was observed exclusively in granular samples, attributed to Na colloids, agglomerations of sodium atoms within the crystal lattice that form through the progressive clustering of F-centres under sustained irradiation[3]. The absence of this feature in compact slabs further demonstrated that the physical microstructure of the ice, and not merely its chemical composition, governs the radiation products that form. Crucially, however, these findings concern the optical and structural response of salt-bearing ices to irradiation. The question of whether a NaCl substrate actively modifies the radiation chemistry of organic molecules deposited upon it, altering their destruction rates, product yields, and reaction pathways, was not addressed

[2]F-centres, from the German *Farbzentrum* (colour centre), are point defects in an ionic crystal lattice in which an electron becomes trapped at an anion (Cl^-) vacancy, producing a characteristic broad absorption near 460 nm in laboratory NaCl crystals; the analogous feature observed in HST spectra of Europa appears at approximately 450 nm, a slight blue-shift attributed to the surface radiation environment. M-centres, which absorb near 720 nm, formed from two adjacent F-centres (merged anion vacancies, each with a trapped electron); their formation requires sufficient radiation dose and is sensitive to temperature, [207].

[3]Na colloid formation in irradiated NaCl has been documented in studies of radiation damage in alkali halides, where F-centres act as mobile lattice defects that nucleate into metallic sodium clusters at sufficient dose, [206].

and remained an open problem at the outset of the work presented in this thesis.

Understanding which salt phases are actually present on Europa's surface requires consideration of the freezing behaviour of realistic ocean-derived brines, rather than idealised binary salt-water systems. Thompson et al. (2021) [208], addressed this by freezing a chondrite-like Na–Mg–Ca–SO_4–Cl solution representing a model Europan ocean composition under two contrasting cooling regimes: rapid freezing and ultra-slow freezing over 242 days. Mineral precipitation was monitored throughout using in-situ synchrotron X-ray powder diffraction, a technique in which the characteristic diffraction patterns produced by crystalline phases under an intense X-ray beam allow their identification and relative abundances to be tracked in real time. Slow cooling initially followed equilibrium thermodynamic predictions before producing $Na_2Mg(SO_4)_2{\cdot}16H_2O$ after 50 days at 245 K, a highly hydrated sulphate phase only recently characterised. Rapid freezing, by contrast, produced a complex multi-phase assemblage within minutes, including mirabilite, meridianiite, pentahydrite, epsomite, hydrohalite, gypsum, and bloedite, demonstrating that the mineral inventory of a realistic Europan surface is likely considerably more complex than binary-salt spectral libraries imply. Critically, both chloride and sulphate phases co-precipitated under realistic conditions, supporting a mixed-salt surface rather than one dominated by either composition alone. These results demonstrated that the mineral phases available to interact with radiation at Europa's surface are far more diverse than previously modelled, and that the specific phases present depend sensitively on the thermal history of the brine, providing geochemical grounding for the experimental move toward more realistic, multi-phase salt-bearing ice analogues.

The most recent analogue experiments have begun to combine thermal and radiative processing simultaneously, reflecting the recognition that real Europan surfaces are subject to both concurrently. Ottersberg et al. (2025) [209], studied the evolution of Vis-NIR reflectance spectra of granular NaCl-, $MgSO_4$-, and $MgCl_2$-bearing ice analogues in a simulation chamber under Europa-relevant conditions. A key methodological advance was the custom calibration of a thermopile sensor, a non-contact thermal detector that measures surface temperature from far-infrared emission, enabling direct

measurement of the ice surface temperature rather than that of the sample holder. This allowed the observed spectral changes to be scaled to equivalent timescales on Europa's surface. Sublimation alone produced significant changes in the depth and shape of the broad water absorption bands on timescales of a few thousand years under equatorial Europa conditions, a result with direct implications for the interpretation of remote-sensing data, and a narrow absorption feature attributed to hydrohalite ($NaCl{\cdot}2H_2O$) formed in the NaCl-bearing samples during sublimation. Subsequent electron irradiation at Europa-like fluences demonstrated, however, that hydrohalite is rapidly dehydrated under particle bombardment, implying it would not persist at the surface unless emplaced very recently or within localised thermal anomalies, with survival estimated at under approximately 10 years above 145 K. Detection of hydrohalite at Europa's surface would therefore constitute strong evidence for very recent geological activity, a result of direct relevance to the upcoming Europa Clipper and JUICE missions. The study focused on Vis-NIR reflectance spectroscopy of granular particulate samples and did not address the fate of organic molecules within salt-bearing ices, nor the influence of the NaCl substrate on the radiation chemistry of molecular species deposited upon it. This gap, the role of a salt substrate in determining the radiolytic fate of prebiotically relevant organics, defines the experimental niche that this thesis seeks to address.

Taken together, the studies reviewed in this subsection demonstrate that salt minerals are not spectroscopically or chemically inert constituents of icy moon surfaces, but active participants in both the optical and radiation-chemical evolution of the ice. The spectral matching work of Dalton and colleagues established that the composition of salt-bearing surfaces determines which near-infrared features are observed, while the irradiation experiments of Cerubini et al. (2022) [206], showed that the same composition, and indeed the same physical microstructure, governs which radiation-induced defects form and in what abundance. Thompson et al. (2021) [208], extended this picture geochemically, demonstrating that the range of mineral phases likely to be present on Europa's surface is considerably broader than binary-salt models imply and sensitive to the thermal history of the source brine. Most recently, Ottersberg et al.

(2025) [209], confirmed that combined thermal and radiative processing produces measurable spectral evolution on timescales relevant to the Jovian radiation environment, with the stability of individual phases depending critically on local temperature and irradiation history. What emerges from this body of work is a consistent and important conclusion: the substrate cannot be treated as a passive support in experiments designed to simulate the surfaces of the Jovian moons. It modulates energy transfer, controls defect formation, determines product retention, and shapes the morphological evolution of the ice in ways that pure-water or simple mixed-ice models are fundamentally unable to capture. The chemical behaviour of irradiated icy surfaces in the Jovian system is therefore inseparable from the mineralogical character of the substrate upon which the ice resides.

2.5.4 Experimental Studies Directly Relevant to Formamide

The preceding subsections have traced the development of laboratory analogue experiments from pure water ice through to increasingly complex salt-bearing systems, and established that substrate identity is a chemically active variable, not a passive support. Formamide (NH_2CHO), having been detected in cometary environments from which material may be delivered to the surfaces of the icy Galilean moons, as discussed in Section 2.3 and Section 2.4.1.1, is a molecule whose radiation chemistry in the solid state is therefore of direct relevance to the Jovian context. A body of experimental literature exists on the irradiation of formamide-bearing ices, though it developed primarily within ISM and cometary frameworks rather than with Jovian surfaces. It should also be noted that ion irradiation of astrophysically relevant ice mixtures has been shown to produce formamide as a synthesis product rather than destroy it, [210], a result that underscores the chemical richness of energetically processed ices and the potential for formamide to be generated in situ on icy surfaces as well as delivered exogenously. The following paragraphs review the formamide irradiation literature with the specific aim of identifying what it leaves unresolved in the Jovian context.

Prior to any irradiation work, a reliable spectroscopic characterisation of solid-state formamide was an essential prerequisite, since monitoring radiation-driven molec-

ular changes depends entirely upon accurate band assignments. Sivaraman et al. (2013) [211], provided this foundation by recording temperature-dependent FTIR spectra of vapour-deposited formamide ice across 30-210 K, identifying a phase transition between 155 and 165 K associated with pronounced shifts in the NH_2 stretching and scissoring modes and attributing the spectral evolution to rearrangement between formamide dimers at higher temperatures. The band assignments established in this work, particularly for the diagnostic C=O stretching and NH_2 bending modes, form the spectroscopic basis upon which subsequent irradiation studies, including those presented in this thesis, rely to track molecular destruction and product formation. The first experimental study of formamide under energetic processing in the solid phase was reported by Brucato et al. (2006) [212], who deposited pure amorphous formamide ice at 20 K on a silicon substrate and irradiated it with 200 keV H^+ ions at doses up to 24 eV/16u. The primary radiolysis products identified were CO, CO_2, N_2O, HNCO, and the $NH_4^+OCN^-$ complex, with around two-thirds of formamide molecules destroyed at the lower dose, rising to approximately three-quarters at the higher dose, providing the first quantitative destruction measurements for formamide in the condensed phase and demonstrating that the ammonium cyanate complex persists at room temperature in the irradiated residue. A significant step toward greater experimental realism was made by Dawley et al. (2014) [213], who investigated both Lyα (121.6 nm) photon and 1 keV electron irradiation of pure formamide and H_2O:formamide mixed ices deposited on high-surface-area SiO_2 nanoparticles, employed explicitly as a silicate grain analogue, at 70 K. The primary photoproducts were OCN^- and CO, with the water matrix found to enhance both yields under VUV irradiation, with the SiO_2 substrate proposed as a possible contributor to dissociative electron attachment, suggesting active substrate participation in the radiation chemistry. Dawley et al. (2014) remains the only prior formamide irradiation study to combine a mineralogically motivated substrate with a formamide:water mixed ice, making it the most directly comparable precursor to the experimental work presented in this thesis.

The known radiation chemistry of formamide was extended into the VUV regime by Suhasaria et al. (2024) [214], who irradiated amorphous and crystalline formamide ice

at 16 K with Lyα photons in the presence and absence of an amorphous olivine silicate substrate deposited by laser ablation. The olivine substrate was found not to alter the destruction cross-section of formamide but did suppress the formation of NH_3, HNCO, and HCN, with the product suite reduced to CO, CO_2, and OCN^-, thereby demonstrating directly that substrate identity can modify the product distribution of formamide radiolysis even when the overall destruction rate is unchanged. Crystalline formamide was additionally found to be destroyed approximately an order of magnitude faster than amorphous ice under Lyα irradiation. Taken together, these studies established that the primary radiolysis products of formamide in the solid state, namely CO, CO_2, and OCN^-, are broadly consistent across radiation types and ice compositions, with HNCO observed under some conditions but subject to suppression by substrate identity, that the presence of water modifies both yields and reaction pathways, and that substrate identity can influence product distributions even when parent destruction rates are unaffected.

Despite these advances, the existing body of work left three specific aspects of formamide radiation chemistry in icy matrices unaddressed, aspects that become directly relevant when the Jovian context established in the preceding subsections is brought to bear. First, none of the studies above reported G-values (radiation-chemical yields, expressed in molecules per 100 eV) for formamide destruction or for the formation of its radiolysis products in a formamide:H_2O ice system. Without these, quantitative comparison of destruction efficiency across radiation types or substrates is not possible, and extrapolation to survival timescales under Europa's radiation environment cannot be performed on a rigorous basis. Second, no single experimental programme has subjected the same formamide:water ice system to systematic comparison across ion, electron, and VUV irradiation whilst holding ice composition and substrate constant. As demonstrated for other molecular ice systems, [190], radiation type and not dose alone controls product yields, making such a comparison essential for understanding how Europa's mixed radiation environment processes formamide-bearing ices. Third, and most directly motivated by the experimental picture developed in the preceding subsection, no study had investigated the influence of a salt substrate on formamide

radiation chemistry. Dawley et al. (2014) and Suhasaria et al. (2024) demonstrated that substrate identity influences product distributions; however, both employed silicate analogues, which do not reflect the NaCl-dominated mineralogy now established for Europa's surface. Given that NaCl substrates have been shown to actively modulate defect formation, product retention, and morphological evolution in irradiated salt-bearing ices , [206, 209], their potential influence on the radiation-driven chemistry of formamide-water ices constitutes a well-defined and well-motivated open question. These three gaps, the absence of quantitative yield data, the lack of a systematic radiation-type comparison on a consistent ice system, and the unexplored role of a salt substrate, define the experimental scope of this thesis and are addressed directly in Chapters 5, 6, and 7.

2.5.5 Summary Table

Table 2.1 summarises the studies discussed above, alongside their relevance to the experimental approach adopted in this thesis.

Table 2.1: Representative laboratory analogue experiments performed relevant to the icy moons of Jupiter and the study of ice-mineral interfaces.

Reference	Experimental Setup	Main Findings	Relevance to This Thesis
Moore & Hudson (2000)	H_2O:CO_2 and H_2O:O_2 ice; proton irradiation; 80 K; substrate not specified	H_2O_2 produced in CO_2-bearing mixtures under Europa-relevant conditions; ice composition governs which oxidation products accumulate.	Demonstrates that ice composition controls oxidation product accessibility.
Moore et al. (2007a)	H_2O:NH_3 ice; proton irradiation; range of temperatures; substrate not specified	NH_4^+ dominant product; formation sensitive to ice composition and phase; nitrogen-bearing pathways introduced by NH_3 addition.	Shows that volatile additions open reaction pathways absent from pure water ice.
Moore, Hudson & Carlson (2007b)	H_2O:SO_2 and H_2O:H_2S ice; 0.8 MeV protons; 86, 110, and 132 K; substrate not specified	H_2S_2, sulphur oxyanions (HSO_3^-, HSO_4^-, SO_4^{2-}), and hydrated sulphuric acid identified; radiation half-lives of SO_2 and H_2S determined.	Directly relevant to sulphur chemistry on Galilean satellite surfaces; products link to the observational debate on Europa's surface composition.

Continued on next page

Table 2.1 – *continued from previous page*

Reference	**Experimental Setup**	**Main Findings**	**Relevance to This Thesis**
Mifsud et al. (2021)	Sulphur-bearing ices (review); spectroscopy, photochemistry, radiolysis, and ion implantation; various substrates	Comprehensive survey of sulphur ice astrochemistry; Jovian magnetospheric irradiation identified as key processing mechanism for Galilean satellite surfaces.	Establishes experimental and observational context for sulphur chemistry at the Galilean satellites.
Mifsud et al. (2023)	CH_4:H_2O ice; 1 MeV protons and 2 keV electrons; 20 K; ZnSe substrate	Extensive suite of daughter molecules detected (C_2H_6, C_3H_8, C_2H_2, CH_3OH, CO, CO_2, tentatively H_2CO); proton irradiation more effective than electron irradiation despite lower dose.	Demonstrates matrix-dependent radiation chemistry; ZnSe substrate directly comparable to this thesis.
Dalton et al. (2005)	Hydrated sulphate minerals (epsomite, mirabilite, bloedite); cryogenic reflectance spectroscopy (passive); ∼100 K; no irradiation	Hydrated sulphates reproduced key distortions in Galileo NIMS near-infrared absorption bands of Europa's lineae and chaos terrain; spectral library approach established.	Provides observational baseline motivating salt-bearing ice irradiation experiments; demonstrates surface composition cannot be inferred from water-ice models alone.
Dalton (2007)	Hydrated sulphate and chloride minerals, sulphuric acid hydrate; linear mixture modelling of NIMS spectra (passive); 77–130 K; no irradiation	No single mineral phase reproduced NIMS spectra; sulphuric acid hydrate dominated best-fit mixture (∼62%); mixtures of hydrated phases required.	Demonstrates compositional complexity of Europa's surface; motivates multi-phase salt-bearing analogue experiments.
Cerubini et al. (2022)	NaCl:H_2O ice (compact slabs and granular particles, 5 and 70 μm); 1 and 5 keV electrons; 100 K; NaCl self-substrate	F-centres (460 nm) formed in all sample types; M-centres near detection limit in compact slabs only; Na colloid feature (580 nm) exclusive to granular samples; microstructure governs radiation-induced defect population.	First demonstration that salt-bearing ice microstructure, not just composition, determines radiation products; directly motivates substrate-dependent irradiation experiments involving organic molecules.
Thompson et al. (2021)	Model Europan ocean brine (Na–Mg–Ca–SO_4–Cl); in situ synchrotron X-ray powder diffraction; rapid and ultra-slow controlled freezing	Slow cooling produced $Na_2Mg(SO_4)_2{\cdot}16H_2O$ after ∼50 days at 245 K; rapid freezing yielded multi-phase assemblage (mirabilite, meridianiite, hydrohalite, epsomite, bloedite, and others) within minutes; chloride and sulphate phases co-precipitated.	Establishes geochemical realism for salt-bearing analogue experiments; demonstrates Europa's surface mineralogy is far more complex than binary-salt models imply.

Continued on next page

Table 2.1 – *continued from previous page*

Reference	**Experimental Setup**	**Main Findings**	**Relevance to This Thesis**
Ottersberg et al. (2025)	Granular NaCl-, $MgSO_4$-, and $MgCl_2$-bearing ice; sublimation followed by 2 keV electron irradiation; Vis-NIR reflectance spectroscopy; granular particulate substrate	Sublimation altered water absorption bands on timescales of thousands of years; hydrohalite formed during sublimation but rapidly dehydrated by electron irradiation; survival <10 yr above 145 K.	Current state of the art for combined thermal and radiative processing of salt-bearing ices; does not address organic molecule chemistry or substrate effects on reaction pathways.
Sivaraman et al. (2013)	Pure formamide ice; thermal annealing (passive characterisation); 30–210 K; ZnSe substrate	Phase transition identified between 155 and 165 K; band assignments established for NH_2 stretching, scissoring, and C=O stretching modes.	Provides the spectroscopic baseline for formamide band assignments used throughout this thesis.
Brucato et al. (2006)	Pure formamide ice; 200 keV H^+ ions; doses up to 24 eV/16u; 20 K; silicon substrate	CO, CO_2, N_2O, HNCO, and $NH_4^+OCN^-$ identified; ∼two-thirds of formamide destroyed at lower dose, ∼three-quarters at higher dose.	First quantitative destruction measurements for solid-phase formamide; establishes the primary product suite against which this thesis is compared.
Dawley et al. (2014)	Pure formamide and H_2O:formamide ice; Lyα photons and 1 keV electrons; 70 K; SiO_2 nanoparticles (silicate grain analogue)	OCN^- and CO primary products; water matrix enhanced yields under VUV; SiO_2 substrate proposed as contributor to dissociative electron attachment.	Only prior study to combine a mineralogically motivated substrate with a formamide:H_2O mixed ice; most directly comparable precursor to this thesis.
Kaňuchová et al. (2016)	H_2O:CH_4:N_2, H_2O:CH_4:NH_3, and CH_3OH:N_2 ice mixtures; 30–200 keV H^+ and He^+ ions; 10–20 K; silicon and KBr substrates	Formamide and HNCO synthesised as irradiation products; formamide yields sufficient to account for cometary and circumstellar abundances at low doses.	Demonstrates formamide can be generated in situ within irradiated astrophysical ices, supporting its potential presence on icy moon surfaces through in-situ synthesis as well as cometary delivery.
Suhasaria et al. (2024)	Pure formamide ice (amorphous and crystalline), with and without olivine substrate; Lyα VUV irradiation; 16 K; CsI substrate with/without amorphous olivine silicate overlayer	Olivine substrate suppressed NH_3, HNCO, and HCN formation, reducing products to CO, CO_2, and OCN^-; crystalline formamide destroyed ∼order of magnitude faster than amorphous ice.	Demonstrates directly that substrate identity modifies formamide radiolysis product distributions; motivates investigation of salt substrates not represented in prior work.

Continued on next page

Table 2.1 – *continued from previous page*

Reference	**Experimental Setup**	**Main Findings**	**Relevance to This Thesis**
This thesis	Formamide:H_2O ice; H^+, O_2^+, and S^{5+} ion irradiation; 2 keV electron irradiation; 9 eV VUV photon irradiation; 90 K; NaCl and ZnSe substrates	NH_2CHO destruction and formation of CO, CO_2, and OCN^- confirmed under all radiation types; G-values calculated for formamide destruction and key product formation; NaCl produced significantly more efficient destruction and greater product yields than ZnSe under ion and electron irradiation; VUV photochemistry strongly temperature-dependent.	First systematic G-value dataset for formamide:H_2O ices across multiple radiation types; addresses three gaps: quantitative yield data, radiation-type comparison on a consistent ice system, and influence of a salt substrate under Europa-relevant conditions.

2.6 Research Gap and Objectives of the Thesis

As discussed in Sections 2.4 and 2.4.1, formamide is abundant in astrophysical environments, having been detected in star-forming regions, molecular clouds, protostellar shocks, and comets [138, 215]. It is considered significant in prebiotic chemistry as a potential precursor to essential biomolecules, including amino acids, nucleobases, nucleosides, and sugars. For this reason, formamide and its synthetic pathways have been extensively studied under laboratory conditions [216].

Section 2.5.4 identified three specific gaps in the existing formamide irradiation literature: the absence of quantitative radiation-chemical yield (G-value) data for formamide destruction and product formation; the lack of a systematic comparison across ion, electron, and VUV irradiation on a single, consistent formamide-water ice system; and the unexplored influence of a salt substrate on formamide's radiation chemistry, despite the demonstrated chemical activity of NaCl in irradiated inorganic ice systems (Section 2.5.3). The remainder of this section develops each of these gaps within the specific environmental context of Europa, before setting out the formal research objectives that this thesis addresses.

Laboratory research has focused on understanding the chemical behaviour of formamide in biological and prebiotic contexts, as well as its formation from simpler

molecules; for example, Meng et al. [217] demonstrated the electrosynthesis of formamide from methanol and ammonia under ambient conditions, illustrating how it can form abiotically from simple molecular precursors. In prebiotic and astrochemical simulations, formamide is commonly studied in interstellar ice analogues, where experiments aim to identify its infrared spectral features and destruction and formation mechanisms under various energy inputs; Brucato et al. [212], for instance, characterised the infrared spectrum of pure and ion-irradiated solid formamide, providing key spectral reference data used in this and subsequent studies. These studies provide valuable insight into how formamide might form and survive in space. However, despite its rich prebiotic potential, much remains unknown about how formamide behaves under radiation conditions relevant to icy environments in the Solar System.

As discussed in Section 2.3, formamide on icy bodies such as Europa would be exposed to extreme conditions: mean surface temperatures near 90 K - well below those required for significant thermal reactivity - and constant bombardment by high-energy ionising radiation. These factors are likely to contribute to both the destruction of formamide and the formation of secondary products. While much attention has been paid to formamide's synthetic potential, far less work has been done to explore its survivability and degradation pathways under simulated space-like radiation environments.

In particular, most experimental studies have focused on pure formamide, even though it is unlikely to exist in isolation on icy bodies. Instead, it would be embedded in H_2O-rich ices, delivered via cometary material or formed through surface chemistry. Water is not a passive matrix - it radiolytically produces secondary species such as OH· and H· under irradiation, which may significantly alter the chemical fate of formamide. Despite this, very few studies have examined radiation-driven degradation in formamide-water ice mixtures at cryogenic temperatures, representing a significant gap in our understanding.

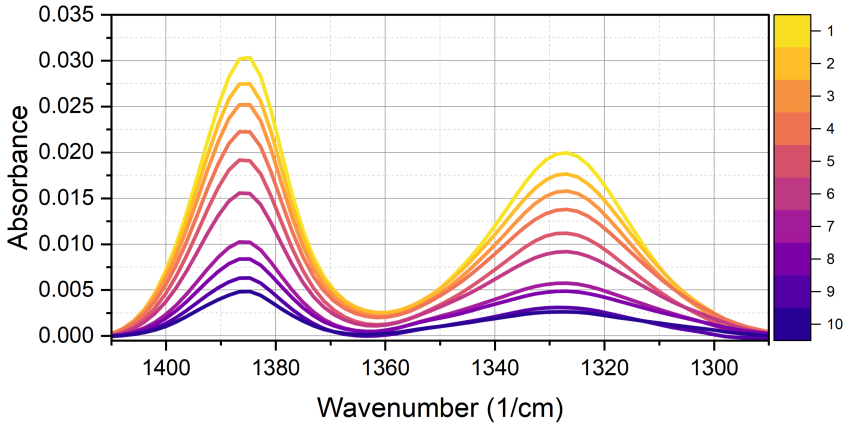


Figure 2.20: Incremental ion irradiation of a 1:1 formamide-water ice mixture deposited on a NaCl substrate at 90 K. The sample was irradiated with S^{5+} ions at 60 keV. Infrared absorbance spectra are shown across ten irradiation intervals, from pre-irradiation (spectrum 1, yellow) to post-final irradiation (spectrum 10, dark purple). The two featured absorption bands at ∼1385 cm^{-1} and ∼1328 cm^{-1} correspond to vibrational modes of formamide. The systematic decrease in absorbance intensity indicates the progressive destruction of formamide under irradiation with sulphur ions.

Additionally, there is minimal comparative data on how different ionising radiation types - ions, electrons, and VUV photons, which together represent the dominant components of Europa's magnetospheric radiation environment - affect the destruction pathways of formamide-water ices. G-values (radiation chemical yields) have not been reported for formamide degradation, nor have they been calculated for product formation in these mixtures. Furthermore, the influence of substrate materials, such as NaCl, chosen as a geochemically relevant analogue for Europa's chloride-rich surface, and ZnSe, chosen as a chemically inert reference substrate, on reaction pathways has not been systematically explored. This gap is exemplified in Figure 2.20, which shows the progressive degradation of formamide in a water-ice matrix under sulphur ion irradiation at 90 K. The reduction in absorbance intensity of characteristic formamide peaks provides a clear indication of molecular destruction, highlighting the need for quantitative treatment through G-value analysis.

This thesis directly addresses these gaps by analysing the destruction of formamide-water ices and the formation of radiolysis products at 90 K under various forms of ionising radiation. At Atomki's ECRIS facility, H^+, O^{2+}, and S^{5+} ions were used to irradiate samples. Complementary experiments using electrons and VUV photons

were carried out at the National Synchrotron in Taiwan. Where possible, G-values were calculated from the spectra and used to compare the relative destruction rates and chemical yields. FTIR and VUV spectroscopy were employed to monitor both formamide loss and new product formation, and a comparison between NaCl and ZnSe substrates was conducted to investigate potential matrix effects.

In summary, while prior laboratory studies have identified formamide's fragmentation products and some destruction cross-sections [213, 218], key astrochemical parameters remain poorly constrained. These include G-values, survivability timescales under realistic space conditions, and the behaviour of mixed ices under different radiation types. This thesis, therefore, aims to experimentally assess the destruction and transformation pathways of formamide under outer Solar System conditions. The formal research aims are outlined in the following section.

Bibliography

[1] Wagner AJ, Blackmond DG. The future of prebiotic chemistry. ACS Cent Sci. 2016 Nov;2(11):775-7.

[2] McCollom TM. Miller-Urey and Beyond: What Have We Learned About Prebiotic Organic Synthesis Reactions in the Past 60 Years? Annual Review of Earth and Planetary Sciences. 2013 May;41:207-29.

[3] Cleaves HJ II. Prebiotic chemistry: What we know, what we don't. Evolution (N Y). 2012 Sep;5(3):342-60.

[4] Akre K, Rafferty JP. In: Miller-Urey experiment; 2024. .

[5] Ferus M, Pietrucci F, Saitta AM, Knížek A, Kubelík P, Ivanek O, et al. Formation of nucleobases in a Miller–Urey reducing atmosphere. Proceedings of the National Academy of Sciences. 2017;114(17):4306-11.

[6] Miller SL. A Production of Amino Acids Under Possible Primitive Earth Conditions. Science. 1953;117(3046):528-9.

[7] Criado-Reyes J, Bizzarri BM, García-Ruiz J, Saladino R, Mauro ED. The role of borosilicate glass in Miller–Urey experiment. Scientific Reports. 2021;11.

[8] Strecker A. Ueber die künstliche Bildung der Milchsäure und einen neuen, dem Glycocoll homologen Körper;. Justus Liebigs Ann Chem. 1850 Jan;75(1):27-45.

[9] Strecker Synthesis – Master Organic Chemistry — masterorganicchemistry.com;. [Accessed 10-11-2025]. `https://www.masterorganicchemistry.com/reaction-guide/strecker-synthesis/`.

[10] Alabduladhem TO, Bordoni B. Physiology, Krebs Cycle. StatPearls Publishing; 2022.

[11] Davey SG. Origin of Life: Cycling citrate sans enzymes. Nat Rev Chem. 2017 Apr;1(5).

[12] Cassidy LM, Burcar BT, Stevens W, Moriarty EM, McGown LB. Guanine-Centric Self-Assembly of Nucleotides in Water: An Important Consideration in Prebiotic Chemistry. Astrobiology. 2014;14(10):876-86. PMID: 25285982.

[13] Liu Z, Wu LF, Xu J, Bonfio C, Russell DA, Sutherland JD. Harnessing chemical energy for the activation and joining of prebiotic building blocks. Nat Chem. 2020 Nov;12(11):1023-8.

[14] Ranjan S, Kufner CL, Lozano GG, Todd ZR, Haseki A, Sasselov DD. UV Transmission in Natural Waters on Prebiotic Earth. Astrobiology. 2022;22(3):242-62. PMID: 34939825.

[15] Lazcano A. In: Primordial Soup; 2015. p. 2010-4.

[16] Dubuc B. The Brain From Top To Bottom — thebrain.mcgill.ca;. [Accessed 12-11-2025]. https://thebrain.mcgill.ca/flash/d/d_05/d_05_m/d_05_m_her/d_05_m_her_g4_1.html.

[17] Prebiotic Chemistry around Shallow-Sea Vents — astrobiology.nasa.gov;. [Accessed 16-08-2024]. https://astrobiology.nasa.gov/news/prebiotic-chemistry-around-shallow-sea-vents/#:~:text=NASA%2Dsupported%20Astrobiologists%20have%20revealed,life%20on%20the%20early%20Earth.

[18] Colín-García M. Hydrothermal vents and prebiotic chemistry: a review. Bol Soc Geol Mex. 2016;68(3):599-620.

[19] Martin W, Baross J, Kelley D, Russell MJ. Hydrothermal vents and the origin of life. Nature Reviews Microbiology. 2008;6(11):805-14.

[20] Jones CK, Leung M, Tu C, Ebadirad S, Marshall N, Tan L, et al. Setting the stage: Building and maintaining a habitable world and the early conditions that could favor life's beginnings on Earth and beyond. arXiv (preprint). 2024.

[21] Where life began — esa.int;. [Accessed 16-08-2024]. https://www.esa.int/Science_Exploration/Space_Science/Rosetta/Where_life_began.

[22] Klessen R, Glover S. Physical Processes in the Interstellar Medium. arXiv: Astrophysics of Galaxies. 2014.

[23] Cia AD, Jenkins E, Fox A, Ledoux C, Ramburuth-Hurt T, Konstantopoulou C, et al. Large metallicity variations in the Galactic interstellar medium. Nature. 2020;597:206 208.

[24] Saintonge A, Catinella B. The Cold Interstellar Medium of Galaxies in the Local Universe. Annual Review of Astronomy & Astrophysics. 2022.

[25] Hu Y. Origin of the Multiphase Interstellar Medium: The Effects of Turbulence and Magnetic Field. The Astrophysical Journal. 2025;986.

[26] Hennebelle P, Inutsuka S. The Role of Magnetic Field in Molecular Cloud Formation and Evolution. Frontiers in Astronomy & Space Sciences. 2019.

[27] Chevance M, Kruijssen J, Vázquez-Semadeni E, Nakamura F, Klessen R, Ballesteros-Paredes J, et al. The Molecular Cloud Lifecycle. Space Science Reviews. 2020;216.

[28] McClure M, Rocha W, Pontoppidan K, Crouzet N, Chu L, Dartois E, et al. An Ice Age JWST inventory of dense molecular cloud ices. Nature Astronomy. 2023;7:431-43.

[29] Müller B, Giuliano B, Goto M, Caselli P. Spectroscopic measurements of CH3OH in layered and mixed interstellar ice analogues. Astronomy & Astrophysics. 2021.

[30] Shingledecker C, Tennis J, Gal RL, Herbst E. On Cosmic-Ray-driven Grain Chemistry in Cold Core Models. The Astrophysical Journal. 2018;861.

[31] Arumainayagam CR, Garrod R, Boyer MC, Hay A, Bao S, Campbell JS, et al. Extraterrestrial prebiotic molecules: photochemistry vs. radiation chemistry of interstellar ices. Chemical Society reviews. 2019;48 8:2293-314.

[32] Jin M, Garrod R. Formation of Complex Organic Molecules in Cold Interstellar Environments through Nondiffusive Grain-surface and Ice-mantle Chemistry. The Astrophysical Journal Supplement Series. 2020;249.

[33] Simons M, Lamberts T, Cuppen H. Formation of COMs through CO hydrogenation on interstellar grains. Astronomy & Astrophysics. 2020.

[34] Rimola A, Skouteris D, Balucani N, Ceccarelli C, Enrique-Romero J, Taquet V, et al. Can Formamide Be Formed on Interstellar Ice? An Atomistic Perspective. ACS Earth and Space Chemistry. 2018.

[35] Martínez-Bachs B, Rimola A. Gas-Phase vs. Grain-Surface Formation of Interstellar Complex Organic Molecules: A Comprehensive Quantum-Chemical Study. International Journal of Molecular Sciences. 2023;24.

[36] Scibelli S, Shirley Y. Prevalence of Complex Organic Molecules in Starless and Prestellar Cores within the Taurus Molecular Cloud. The Astrophysical Journal. 2020;891.

[37] Scibelli S, Shirley Y, Meg'ias A, Jim'enez-Serra I. Survey of Complex Organic Molecules in Starless and Prestellar Cores in the Perseus Molecular Cloud. 2024.

[38] Agúndez M, Loison J, Hickson K, Wakelam V, Fuentetaja R, Cabezas C, et al. Detection of ethanol, acetone, and propanal in TMC-1. New O-bearing complex organics in cold sources. Astronomy & Astrophysics. 2023.

[39] Ligterink N, Ahmadi A, Coutens A, Calcutt L, Dishoeck E, Linnartz H, et al. The prebiotic molecular inventory of Serpens SMM1. Astronomy & Astrophysics. 2020;647.

[40] Li J, Shen Z, Wang J, Chen X, Li D, Wu Y, et al. Widespread Presence of Glycolaldehyde and Ethylene Glycol around Sagittarius B2. The Astrophysical Journal. 2017;849.

[41] Belloche A, Muller H, Menten K, Schilke P, Comito C. Complex organic molecules in the interstellar medium: IRAM 30 m line survey of Sagittarius B2(N) and (M). Astronomy & Astrophysics. 2013;559.

[42] Priestley FD, Clark PC, Ragan S, Scibelli S, Cusack MT, Glover S, et al. NEATH IV: an early onset of complex organic chemistry in molecular clouds. Monthly Notices of the Royal Astronomical Society. 2025.

[43] Booth A, Wölfer L, Temmink M, Calahan JK, Evans L, Law C, et al. Ice Sublimation in the Dynamic HD 100453 Disk Reveals a Rich Reservoir of Inherited Complex Organics. The Astrophysical Journal Letters. 2025;986.

[44] Booth A, Walsh C, van Scheltinga JT, van Dishoeck EV, Ilee J, Hogerheijde M, et al. An inherited complex organic molecule reservoir in a warm planet-hosting disk. Nature Astronomy. 2021;5:684 690.

[45] Bergner J, Ciesla F. Ice Inheritance in Dynamical Disk Models. The Astrophysical Journal. 2021;919.

[46] Ishii H, Bradley J, Bechtel H, Brownlee D, Bustillo K, Ciston J, et al. Multiple generations of grain aggregation in different environments preceded solar system body formation. Proceedings of the National Academy of Sciences of the United States of America. 2018;115:6608 6613.

[47] Jones G, Knight M, Battams K, Boice D, Brown JC, Giordano S, et al. The Science of Sungrazers, Sunskirters, and Other Near-Sun Comets. Space Science Reviews. 2017;214:1-86.

[48] Blum J, Bischoff D, Gundlach B. Formation of Comets. Universe. 2022.

[49] Yar SSM. Comets from Ancient Superstitions to Scientific Facts. Kunduz University International Journal of Islamic Studies and Social Sciences. 2024.

[50] Rubin M, Engrand C, Snodgrass C, Weissman P, Altwegg K, Busemann H, et al. On the Origin and Evolution of the Material in 67P/Churyumov-Gerasimenko. Space Science Reviews. 2020;216.

[51] Hoppe P, Rubin M, Altwegg K. A Comparison of Presolar Isotopic Signatures in Laboratory-Studied Primitive Solar System Materials and Comet 67P/Churyumov-Gerasimenko: New Insights from Light Elements, Halogens, and Noble Gases. Space Science Reviews. 2023;219.

[52] Ahmed S, Acharyya K. The extent of formation of organic molecules in the comae of comets showing relatively high activity. Icarus. 2022.

[53] Biver N, Bockelée-Morvan D, Moreno R, Crovisier J, Colom P, Lis D, et al. Ethyl alcohol and sugar in comet C/2014 Q2 (Lovejoy). Science Advances. 2015;1.

[54] Biver N, Bockelée-Morvan D. Complex Organic Molecules in Comets from Remote-Sensing Observations at Millimeter Wavelengths. ACS Earth and Space Chemistry. 2019.

[55] Rubin M, Bekaert D, Broadley M, Drozdovskaya M, Wampfler S. Volatile Species in Comet 67P/Churyumov-Gerasimenko: Investigating the Link from the ISM to the Terrestrial Planets. ACS Earth and Space Chemistry. 2019.

[56] Zellner N, Mccaffrey V, Butler J. Cometary Glycolaldehyde as a Source of Pre-RNA Molecules. Astrobiology. 2020.

[57] Anslow RJ, Bonsor A, Rimmer PB. Can comets deliver prebiotic molecules to rocky exoplanets? Proceedings of the Royal Society A. 2023;479.

[58] Morse A, Chan Q. Observations of Cometary Organics: A Post Rosetta Review. ACS Earth and Space Chemistry. 2019.

[59] Altwegg K, Balsiger H, Geiss J. Composition of the Volatile Material in Halley's Coma from In Situ Measurements. Space Science Reviews. 1999;90:3-18.

[60] WISE/NEOWISE - NASA Science — science.nasa.gov;. [Accessed 14-11-2025]. https://science.nasa.gov/mission/neowise/.

[61] Researchers Catch Comet Lovejoy Giving Away Alcohol - NASA — nasa.gov;. [Accessed 14-11-2025]. https://www.nasa.gov/solar-system/researchers-catch-comet-lovejoy-giving-away-alcohol/.

[62] Biver N, Moreno R, Bockelée-Morvan D, Sandqvist A, Colom P, Crovisier J, et al. Isotopic ratios of H, C, N, O, and S in comets C/2012 F6 (Lemmon) and C/2014 Q2 (Lovejoy). Astronomy & Astrophysics. 2016;589.

[63] Russo ND, Vervack R, Kawakita H, Bonev B, DiSanti M, Gibb E, et al. Volatile Abundances, Extended Coma Sources, and Nucleus Ice Associations in Comet C/2014 Q2 (Lovejoy). The Planetary Science Journal. 2022;3.

[64] Bockelée-Morvan D, Crovisier J, Mumma M, Weaver H. The composition of cometary volatiles. 2004:391.

[65] Altwegg K, Balsiger H, Fuselier S. Cometary Chemistry and the Origin of Icy Solar System Bodies: The View After Rosetta. Annual Review of Astronomy & Astrophysics. 2019.

[66] Sandford S, Aléon J, Alexander C, Araki T, Bajt S, Baratta G, et al. Organics Captured from Comet 81P/Wild 2 by the Stardust Spacecraft. Science. 2006;314:1720 1724.

[67] Brownlee D, Tsou P, Aléon J, Alexander C, Araki T, Bajt S, et al. Comet 81P/Wild 2 Under a Microscope. Science. 2006;314:1711 1716.

[68] Flynn G, Keller L, Wirick S, Jacobsen C. Organic matter in interplanetary dust particles. Proceedings of the International Astronomical Union. 2008;4:267 276.

[69] Gronoff G, Maggiolo R, Cessateur G, Moore WB, Airapetian V, Airapetian V, et al. The Effect of Cosmic Rays on Cometary Nuclei. I. Dose Deposition. The Astrophysical Journal. 2020;890.

[70] Garrod R. Simulations of Ice Chemistry in Cometary Nuclei. The Astrophysical Journal. 2019;884.

[71] Willis E, Christianson DA, Garrod R. Ice chemistry modeling of active phase comets: Hale-Bopp. Icarus. 2024.

[72] Hudson R, Moore M. Radiation chemical alterations in solar system ices: An overview. Journal of Geophysical Research. 2001;106:33275-84.

[73] Butscher T, Duvernay F, Danger G, Chiavassa T. Radical-induced chemistry from VUV photolysis of interstellar ice analogues containing formaldehyde. Astronomy & Astrophysics. 2016;593.

[74] Öberg K. Photochemistry and Astrochemistry: Photochemical Pathways to Interstellar Complex Organic Molecules. Chemical reviews. 2016;116 17:9631-63.

[75] Chuang K, Fedoseev G, Ioppolo S, Dishoeck EV, Linnartz H. H-atom addition and abstraction reactions in mixed CO, H2CO and CH3OH ices – an extended view on complex organic molecule formation. Monthly Notices of the Royal Astronomical Society. 2016;455:1702-12.

[76] He J, Góbi S, Ragupathy G, Tarczay G, Henning T. Radical Recombination during the Phase Transition of Interstellar CO Ice. The Astrophysical Journal Letters. 2022;931.

[77] del Burgo Olivares C, Carrascosa H, Caro GMM, Muñoz-Arnanz J, González-Díaz C, Chen YJ. Synthesis of new hexamethylenetetramine-based products (HMT-R) in UV-irradiated pre-cometary ice analogues. Astronomy & Astrophysics. 2025.

[78] Henderson B, Gudipati M. Direct Detection Of Complex Organics Products In Ultraviolet (Lyα) And Electron-Irradiated Astrophysical And Cometary Ice Analogs Using Two-Step Laser Ablation And Ionization Mass Spectrometry. The Astrophysical Journal. 2015;800.

[79] Nuevo M, Bredehöft J, Meierhenrich U, d'Hendecourt L, Thiemann W. Urea, glycolic acid, and glycerol in an organic residue produced by ultraviolet irradiation of interstellar/pre-cometary ice analogs. Astrobiology. 2010;10 2:245-56.

[80] Méndez A, Rivera-Valentín EG, Schulze-Makuch D, Filiberto J, Ramírez RM, Wood TE, et al. Habitability Models for Astrobiology. Astrobiology. 2021;21(8):1017-27. PMID: 34382857.

[81] NASA Science Editorial Team. Sending Signals Through the Ice on Ocean Worlds; 2023. NASA Science. Figure 1 credit: K. Hand et al./NASA/JPL.

[Accessed 11-10-2026]. https://science.nasa.gov/science-research/science-enabling-technology/technology-highlights/sending-signals-through-the-ice-on-ocean-worlds/.

[82] Ruslik0. Currents in Jovian Magnetosphere; 2009. Wikimedia Commons. Licensed under CC BY-SA 3.0, [Accessed 12-11-2025]. https://commons.wikimedia.org/wiki/File:Currents_in_Jovian_Magnetosphere.png.

[83] Pollack JB, Witteborn FC, Erickson EF, Strecker DW, Baldwin BJ, Bunch TE. Near-infrared spectra of the Galilean satellites: Observations and compositional implications. Icarus. 1978;36(3):271-303.

[84] Consolmagno GJ, Lewis JS. Structural and thermal models of icy Galilean satellites. In: Gehrels T, Matthews S, editors. IAU Colloq. 30: Jupiter: Studies of the Interior, Atmosphere, Magnetosphere and Satellites; 1976. p. 1035-51.

[85] How Jupiter Moon Europa's Underground Ocean Was Discovered — space.com;. [Accessed 16-08-2024]. https://www.space.com/19750-voyager-mission-jupiter-moon-europa-ocean.html.

[86] Ingredients for Life | Why Europa – NASA's Europa Clipper — europa.nasa.gov;. [Accessed 16-08-2024]. https://europa.nasa.gov/why-europa/ingredients-for-life/#:~:text=NASA%2FJPL%2DCaltech-,Europa's%20surface%20is%20blasted%20by%20radiation%20from%20Jupiter.,in%20Europa's%20extremely%20tenuous%20atmosphere.

[87] Kattenhorn SA, Prockter LM. Evidence for subduction in the ice shell of Europa. Nature Geoscience. 2014 Oct;7(10):762-7.

[88] Trumbo S, Brown ME. The distribution of CO2 on Europa indicates an internal source of carbon. Science. 2023;381:1308 1311.

[89] Carlson R, Anderson M, Johnson RE, Schulman MB, Yavrouian A. Sulfuric Acid Production on Europa: The Radiolysis of Sulfur in Water Ice. Icarus. 2002;157:456-63.

[90] Scientists excited to find ocean of one of Jupiter's moons contains carbon — theguardian.com;. [Accessed 17-08-2024]. https://www.theguardian.com/science/2023/sep/21/scientists-excited-to-find-ocean-of-one-of-jupiters-moons-contains-carbon.

[91] Raulin F. Exo-Astrobiological Aspects of Europa and Titan: From Observations to Speculations. Space Science Reviews. 2005 Jan;116(1-2):471-87.

[92] Gavin P, Vance S. Modeling Hydrothermal Vents on Europa. In: AGU Fall Meeting Abstracts. vol. 2011; 2011. p. P23D-1743.

[93] Marion G, Fritsen C, Eicken H, Payne M. The search for life on Europa: limiting environmental factors, potential habitats, and Earth analogues. Astrobiology. 2003;3 4:785-811.

[94] Melosh HJ, Ekholm AG, Showman AP, Lorenz RD. The temperature of Europa's subsurface water ocean. Icarus. 2004;168(2):498-502.

[95] Ashkenazy Y. The surface temperature of Europa. Heliyon. 2016;5.

[96] Jupiter's radiation belts – and how to survive them — esa.int;. [Accessed 17-08-2024]. https://www.esa.int/Enabling_Support/Space_Engineering_Technology/Jupiter_s_radiation_belts_and_how_to_survive_them.

[97] Kollmann P, Clark G, Paranicas C, Mauk B, Roussos E, Nénon Q, et al. Jupiter's Ion Radiation Belts Inward of Europa's Orbit. Journal of Geophysical Research: Space Physics. 2020;126.

[98] Paranicas C, Ratliff JM, Mauk B, Cohen C, Johnson RE. The ion environment near Europa and its role in surface energetics. Geophysical Research Letters. 2002;29.

[99] Paranicas C, Cooper JF, Garrett HB, Johnson RE, Sturner SJ. Europa's Radiation Environment and Its Effects on the Surface. Europa (University of Arizona Space Science Series). 2009.

[100] Nordheim T, Hand K, Paranicas C. Preservation of potential biosignatures in the shallow subsurface of Europa. Nature Astronomy. 2018;2:673-9.

[101] Johnson RE, Burger MH, Cassidy TA, Leblanc F, Marconi M, Smyth WH. Composition and Detection of Europa's Sputter-induced Atmosphere. 2009.

[102] Li J, Gudipati M, Yung Y. The influence of Europa's plumes on its atmosphere and ionosphere. Icarus. 2020.

[103] Cassidy T, Johnson RE, McGrath M, Wong M, Cooper J. The spatial morphology of Europa's near-surface O2 atmosphere. Icarus. 2007;191:755-64.

[104] Shematovich V, Johnson R, Cooper J, Wong M. Surface-bounded atmosphere of Europa. Icarus. 2005;173:480-98.

[105] Juice — esa.int;. [Accessed 14-11-2025]. https://www.esa.int/Science_Exploration/Space_Science/Juice.

[106] JUICE — dlr.de;. [Accessed 15-11-2025]. https://www.dlr.de/en/wr/research-transfer/projects/planetary-research/juice.

[107] The moons of Jupiter: What will Juice discover?;. Available from: https://www.esa.int/Science_Exploration/Space_Science/Juice/The_moons_of_Jupiter_What_will_Juice_discover.

[108] ESA Science & Technology - JUICE's instruments — sci.esa.int;. [Accessed 29-11-2025]. https://sci.esa.int/web/juice/-/61110-juice-instruments.

[109] Juice factsheet;. Available from: https://www.esa.int/Science_Exploration/Space_Science/Juice/Juice_factsheet#:~:text=Juice%20will%20be%20the%20first,Ganymede%2C%20Europa%20and%20Callisto).

[110] Poulet F, Piccioni G, Langevin Y, Dumesnil C, Tommasi L, Carlier V, et al. Moons and Jupiter Imaging Spectrometer (MAJIS) on Jupiter Icy Moons Explorer (JUICE). Space Science Reviews. 2024.

[111] SWI — mps.mpg.de;. [Accessed 15-11-2025]. https://www.mps.mpg.de/planetary-science/juice-swi.

[112] Gladstone R, Retherford K, Steffl A, Eterno J, Davis M, Versteeg M, et al. The Ultraviolet Spectrograph (UVS) on ESA's JUICE Mission. In: AAS/Division for Planetary Sciences Meeting Abstracts #45. vol. 45 of AAS/Division for Planetary Sciences Meeting Abstracts; 2013. p. 211.04.

[113] Molyneux PM, Gladstone R, Retherford KD, Davis MW, Ferrell SA, Greathouse TK, et al. JUICE-UVS: First Light and Prospects for Future Exploration of the Jupiter System. In: AGU Fall Meeting Abstracts. vol. 2023 of AGU Fall Meeting Abstracts; 2023. p. P31E-3.

[114] Su H, Zhao D, Heidari AA, Liu L, Zhang X, Mafarja MM, et al. RIME: A physics-based optimization. Neurocomputing. 2023;532:183-214.

[115] ESA Science & Technology - Science Payload — sci.esa.int;. [Accessed 15-11-2025]. https://sci.esa.int/web/juice/-/50073-science-payload.

[116] ESA Science & Technology - JUICE's secondary target: Europa — sci.esa.int;. [Accessed 15-11-2025]. https://sci.esa.int/web/juice/-/59906-juice-s-secondary-target-europa.

[117] Europa Clipper - NASA Science — science.nasa.gov;. [Accessed 15-11-2025]. https://science.nasa.gov/mission/europa-clipper/.

[118] Europa Clipper Spacecraft Instruments — science.nasa.gov;. [Accessed 15-11-2025]. https://science.nasa.gov/mission/europa-clipper/spacecraft-instruments/.

[119] Waite JH, Burch JL, Brockwell T, Young DT, Miller G, Persyn S, et al. MASPEX-Europa: The Europa Clipper Neutral Gas Mass Spectrometer Investigation. Space Science Reviews. 2024.

[120] Europa Clipper MISE — science.nasa.gov;. [Accessed 17-11-2025]. https://science.nasa.gov/mission/europa-clipper/spacecraft-instruments-mise/.

[121] Blaney D, Hibbitts K, Diniega S, Davies AG, Clark R, Green RO, et al. The Mapping Imaging Spectrometer for Europa (MISE). Space Science Reviews. 2024;220.

[122] SUDA - NASA Science — science.nasa.gov;. [Accessed 17-11-2025]. https://science.nasa.gov/mission/europa-clipper/spacecraft-instruments-suda/.

[123] SUDA — lasp.colorado.edu;. [Accessed 17-11-2025]. https://lasp.colorado.edu/instruments/suda/.

[124] Christensen PR, Spencer JR, Mehall G, Patel M, Anwar S, Brick M, et al. The Europa Thermal Emission Imaging System (E-THEMIS) Investigation for the Europa Clipper Mission. Space Science Reviews. 2024.

[125] Spacecraft Instruments EIS — science.nasa.gov;. [Accessed 17-11-2025]. https://science.nasa.gov/mission/europa-clipper/spacecraft-instruments-eis/.

[126] Cowing K. Europa Clipper: Radar for Europa Assessment and Sounding: Ocean to Near-Surface (REASON) - Astrobiology — astrobiology.com;. [Accessed 17-11-2025]. https://astrobiology.com/2024/09/europa-clipper-radar-for-europa-assessment-and-sounding-ocean-to-near-surface-reason.html.

[127] Europa Clipper ECM — science.nasa.gov;. [Accessed 17-11-2025]. https://science.nasa.gov/mission/europa-clipper/spacecraft-instruments-ecm/.

[128] C-1 Building Blocks in Organic Synthesis - Thieme Chemistry - Georg Thieme Verlag — thieme.de;. [Accessed 29-04-2025]. https://www.thieme.de/en/thieme-chemistry/sos-c-1-building-blocks-in-organic-synthesis-55594.htm.

[129] Pace V, de la Vega-Hernández K, Urban E, Langer T. Chemoselective Schwartz Reagent Mediated Reduction of Isocyanates to Formamides. Organic letters. 2016;18 11:2750-3.

[130] Bruffaerts J, von Wolff N, Diskin-Posner Y, Ben-David Y, Milstein D. Formamides as isocyanate surrogates: A mechanistically-driven approach to the development of atom-efficient, selective catalytic syntheses of ureas, carbamates and heterocycles. Journal of the American Chemical Society. 2019.

[131] Saladino R, Botta G, Pino S, Costanzo G, Mauro ED. Genetics first or metabolism first? The formamide clue. Chemical Society reviews. 2012;41 16:5526-65.

[132] Shanker U, Bhushan B, Bhattacharjee G, Kamaluddin. Formation of nucleobases from formamide in the presence of iron oxides: implication in chemical evolution and origin of life. Astrobiology. 2011;11 3:225-33.

[133] Saladino R, Carota E, Botta G, Kapralov M, Timoshenko G, Rozanov AY, et al. Meteorite-catalyzed syntheses of nucleosides and of other prebiotic compounds from formamide under proton irradiation. Proceedings of the National Academy of Sciences. 2015;112:E2746 E2755.

[134] Adandé G, Woolf N, Ziurys L. Observations of interstellar formamide: availability of a prebiotic precursor in the galactic habitable zone. Astrobiology. 2013;13 5:439-53.

[135] Saladino R, Crestini C, Ciciriello F, Costanzo G, Di Mauro E. Formamide Chemistry and the Origin of Informational Polymers. Chemistry & Biodiversity. 2007;4.

[136] Pietrucci F, Saitta AM. Formamide reaction network in gas phase and solution via a unified theoretical approach: Toward a reconciliation of different prebiotic scenarios. Proceedings of the National Academy of Sciences. 2015;112:15030 15035.

[137] Bizzarri BM, Saladino R, Delfino I, García-Ruiz J, Mauro ED. Prebiotic Organic Chemistry of Formamide and the Origin of Life in Planetary Conditions: What We Know and What Is the Future. International Journal of Molecular Sciences. 2021;22.

[138] Kahane C, Ceccarelli C, Faure A, Caux E. Detection of Formamide, The Simplest But Crucial Amide, in a Solar-type Protostar. The Astrophysical Journal Letters. 2013;763.

[139] Corby J, Jones PA, Cunningham M, Menten K, Belloche A, Schwab F, et al. An ATCA survey of Sagittarius B2 at 7 mm: chemical complexity meets broad-band interferometry. Monthly Notices of the Royal Astronomical Society. 2015;452:3969-93.

[140] Hollis J, Lovas F, Remijan A, Jewell P, Ilyushin V, Kleiner I. Detection of Acetamide (CH3CONH2): The Largest Interstellar Molecule with a Peptide Bond. The Astrophysical Journal Letters. 2006;643:L25 L28.

[141] Ribes J, Ables J, Godfrey P, Brown R. Observations of formamide at 6-cm in Sagittarius B2. Australian Journal of Physics. 1973;26:79-84.

[142] López-Sepulcre A, Balucani N, Ceccarelli C, Codella C, Dulieu F, Theul'e P. Interstellar Formamide (NH2CHO), a Key Prebiotic Precursor. ACS Earth and Space Chemistry. 2019.

[143] Halfen D, Ilyushin V, Ziurys L. Formation Of Peptide Bonds In Space: A Comprehensive Study Of Formamide And Acetamide In Sgr B2(N). The Astrophysical Journal. 2011;743.

[144] Biver N, Bockelée-Morvan D, Debout V, Crovisier J, Boissier J, Lis D, et al. Complex organic molecules in comets C/2012 F6 (Lemmon) and C/2013 R1 (Lovejoy): detection of ethylene glycol and formamide. Astronomy & Astrophysics. 2014;566.

[145] López-Sepulcre A, López-Sepulcre A, Jaber A, Jaber A, Mendoza E, Lefloch B, et al. Shedding light on the formation of the pre-biotic molecule formamide with ASAI. Monthly Notices of the Royal Astronomical Society. 2015;449:2438-58.

[146] Frigge R, Zhu C, Turner A, Abplanalp M, Bergantini A, Sun B, et al. A Vacuum Ultraviolet Photoionization Study on the Formation of N-methyl Formamide

(HCONHCH3) in Deep Space: A Potential Interstellar Molecule with a Peptide Bond. The Astrophysical Journal. 2018;862.

[147] Motiyenko R, Tercero B, Cernicharo J, Margulès L. Rotational spectrum of formamide up to 1 THz and first ISM detection of its ν12 vibrational state. Astronomy & Astrophysics. 2012;548.

[148] Thripati S, Ramabhadran RO. Pathways for the Formation of Formamide, a Prebiotic Biomonomer: Metal-Ions in Interstellar Gas-Phase Chemistry. The journal of physical chemistry A. 2021.

[149] Goesmann F, Rosenbauer H, Bredehöft JH, Cabane M, Ehrenfreund P, Gautier T, et al. Organic compounds on comet 67P/Churyumov-Gerasimenko revealed by COSAC mass spectrometry. Science. 2015;349(6247):aab0689.

[150] Despois D. In: Gargaud M, Irvine WM, Amils R, Cleaves HJJ, Pinti DL, Quintanilla JC, et al., editors. Formamide. Berlin, Heidelberg: Springer Berlin Heidelberg; 2015. p. 872-3.

[151] Rubin RH, G W Swenson J, Benson RC, Tigelaar HL, Flygare WH. Microwave Detection Of Interstellar Formamide. The Astrophysical Journal. 1971.

[152] Motte F, Bontemps S, Louvet F. High-Mass Star and Massive Cluster Formation in the Milky Way. Annual Review of Astronomy & Astrophysics. 2018.

[153] Belloche A, Meshcheryakov A, Garrod R, Ilyushin V, Alekseev E, Motiyenko R, et al. Rotational spectroscopy, tentative interstellar detection, and chemical modeling of N-methylformamide. Astronomy & Astrophysics. 2017;601.

[154] Li J, Quan D, Wang J, Zhang X, Lu X, Gou Q, et al. Tentative detection of cyanoformamide NCCONH2 in space. Publications of the Astronomical Society of Japan. 2023.

[155] Belloche A, Garrod R, Müller HSP, Menten K, Medvedev I, Thomas JR, et al. Re-exploring Molecular Complexity with ALMA (ReMoCA): interstellar detection of urea. Astronomy & Astrophysics. 2019.

[156] Zeng S, Rivilla V, Jímenez-Serra I, Colzi L, Martín-Pintado J, B T, et al. Amides inventory towards the G+0.693-0.027 molecular cloud. Monthly Notices of the Royal Astronomical Society. 2023.

[157] Jørgensen J, Wiel M, Coutens A, Lykke J, Müller H, Dishoeck E, et al. The ALMA Protostellar Interferometric Line Survey (PILS). 2016.

[158] Marcelino N, Gerin M, Cernicharo J, Fuente A, Wootten H, Chapillon E, et al. ALMA observations of the young protostellar system Barnard 1b: signatures of an incipient hot corino in B1b-S. Astronomy & astrophysics. 2018;620.

[159] Bianchi E, L'opez-Sepulcre A, Ceccarelli C, Codella C, Podio L, Bouvier M, et al. The Two Hot Corinos of the SVS13-A Protostellar Binary System: Counterposed Siblings. The Astrophysical Journal Letters. 2022;928.

[160] Lee JE, Evans N, Baek G, Kim CH, Noh J, Yang YL. A Natural Laboratory for Astrochemistry: The Variable Protostar B335. The Astrophysical Journal Letters. 2024;978.

[161] Codella C, Ceccarelli C, Ceccarelli C, Caselli P, Balucani N, Barone V, et al. Seeds of Life in Space (SOLIS) II. Formamide in protostellar shocks: Evidence for gas-phase formation. Astronomy & Astrophysics. 2017;605.

[162] Chuang K, Jäger C, Krasnokutski S, Fulvio D, Henning T. Formation of the Simplest Amide in Molecular Clouds: Formamide (NH2CHO) and Its Derivatives in H2O-rich and CO-rich Interstellar Ice Analogs upon VUV Irradiation. The Astrophysical Journal. 2022;933.

[163] Dulieu F, Nguyen T, Congiu E, Baouche S, Taquet V. Efficient formation route of the prebiotic molecule formamide on interstellar dust grains. Monthly Notices of the Royal Astronomical Society: Letters. 2019.

[164] Fredon A, Radchenko A, Cuppen H. Quantification of the Role of Chemical Desorption in Molecular Clouds. Accounts of Chemical Research. 2021;54:745 753.

[165] Vazart F, Calderini D, Puzzarini C, Skouteris D, Barone V. State-of-the-Art Thermochemical and Kinetic Computations for Astrochemical Complex Organic Molecules: Formamide Formation in Cold Interstellar Clouds as a Case Study. Journal of chemical theory and computation. 2016;12 11:5385-97.

[166] Barone V, Latouche C, Skouteris D, Vazart F, Balucani N, Ceccarelli C, et al. Gas-phase formation of the prebiotic molecule formamide: insights from new quantum computations. Monthly Notices of the Royal Astronomical Society. 2015;453.

[167] L'opez-Sepulcre A, Codella C, Ceccarelli C, Podio L, Robuschi J. Full interferometric map of the L1157 southern outflow: Formamide (NH_2CHO) can form in the gas, after all. Astronomy & Astrophysics. 2024.

[168] Bisschop S, Jørgensen J, Dishoeck EV, Hnco, NH2CHO. Testing grain-surface chemistry in massive hot-core regions. Astronomy & Astrophysics. 2007;465:913-29.

[169] Mendoza E, Mendoza E, Lefloch B, López-Sepulcre A, Ceccarelli C, Codella C, et al. Molecules with a peptide link in protostellar shocks: a comprehensive study of L1157. Monthly Notices of the Royal Astronomical Society. 2014;445:151-61.

[170] Bockelée-Morvan D, Lis DC, Wink JE, Despois D, Crovisier J, Bachiller R, et al. New molecules found in comet C/1995 O1 (Hale-Bopp). Investigating the link between cometary and interstellar material. Astronomy & Astrophysics. 2000 Jan;353:1101-14.

[171] Cassone G, Saija F, Sponer J, Sponer JE, Jiménez-Escobar A, Ciaravella A, et al. Atomistic simulations of the free-energy landscapes of interstellar chemical reactions: the case of methyl isocyanate. Monthly Notices of the Royal Astronomical Society. 2021 04;504(2):1565-70.

[172] Rosetta — esa.int;. [Accessed 28-04-2025]. https://www.esa.int/Science_Exploration/Space_Science/Rosetta#:~:text=The%20mission,%2C%20MPS%2C%20CNES%20and%20ASI.

[173] 67P/Churyumov-Gerasimenko - NASA Science — science.nasa.gov;. [Accessed 28-04-2025]. https://science.nasa.gov/solar-system/comets/67p-churyumov-gerasimenko/.

[174] Pizzarello S. Molecular Asymmetry in Prebiotic Chemistry: An Account from Meteorites. Life. 2016;6(2).

[175] Ligier N, Paranicas C, Carter J, Poulet F, Calvin WM, Nordheim T, et al. Surface composition and properties of Ganymede: Updates from ground-based observations with the near-infrared imaging spectrometer SINFONI/VLT/ESO. Icarus. 2019.

[176] Clark R. Ganymede, Europa, Callisto, and Saturn's rings: Compositional analysis from reflectance spectroscopy . Icarus. 1980;44:388-409.

[177] Johnson RE, Quickenden TI. Photolysis and radiolysis of water ice on outer solar system bodies. Journal of Geophysical Research. 1997;102:10985-96.

[178] https://www space com/author/elizabeth howell. Voyager 2 Transformed Our Ideas of Jupiter's Moons 40 Years Ago — space.com;. [Accessed 13-06-2026]. https://www.space.com/voyager-2-jupiter-flyby-anniversary.html.

[179] 40 Years Ago: Voyager 2 Explores Jupiter - NASA — nasa.gov;. [Accessed 13-06-2026]. https://www.nasa.gov/history/40-years-ago-voyager-2-explores-jupiter/.

[180] The biggest discoveries of Voyagers — NASA's most distant explorers — snexplores.org;. [Accessed 13-06-2026]. https://www.snexplores.org/article/voyagers-biggest-discoveries-nasa-space.

[181] Brown W, Lanzerotti L, Poate J, Augustyniak W. "Sputtering" of ice by MeV light ions. Physical Review Letters. 1978;40:1027-30.

[182] Lanzerotti L, Brown W, Poate J, Augustyniak W. On the contribution of water products from Galilean satellites to the Jovian magnetosphere. Geophysical Research Letters. 1978;5:155-8.

[183] Teolis B, Plainaki C, Cassidy T, Raut U. Water Ice Radiolytic O2, H2, and H2O2 Yields for Any Projectile Species, Energy, or Temperature: A Model for Icy Astrophysical Bodies. Journal of Geophysical Research: Planets. 2017;122:1996 2012.

[184] Rogalski A. History of infrared detectors. Opto-Electronics Review. 2012;20:279-308.

[185] Gillett F, Houck J. The Decade of Infrared Astronomy. Physics Today. 1991;44:32-7.

[186] Öberg K, van Dishoeck EV, Linnartz H, Andersson S. The Effect Of H2O on Ice Photochemistry. The Astrophysical Journal. 2010;718:832 840.

[187] Öberg K, Garrod R, Dishoeck EV, Linnartz H. Formation rates of complex organics in UV irradiated CH3OH-rich ices I: Experiments. Astronomy & Astrophysics. 2009;504:891-913.

[188] Moore M, Hudson R. IR Detection of H2O2 at 80 K in Ion-Irradiated Laboratory Ices Relevant to Europa. Icarus. 2000;145:282-8.

[189] Moore M, Ferrante R, Hudson R, Stone J. Ammonia–water ice laboratory studies relevant to outer Solar System surfaces. Icarus. 2007;190:260-73.

[190] Mifsud D, Herczku P, Sulik B, Juhász Z, Vajda I, Rajta I, et al. Proton and Electron Irradiations of CH4:H2O Mixed Ices. Atoms. 2023.

[191] Becker T, Trumbo S, Molyneux P, Retherford K, Hendrix A, Roth L, et al. Mid-ultraviolet Hubble Observations of Europa and the Global Surface Distribution of SO2. The Planetary Science Journal. 2022;3.

[192] Mifsud D, Kaňuchová Z, Herczku P, Ioppolo S, Juhász Z, Kovács S, et al. Sulfur Ice Astrochemistry: A Review of Laboratory Studies. Space Science Reviews. 2021;217:1-34.

[193] Moore M, Hudson R, Carlson R. The radiolysis of SO2 and H2S in water ice: Implications for the icy jovian satellites. Icarus. 2007;189:409-23.

[194] Krass M. Ice On Planets of the Solar System. Journal of Glaciology. 1984;30:259 274.

[195] Pilcher C, Ridgway S, McCord T. Galilean Satellites: Identification of Water Frost. Science. 1972;178:1087 1089.

[196] Lewis JS. Satellites of the Outer Planets: Their Physical and Chemical Nature. Icarus. 1971;15:174-85.

[197] Carr M, Belton M, Chapman C, Davies M, Geissler P, Greenberg R, et al. Evidence for a subsurface ocean on Europa. Nature. 1998;391:363-5.

[198] McCord T, Hansen GB, Fanale F, Carlson RW, Matson DL, Johnson TV, et al. Salts on Europa's surface detected by Galileo's near infrared mapping spectrometer. The NIMS Team. Science. 1998;280 5367:1242-5.

[199] McCord T, Hansen G, Matson D, Johnson T, Crowley JK, Fanale F, et al. Hydrated salt minerals on Europa's surface from the Galileo near-infrared mapping spectrometer (NIMS) investigation. Journal of Geophysical Research. 1999;104:11827-51.

[200] Trumbo S, Brown M, Hand K. Sodium chloride on the surface of Europa. Science Advances. 2019;5.

[201] Hand K, Carlson RW. Europa's surface color suggests an ocean rich with sodium chloride. Geophysical Research Letters. 2015;42:3174 3178.

[202] Trumbo S, Becker T, Brown M, Denman W, Molyneux P, Hendrix A, et al. A New UV Spectral Feature on Europa: Confirmation of NaCl in Leading-hemisphere Chaos Terrain. The Planetary Science Journal. 2022;3.

[203] Dalton JB, Prieto-Ballesteros O, Kargel J, Jamieson C, Jolivet J, Quinn R. Spectral comparison of heavily hydrated salts with disrupted terrains on Europa. Icarus. 2005;177:472-90.

[204] Spencer, Tamppari, Martin, Travis. Temperatures on europa from galileo photopolarimeter-radiometer: nighttime thermal anomalies. Science. 1999;284 5419:1514-6.

[205] Dalton JB. Linear mixture modeling of Europa's non-ice material based on cryogenic laboratory spectroscopy. Geophysical Research Letters. 2007;34.

[206] Cérubini R, Pommerol A, Galli A, Jost B, Wurz P, Thomas N. VIS spectroscopy of NaCl – water ice mixtures irradiated with 1 and 5 keV electrons under Europa's conditions: Formation of colour centres and Na colloids. Icarus. 2022.

[207] Poston M, Carlson R, Hand K. Spectral Behavior of Irradiated Sodium Chloride Crystals Under Europa-Like Conditions. Journal of Geophysical Research: Planets. 2017;122:2644 2654.

[208] Thompson SP, Kennedy H, Butler BM, Day S, Safi E, Evans A. Laboratory exploration of mineral precipitates from Europa's subsurface ocean. Journal of Applied Crystallography. 2021;54:1455 1479.

[209] Ottersberg R, Pommerol A, Stöckli L, Obersnel L, Galli A, Murk A, et al. Evolution of granular salty ice analogs for Europa: Sublimation and irradiation. Icarus. 2025.

[210] Kaňuchová Z, Urso R, Baratta G, Brucato J, Palumbo M, Strazzulla G. Synthesis of formamide and isocyanic acid after ion irradiation of frozen gas mixtures. Astronomy & Astrophysics. 2016;585.

[211] Sivaraman B, Sekhar BN, Nair B, Hatode V, Mason NJ. Infrared spectrum of formamide in the solid phase. Spectrochimica acta Part A, Molecular and biomolecular spectroscopy. 2013;105:238-44.

[212] Brucato J, Baratta G, Strazzulla G. An infrared study of pure and ion irradiated frozen formamide. Astronomy & Astrophysics. 2006;455:395-9.

[213] Dawley MM, Pirim C, Orlando T. Radiation processing of formamide and formamide:water ices on silicate grain analogue. The journal of physical chemistry A. 2014;118 7:1228-36.

[214] Suhasaria T, Henning T, Mennella V. Stability of solid-state formamide under Ly alpha irradiation. Astronomy & Astrophysics. 2024.

[215] Adandé G, Woolf N, Ziurys L. Observations of interstellar formamide: availability of a prebiotic precursor in the galactic habitable zone. Astrobiology. 2013;13 5:439-53.

[216] Mcconaughy B, Laird C, Mccarthy B. Nucleic acid reassociation in formamide. Biochemistry. 1969;8 8:3289-95.

[217] Meng N, Shao J, Li H, Wang Y, Fu X, Liu C, et al. Electrosynthesis of formamide from methanol and ammonia under ambient conditions. Nature Communications. 2022;13.

[218] Suhasaria T, Mennella V. Lyα irradiation of solid-state formamide. Astronomy & Astrophysics. 2022;662:A73.

Chapter 3

Physical Chemistry & Spectroscopy Fundamentals

3.1 Basics of IR and VUV Spectroscopy

This section outlines the fundamental principles behind the two primary spectroscopic techniques used throughout this study: Infrared (IR) spectroscopy and Vacuum Ultraviolet (VUV) spectroscopy. Each method probes a different region of the electromagnetic spectrum and is sensitive to distinct molecular properties. While IR spectroscopy reveals how molecules vibrate - highlighting changes in bonding or structure - VUV spectroscopy is capable of probing high-energy electronic transitions and photodissociation pathways. Together, these techniques provide a comprehensive view of how formamide-water ices respond to ionising radiation under cryogenic, space-like conditions.

3.1.1 Infrared Spectroscopy

Infrared (IR) spectroscopy plays a central role in this study by providing in-situ information on the molecular structure of cryogenic ices. By tracking characteristic vibrational modes, it is possible to identify functional groups, follow changes in bonding, and distinguish between different molecular environments within the ice. The following section explains the fundamental principles of IR spectroscopy, including molecular vibrations, absorption features, and how these relate to the interpretation of spectra acquired for formamide-water ices.

3.1.1.1 Principles

Molecules exhibit several types of vibrational motions, including symmetric and asymmetric stretching, bending (e.g., scissoring, rocking, wagging, twisting), and other deformation modes [1]. In larger molecules, many bending and deformation modes are strongly mixed and are therefore often described as “skeletal” vibrations, since they involve concerted motion of the molecular framework rather than a single isolated bond. Stretching involves a change in bond length, while bending consists of a change in bond angle. These vibrational modes are sensitive to molecular bonding and structure: some absorptions can be associated with particular bonds or functional groups, whereas others reflect motion of the wider molecular framework, particularly for bending and

deformation modes. In practice, it is the overall pattern of absorption bands that forms the basis for molecular "fingerprinting" using IR spectroscopy. Molecules often exhibit symmetric or antisymmetric stretching, as illustrated in Figure 3.1. Symmetric stretching describes the case where equivalent bonds change length in phase (i.e., they lengthen together and shorten together). In contrast, antisymmetric stretching occurs when equivalent bonds change length out of phase (i.e., one bond lengthens while another shortens).

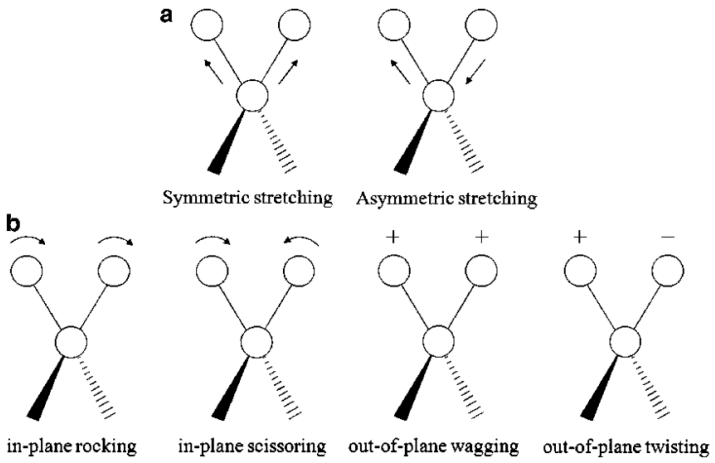


Figure 3.1: Types of molecular vibrations include: (a) stretching vibrations and (b) bending vibrations. The "+" and "−" symbols represent atomic motion directed out of and into the plane of the page, respectively. **Credit:** Reproduced with permission from Springer Nature: J. J. Ojeda and M. Dittrich, Fourier Transform Infrared Spectroscopy for Molecular Analysis of Microbial Cells, *Microbial Systems Biology*, Methods in Molecular Biology, vol. 881, pp. 187–211, Humana Press, 2012, Springer Nature, [1].

Only a subset of vibrational modes are observed in an IR spectrum: a mode is "IR active" if the vibration involves a change in the molecule's dipole moment, allowing it to couple to the incident infrared radiation. Each IR-active vibrational mode corresponds to a specific absorption in the IR spectrum, allowing for detailed analysis of molecular structure and bonding. Since many functional groups absorb in characteristic wavenumber ranges, IR spectroscopy is effective for identifying functional groups and tracking changes in bonding or chemical environment. At the same time, the combined set of bands across the spectrum - sometimes referred to as the 'fingerprint region' - provides a pattern of absorptions that is unique to each molecule, enabling unambiguous identification of chemical species and allowing specific structural features, such as amide bonds or carbonyl groups, to be monitored within complex organic

molecules. This fingerprinting capability is particularly valuable for prebiotic compounds like formamide, whose characteristic vibrational bands in the mid-IR provide a sensitive probe of its molecular environment, bonding state, and radiation-driven chemical evolution [2–4].

In this work, Fourier-transform infrared (FTIR) spectroscopy was used to collect in-situ IR spectra of irradiated ices. In FTIR, a broadband IR beam is split into two paths within an interferometer; a moving mirror varies the optical path difference between these paths, and the resulting interference signal recorded at the detector as a function of mirror displacement is known as the interferogram. FTIR employs a mathematical Fourier transform[1] to convert raw interferogram data into usable spectra, allowing for fast, high-resolution acquisition across the full Mid-Infrared (MIR) range [5]. The technique works by measuring the absorption of IR radiation as a function of wavenumber, enabling the detection of vibrational transitions in molecules. Unlike dispersive IR methods, FTIR captures all wavelengths simultaneously, improving signal-to-noise ratio and acquisition speed.

These principles form the basis for the IR spectral analysis carried out in Chapters 5-7, where changes in vibrational bands are used to monitor molecular degradation and product formation in formamide-water ice.

[1]The Fourier-transform is a mathematical function that decomposes a waveform as a function of time to a function of frequency.

3.1.1.2 Applications to Astrochemistry



Figure 3.2: The Horsehead Nebula (Barnard 33) and NGC 2023, captured in visible light. NGC 2023 is visible in the lower left of the image. **Credit:** Jonathan Lodge, Telescope Live, [6].

IR spectroscopy plays a critical role in astrochemistry, where it is used to characterise interstellar and circumstellar ices, particularly in identifying abundant ice constituents such as CO, CO_2, H_2O, CH_3OH, NH_3, CH_4, and H_2S. In laboratory and astronomical spectra, it can also be used to track additional (often more complex) products and structural changes that emerge as ices are thermally processed or irradiated. It provides insights into the composition and physical state (amorphous or crystalline) of these ices, which are crucial for understanding chemical processes in space environments [7, 8]. Observations of sources like NGC 2023, shown in Figure 3.2, have revealed over 100 Near-Infrared (NIR) emission lines from rovibrational transitions of molecular hydrogen, helping to constrain local density, temperature, and radiation fields [9]. In laboratory astrochemistry, IR spectroscopy is used to monitor radiation- and temperature-induced changes in astrophysical ices, providing experimental analogues to observe interstellar features. These studies help trace the origins of molecules necessary for life [7, 9].

IR spectroscopy can also be used to monitor structural or chemical changes in ices resulting from thermal processing or other energetic inputs [7]. This is vital for

interpreting astronomical observations and understanding the chemical evolution of comets and icy bodies.

In the context of this work, IR spectroscopy was used to monitor the vibrational signatures of formamide and its radiolysis products within H_2O-rich ices deposited at 90 K. Peaks at 1388 cm^{-1} and 1328 cm^{-1} (in amorphous solid formamide and formamide-containing ices at cryogenic temperatures), for example, correspond to the CH scissoring and CN stretching - vibrational modes of the formamide molecule - respectively [10]. The evolution of these peaks under ionising irradiation enables quantitative tracking of formamide destruction, identification of new species formed by radiolysis, and quantitative estimation of G-values[2] based on peak evolution.

IR absorbance data were used not only to track the presence or loss of specific vibrational features but also to quantify the degree of molecular degradation. By integrating absorbance peaks before and after irradiation, radiation induced chemical yields (G-values) were estimated, enabling direct comparisons across different radiation sources and substrate conditions. This spectroscopic tracking also enabled comparison of degradation rates across different experimental variables - including irradiation type (ions, electrons, VUV), ion energy, substrate material, and ice composition. Changes in peak shape and intensity under each condition revealed differences in radiation chemistry and matrix effects, central to understanding formamide's survivability.

[2]G-values (radiation-chemical yields) quantify the number of molecules formed or destroyed per unit energy absorbed, commonly reported as molecules per 100 eV. Further details are provided in Section 3.3.

3.1.1.3 Formamide in the IR

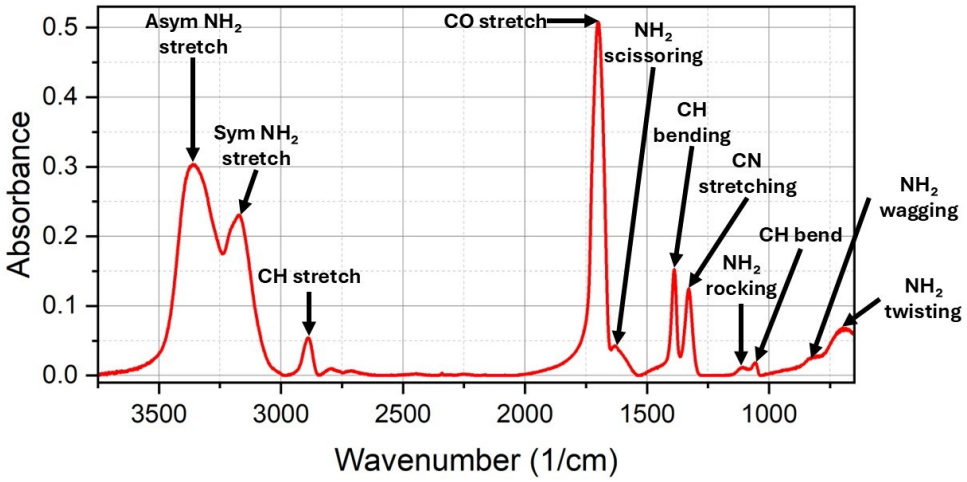


Figure 3.3: IR spectrum of pure formamide deposited at 105 K. Annotated with vibrational band assignments typically observed for formamide [11, 12]. **Credit:** Plot reproduced from the Leiden Ice Database for Astrochemistry (LIDA; Rocha et al. 2022) [13]; data from Slavicinska et al. (2023) [11]. Band assignment annotations added by the author.

Formamide exhibits a relatively simple yet highly diagnostic mid-IR spectrum in the solid state, reflecting its small size and the strongly hydrogen-bonded amide group. As illustrated in Figure 3.3, the spectrum of pure amorphous formamide ice can be divided into three main regions. At high wavenumber (4000-3000 cm^{-1}), a pair of broad features near ∼3370 and ∼3180 cm^{-1} corresponds to the NH_2 asymmetric and symmetric stretching modes of the primary amide group [12]. These bands are strongly broadened and slightly red-shifted relative to the gas phase, consistent with the formation of an extended N-H$\cdots$O hydrogen-bond network in the solid phase (Section 3.1.3). A weaker CH stretching mode appears near 2890 cm^{-1} [12, 14]. In pure formamide this falls in a relatively uncluttered part of the spectrum; however, in the mixed formamide-water ices considered throughout this thesis the same region becomes increasingly congested due to overlapping absorptions from the water-rich matrix and associated broadening, and is therefore not the primary focus of this work.

The central part of the spectrum (1800-1500 cm^{-1}) is dominated by the carbonyl stretching vibration (C=O) and the in-plane NH_2 scissoring mode. In amorphous formamide ices deposited near 20-30 K, these appear as strong, partially overlapping bands

around 1700 and 1630 cm^{-1} [11, 14]. Their exact positions and profiles are sensitive to temperature and phase: as the ice is warmed and begins to relax or crystallise, the C=O and NH_2 scissoring bands narrow, shift, and in some cases partially split, reflecting changes in hydrogen-bond geometry and the formation of more ordered molecular arrangements [11, 12]. Since these modes are both intense and strongly environment-dependent, they serve as useful probes of phase transitions in pure formamide, but they are less convenient as quantitative tracers in mixed ices where they overlap with the strong H_2O bending mode.

For the purposes of this thesis, the most important part of the formamide spectrum lies in the 1500–1200 cm^{-1} region. Here, two relatively isolated bands at ∼1388 and ∼1328 cm^{-1} correspond to the in-plane CH bending ("CH scissoring") and CN stretching modes, respectively [11, 14]. These features are intense, show only modest shifts with temperature, and suffer comparatively little overlap with the major bands of common ice components such as H_2O, CO, and CO_2. As a result, they have been identified as robust observational tracers of solid formamide in astrophysical spectra [11] and are widely adopted as diagnostic bands in laboratory radiolysis studies of formamide-containing ices [14, 15]. In this work, the evolution of the 1388 and 1328 cm^{-1} bands in Figure 3.3 are used to quantify the destruction of formamide under ion, electron, and VUV irradiation (Sections 3.3 and Chapters 5-7).

3.1.1.4 Challenges and Limitations of IR Spectroscopy

One challenge in using IR spectroscopy for cryogenic ices is the potential for overlapping absorption features, particularly in complex mixtures such as formamide-water. The strong, broad absorption bands of water can obscure or distort peaks associated with formamide or its degradation products. Additionally, the substrate (NaCl or ZnSe) can affect band positions or introduce baseline artefacts. Both NaCl and ZnSe are chosen for their broad mid-IR transparency - NaCl transmits across ∼400-40,000 cm^{-1} and ZnSe across ∼550-20,000 cm^{-1} - and neither substrate contributes intrinsic absorption bands within the mid-IR working range used in this study. The artefacts referred to here therefore arise from optical effects at the substrate-ice interface, such as Fresnel reflections and thin-film interference fringes, rather than from substrate IR absorption.

Matrix effects - such as hydrogen bonding within the ice - may cause shifts in peak positions or intensities, complicating spectral assignments. These limitations were mitigated by careful baseline correction, substrate comparison, and complementary spectral interpretation strategies.

Despite these challenges, IR spectroscopy remains an indispensable tool in this study for in-situ, real-time monitoring of radiation-induced chemical changes in complex ice systems.

3.1.2 Vacuum Ultraviolet Spectroscopy

VUV spectroscopy is a valuable analytical tool in this study, enabling the investigation of high-energy electronic transitions during the irradiation of formamide-water ices. Unlike IR spectroscopy, which examines vibrational modes, VUV spectroscopy is sensitive to photon-induced electronic excitations and photodissociation processes. This makes it particularly well-suited for monitoring the initial stages of bond-breaking and chemical transformation under photon or charged-particle irradiation. The following section outlines the principles of VUV spectroscopy, its relevance to astrochemistry, and its application in this research to assess the photochemical evolution of irradiated ice samples.

3.1.2.1 Principles

VUV spectroscopy is a powerful technique for investigating the electronic structure of atoms, molecules, and condensed phases. It operates in the spectral range of approximately 10-200 nm (6-10 eV), where photons are energetic enough to induce electronic transitions, typically from valence or bonding orbitals to antibonding or Rydberg states[3]. Since Earth's atmosphere absorbs VUV radiation as a result of the presence of molecular nitrogen and oxygen [17], VUV spectroscopy requires specialised vacuum instrumentation, hence the 'vacuum' in vacuum ultraviolet. This is commonly performed using synchrotron light sources, discharge lamps (e.g., deuterium or hydrogen), or laser-based systems.

[3]Rydberg states are high-energy states where an electron is promoted to a diffuse orbital with principal quantum number $n \gg 1$ [16]

When a molecule absorbs a VUV photon, an electron is excited from a lower-energy (ground) state to a higher-energy (excited) state [18]. The specific energy of this transition depends on the molecule's electronic structure, giving rise to a characteristic absorption spectrum. In VUV spectroscopy, electronic transitions involve the movement of electrons between specific molecular orbitals. This is usually in the form of promoting electrons from bonding (σ or π) or non-bonding (n) orbitals to higher-energy antibonding (σ^* or π^*), or diffuse Rydberg states (ns, np, nd). There are several types of orbital transitions characteristic of VUV spectroscopy, including promotions from bonding or non-bonding orbitals into antibonding or Rydberg states (e.g. $\pi \rightarrow \pi^*$, $n \rightarrow \pi^*$, $n \rightarrow 3s$). These transitions are summarised in Table 3.1. In contrast to IR spectroscopy, which probes vibrational motions, VUV spectroscopy tracks changes in a molecule's electronic structure. The spectra of formamide illustrate this distinction: the IR spectrum (Figure 3.3) exhibits sharp vibrational bands such as CH scissoring and CN stretching, whereas the VUV spectrum (Figure 3.5) is dominated by broad electronic features including the W, R_1, and V_1 bands, arising from $n \rightarrow \pi^*$, Rydberg, and $\pi \rightarrow \pi^*$ excitations. These examples highlight the fundamental difference between vibrational and electronic excitation probed by the two techniques.

Table 3.1: Common electronic transitions observed in the VUV region, including typical origin and destination orbitals [19, 20].

Transition Type	**Orbitals Involved**	**Typical Characteristics**
$\pi \rightarrow \pi^*$	Bonding $\rightarrow$ antibonding	Strong transition; lower energy than $\sigma \rightarrow \sigma^*$. Often observed in the 200–300 nm region.
n $\rightarrow \pi^*$	Nonbonding $\rightarrow$ antibonding	Moderate intensity; frequently involved in photodissociation. Lower energy than $\pi \rightarrow \pi^*$.
$\sigma \rightarrow \sigma^*$	Bonding $\rightarrow$ antibonding	Very strong but requires high photon energies; typically < 150 nm.
n $\rightarrow \sigma^*$	Nonbonding $\rightarrow$ antibonding	Generally weak and often broad.
n $\rightarrow$ Rydberg	Nonbonding $\rightarrow$ diffuse Rydberg orbital	Higher-energy transitions; usually sharp in gas-phase spectra.

VUV photons possess sufficient energy to access low-lying electronic states, especially $\pi \rightarrow \pi^*$, n$\rightarrow \pi^*$, and $\sigma \rightarrow \sigma^*$ transitions, which are not observable in the UV-Vis or IR regions. Absorption in this range can induce photodissociation, photoionisation, and fragmentation, and nearly all molecules display intense and distinctive absorption

features in the VUV, making this region particularly sensitive to molecular identity, conformation, and chemical environment [21]. As a result, VUV spectroscopy is a powerful tool for studying the early stages of radiation-driven chemistry in condensed astrochemical ices and gases, where electronic excitation directly initiates radical formation and bond cleavage [22, 23].

In astrochemical contexts, researchers have thoroughly characterised the electronic transitions of simple ice components such as CO, CO_2, H_2O, CH_3OH, and NH_3, providing robust reference points for interpreting VUV spectra. For instance, CO exhibits narrow $\pi \rightarrow \pi^*$ and Rydberg transitions below ∼150 nm, features well documented in laboratory VUV measurements and known to influence its photodissociation rate in dense clouds [24, 25]. Water ice shows strong absorption below ∼165 nm attributed to the $\tilde{B}^1A_1 \leftarrow \tilde{X}^1A_1$ transition, leading efficiently to the formation of H · and OH · radicals upon photodissociation [26]. Methanol and ammonia ices display broader n→ σ^* and n→ π^* bands that fragment extensively under VUV irradiation, producing radicals such as CH_3 · and NH_2 · that drive subsequent organic reaction networks [27–29]. These benchmark systems demonstrate how specific VUV absorption features map onto bond-cleavage pathways and radical formation, establishing a spectroscopic foundation for interpreting more complex molecules. This framework is essential for understanding the behaviour of formamide under exposure to high-energy photons. In this thesis, these principles underpin the analysis of VUV-induced electronic transitions in formamide-water ices, linking their spectral evolution to the earliest stages of photodissociation and ice chemistry.

3.1.2.2 Applications to Astrochemistry

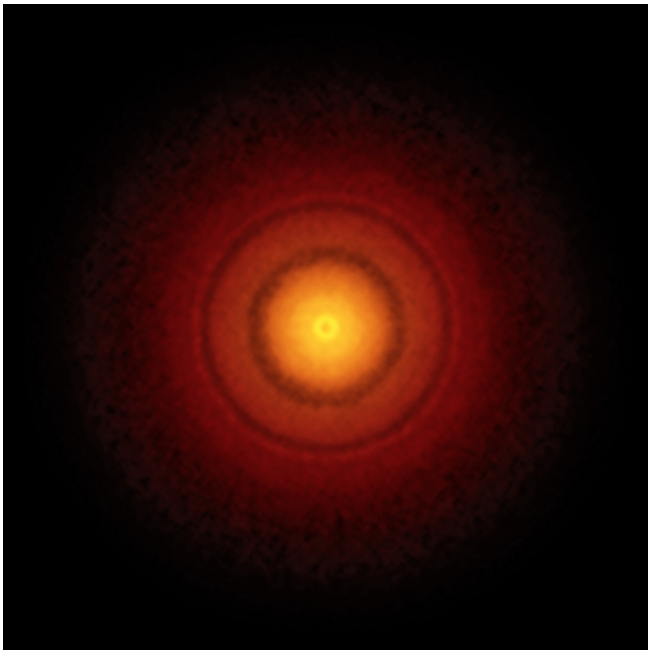


Figure 3.4: An ALMA image of the protoplanetary disc surrounding the nearby young star TW Hydrae, revealing the classic rings and gaps that signify planets are in formation in this system. **Credit:** S. Andrews (Harvard-Smithsonian CfA); B. Saxton (NRAO/AUI/NSF); ALMA (ESO/NAOJ/NRAO), CC BY 4.0.

VUV absorption spectroscopy is widely used in astrochemistry to probe the stability and photoreactivity of interstellar ices, prebiotic molecules, and planetary surface analogues under space-like irradiation conditions [30]. As discussed in Section 3.1.2.1, VUV spectra constrain where a molecule absorbs and which photon energies are capable of driving photodissociation and photofragmentation, thereby informing the energetics and pathways of photo-driven chemistry. This is essential for building and validating reaction networks in environments where VUV photons are abundant (star-forming regions, the interstellar medium, and planetary magnetospheres) and where photo-induced processes shape both composition and dynamics [31, 32].

VUV measurements are obtained both observationally (e.g., via UV emission/absorption features measured by space telescopes) and through laboratory irradiation experiments. Figure 3.4 shows TW Hydrae, a young star surrounded by a protoplanetary disc. In this system, the detection of gas-phase CH_3CN has been interpreted as being linked to VUV-driven processing of CH_3CN-bearing ices (via photodesorption and/or photodissociation-driven chemistry), motivating laboratory studies in which

$CO:CH_3CN$ and $H_2O:CH_3CN$ ices are irradiated with VUV photons to quantify the production of gas-phase CH_3CN.

VUV photons are also critical drivers of chemical reactions in icy mantles found on interstellar grains and icy bodies. Their high energy enables them to break molecular bonds, leading to photodissociation, bond cleavage, and the formation of reactive radicals - key steps in the creation of complex organic molecules in space. VUV photons can promote chemical reactions and photodissociation, and play a critical role in the synthesis and destruction of prebiotically relevant chemicals, such as formamide. Laboratory experiments frequently use VUV spectroscopy to simulate these processes, measuring absorption cross-sections and photolytic behaviour of simple and complex ices under astrophysical conditions. Such work has shown, for example, that molecules like CO, CH_4, H_2O, and formamide undergo fragmentation or rearrangement under VUV exposure, leading to the formation of new photoproducts including radicals, ions, and prebiotic intermediates [33]. These results help contextualise data from telescopic observations and spacecraft flybys, where VUV emissions and absorptions are observed but often challenging to interpret without laboratory reference spectra.

Synchrotron-based VUV spectroscopy provides high-resolution absorption spectra that are valuable both for mechanistic studies and for building spectral libraries of astrochemically relevant ices. Such libraries support the interpretation of observational datasets and improve models of chemical evolution in extreme environments, complementing existing resources such as the ACID ice-spectra database [34] and the MPI-Mainz UV/VIS spectral atlas of gaseous molecules [35]. When used alongside IR spectroscopy, VUV measurements add an electronic "fingerprint" that can be sensitive to primary photo-processing pathways that are not always apparent from vibrational bands alone.

In this thesis, VUV spectroscopy was used in-situ to monitor electronic transitions in formamide-water ices deposited at 90 K during photon irradiation. Absorption features in the 120-200 nm range were tracked to quantify the evolution of formamide and its VUV-active photoproducts. Formamide absorbs strongly in this region via n$\rightarrow \pi^*$ and $\pi \rightarrow \pi^*$ transitions associated with its carbonyl and amide functional

groups; irradiation-driven changes in band position, width, and intensity were used to quantify relative formamide loss and to infer the emergence of new electronic species. Where possible, changes in optical depth were used to estimate destruction efficiencies.

3.1.2.3 Formamide in the VUV

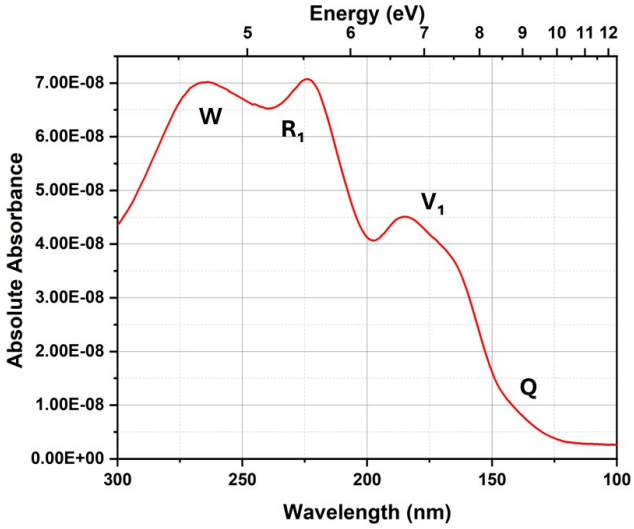


Figure 3.5: VUV spectrum of pure formamide deposited at 10 K on a LiF window. Annotated with transitional modes typically observed for formamide [36, 37].

Figure 3.5 shows the VUV absorption spectrum of pure formamide ice at 10 K on a LiF window. The broad feature from ∼280-240 nm is assigned to the W band, arising from the $n \rightarrow \pi^*$ excitation of the carbonyl group (C=O); in the gas phase, this transition appears near 219nm, but in condensed phases it is broadened and red-shifted due to hydrogen bonding and dielectric effects [36, 38]. The peak at ∼235 nm corresponds to the R_1 band, the first Rydberg excitation ($n \rightarrow 3s$), which is well known in both gas-phase and matrix-isolation studies. At shorter wavelengths, a broad absorption between ∼200-170 nm is assigned to the V_1 band, the primary $\pi \rightarrow \pi^*$ transition of the amide chromophore; in amorphous ices at 10 K, this band is substantially broadened and partially overlapped with higher-lying states [37]. Below ∼160 nm, the absorbance rises steeply into the Q band, a mixed valence-Rydberg manifold that extends into the deep-VUV; the substantial increase below ∼150 nm marks the onset of the near-ionisation continuum and higher Rydberg states [39]. Overall, the positions and relative intensities of the W, R_1, V_1, and Q bands are consistent with previous

VUV measurements of formamide and reflect the expected low-temperature solid-state shifts.

3.1.2.4 Challenges and Limitations of VUV Spectroscopy

One of the challenges of using VUV spectroscopy is that ultra-high vacuum conditions are required, as atmospheric gases strongly absorb VUV photons. This limits the experimental constraints under which VUV spectroscopy and irradiation can be performed. Furthermore, absorption features in the VUV region are often broad and overlapping, particularly in condensed-phase samples, which can complicate spectral interpretation even in binary mixed ices such as H_2O-formamide, where matrix effects and overlapping electronic bands can obscure weaker features.

Another limitation of VUV spectroscopy is the challenge of clearly associating spectral features with specific photoproducts. Many small molecules and fragments exhibit overlapping absorption bands in the VUV region. Additionally, the absence of comprehensive spectral libraries for condensed-phase organics at cryogenic temperatures can complicate confident identification. Furthermore, subtle variations in optical depth or band shape can be difficult to distinguish from noise or instrumental fluctuations, especially when product concentrations are low.

Despite these challenges, VUV spectroscopy is a powerful and sensitive tool for detecting primary photochemical changes, particularly when combined with IR spectroscopy. In this study, we employed careful calibration, background subtraction, and complementary IR data to enhance spectral assignments and interpret electronic transitions with greater confidence.

3.1.3 Formamide Ice Structure and Phase Behaviour

Having outlined the spectroscopic tools used to probe the ice samples, it is helpful to summarise the key physical and structural properties of formamide in the solid state, and how these compare to (and interfere with) the more familiar behaviour of water ice. This section focuses on the molecular-scale hydrogen bonding in condensed formamide, the thermal evolution of its amorphous and crystalline phases, and the consequences

of mixing formamide with H_2O. These factors underpin the interpretation of the IR and VUV spectra presented in later chapters, and are essential for understanding how formamide behaves in Europa-like ices.

Molecular structure and hydrogen bonding in condensed formamide

Formamide (NH_2CHO) is a small, planar, strongly polar molecule in which the carbonyl and amide groups are conjugated. The amide resonance delocalises electron density over the C=O and C-N bonds, making the N-H protons relatively acidic and giving both the carbonyl oxygen and the amide nitrogen significant lone-pair character. In practice, an individual formamide molecule can act as a hydrogen-bond donor via one or two N-H donor sites (i.e., its two N-H bonds) and as a hydrogen-bond acceptor via the carbonyl oxygen (and, more weakly, the nitrogen lone pair). This combination of a significant dipole moment and multiple donor/acceptor sites allows up to four hydrogen bonds per molecule in favourable environments. As a result, formamide readily forms hydrogen bonds in the condensed phase [40, 41].

Gas-phase and cluster studies show that formamide does not merely form isolated pairs of molecules but readily forms small hydrogen-bonded structures, such as dimers, short chains, and rings. High-level calculations indicate that the most stable dimers adopt N-H$\cdots$O=C geometries, often in symmetric arrangements with two nearly linear hydrogen bonds between the carbonyl oxygen of one molecule and the amide hydrogens of its neighbour [42]. These local motifs extend into chains and sheets in larger aggregates, with formamide molecules linking head-to-tail via N-H$\cdots$O interactions and occasional side-on bonds to the nitrogen lone pair [40, 41]. Accordingly, even in the absence of water, condensed formamide forms a continuous three-dimensional N-H$\cdots$O hydrogen-bonded network, in which essentially every molecule is connected to its neighbours via hydrogen bonds. This "self-solvating" network is the structural backbone of both amorphous and crystalline formamide ices and is central to how they respond to thermal and radiolytic processing.

Amorphous and crystalline formamide ices

A crystalline solid has long-range periodic order: the molecules adopt a repeating arrangement that extends throughout the material. An amorphous solid lacks this long-range periodicity and is better thought of as a "frozen liquid", with local structure but no repeating pattern. A glassy solid is an amorphous solid obtained by cooling a liquid (or a deposit) fast enough that it does not have time to crystallise; in other words, the disordered liquid structure is kinetically trapped. Materials that readily form such amorphous solids on cooling are often referred to as glass-formers.

Under typical laboratory astrochemistry conditions, vapour-deposited formamide at low temperature (15–30 K) forms an amorphous solid, closely analogous to amorphous solid water. Infrared spectra of such deposits are dominated by broad bands, especially in the NH_2 stretching and bending modes and the C=O stretch, reflecting a disordered distribution of hydrogen-bond strengths and local environments within the extended network [10–12]. This amorphous form is the natural starting point for irradiation experiments in this thesis, and for most ice-analogue work.

On slow warm-up, the amorphous formamide ice undergoes structural relaxation and crystallisation over a relatively narrow temperature interval. Sivaraman et al. report clear IR spectral changes between ∼155 and 165 K, with NH_2 bands narrowing and shifting and new, sharper features appearing, which they attribute to a transition from a disordered glassy solid to a more ordered crystalline phase [12]. Brucato et al. observed similar behaviour in pure formamide ices deposited at 20 K, and showed that ion irradiation modifies but does not suppress this thermal evolution [10]. More recent work by Slavičinská et al. measured both amorphous and crystalline band profiles from 15-212 K, confirming that formamide behaves as a typical hydrogen-bonded glass-former: low-temperature amorphous deposits gradually relax and then crystallise upon annealing, with distinct crystalline features emerging above ∼150 K [11].

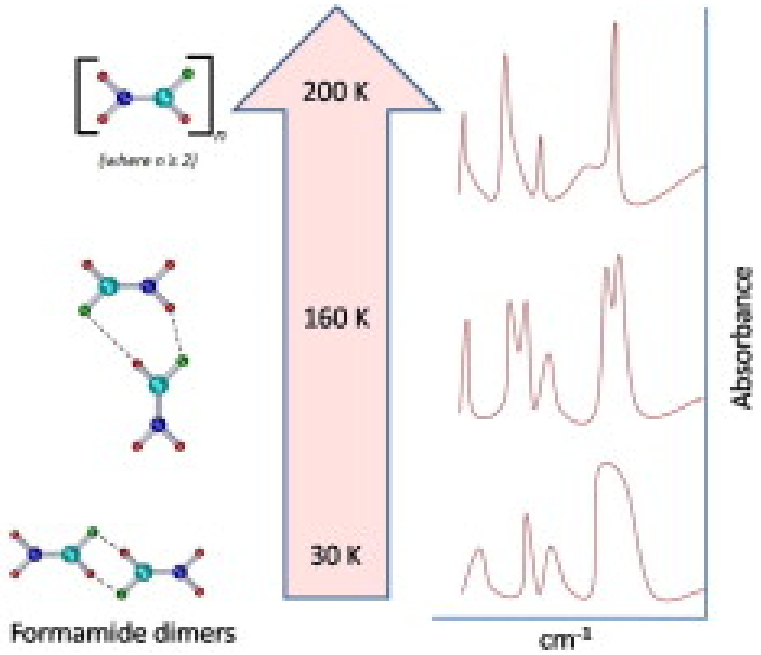


Figure 3.6: Mid-IR spectra of solid formamide at 30, 160, and 200 K, showing the evolution from broad bands in the low-temperature amorphous solid to sharper features in the crystalline/aggregated phase. Schematics on the left indicate representative hydrogen-bonded dimers and their association into larger motifs. **Credit:** Reprinted from Spectrochimica Acta Part A: Molecular and Biomolecular Spectroscopy, Vol. 105, B. Sivaraman, B. N. Raja Sekhar, B. G. Nair, V. Hatode, N. J. Mason, Infrared spectrum of formamide in the solid phase, Pages 238–244, Copyright (2013), with permission from Elsevier, [12].

Figure 3.6 provides an example of this temperature-dependent spectral evolution for pure formamide ice. Desorption of bulk formamide ice occurs only at comparatively high temperatures in high vacuum, typically in the 190-220 K region depending on thickness and heating rate [11]. Thus, over the temperature range relevant to Europa's surface ($\lesssim$130 K), pure formamide ices are expected to remain in an amorphous or partially relaxed state rather than fully crystallising or sublimating. In the laboratory experiments discussed in this thesis, ices for ion and electron irradiation were deposited and held at 90 K, so the thermal evolution probed by those experiments is confined to the low-temperature amorphous regime and the early stages of structural relaxation, rather than the complete crystalline transition or desorption. In contrast, the VUV measurements on mixed ices span 10-130 K, and therefore sample how the electronic spectrum responds as the ice evolves from a freshly deposited amorphous solid towards a more relaxed, structurally reorganised state with increasing temperature.

Comparison with water ice

Water ice exhibits its own rich phase behaviour, which provides a valuable reference point for understanding formamide. Vapour-deposited H_2O at low temperatures forms amorphous solid water (ASW), with multiple amorphous modifications and well-defined transitions on warm-up. Pioneering work by Jenniskens and Blake shows that ASW undergoes a sequence of structural changes: an amorphous-amorphous transition from a high-density to a low-density form at ∼40-70 K, followed by a further structural relaxation near 130 K, and finally crystallisation to cubic ice in the 145-160 K range, before relaxing towards hexagonal ice at higher temperatures [43]. These transformations are closely tied to changes in radical mobility, gas retention, and desorption behaviour in astrophysical ices, [43, 44].

Compared to water, formamide's hydrogen-bond network is built from directional N-H$\cdots$O bonds between whole formamide molecules, rather than from a tetrahedral O-H$\cdots$O framework in which oxygen atoms form a continuous lattice. As a result, its amorphous-to-crystalline transition occurs at somewhat higher temperatures than the crystallisation of ASW. The resulting crystalline structures are molecular crystals in which intact formamide molecules pack into a repeating pattern, rather than an extended oxygen lattice like that in ice I_h[4] [45]. Nevertheless, both systems share key features: they form strongly hydrogen-bonded amorphous solids at low temperature; they undergo progressive structural relaxation on warm-up; and they exhibit relatively sharp spectral signatures associated with crystallisation. For the purposes of this thesis, the main practical difference is that formamide remains bound to the solid phase at temperatures where water ice has already begun to restructure and, in some environments, desorb, meaning that mixed H_2O-formamide ices can become enriched in formamide as water is removed.

Binary formamide and water ice mixtures

When formamide is mixed with water, the phase behaviour becomes more complex

[4]Ice I_h is the common hexagonal crystalline phase of water at ambient pressure.

but also more relevant to astrochemical and planetary contexts. Molecular dynamics simulations of liquid H_2O/formamide mixtures show that water does not simply act as an inert diluent. Instead, both components participate in a single, continuous hydrogen-bond network in which water molecules readily substitute into the formamide network and vice versa [41]. Since the H_2O-formamide hydrogen bonds are at least as strong and numerous as the H_2O-H_2O and formamide-formamide bonds, the mixture does not behave as an "ideal" solution - that is, one in which unlike-molecule interactions are equivalent to like-molecule interactions, producing strictly linear composition dependences of properties such as freezing point and vapour pressure - with simple, linear composition dependences. Instead, the strong mutual solvation of the two components leads to significant changes in their freezing behaviour and in the way the disordered (glassy) state is stabilised on cooling.

Bulk phase diagrams of formamide-water solutions reveal a pronounced eutectic point, i.e. a specific composition at which the mixture has its lowest freezing/melting temperature and solidifies into two coexisting solid phases, with the eutectic composition near ∼46 wt% formamide and ∼54 wt% water [46, 47]. Compared with pure water, the presence of formamide significantly depresses the freezing point and broadens the temperature range over which the mixture remains either a liquid or an amorphous glass (a frozen-in, disordered structure that no longer flows).

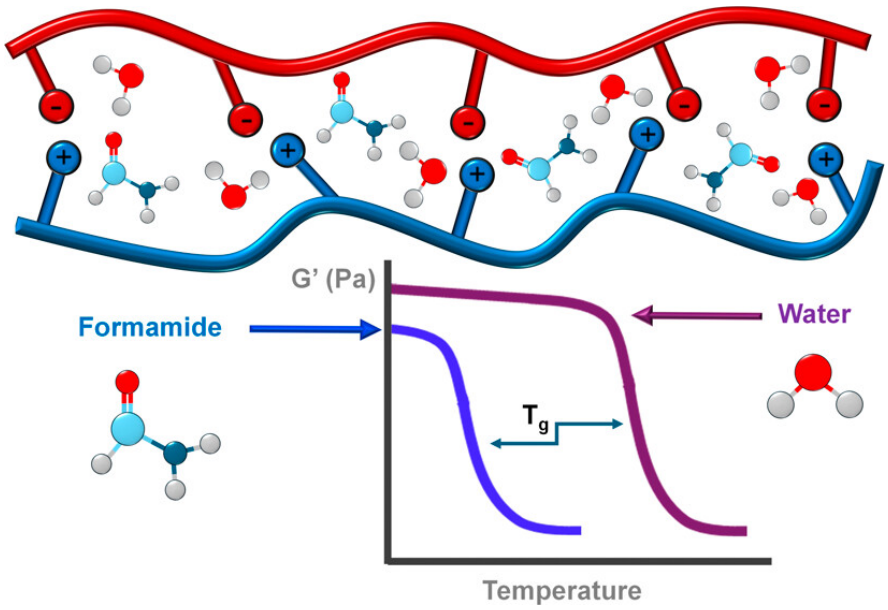


Figure 3.7: Illustration of how formamide (blue) plasticises a hydrogen-bonded polymer network more strongly than water (purple). The storage modulus G' drops at lower temperatures in the presence of formamide, reflecting a lower glass-transition temperature T_g and stabilisation of liquid/glassy states. **Credit:** Used with permission of the American Chemical Society, from Formamide as a Robust Alternative to Water for Plasticizing Polyelectrolyte Complexes, S. Hassoun, Z. A. Digby, N. Abou Hamad and J. B. Schlenoff, *Macromolecules*, vol. 57, 2024; permission conveyed through Copyright Clearance Center, Inc., [48].

An example of how formamide lowers the glass transition relative to water in a hydrogen-bonded system is shown schematically in Figure 3.7. More recent work on related deep eutectic and so-called "chaotropic" mixtures (a solute that disrupts the ordered hydrogen-bond network of water) has highlighted that formamide is particularly effective at disrupting the H_2O hydrogen-bond network and stabilising supercooled or glassy states at low temperatures [49]. In other words, adding formamide to water does not just shift a single melting point; it qualitatively changes how the hydrogen-bond network freezes and relaxes.

Laboratory ice studies support this picture under astrochemically relevant conditions. Slavičinská et al. studied MIR spectra of pure formamide and mixed ices with H_2O and other common ice components (CO, CO_2, NH_3, CH_3OH) between 15 and 212 K [11]. Mixed formamide-water ices deposited at 15 K are amorphous, with band positions and profiles that already indicate strong hydrogen-bond coupling between the two species. On warm-up, the sharp amorphous-to-crystalline transition seen in pure formamide is suppressed and broadened: the onset of crystallisation is shifted,

and the IR features of both H_2O and formamide are modified relative to their pure-ice counterparts. This behaviour is consistent with an intimately mixed hydrogen-bond network in which water and formamide co-structure the ice, rather than segregated domains of pure H_2O and pure formamide. In this broader context, mixtures with weakly hydrogen-bonding species such as CO and CO_2 tend to show more "separable" behaviour (i.e., less mutual perturbation of the hydrogen-bond network), whereas strongly hydrogen-bonding partners such as NH_3 and CH_3OH are more likely to substantially reshape band profiles and temperature evolution through matrix interactions.

In the experiments in this thesis, 90 K H_2O-formamide ices should therefore be viewed as structurally disordered, hydrogen-bonded mixtures that occupy a glassy or partially relaxed regime of the phase diagram. The mixture will not behave like a simple sum of "water ice + frozen solute"; instead, the presence of formamide modifies the water network, alters the temperatures of structural transitions, and changes how radicals and photoproducts are trapped or mobilised. The VUV experiments, which follow mixed ices from 10 to 130 K, additionally probe how this mixed hydrogen-bond network reorganises with temperature, providing a complementary view of phase evolution to that obtained from the fixed-temperature IR measurements at 90 K.

3.2 Fundamentals of Radiation Chemistry

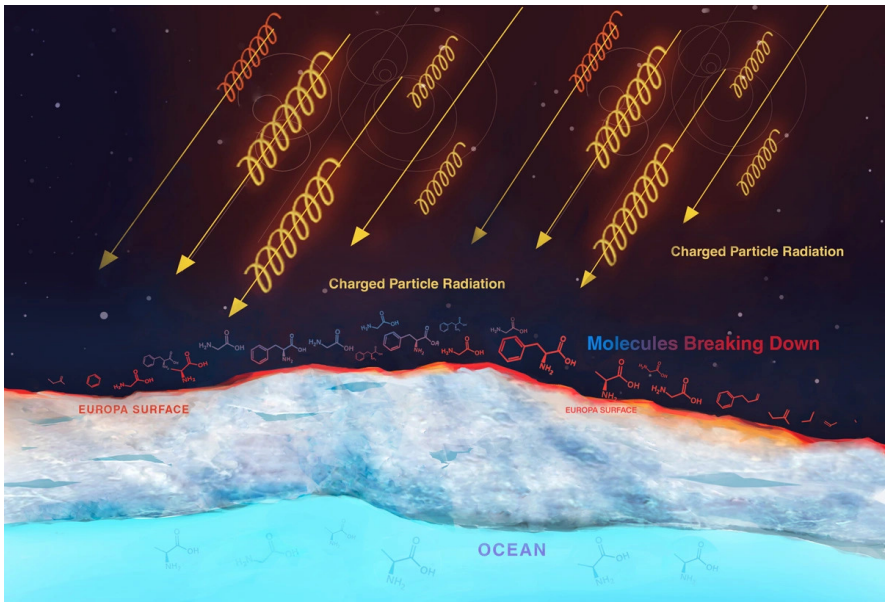


Figure 3.8: An artist's rendition of the surface of Europa being bombarded by radiation from Jupiter's magnetosphere. **Credit:** NASA/JPL-Caltech.

Radiation chemistry is the study of the effects of the interaction of ionising[5] high-energy particles, such as cosmic rays or high-energy photons, on matter [51]. This also includes investigating the subsequent chemical transformations. Radiation chemistry is particularly pertinent in astrochemistry, as it aids in the understanding of how complex and prebiotic molecules form and evolve in space environments. It drives the formation and destruction of key chemical species, as radiation is present throughout space in various forms [52].

In cryogenic ices, such as those formed from water and simple organic compounds (e.g., formamide), radiation effects are significant. When energy is deposited into these ices, primary interactions produce ions, radicals, and excited species [10, 53]. Secondary processes, including radical diffusion and recombination, then give rise to complex reaction networks [53, 54]. These processes are fundamental to the chemical evolution observed in astrophysical environments and may contribute to the synthesis of biologically relevant molecules [52]. Figure 3.8 illustrates the effect of charged particle radiation on Europa's surface, where high-energy ions from Jupiter's magnetosphere

[5]Ionising radiation refers to photons or particles energetic enough to remove electrons from atoms or molecules, creating ions [50].

interact with surface ices, triggering molecular breakdown and radiolytic processing. A primary aim of the work reported in this thesis was to simulate these processes under controlled laboratory conditions using selected radiation sources.

This section outlines the fundamental physical and chemical processes governing the interactions between radiation and matter, with a particular focus on mechanisms relevant to condensed-phase ices at low temperatures. It aims to provide a theoretical foundation for understanding how different types of radiation (ions, electrons, and photons) interact with ice matrices, the species they generate, and the implications for molecular survivability and transformation. These principles are essential for interpreting the experimental results presented later in this thesis.

3.2.1 Energy Sources and Radiation Fields in the ISM and Jovian System

Ionising radiation in space exists in a range of forms, including charged particles, electrons, and high-energy photons. These radiation types deposit energy into matter through different mechanisms, leading to a variety of physical and chemical effects such as ionisation, excitation, bond cleavage, and radical formation. In the context of this study, understanding how different radiation sources interact with cryogenic formamide-water ices is essential to interpret the resulting molecular degradation and chemical evolution. The following sections provide an overview of the radiation types used in the experiments - namely, heavy ions (H^+, O^{2+}, S^{5+}), low-energy electrons, and vacuum ultraviolet (VUV) photons - and their relevance to astrochemical environments such as icy moons, interstellar ices, and cometary surfaces.

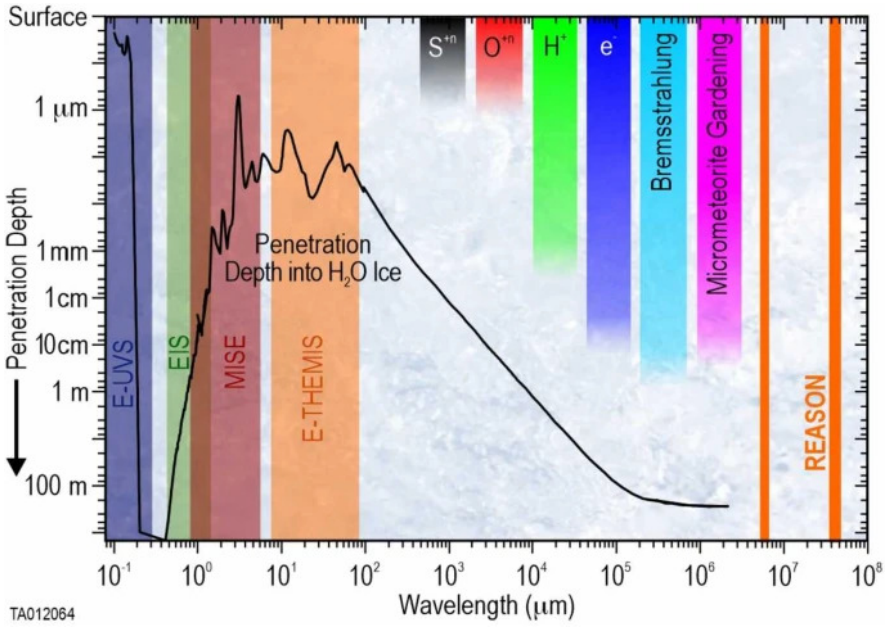


Figure 3.9: Estimated penetration depths of various forms of ionising radiation into bulk H_2O ice, shown as a function of wavelength and energy. Coloured bars represent the dominant stopping ranges for S^+, O^+, H^+ ions, electrons, Bremsstrahlung X-rays, and micrometeoroid impacts in the icy surface of Europa. These depths are relevant to both surface processing and the chemistry probed by laboratory analogues. **Credit:** Reproduced from Becker et al. (2024), Fig. 18 [55], CC BY 4.0. Underlying data from Warren and Brandt [56], the NIST PSTAR/ESTAR databases, and Costello et al. [57].

3.2.1.1 Heavy Ion Irradiation: H^+, O^{2+}, S^{5+}

Jupiter harbours the Solar System's largest magnetosphere, and within that, some of the strongest and most dangerous radiation belts, as discussed in 2.3. These radiation belts are home to various forms of ionising radiation, from ultra-relativistic protons and electrons, to positively charged heavier ions such as O^{n+} and S^{n+}. These charged particles primarily originate from Jupiter's moon, Io, a moon known for its volcanic activity. Io's volcanic activity and interaction with Jupiter's magnetic field drive the creation, acceleration, and loss of charged particles throughout the system [58]. Therefore, simulating Europa's surface chemistry requires replicating its dominant ionising agents experimentally. H^+, O^{2+}, and S^{5+} were selected based on their relative abundance, origin, and energy profiles in the Jovian magnetosphere.

As shown in Figure 3.9, different types of ionising radiation penetrate H_2O ice to varying depths, with heavy ions such as S^+ depositing their energy within the top few micrometres, while electrons and Bremsstrahlung X-rays extend deeper into the subsurface. This difference in penetration directly influences the spatial distribution

of radiation-driven chemistry and helps contextualise the fluences and stopping ranges used in the experiments discussed. In charged-particle irradiation, the deposited energy is not uniform with depth: as an ion slows down, its stopping power $-\mathrm{d}E/\mathrm{d}x$ generally increases, producing a pronounced maximum in the depth–dose profile near the end of its range (the Bragg peak) [59, 60]. For thin films, whether this peak lies within the ice layer determines whether most of the projectile energy is deposited in the sample or transmitted into the substrate. Table 3.2 illustrates the typical energies used in this study, along with their typical linear energy transfer[6] (LET) values in water ice. High LET ions deposit large amounts of energy into small volumes of matter, leading to dense ionisation tracks that can break chemical bonds and initiate complex radiation chemistry. Since formamide is a low-abundance organic species, when embedded in water ice energy deposition profiles influence not just its destruction rate but also the pathways and likelihood of producing specific byproducts.

H^+ ions penetrate significantly deeper into H_2O ice compared to heavier ions such as sulfur and oxygen, demonstrated in Figure 3.9. While heavy ions dominate the plasma environment of Jupiter's magnetosphere, protons originating from Jupiter's ionosphere - and to a lesser extent from the solar wind and the Galilean moons - play a crucial role in auroral processes, plasma transport, and the broader magnetospheric dynamics [62, 63]. On Europa, protons are a major contributor to the radiation environment, dominating the radiation dose delivered below the ice's surface layers [64].

Protons are the lightest and most mobile of the ion species in Jupiter's magnetosphere [63]. Penetrating relatively deeply into the ice, protons allow radiolytic processing not only at the surface but also within subsurface layers, down to several millimetres, depending on their energy.

Jupiter's moon Io is the primary source of heavy ions in the planet's magnetosphere, particularly oxygen ions. Volcanically emitted SO_2 from Io is released into space, where it dissociates and ionises, generating significant amounts of oxygen that become concentrated along Io's orbit [65, 66]. These oxygen ions make up a substantial portion of the plasma mass density, often exceeding the contributions from both protons and

[6]Linear energy transfer (LET) is a key concept in radiation chemistry that describes the amount of energy deposited by an ionising particle - per unit distance - as it travels through matter [61].

sulphur ions [67, 68].

Oxygen ions play a key role in altering Europa's surface chemistry, given their abundance and the energetic environment of Jupiter's magnetosphere. Their interaction with the surface drives both physical erosion and chemical transformation processes, providing important implications for planetary geology and astrobiology [69–71]. Being heavier than protons, oxygen ions have a shorter penetration depth but a higher LET, resulting in more concentrated energy deposition in the near-surface layers of H_2O ice. As such, they represent an intermediate-mass species capable of driving effective radiolytic decomposition and sputtering, particularly within the uppermost microns to millimetres of Europa's ice shell.

S^{5+} is one of the heaviest ion species present in the Jovian magnetosphere, and deposits energy over extremely short distances, creating dense tracks of ionisation [72]. Sulphur ions present in Jupiter's magnetosphere are a product of the SO_2 expulsion from Io's volcanic activity. The sulphur compounds are ionised by solar radiation and other energetic particles, producing sulphur ions that become trapped in Jupiter's magnetic field [65, 73]. The resulting "Io plasma torus" is a dense ring of ionised sulfur and oxygen that encircles the inner magnetosphere of Jupiter, dominating the plasma composition [74]. As shown in Figure 3.10, the Io plasma torus lies within Jupiter's magnetosphere, [75], and is central to Europa's radiation environment. These ions drive the formation of sulfuric acid, alter surface reflectance, and contribute to Europa's unique chemical environment, with implications for both surface processes and potential habitability [76]. These characteristics make it highly relevant for simulating near-surface degradation pathways and potential residue formation.

Table 3.2: Ion properties and energy deposition characteristics for H^+, O^{2+}, and S^{5+} irradiating a 50:50 H_2O/formamide ice mixture at 90 K. Deposited energy and linear energy transfer (LET) values are based on SRIM simulations, assuming ice thicknesses between 237-278 nm [77]. For protons, only partial energy deposition occurs, while oxygen and sulfur ions deposit their full energy within the ice.

Ion Type	**Ion Mass (amu)**	**Charge**	**Deposited Energy (keV)**	**LET (keV/μm)**	**Comments**
H^+	1.007276	+1	12.598-13.454	48.4-53.2	Partial deposition
O^{2+}	15.9979	+2	30	291.3	Full deposition
S^{5+}	32.0598	+5	60	582.5	Full deposition

3.2.1.2 Low-Energy Electrons

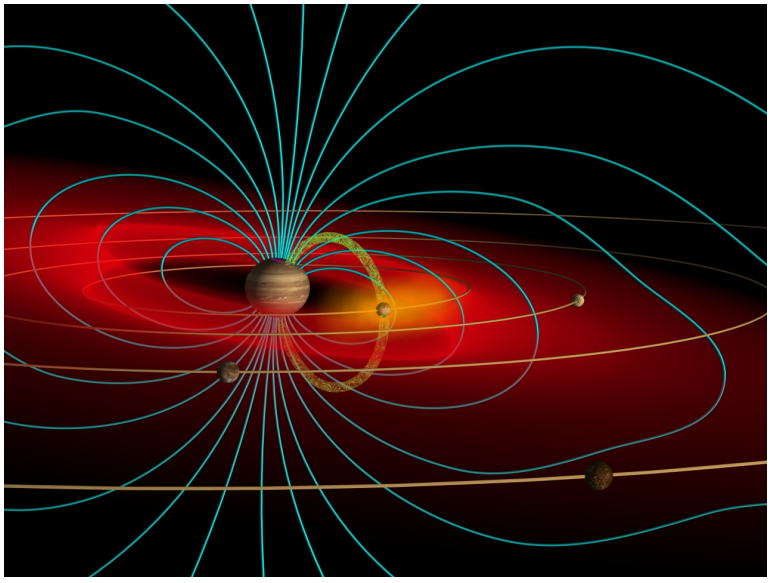


Figure 3.10: Schematic of Jupiter's magnetosphere illustrating key structural features: Io's plasma torus in red, the orbits of the Galilean moons (Io, Europa, Ganymede, Callisto) in orange, and magnetic field lines in blue. This diagram visually represents the sources and trapping regions of charged radiation, ions and electrons that irradiate Europa's surface. Adapted from [75].

Electrons are ubiquitous and highly mobile components of Jupiter's magnetosphere, and form a major part of its radiation environment [78, 79]. They originate from both internal and external sources: internally, electrons are generated through the ionisation of material ejected by Io's volcanoes (and, to a lesser extent, other Galilean moons) [80]; externally, they can be injected from the solar wind [81]. In addition, Jupiter's ionosphere plays a key role in maintaining the magnetospheric electron population [82]. Here, atmospheric gases are ionised by solar extreme ultraviolet (EUV)

radiation and by impact with existing magnetospheric electrons [83], producing free electrons that become part of the ionospheric plasma and can diffuse upward into the magnetosphere, augmenting the broader population of trapped energetic electrons [84]. Although electrons are lighter than ions, they can be highly energetic and penetrate deeper into Europa's surface, driving significant radiolytic processing.

Electrons primarily interact with matter through three main processes: ionisation, excitation, and secondary electron cascades. Ionisation produces free electrons that may, in turn, ionise other atoms or molecules, initiating a secondary electron cascade. These cascades involve successive generations of electrons being ejected, each with enough energy to continue ionising surrounding material [85]. This chain reaction rapidly multiplies the number of low-energy electrons, distributing the initial energy input across a larger volume of material and leading to widespread chemical and physical changes [86, 87]. Excitation creates excited species that may subsequently relax by emitting photons or undergoing non-radiative decay via collisional processes.

Magnetospheric electrons typically have energies ranging from a few keV to several MeV, which enables them to penetrate deeper into icy surfaces compared to heavy ions, as shown in Figure 3.9, making them highly effective at driving chemical changes in the subsurface. Despite their deeper penetration, electrons have a significantly lower LET than heavy ions, leading to more diffuse energy deposition. This makes them efficient at bulk processing but less likely to form dense ionisation tracks. In the case of Europa, these electrons are crucial for modifying the near-subsurface chemistry of irradiated ice mixtures. Therefore, they play a central role in simulating realistic surface processing conditions.

3.2.1.3 VUV Photons and Electronic Excitation

It is important to note that VUV photons play a dual role in this study: they are used both as a spectroscopic probe (see Section 3.1.2.1) and as an energetic radiation source capable of driving photodissociation and radiolysis (Section 3.2.1.3). In the context of radiation chemistry, VUV photons function analogously to charged particles, depositing energy into ice via discrete photoabsorption events that break chemical bonds and generate radicals.

In this thesis, "VUV" refers to photons with wavelengths between ∼120 and 200 nm (6-10 eV), i.e. the part of the ultraviolet spectrum energetic enough to drive electronic excitations and bond cleavage in common ice constituents, but below the soft X-ray regime [28, 30]. As discussed in Section 3.1.2.1, absorption of such photons promotes electrons from valence or non-bonding orbitals into antibonding or Rydberg states, opening efficient channels for photodissociation and photoionisation.

In Europa-like environments, VUV photons arise primarily from solar UV radiation shortward of ∼200 nm and from magnetospheric and auroral emissions in the Jovian system. Although the intense charged-particle flux in Jupiter's radiation belts dominates the deeper energy deposition in Europa's ice shell, VUV photons are particularly important for processing the uppermost monolayers of the surface, where they can drive photodesorption and alter the chemistry of exposed or freshly sputtered ices. Similar VUV-driven chemistry is invoked in dense interstellar clouds, protoplanetary discs, and other icy bodies, where secondary UV photons produced by cosmic-ray interactions penetrate regions that would otherwise be shielded from direct stellar radiation [28, 88].

Table 3.3: Energy deposition characteristics of electrons and VUV photons used to irradiate cryogenic formamide-water ices. Penetration depth and LET for electrons are approximate, based on ESTAR simulations in H_2O. Values reflect expected behaviour in H_2O-rich ices at 90 K and may vary slightly with composition.

Ion Type	**Charge**	**Energy Range (keV)**	**Approx. Penetration Depth (nm)**	**LET (keV/μm)**	**Comments**
Electrons	−1	1-10	∼100-300	∼7[6]	Based on NIST ESTAR data for H_2O [89]
VUV Photons	N/A	0.006-0.021	∼50-200	N/A[7]	Surface-localised electronic excitation

Since VUV photons carry no charge, they do not exhibit a well-defined linear energy transfer (LET) in the same way as ions or electrons. Instead, they interact with matter through discrete photoabsorption events governed by the photon energy and

[6]LET is highly energy-dependent, and this value is an approximate mean for two keV electrons in formamide-water ice.

[7]Unlike charged particles, VUV photons do not have a defined LET, as they deposit energy via discrete photoabsorption events rather than continuous ionisation along a track.

the molecular absorption cross section. For typical ice components such as H_2O, CO, CO_2, CH_3OH, and NH_3, VUV absorption cross sections in the 120-160 nm range imply attenuation lengths of only a few tens to a few hundred nanometres [26, 28, 88]. As a result, VUV irradiation is effectively a surface-localised process for the film thicknesses used in this work (of order 0.1-0.3 μm). Most of the incident photons are absorbed within the upper layers of the ice, and essentially all of their energy is available for electronic excitation in that region. This behaviour is reflected in Table 3.3, where VUV photons have no associated LET but a characteristic penetration depth of ∼50-200 nm, depending on wavelength and composition.

Once a VUV photon is absorbed, several competing channels are possible. The excited molecule may relax radiatively by emitting a photon (fluorescence, or phosphorescence), or it may relax non-radiatively via internal conversion and subsequent vibrational relaxation; in the latter case, the electronic excitation energy is transferred into molecular vibrations and dissipated as local heating of the lattice. More importantly for chemistry, the excited state can undergo bond cleavage to produce radicals and fragments, or autoionise to yield cations and low-energy photoelectrons [30, 90]. These primary photoproducts then drive secondary chemistry through radical-radical and radical-molecule reactions, in a manner analogous to the electron- and ion-induced cascades described in Sections 3.2.1.1 and 3.2.1.2, but initiated by a single absorbed photon rather than by a charged particle track. In mixed ices, the fate of the excitation energy is shared between components: absorption by one species can lead to dissociation or desorption of another. This mechanism has been demonstrated in VUV studies of simple astrophysical ices [28, 88].

For water-rich ices, VUV absorption is dominated by the $\tilde{B}^1A_1 \leftarrow \tilde{X}^1A_1$ transition of H_2O below ∼165 nm, leading efficiently to the production of H and OH radicals upon photodissociation [26]. These radicals can recombine or react with embedded species such as CO, CO_2, CH_3OH, or NH_2CHO, seeding more complex chemistry. In the case of formamide, VUV spectroscopy shows strong bands associated with $n \rightarrow \pi^*$ and $\pi \rightarrow \pi^*$ transitions of the amide chromophore (Section 3.1.2.3), and laboratory experiments demonstrate that excitation of these transitions leads to fragmentation

and rearrangement of the molecule in both pure and mixed ices [33, 37]. Thus, VUV photons provide a direct route to breaking the C-N, C=O, and N-H bonds in formamide, complementing the more distributed energy deposition of ions and electrons.

Experimentally, the VUV irradiation in this thesis was carried out using a synchrotron light source that delivers a broadband or tunable VUV photon flux in the 120-200 nm range at controlled intensities (Section 3.1.2.1). The mixed formamide-water ices were deposited between 10 and 130 K and then irradiated while monitoring their VUV and IR spectra in-situ. Since the absorption depth of VUV photons is comparable to the ice thickness, the incident photon fluence multiplied by the photon energy $h\nu$ provides a good measure of the absorbed dose, simplifying comparisons with ion and electron experiments, where LET and stopping powers must be considered explicitly. In this sense, VUV photons act as a high-energy, surface-focused analogue of the charged-particle radiation discussed earlier: they probe the electronic structure of the ice, initiate photochemistry in the top tens of nanometres, and allow the study of how formamide and its products respond to a purely photonic radiation field. Together with heavy-ion and electron irradiation, they complete the suite of radiation types used in this work to mimic the diverse energetic environment of Europa-like icy surfaces.

3.2.2 Molecular Effects of Radiation

Although ions, electrons, and VUV photons differ markedly in mass, charge, and penetration depth (Figures 3.7 and 3.9), at the molecular level they initiate a broadly similar sequence of events in condensed ices. The first stage is the very fast energy-deposition step, occurring on femtosecond timescales ($\lesssim 10^{-15}$ s), in which the incident projectile transfers energy to the solid by electronic excitation and ionisation. Along the track of a heavy ion or energetic electron, this produces a dense cluster of ion-electron pairs, electronically excited molecules, and a swarm of secondary electrons with a broad energy distribution. In the case of VUV photons, the same types of excited and ionised species are created, but in discrete photoabsorption events rather than along a continuous track [91–93].

These primary species then evolve through ultrafast relaxation and “spur” chem-

istry [92–94]. Secondary electrons rapidly lose energy through further ionisation and excitation events before thermalising at a few eV or less, at which point they can attach to, or scatter inelastically from, nearby molecules. Excited states undergo internal conversion and vibrational relaxation, converting electronic energy into local heating of the lattice, or dissociate directly to yield neutral fragments such as H, OH, NH_2, and CO. Ions and radicals formed in this way are initially confined within small volumes (spurs) along the track. Within a given spur, an ejected electron (or radical) can recombine with its parent ion before it has separated into the surrounding matrix (geminate recombination). If reactive fragments do separate, they can then undergo secondary radical chemistry within the cage, including hydrogen-atom abstraction and disproportionation, i.e. H-atom transfer between two radicals that yields one more reduced and one more oxidised product. The balance between recombination and escape depends strongly on the local energy density: high-LET ions tend to produce dense spurs where recombination is efficient, whereas low-LET projectiles and VUV photons create more sparsely distributed reactive sites [86, 91].

On longer timescales (picoseconds to seconds), as the lattice relaxes and the sample equilibrates at the substrate temperature, the surviving radicals and metastable species either recombine to regenerate the parent molecules or react with other components of the ice. These secondary reactions gradually build up a population of stable radiolysis products, including small molecules such as CO, CO_2, and OCN^-, as well as more complex organics in some mixtures [95, 96]. In amorphous ices at low temperature, radical diffusion is limited, and chemistry tends to occur within or near the original spurs. Upon warming, increased mobility allows radicals and ions to meet over larger distances, driving further reorganisation of both the chemical composition and the ice structure [95, 97]. The IR and VUV measurements used in this thesis probe the net outcome of this cascade: the loss of parent formamide, the appearance of new functional groups and electronic absorbers, and the way these changes depend on the type and dose of incident radiation.

3.2.3 Radiation Processing of Astrophysical Ices

In astrophysical settings, the microscopic processes outlined above operate continuously over geological timescales, gradually transforming simple ices into chemically and structurally more complex materials [98, 99]. On interstellar grains, cosmic rays, secondary UV photons, and low-energy electrons irradiate mixed H_2O, CO, CO_2, CH_3OH, and NH_3 mantles, driving the formation of radicals and new molecules with each energy-deposition event [98–100]. On icy moons and comets, magnetospheric ions and electrons, micrometeoroid impacts, and solar UV photons all contribute to a steady radiolytic and photolytic processing of surface and near-surface ices, as discussed in Section 3.2.3 [101]. Over time, this processing can both destroy fragile molecules and synthesise new species, including prebiotically relevant organics such as formamide, amino-acid precursors, and simple carboxylic or nitrile-bearing compounds [102, 103].

Laboratory ice experiments are designed to reproduce the essential ingredients of this processing under controlled conditions: a well-characterised ice composition and thickness, a known radiation field (ion, electron, or photon), and in-situ diagnostics to monitor how the ice responds [99]. IR spectroscopy is particularly well suited to tracking the evolution of functional groups and molecular backbones, providing direct information on the destruction of the parent species and the formation of stable radiolysis products [104, 105]. VUV spectroscopy complements this by probing the electronic structure and photodissociation thresholds of both parents and products, and by revealing how the absorption cross section of the ice changes as it is processed [26, 28, 88]. Together, these techniques allow thin-film experiments to capture, in accelerated form, the same basic chemistry that occurs in interstellar clouds, protoplanetary discs, and on icy bodies such as Europa.

For formamide-containing ices, radiation processing has two, often competing, consequences. On the one hand, high-energy irradiation tends to fragment molecules, reducing their abundance over time [11, 12, 33]. On the other hand, formamide itself can be produced by radiolysis and photolysis of simpler precursors, and its breakdown can feed into more complex prebiotic pathways [102, 103, 106]. Quantifying which outcome dominates under Europa-like conditions requires a dose-normalised measure

of chemical change and a clear understanding of how the surrounding ice matrix modulates the radiation chemistry. These aspects are addressed in the following sections using G-values and destruction cross-sections.

3.2.4 Environmental Influences

The efficiency and outcome of radiation chemistry in ices are not fixed; they depend sensitively on the physical environment in which the energy is deposited. Temperature is one of the most critical parameters. At very low temperatures (∼10-30 K), typical of dark interstellar clouds, radicals and ions produced by radiolysis are immobilised mainly in the amorphous matrix [98, 99]. Chemistry is then dominated by prompt, local reactions within spurs and by recombination of adjacent species. As the temperature increases into the 60-130 K range relevant for outer Solar System surfaces, diffusion becomes more efficient, enabling radicals to migrate, encounter new partners, and participate in more extended reaction networks [99, 100]. Thermal annealing over this range also drives structural transitions in the ice (e.g. amorphous relaxation or crystallisation), which in turn affect porosity, trapping efficiencies, and desorption behaviour [43, 107].

The composition and phase of the ice matrix exert equally strong controls. Water-rich, amorphous ices provide a strongly hydrogen-bonded environment in which embedded species such as formamide are efficiently solvated, and where radiolysis of H_2O itself produces copious H and OH radicals [26]. In contrast, CO- or CO_2-rich matrices offer fewer hydrogen-bond donors and different radical inventories, leading to distinct product distributions under irradiation [104, 105]. As discussed in Section 3.1.3, formamide-water mixtures do not behave as ideal solutions: formamide modifies the H_2O network, alters the temperatures of structural transitions, and stabilises glassy states over a broader temperature interval [11, 48]. These matrix effects influence not only which products form, but also how readily newly formed species can diffuse, recombine, or desorb.

Finally, the nature of the radiation field and the geometry of energy deposition introduces an additional layer of complexity. High-LET ions deposit energy in dense

tracks within the upper micrometres of the surface; lower-LET electrons deliver energy more diffusely and can penetrate to greater depths; VUV photons are absorbed within the top tens to hundreds of nanometres (Figures 3.9 and 3.3) [28, 88, 101]. In a real astrophysical setting, all of these components are present to varying degrees, so that any given parcel of ice experiences a mixture of surface-localised photochemistry and deeper, track-driven radiolysis. The net chemical evolution, therefore, depends on the interplay between energy-deposition profiles, temperature-dependent mobility, and ice composition.

These environmental factors vary widely between, for example, an interstellar grain and Europa's surface, therefore a simple comparison of fluences or irradiation times between laboratory and astrophysical conditions is not sufficient [108]. Instead, it is more meaningful to normalise chemical changes to the energy actually absorbed by the ice, and to characterise reaction efficiencies in terms of G-values and destruction cross-sections. The following section introduces these quantities and outlines their derivation and use in this thesis.

3.3 G-Values: Definition and Interpretation

Radiation-chemical yields, or G-values, provide a quantitative link between the energy deposited in an ice and the resulting chemical change. The experiments in this thesis involve multiple irradiation types; ions, electrons, and VUV photons, each of which deposits energy in fundamentally different ways so a common metric is required to compare their radiolytic effects. G-values supply this framework by expressing molecular destruction and product formation in terms of molecules produced or removed per 100 eV of absorbed energy. This section introduces the concept of the G-value, explains why it is the most appropriate measure for comparing disparate radiation environments, and outlines the methodology for deriving G-values from the infrared data obtained in this work.

3.3.1 What is a G-Value?

In radiation chemistry, the G-value, otherwise known as the radiation-chemical yield, quantifies the number of molecules formed or destroyed per 100 eV of absorbed energy [109, 110]. Since G-values are typically expressed as the number of molecules formed/destroyed per 100 eV, G-values are inherently normalised to the absorbed dose as opposed to rate or time. A typical G-value equation is as follows:

$$G_X = \frac{\Delta N_X}{E_{\text{abs}}} \times 100 \tag{3.1}$$

where ΔN_X is the number of molecules of 'X' formed (+) or destroyed (-) and E_{abs} is the energy absorbed by the sample in eV. G_X is expressed in molecules per 100 eV[7].

In radiolysis, a G-value may describe either the loss of a parent species or the appearance of a product. Formally, a negative slope $\mathrm{d}N/\mathrm{d}E$ indicates destruction, while a positive slope indicates formation. In practice, it is common in laboratory ice studies to report the magnitude of each yield and specify its meaning through notation rather than through a sign. Following this convention, two types of G-values are used throughout this thesis:

- $G(-M)$: the destruction yield of a molecular precursor (here formamide). It represents the number of parent molecules lost per 100 eV of absorbed energy.
- $G(+P)$: the formation yield of a radiolysis product (e.g. CO, CO_2, OCN^-). It represents the number of molecules produced per 100 eV.

Even though destruction formally corresponds to a negative derivative, the tabulated values for $G(-M)$ and $G(+P)$ are presented as positive quantities, with the sign included in the notation. This method allows for direct comparison between precursors and products without mixing positive and negative numbers. The original slope remains evident through the sign convention:

$$G(-M) = -100\left(\frac{\mathrm{d}N}{\mathrm{d}E}\right) \quad \text{and} \quad G(+P) = \quad 100\left(\frac{\mathrm{d}N}{\mathrm{d}E}\right), \tag{3.2}$$

[7]It should be noted that it is common in radiation-chemistry texts to define G in mol/100 eV per 100g, but in astrochemistry ice work it is common to use mol/100 eV, especially for thin films [111, 112].

where N is the column density (molecules cm^{-2}) and E is the absorbed energy (eV cm^{-2}).

This notation matches earlier radiolysis studies on astrophysical ices, where the focus is on the yield magnitude (molecules per 100 eV) rather than the algebraic sign. This approach allows the discussion of destruction and formation together in a single framework.

G-values are also directly connected to the concept of dose and energy deposition. In thin astrophysical ice films, the absorbed dose is typically expressed in units of eV cm^{-2} rather than per unit mass, since the irradiated volume is small and well defined. The rate at which this absorbed dose builds up depends on the linear energy transfer (LET) of the incident radiation, which quantifies how much energy a particle deposits per unit track length in the solid [113]. High-LET projectiles (e.g. heavy ions) deliver energy densely and therefore produce rapid changes in molecular abundance per fluence, whereas low-LET projectiles (e.g. protons or electrons) deposit energy more diffusely. The G-value then describes how efficiently a given molecule responds to that deposited energy; in other words, LET determines how fast the dose accumulates, whereas the G-value determines how much chemistry occurs per 100 eV of that dose.

3.3.2 Why Use G-Values?

When comparing experimental results, doing so using an absolute change (such as % loss of a molecule after irradiation) can be misleading, especially across different radiation sources. These endpoints alone cannot reflect the chemical efficiency of different radiation environments, making it harder to compare results across differing variables. Since different particles deposit vastly different amounts of energy per impact, identical fluences produce very different chemical outcomes, and this needs to be accounted for: VUV photons carry 6-10 eV each, electrons may carry energies from a few keV to MeV and deposit their energy over extended tracks, and ions deposit tens of keV with high LET on nm-scales. Therefore, comparing only with fluence can also provide misleading conclusions as fluence alone is not a universal measure of radiolytic processing. This is because an identical number of incident particles (e.g. 10^{15} photons, electrons, or ions)

does not correspond to an equivalent amount of deposited energy, and therefore cannot be compared directly without giving rise to misleading conclusions about chemical efficiency.

In astrochemistry, G-values are especially important because they provide a dose-normalised measure of chemical reactivity that is independent of the specific radiation source. Ionising radiation in astrophysical settings covers a wide range of energies and particles, from keV to MeV electrons and ions in planetary magnetospheres to UV photons and cosmic rays in dense interstellar clouds. All these processes ultimately deposit energy into icy grains and molecular solids. By expressing radiolysis and photolysis efficiencies as molecules formed or destroyed per 100 eV, G-values allow direct comparisons of laboratory measurements across different irradiation types, beam energies, or fluence conditions. This creates a practical link between controlled laboratory experiments and real astrophysical situations, where the key factor is the local radiation dose rather than the incoming flux of a specific particle. In modelling studies of the ISM and icy bodies in the Solar System, G-values are often used to estimate chemical production rates, destruction timescales, and the overall radiation-driven changes of organic molecules under realistic cosmic-ray or magnetospheric dose rates. Thus, G-values create a shared quantitative framework for connecting laboratory radiochemistry to astrochemical environments [108, 114, 115].

In addition to G-values, radiation-induced destruction cross-sections are widely used in astrochemical laboratory studies. A destruction cross-section provides a measure of the probability that a molecule will be removed upon interaction with a single incident particle (e.g. an ion, electron, or photon) [116, 117]. In this sense, destruction cross-sections and G-values are complementary: cross-sections describe the reactivity per projectile, whereas G-values describe the chemical effect per unit energy absorbed. The former is tied to the particle flux, while the latter is tied to the deposited dose.

Destruction Cross-Sections

Destruction cross-sections are typically derived from the exponential decay of a

parent-band column density as a function of fluence, using the relationship:

$$N(F) = N_0 \exp(-\sigma_{\mathrm{d}} F), \tag{3.3}$$

where N_0 is the initial column density, F is the cumulative fluence (particles cm^{-2}), and σ_{d} is the effective probability that one incident particle will remove the target molecule.

This method has been used extensively in the laboratory astrochemistry literature, including studies of mixed organic and water-ice systems directly relevant to this work [53, 118]. Numerous UV-photolysis studies determine molecular destruction rates by fitting exponential decays in precisely this form, including classic work on CO-, H_2O-, and CH_3OH-rich ices [104, 105]. Ion-irradiation studies also routinely use destruction cross-sections to quantify radiolytic efficiency in mixed molecular ices (e.g. CO:NH_3, H_2O:CO_2, CH_3OH:CO) [119], as do electron-irradiation experiments on prebiotic organics and astrophysical ices [120]. These studies form the methodological foundation for the use of σ_{d} in this work

3.3.3 Determining G-Values

Before deriving G-values, it is essential to outline the spectral inputs used in this work. For the ion-irradiation experiments, FTIR spectra were collected after each fluence step, providing dose-resolved evolution of the formamide and product bands. In contrast, the electron-irradiation experiments provide only pre- and post-irradiation spectra, and VUV irradiation was monitored independently by VUV absorption rather than IR, so quantitative G-values are derived solely from the IR datasets. The analysis therefore focuses on a set of diagnostic bands that remain sufficiently isolated within the H_2O-rich ice mixture: the formamide features at 1388 and 1328 cm^{-1}, and the product bands of CO_2 (2340 cm^{-1}), OCN^- (2165 cm^{-1}), and CO (2135 cm^{-1}). These bands were integrated from baseline-corrected absorbance spectra using consistent limits and converted to column densities using literature band strengths measured for cryogenic ices at temperatures as close as possible to those used here; where mixture-specific A-values were unavailable, the nearest-temperature pure-ice values were adopted as the

best available approximation [14, 121, 122]. These processed spectra form the starting point for the dose-response analysis that underpins the G-value calculations.

The calculation of G-values in this work follows a multi-step procedure that links the measured infrared spectra to a quantitative estimate of the early-time radiolysis rate. First, each diagnostic vibrational band (for formamide and its products) was integrated and converted into a molecular column density using literature band strengths. These column densities were then plotted as a function of the absorbed energy, rather than particle fluence, where the absorbed dose for each irradiation step was determined from the particle or photon fluence multiplied by the deposited energy. The resulting dose-response curves were fitted with analytical decay or growth functions, which provided a smooth mathematical description of how each species evolves with increasing dose. From these fitted functions, the initial, low-dose portion of the curve, where the behaviour is approximately linear, was isolated and subjected to a linear regression. The slope of this linear region corresponds to $\mathrm{d}N/\mathrm{d}E$, the number of molecules lost or formed per eV of absorbed energy. Finally, multiplying this slope by 100 yields the G-value in molecules per 100 eV. This pipeline ensures that the derived G-values reflect each species' true initial radiochemical efficiency and are directly comparable across different radiation types, ice compositions, and substrate conditions.

To convert the integrated absorbance into column density, the following equation was used:

$$N = \frac{\ln(10) \int A(\tilde{\nu})\, d\tilde{\nu}}{A} \tag{3.4}$$

where $A(\tilde{\nu})$ is the baseline-corrected absorbance, defined as $\log_{10}\left(\frac{I_0}{I}\right)$ - I is the transmitted intensity and I_0 is the incident light intensity - and A is the band strength (cm molecule^{-1}) taken from literature [14, 118, 122]. Uncertainties in the column densities arise primarily from the adopted band strengths, which typically dominate the error budget; additional contributions come from baseline placement, overlaps between neighbouring features, and variations in the integrated band area introduced by noise in the FTIR spectra.

The absorbed energy was calculated by multiplying the particle or photon fluence by the energy deposited per incident particle. In the ion experiments, the deposited

energy per ion was obtained from SRIM (discussed in Section 4.4.2) stopping powers evaluated over the measured ice thickness, allowing the LET to be converted into an energy deposition (eV ion^{-1}). In the electron experiments, the deposited energy per electron was determined from ESTAR electron ranges at two keV. In contrast, for VUV irradiation, the absorbed energy is simply the product of the photon fluence and photon energy ($h\nu$). This yields an absorbed dose expressed in eV cm^{-2}, which is used as the x-axis for all G-value analyses.

As an illustrative example, an O^{2+} ion with a stopping power of order 10^2 keV μm^{-1} traversing a $\sim$0.2-0.3 μm ice film deposits tens of keV per ion; when multiplied by an ion fluence of $\sim 10^{15}$ ions cm^{-2}, the resulting absorbed dose is $\sim 10^{19}$ eV cm^{-2}.

Before extracting the low-dose linear behaviour required for the G-value analysis, each dose-response curve was first fitted with an analytical function to provide a smooth representation of its overall evolution. For formamide destruction, multi-exponential decay functions were required because the parent bands typically exhibited an initial rapid loss followed by a slower secondary decline; such multi-timescale behaviour is well established in radiolysis studies, where compaction, radical trapping, and matrix restructuring all contribute to non-single-exponential decay. In contrast, the formation of CO, CO_2, and OCN^- was better described using logarithmic or saturating growth functions, which capture the fast initial rise in product abundance and the subsequent plateau as precursor availability decreases. These analytical fits are therefore used purely as smooth interpolators: they reduce the influence of point-to-point spectral noise, preserve the overall physical shape of the dose-response, and allow the early, approximately linear region to be identified with greater precision.

To obtain the initial radiochemical yield, the G-values were then derived from the low-dose regime of these fitted functions. An upper energy-fluence limit, $E_{\max}$, was chosen by visual inspection of each fitted curve as the point at which the behaviour remained approximately linear - i.e. before curvature due to saturation, secondary chemistry, or significant precursor depletion became apparent. The fitting script subsequently generated a small number of evenly spaced synthetic data points between 0 and $E_{\max}$, and a straight line was fitted only to the first subset of these points,

corresponding to the truly linear portion of the response. The slope of this linear fit, $\mathrm{d}N/\mathrm{d}E$, represents the primary radiolysis rate prior to the onset of non-linear effects and forms the basis of the G-values reported in this thesis. A full step-by-step account of this procedure, including the fitted equations and uncertainty propagation, is given in Appendix A.

3.3.4 Limitations and Considerations for the Derived G-Values

Several limitations and sources of uncertainty must be considered when interpreting the G-values derived in this work. The dominant contribution arises from the use of literature band strengths to convert integrated absorbance into column density, since these values can vary with temperature, mixture composition, and matrix environment; this uncertainty propagates directly into the absolute scale of $N(E)$ and hence the absolute G-values. Additional contributions stem from baseline placement, residual overlap between neighbouring absorption features in the formamide-water matrix, and point-to-point noise in the FTIR spectra, all of which affect integrated band areas and therefore the constructed dose-response curves. Where analytical functions were fitted to interpolate the full dose range, uncertainty in the best-fit parameters introduces additional variation in the synthetic low-dose points used to derive the initial linear slope. Finally, the linear regression itself carries a statistical uncertainty in the fitted slope (estimated from the covariance of the fit), which is propagated directly into the reported G-value. Taken together, these terms provide a conservative estimate of the overall uncertainty associated with each reported value.

A further consideration is that G-values are defined in the limit of low dose, where the radiolysis response is approximately linear and dominated by primary chemical events. At higher doses, the dose-response curves become increasingly influenced by non-linear behaviour such as precursor depletion, secondary radical-radical reactions, matrix compaction, or changes in ice morphology. These processes alter both the apparent decay rate of formamide and the growth rates of CO, CO_2, and OCN^-, meaning that the analytical functions used to interpolate the full dose range should not be interpreted as mechanistic models. Instead, they serve as smooth approximations

that isolate the initial linear regime; the resulting G-values therefore reflect only the early-stage radiochemical efficiency, not the full complexity of high-dose chemistry.

Finally, the choice of substrate introduces an additional methodological complication. As demonstrated in Chapters 5 and 6, NaCl and ZnSe substrates do not affect the experiments in the same way: ZnSe is comparatively chemically inert, but still differs in optical properties (e.g., refractive index) and in its interaction with charged-particle irradiation (e.g., charging behaviour and secondary electron yield), which can influence apparent destruction and formation rates. By contrast, NaCl can additionally perturb the local chemical environment of the ice and enhance radiolytic processing. These effects are most apparent for low-LET irradiation such as H^+ and 2 keV electrons. The substrate, therefore, alters the effective radiolysis environment experienced by the ice, and G-values must be interpreted with this in mind. In the case of electron irradiation and VUV processing, the lack of incremental IR spectra restricts the calculation to pre- and post-irradiation states, limiting the precision with which the initial linear response can be accessed. These factors do not invalidate the derived G-values. But, they define the conditions under which they should be compared and emphasise that G-values are intrinsically context-dependent quantities tied to both the irradiation conditions and the physical properties of the ice-substrate system.

3.3.5 Survivability Under Europan Radiation

In addition to determining laboratory G-values, it is useful to translate these destruction yields into an estimate of how long formamide would survive on Europa's surface under continuous irradiation. This survivability calculation combines the experimentally measured destruction yield with the ion energy–dose rates expected at Europa's surface, allowing the radiolytic lifetime of formamide to be expressed in physical time units (years). The method used here follows directly from the laboratory definitions of G-values but applies them to the steady-state magnetospheric environment of Europa.

The destruction G-value, $G(-M)$, gives the number of molecules destroyed per 100 eV of absorbed energy. To apply this to Europa, the surface radiation field must be expressed as an energy-dose rate. Dose rates for H^+, O^{n+}, and S^{n+} ions were

obtained by digitising the flux-energy spectra presented in the ESA "Europa Surface Environment" report (page 16) [123], and converting these fluxes into dose rates using the standard relation 1 rad $= 6.242 \times 10^{13}$ eV g^{-1}. This yields an ion-specific dose rate, $\dot{D}$ (eV g^{-1} s^{-1}), representing the rate at which magnetospheric ions deposit energy into the upper microns of the ice.

The destruction rate of formamide per gram of ice is then:

$$R_{\mathrm{g}} = \frac{G(-M)}{100}\,\dot{D},$$

This gives the number of formamide molecules lost per gram of mixed ice per second. To convert this to an absolute destruction rate for the deposited films used in this work, the mass of the irradiated ice was determined from the measured film thickness, a beam area of 0.785 cm^2, and the density of the H_2O:NH_2CHO mixture. The density of the H_2O:NH_2CHO mixture was estimated by harmonic mixing of literature densities for pure formamide and water. For H_2O, the density of vapour-deposited amorphous solid water at 90 K was adopted ($\rho_{\mathrm{ASW}} = 0.934$ g cm^{-3}), consistent with the phase expected under cryogenic deposition conditions [124]; for formamide, the density of solid (ice) formamide was taken as $\rho_{\mathrm{FA,ice}} = 0.937$ g cm^{-3} [14]. Multiplying R_{g} by the formamide mass present in the film gives the total removal rate, R (molecules s^{-1}).

The initial number of formamide molecules, N_0, was calculated from the known mass fraction of formamide in each film, the total ice mass, and the molar mass of formamide. The survivability, expressed as a radiolytic lifetime τ, is then defined as the time required for the existing population to be removed at the Europa-relevant destruction rate:

$$\tau = \frac{N_0}{R},$$

This provides a direct physical timescale (in seconds or years) for the persistence of formamide at Europa's surface. This definition corresponds to the mean lifetime of an initially present formamide inventory under steady irradiation, and is appropriate here because the destruction response is approximately linear over the radiation doses relevant to Europa's environment. It is noted, however, that this formulation implicitly assumes net destruction (i.e. it neglects any in-situ replenishment of NH_2CHO during

irradiation). Laboratory and theoretical studies show that formamide formation in processed ices is chemically plausible under some conditions [15, 125–127], but the net importance of such production on Europa depends on the local availability of suitable precursors and their co-location with the irradiated region. The lifetimes reported here should therefore be interpreted as destruction-limited estimates for a pre-existing formamide abundance; any significant in-situ production would act to increase the steady-state abundance and extend the effective persistence time.

Europa's surface receives contributions from multiple ion species, each with different fluxes, LET values, and dose rates. To combine these contributions, a Monte Carlo scheme was used in which ion species were randomly sampled according to their relative flux (or dose) weighting and the corresponding G-values were accumulated over many trials to obtain an effective, mixed-field result. For each species, the destruction rate and its uncertainty were sampled from a normal distribution, and the total destruction rate was obtained by summing over all contributing ions (H^+, O^{2+}, S^{5+}). Repeating this procedure for many iterations (typically 10^4 trials) yields a distribution of possible survival times, from which a mean lifetime and confidence interval can be extracted.

This framework provides a quantitative means of translating laboratory radiolysis measurements into astrophysical survival times, thereby allowing the stability of formamide on Europa to be evaluated directly. The resulting lifetimes, presented in later chapters, enable comparison of the destruction efficiencies of different ion species and assessment of whether formamide is likely to persist long enough to be detectable or to contribute to surface–subsurface chemical processes on Europa.

Bibliography

[1] Ojeda J, Dittrich M. Fourier Transform Infrared Spectroscopy for Molecular Analysis of Microbial Cells. Methods in molecular biology (Clifton, NJ). 2012 04;881:187-211.

[2] Nibbering E, Fidder H, Pines E. Ultrafast chemistry: using time-resolved vibrational spectroscopy for interrogation of structural dynamics. Annual review of physical chemistry. 2005;56:337-67.

[3] Błasiak B, Londergan C, Webb LJ, Cho M. Vibrational Probes: From Small Molecule Solvatochromism Theory and Experiments to Applications in Complex Systems. Accounts of chemical research. 2017;50 4:968-76.

[4] Chng CP, Dowd A, Mechler A, Hsia KJ. Molecular dynamics simulations reliably identify vibrational modes in far-IR spectra of phospholipids. Physical chemistry chemical physics : PCCP. 2024.

[5] Stuart BH. Infrared Spectroscopy: Fundamentals and Applications. Analytical techniques in the sciences. J. Wiley; 2004.

[6] The Horsehead Nebula and NGC 2023 — telescope.live;. [Accessed 02-05-2025]. `https://telescope.live/gallery/horsehead-nebula-and-ngc-2023`.

[7] Mifsud D, Kaňuchová Z, Ioppolo S, Herczku P, Muiña AT, Field T, et al. Mid-IR and VUV Spectroscopic Characterisation of Thermally Processed and Electron Irradiated CO2 Astrophysical Ice Analogues. Journal of Molecular Spectroscopy. 2022.

[8] D'iaz CG, Carrascosa H, Caro GMM. Infrared spectroscopy of astrophysical ice analogs at oblique angles. Monthly Notices of the Royal Astronomical Society. 2025.

[9] Mifsud D, Hailey P, Muiña AT, Auriacombe O, Mason N, Ioppolo S. The Role of Terahertz and Far-IR Spectroscopy in Understanding the Formation and Evolution of Interstellar Prebiotic Molecules. 2021;8.

[10] Brucato JR, Baratta GA, Strazzulla G. An infrared study of pure and ion irradiated frozen formamide. Astronomy & Astrophysics. 2006 Aug;455(2):395-9.

[11] Slavicinska K, Rachid M, Rocha W, Chuang K, Dishoeck EV, Linnartz H. The hunt for formamide in interstellar ices. A toolkit of laboratory infrared spectra in astronomically relevant ice mixtures and comparisons to ISO, Spitzer, and JWST observations. Astronomy & Astrophysics. 2023.

[12] Sivaraman B, Sekhar BN, Nair B, Hatode V, Mason NJ. Infrared spectrum of formamide in the solid phase. Spectrochimica acta Part A, Molecular and biomolecular spectroscopy. 2013.

[13] Ice Database — icedb.strw.leidenuniv.nl;. [Accessed 18-11-2025]. `https://icedb.strw.leidenuniv.nl/data/175`.

[14] Brucato J, Baratta G, Strazzulla G. An infrared study of pure and ion irradiated frozen formamide. Astronomy & Astrophysics. 2006;455:395-9.

[15] Kaňuchová Z, Urso R, Baratta G, Brucato J, Palumbo M, Strazzulla G. Synthesis of formamide and isocyanic acid after ion irradiation of frozen gas mixtures. Astronomy & Astrophysics. 2016;585.

[16] Ashfold MNR, Western CM. Multiphoton Spectroscopy, Applications . In: Lindon JC, Tranter GE, Koppenaal DW, editors. Encyclopedia of Spectroscopy and Spectrometry (Third Edition). third edition ed. Oxford: Academic Press; 2017. p. 954-61.

[17] Wilhelm K, Dwivedi B, Marsch E, Feldman U. Observations of the Sun at Vacuum- Ultraviolet Wavelengths from Space. Part I: Concepts and Instrumentation. Space Science Reviews. 2004;111:415-80.

[18] Nakamura H. What are the basic mechanisms of electronic transitions in molecular dynamic processes. International Reviews in Physical Chemistry. 1991;10:123-88.

[19] Park SM, Kim H, Kwon CH. Impact of chlorine substitution on valence orbitals and ionization dynamics in 3-chloropyridine: Insights from high-resolution vacuum ultraviolet mass-analyzed threshold ionization study. The Journal of chemical physics. 2024;161 17.

[20] Vasconcelos H, Meirelles M, Özmenteş R, Korkut A. Vacuum Ultraviolet Spectroscopic Analysis of Structural Phases in TiO2 Sol–Gel Thin Films. Coatings. 2024.

[21] Schug K, Sawicki I, Carlton DD, Fan H, Mcnair H, Nimmo JP, et al. Vacuum ultraviolet detector for gas chromatography. Analytical chemistry. 2014;86 16:8329-35.

[22] Rogério DDO, Cavasso-Filho R, Lago A. VUV-Induced Photodissociation of the Chloroacetone Molecule Studied by Photoelectron-Photoion Coincidence Spectroscopy. Journal of the American Society for Mass Spectrometry. 2021.

[23] Santos IC, Schug KA. Recent advances and applications of gas chromatography vacuum ultraviolet spectroscopy. Journal of Separation Science. 2017;40(1):138-51.

[24] Letzelter C, Eidelsberg M, Rostas F, Breton J, Thieblemont B. Photoabsorption and photodissociation cross sections of CO between 88.5 and 115 nm. Chemical Physics. 1987;114:273-88.

[25] Cottin H, Moore M, Bénilan Y. Photodestruction of Relevant Interstellar Molecules in Ice Mixtures. The Astrophysical Journal. 2003;590:874 881.

[26] Mason N, Dawes A, Holtom P, Mukerji R, Davis MP, Sivaraman B, et al. VUV spectroscopy and photo-processing of astrochemical ices: an experimental study. Faraday Discussions. 2006;133:311-29; discussion 347-74, 449-52.

[27] Bertin M, Romanzin C, Doronin M, Philippe L, Jeseck P, Ligterink N, et al. UV photodesorption of methanol in pure and CO-rich ices: Desorption rates of the intact molecule and of the photofragments. The Astrophysical Journal Letters. 2016;817.

[28] Cruz-Diaz G, Caro GMM, Chen Y, Yih T. Vacuum-UV spectroscopy of interstellar ice analogs - I. Absorption cross-sections of polar-ice molecules. Astronomy & Astrophysics. 2014;562.

[29] Zheng W, Jewitt D, Osamura Y, Kaiser R. Formation of Nitrogen and Hydrogen-bearing Molecules in Solid Ammonia and Implications for Solar System and Interstellar Ices. The Astrophysical Journal. 2008;674:1242 1250.

[30] Chang Y, Ashfold M, Yuan K, Yang X. Exploring the vacuum ultraviolet photochemistry of astrochemically important triatomic molecules. National Science Review. 2023;10.

[31] Gelfand N, Komarova K, Remacle F, Levine R. Nonadiabatic dynamics in a forest of coupled states: Electronic state branching in the VUV photodissociation of N2. The Journal of chemical physics. 2023;158 16.

[32] Zheng W, Jia L, Huang F. Vacuum-Ultraviolet Photon Detections. iScience. 2020;23(6):101145.

[33] Bodi A, Hemberger P. Low-Energy Photoelectron Spectrum and Dissociative Photoionization of the Smallest Amides: Formamide and Acetamide. The journal of physical chemistry A. 2018;123 1:272-83.

[34] ACID-AstroChemical Ices Database — prl.res.in;. [Accessed 29-11-2025]. `https://www.prl.res.in/~dinesh/acid/`.

[35] Sander R, Keller-Rudek H, Moortgat G, Sörensen R. The MPI-Mainz UV/VIS Spectral Atlas of Gaseous Molecules of Atmospheric Interest. Earth System Science Data. 2013;5:365-73.

[36] Gingell J, Mason NJ, Zhao H, Walker I, Siggel M. VUV optical-absorption and electron-energy-loss spectroscopy of formamide. Chemical Physics. 1997;220:191-205.

[37] Sivaraman B, Sekhar BNR, Jones NC, Hoffmann SV, Mason NJ. VUV spectroscopy of formamide ices. Chemical Physics Letters. 2012.

[38] Lundell J, Krajewska M, Räsänen M. Matrix Isolation Fourier Transform Infrared And Ab Initio Studies Of The 193-nm-Induced Photodecomposition Of Formamide. Journal of Physical Chemistry A. 1998;102:6643-50.

[39] Sivaraman B, Nair B, Sekhar B, Jones N, Hoffmann S, Mason N. Electron impact dissociation and VUV photoabsorption of frozen formamide. Chemical Physics Letters. 2014;608:404-7.

[40] Puhovski Y, Rode B. Structure and dynamics of liquid formamide. 1995;190:61-82.

[41] Elola M, Ladanyi B. Computational study of structural and dynamical properties of formamide-water mixtures. The Journal of chemical physics. 2006;125 18:184506.

[42] Frey J, Leutwyler S. An ab initio benchmark study of hydrogen bonded formamide dimers. The journal of physical chemistry A. 2006;110 45:12512-8.

[43] Jenniskens P, Blake D. Structural transitions in amorphous water ice and astrophysical implications. Science. 1994;265:753-6.

[44] Collings MP, Anderson MA, Chen R, Dever JW, Viti S, Williams DA, et al. A laboratory survey of the thermal desorption of astrophysically relevant molecules. Monthly Notices of the Royal Astronomical Society. 2004.

[45] Ladell J, Post B. The Crystal Structure of Formamide. Acta Crystallographica. 1954.

[46] Notley JM, Spiro M. The purification of formamide, and the rate of its reaction with dissolved water. Journal of The Chemical Society B: Physical Organic. 1966:362-6.

[47] Bada J, Chalmers J, Cleaves H. Is formamide a geochemically plausible prebiotic solvent? Physical chemistry chemical physics : PCCP. 2016;18 30:20085-90.

[48] Hassoun S, Digby ZA, Hamad NA, Schlenoff J. Formamide as a Robust Alternative to Water for Plasticizing Polyelectrolyte Complexes. Macromolecules. 2024.

[49] Wang S, Li Y, Yu M, Li Q, Li H, Wang Y, et al. High-performance cryo-temperature ionic thermoelectric liquid cell developed through a eutectic solvent strategy. Nature Communications. 2024;15.

[50] Ionizing radiation and health effects — who.int;. [Accessed 03-07-2025]. `https://www.who.int/news-room/fact-sheets/detail/ionizing-radiation-and-health-effects`.

[51] Maimon E, Samuni U, Goldstein S. Studying mechanism of radical reactions: From radiation to nitroxides as research tools. Radiation Physics and Chemistry. 2018;143:14-9. International Meeting on Radiation Processing (IMRP-18) in Radiation Physics & Chemistry (RPC).

[52] Arumainayagam CR, Garrod R, Boyer MC, Hay A, Bao S, Campbell JS, et al. Extraterrestrial prebiotic molecules: photochemistry vs. radiation chemistry of interstellar ices. Chemical Society reviews. 2019;48 8:2293-314.

[53] Dawley MM, Pirim C, Orlando T. Radiation processing of formamide and formamide:water ices on silicate grain analogue. The journal of physical chemistry A. 2014;118 7:1228-36.

[54] Volosatova AD, Tyurin DA, Feldman V. The Radiation Chemistry of NH3 · · · CO Complex in Cryogenic Media as Studied by Matrix Isolation. The journal of physical chemistry A. 2022.

[55] Becker TM, Zolotov MY, Gudipati MS, Soderblom JM, McGrath MA, Henderson BL, et al. Exploring the Composition of Europa with the Upcoming Europa Clipper Mission. Space Sci. Rev.. 2024 Aug;220(5):49.

[56] Warren SG, Brandt RE. Optical constants of ice from the ultraviolet to the microwave: A revised compilation. Journal of Geophysical Research: Atmospheres. 2008;113(D14).

[57] Costello ES, Phillips CB, Lucey PG, Ghent RR. Impact gardening on Europa and repercussions for possible biosignatures. Nature Astronomy. 2021 Jul;5:951-6.

[58] Roth L, Blöcker A, de Kleer K, Goldstein DB, Lellouch E, Saur J, et al. Mass Supply from Io to Jupiter's Magnetosphere. Space Science Reviews. 2024;221.

[59] Bragg W, Kleeman R. LXXIV. On the ionization curves of radium. Philosophical Magazine Series 1. 1904.

[60] Deasy J. ICRU Report 49, Stopping Powers and Ranges for Protons and Alph Particles. Medical Physics. 1994 May;21(5):709-10.

[61] Kalholm F, Grzanka L, Traneus E, Bassler N. A Systematic Review on the Usage of Averaged LET in Radiation Biology for Particle Therapy. Radiotherapy and oncology : journal of the European Society for Therapeutic Radiology and Oncology. 2021.

[62] Szalay J, Allegrini F, Bagenal F, Bolton S, Clark G, Connerney J, et al. Proton Outflow Associated With Jupiter's Auroral Processes. Geophysical Research Letters. 2020;48.

[63] Bodisch K, Dougherty L, Bagenal F. Survey of Voyager plasma science ions at Jupiter: 3. Protons and minor ions. Journal of Geophysical Research: Space Physics. 2017;122:8277 8294.

[64] Paranicas C, Ratliff JM, Mauk B, Cohen C, Johnson RE. The ion environment near Europa and its role in surface energetics. Geophysical Research Letters. 2002;29.

[65] Cheng A. Effects of Io's volcanos on the plasma torus and Jupiter's magnetosphere. The Astrophysical Journal. 1980;242:812-27.

[66] Smith HT, Koga R, Tsuchiya F, Dols V. Insight Into Io Enabled by Characterization of Its Neutral Oxygen Torus. Journal of Geophysical Research: Space Physics. 2022;127.

[67] Allen R, Paranicas C, Bagenal F, Vines S, Hamilton D, Allegrini F, et al. Energetic Oxygen and Sulfur Charge States in the Outer Jovian Magnetosphere: Insights From the Cassini Jupiter Flyby. Geophysical Research Letters. 2019;46:11709 11717.

[68] Clark G, Mauk B, Kollmann P, Paranicas C, Bagenal F, Allen R, et al. Heavy Ion Charge States in Jupiter's Polar Magnetosphere Inferred From Auroral Megavolt Electric Potentials. Journal of Geophysical Research: Space Physics. 2020;125.

[69] Szalay J, Allegrini F, Ebert R, Bagenal F, Bolton S, Fatemi S, et al. Oxygen production from dissociation of Europa's water-ice surface. Nature Astronomy. 2024;8:567 576.

[70] Ip W, Williams D, Mcentire R, Mauk B. Ion sputtering and surface erosion at Europa. Geophysical Research Letters. 1998.

[71] Plainaki C, Milillo A, Mura A, Orsini S, Massetti S, Cassidy T. The role of sputtering and radiolysis in the generation of Europa exosphere. Icarus. 2012.

[72] Mauk B, Mitchell D, Mcentire R, Paranicas C, Roelof E, Williams DJ, et al. Energetic ion characteristics and neutral gas interactions in Jupiter's magnetosphere. Journal of Geophysical Research. 2004;109.

[73] Spencer J, Schneider N. IO on the eve of the Galileo mission. Annual Review of Earth and Planetary Sciences. 1996;24:125-90.

[74] Yoshikawa I, Suzuki F, Hikida R, Yoshioka K, Murakami G, Tsuchiya F, et al. Volcanic activity on Io and its influence on the dynamics of the Jovian magnetosphere observed by EXCEED/Hisaki in 2015. Earth, Planets and Space. 2017;69:1-11.

[75] Spencer J, Bagenal F, Bartlett S. Jupiter's Magnetosphere Schematic; 2007. Depiction of Jupiterś magnetosphere with magnetic field lines, Io plasma torus, and Galilean moon orbits. Laboratory for Atmospheric and Space Physics (LASP), University of Colorado Boulder. Available from: https://lasp.colorado.edu/mop/resources/graphics/.

[76] Li J, Li C. Sulfur chemistry on the surface ice of Europa. Icarus. 2023.

[77] Ziegler JF, Ziegler MD, Biersack JP. SRIM – The Stopping and Range of Ions in Matter; 2010. Version SRIM-2013. http://www.srim.org/.

[78] Jupiter's magnetic field and radiation belts | EBSCO — ebsco.com;. [Accessed 21-07-2025]. https://www.ebsco.com/research-starters/science/jupiters-magnetic-field-and-radiation-belts.

[79] Staff A. What is the source of Jupiter's radiation? | Astronomy.com — astronomy.com;. [Accessed 21-07-2025]. https://www.astronomy.com/science/what-is-the-source-of-jupiters-radiation/.

[80] Coffin D, Damiano P, Delamere P, Johnson J, Ng C. Broadband Energization of Superthermal Electrons in Jupiter's Inner Magnetosphere. Journal of Geophysical Research: Space Physics. 2022;127.

[81] Montgomery J, Ebert R, Allegrini F, Fuselier S, Bagenal F, Bolton S, et al. Investigating Boundary Layer Properties at Jupiter's Dawn Magnetopause. Journal of Geophysical Research: Space Physics. 2024;129.

[82] Ionospheric irregularities at Jupiter observed by JWST - Nature Astronomy — nature.com;. [Accessed 31-07-2025]. https://www.nature.com/articles/s41550-024-02305-9.

[83] Goertz CK. Jupiter's ionosphere and magnetosphere. Planetary and Space Science. 1973;21(8):1389-98.

[84] Bagenal F, Dowling TE, McKinnon WB. 26. In: Bagenal F, Dowling TE, McKinnon WB, editors. The Radiation Belts of Jupiter. Cambridge, UK: Cambridge University Press; 2004. p. 495-528.

[85] Vázquez H, Kononov A, Kyritsakis A, Medvedev N, Schleife A, Djurabekova F. Electron cascades and secondary electron emission in graphene under energetic ion irradiation. Phys Rev B. 2021 Jun;103:224306.

[86] Ziaja B, Szoeke A, Hajdu J. Electron Cascades Produced by Photoelectrons in Diamond. 2002.

[87] Ziaja B, London R, Hajdu J. Unified model of secondary electron cascades in diamond. Journal of Applied Physics. 2004;97:064905.

[88] Cruz-Diaz GA, Caro GMM, Chen YJ, Yih TS. Vacuum-UV spectroscopy of interstellar ice analogs II. Absorption cross-sections of nonpolar ice molecules. Astronomy & Astrophysics. 2014.

[89] Berger MJ, Coursey JS, Zucker MA, Chang J. ESTAR, PSTAR, and ASTAR: Computer Programs for Calculating Stopping-Power and Range Tables for Electrons, Protons, and Helium Ions. National Institute of Standards and Technology; 2025.

[90] Yabushita A, Hama T, Kawasaki M. Photochemical reaction processes during vacuum-ultraviolet irradiation of water ice. Journal of Photochemistry and Photobiology C-photochemistry Reviews. 2013;16:46-61.

[91] Jay-Gerin J. Fundamentals of Water Radiolysis. Encyclopedia. 2025.

[92] Nikjoo H, Uehara S, Emfietzoglou D, Cucinotta F. Track-structure codes in radiation research. Radiation Measurements. 2006;41:1052-74.

[93] Mozumder A, Magee J. Model of tracks of ionizing radiations for radical reaction mechanisms. Radiation research. 1966;28 2:203-14.

[94] Schwarz H. Applications of the spur diffusion model to the radiation chemistry of aqueous solutions. The Journal of Physical Chemistry. 1969;73:1928-37.

[95] Cuppen H, Linnartz H, Ioppolo S. Laboratory and Computational Studies of Interstellar Ices. Annual Review of Astronomy & Astrophysics. 2024.

[96] Hofmann F, Asanova N, Urso RG, Elsaesser A. Exploring the formation and alteration of organics in ice: experimental insights for astrochemistry and space missions. Earth, Planets and Space. 2025.

[97] Theulé P, Duvernay F, Danger G, Borget F, Bossa JB, Vinogradoff V, et al. Thermal reactions in interstellar ice: A step towards molecular complexity in the interstellar medium. Advances in Space Research. 2013;52:1567-79.

[98] Boogert A, Gerakines P, Whittet D. Observations of the Icy Universe. Annual Review of Astronomy & Astrophysics. 2015;53:541-81.

[99] Cuppen H, Walsh C, Walsh C, Lamberts T, Lamberts T, Semenov D, et al. Grain Surface Models and Data for Astrochemistry. Space Science Reviews. 2017;212:1 58.

[100] Garrod R. A three-phase chemical model of hot cores: The formation of glycine. The Astrophysical Journal. 2013;765.

[101] Johnson RE. Energetic Charged-Particle Interactions with Atmospheres and Surfaces. 1990.

[102] Modica P. From astrophysics to astrobiology : significance of laboratory organic residues from photo-irradiation of cosmic ice analogs. 2014.

[103] Kaiser R, Stockton A, Kim Y, Jensen E, Mathies R. On the formation of dipeptides in interstellar model ices. The Astrophysical Journal. 2013;765.

[104] Gerakines P, Schutte W, Ehrenfreund P. Ultraviolet processing of interstellar ice analogs. I. Pure ices. Astronomy & Astrophysics. 1996;312:289-305.

[105] Gerakines PA, Moore MH, Hudson RL. Ultraviolet photolysis and proton irradiation of astrophysical ice analogs containing hydrogen cyanide. Icarus. 2004.

[106] Saladino R, Crestini C, Pino S, Costanzo G, Mauro ED. Formamide and the origin of life. Physics of life reviews. 2012;9 1:84-104.

[107] Fayolle E, Bertin M, Romanzin C, Michaut X, Öberg K, Linnartz H, et al. CO Ice Photodesorption: A Wavelength-Dependent Study. The Astrophysical Journal Letters. 2011;739.

[108] Shingledecker C, Tennis J, Gal RL, Herbst E. On Cosmic-Ray-driven Grain Chemistry in Cold Core Models. The Astrophysical Journal. 2018;861.

[109] Salata C, David M, Mantuano A, Mota C, Pickler A, Rosado PHG, et al. Determination of the Fricke dosimetry chemical yield, G(Fe3 +), for different low- and medium-energy qualities of X-ray beams and gamma sources. Brazilian Journal of Physics. 2024.

[110] d'Entremont A. Considerations for Defining G-Values for Aluminum-Clad Spent Nuclear Fuel. 2024.

[111] Gehringer P. Radiation Processing of Aqueous Systems. 2004.

[112] Kobayashi K, Ise J, Aoki R, Kinoshita M, Naito K, Udo T, et al. Formation of amino acids and carboxylic acids in weakly reducing planetary atmospheres by solar energetic particles from the young sun. Life. 2023;13.

[113] Charlesby A. Introduction to radiation chemistry: J.W.T. Spinks and R.J. Woods. Wiley-Interscience, New York. 1990. xii + 574 pp. 1990.

[114] Shingledecker C, Herbst E. A general method for the inclusion of radiation chemistry in astrochemical models. Physical chemistry chemical physics : PCCP. 2018;20 8:5359-67.

[115] Bian J, Duran J, Shin W, Ramos-Mendez J, Sankey J, Childress L, et al. GEANT4-DNA simulation of temperature-dependent and pH-dependent yields of chemical radiolytic species. Physics in medicine and biology. 2023;68.

[116] Souza-Corrêa JA, da Costa CAP, da Silveira EF. Compaction and Destruction Cross-Sections for α-Glycine from Radiolysis Process via 1.0 keV Electron Beam as a Function of Temperature. Astrobiology. 2019.

[117] Freitas FM, Pilling S. Experimental Simulation Of Fast Electron Bombardment Of Methanol Ice And Its Implications In Astrochemistry. Revista Univap. 2023.

[118] Gerakines P, Schutte W, Greenberg J, Dishoeck EF. The Infrared Band Strengths of H2O, CO and CO2 in Laboratory Simulations of Astrophysical Ice Mixtures. arXiv: Astrophysics. 1994.

[119] Pilling S, Duarte ES, Domaracka A, Rothard H, Boduch P, Silveira ÊF. Radiolysis of H2O:CO2 ices by heavy energetic cosmic ray analogs. Astronomy & Astrophysics. 2010;523.

[120] Mifsud D, Kaňuchová Z, Herczku P, Ioppolo S, Juhász Z, Kovács S, et al. Sulfur Ice Astrochemistry: A Review of Laboratory Studies. Space Science Reviews. 2021;217.

[121] Gerakines PA, Schutte WA, Greenberg JM, van Dishoeck EF. The infrared band strengths of H2O, CO and CO2 in laboratory simulations of astrophysical ice mixtures. Astronomy & Astrophysics. 1995.

[122] Gerakines P, Materese C, Hudson RL. Establishing an Accurate Infrared Band Strength for the Cyanate Ion in Interstellar Ices. Monthly Notices of the Royal Astronomical Society. 2025.

[123] Team ES. Europa Study 2012 Report: Europa Lander Mission. Jet Propulsion Laboratory Report. 2012.

[124] Loerting T, Bauer M, Kohl I, Watschinger K, Winkel K, Mayer E. Cryoflotation: densities of amorphous and crystalline ices. The journal of physical chemistry B. 2011;115 48:14167-75.

[125] Jones BM, Bennett CJ, Kaiser RI. Mechanistical Studies On The Production Of Formamide (H2NCHO) Within Interstellar Ice Analogs. The Astrophysical Journal. 2011.

[126] Dulieu F, Nguyen T, Congiu E, Baouche S, Taquet V. Efficient formation route of the prebiotic molecule formamide on interstellar dust grains. Monthly Notices of the Royal Astronomical Society: Letters. 2019.

[127] Rimola A, Skouteris D, Balucani N, Ceccarelli C, Enrique-Romero J, Taquet V, et al. Can Formamide Be Formed on Interstellar Ice? An Atomistic Perspective. ACS Earth and Space Chemistry. 2018.

Chapter 4

Methodology and Experimental Apparatus

4.1 Experimental Apparatus and Irradiation Facilities

To aid the reader in navigating the wide range of experimental conditions and equipment configurations used throughout this work, Table 4.1 summarises the key parameters of each irradiation facility. The remainder of this Chapter is dedicated to describing the experimental apparatus and techniques in detail - including chamber configurations, ice preparation methods, radiation sources, and diagnostics - as used across the various facilities.

The parameters listed in Table 4.1 were chosen to balance astrophysical relevance with laboratory constraints. A sample temperature of 90 K was selected to approximate the mean surface temperature of Europa, ensuring consistency with conditions expected on icy bodies in the outer Solar System. Ice thicknesses were targeted in the range of 200-300 nm to achieve complete energy deposition for O^{2+} and S^{5+} projectiles while minimising spectral saturation in the Fourier-transform infrared (FTIR). However, at this thickness, 15 keV protons penetrated beyond the film and therefore deposited only part of their energy. The adopted 50:50 formamide-water ratio allowed for a controlled analogue mixture while acknowledging minor deviations introduced by the incremental background-dosing procedure. Finally, the different irradiation sources (ions, electrons, and VUV photons) reflect the dominant components of Europa's radiation environment. However, direct comparison is limited by their differing modes of energy deposition: ions and electrons primarily dissipate energy through collision cascades and secondary electron production, whereas VUV photons interact via electronic excitation over the full film depth.

Table 4.1: Combined experimental irradiation conditions for formamide-water ices across ion, electron, and photon experiments. Energies are listed with native units (keV for ions/electrons, eV for photons). Dashes indicate not applicable or not reported.

Irradiation Type	Species	Window	Energy	Ice Comp.[a]	Ice Thick. (nm)[b]	Temp. (K)	Fluence (cm^{-2})	Set
Ion	H^+	NaCl	15 keV	52:48	237	90	1.10×10^{16}	-
	O^{2+}		30 keV	45:55	223	90	1.92×10^{15}	-
	S^{5+}		60 keV	49.6:50.3	226	90	9.65×10^{14}	-
	H^+	ZnSe	15 keV	46:54	278	90	1.94×10^{17}	-
	O^{2+}		30 keV	47:53	210	90	3.16×10^{15}	-
	S^{5+}		60 keV	47:53	222	90	1.08×10^{15}	-
Electron	e^-	NaCl	2 keV	12:88	587	90	3.37×10^{19}	-
	e^-	ZnSe	2 keV	8:92	225	90	3.37×10^{19}	-
Photon	$h\nu$	NaCl	9 eV	-	99.58	10	$(2.4 \pm 1.3) \times 10^{19}$	Run 1
					75.71	50	$(2.4 \pm 1.3) \times 10^{19}$	Run 1
					57.26	90	$(2.4 \pm 1.3) \times 10^{19}$	Run 1
					225.80	10	$(2.4 \pm 1.3) \times 10^{19}$	Run 2
					58.12	50	$(2.4 \pm 1.3) \times 10^{19}$	Run 2
					77.84	90	$(2.4 \pm 1.3) \times 10^{19}$	Run 2
					30.73	110	$(2.4 \pm 1.3) \times 10^{19}$	Run 2
					40.05	130	$(2.4 \pm 1.3) \times 10^{19}$	Run 2

[a] Molar ratio of formamide to water.

[b] Typical systematic uncertainties: composition ∼15% per component; ion/electron thickness ∼40-50%. Photon-irradiation ice thicknesses are estimates derived from dosing/attenuation metrics. A dash (-) indicates not applicable or not reported.

Accordingly, the experimental campaigns described in this chapter target Europa-relevant surface conditions (cryogenic temperatures, high vacuum, and irradiation by ions, electrons, and VUV photons), as summarised in Table 4.1. The following sections describe the chamber configurations, ice preparation procedures, irradiation sources, and diagnostics used at each facility.

4.2 ECRIS at AQUILA

The Atomki facility in Debrecen, Hungary, is home to the ECRIS laboratory and the Atomki-Queen's University Ice Laboratory for Astrochemistry (AQUILA). Established in 1996, the ECR Ion Source (ECRIS) is used primarily to investigate the effects of ion irradiation on astrophysical ice analogues. The AQUILA facility (commissioned in 2023) includes a chamber for growing ice analogues at cryogenic temperatures, see Figure 4.1. These ices are then irradiated with ions, and the resulting changes in their chemistry and physics are analysed using mid-infrared spectroscopy. In this project, the facility was used to simulate radiation conditions similar to those on Europa, in particular, the ions incident on Europa's surface.

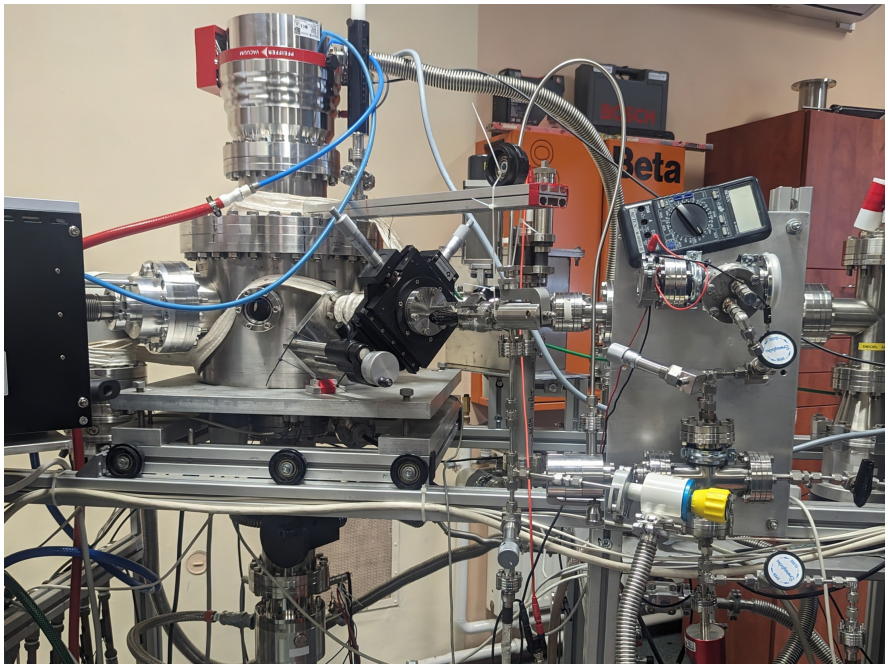


Figure 4.1: Image of the ECRIS system in the AQUILA laboratory.

ECRIS can generate ion beams from a wide variety of materials by employing methods such as sputtering, evaporation, and the MIVOC (Metal Ions from Volatile

Compounds) technique. H^+, O^{2+}, and S^{5+} are among the most abundant ions that bombard the surface of Europa [1, 2], as discussed in Section 2.3.1 and illustrated in Figure 2.10. Therefore, in this chamber, specifically, the effects of H^+, O^{2+}, and S^{5+} irradiation of formamide-water ice, as a potential prebiotic analogue of the Europan ocean, were explored.

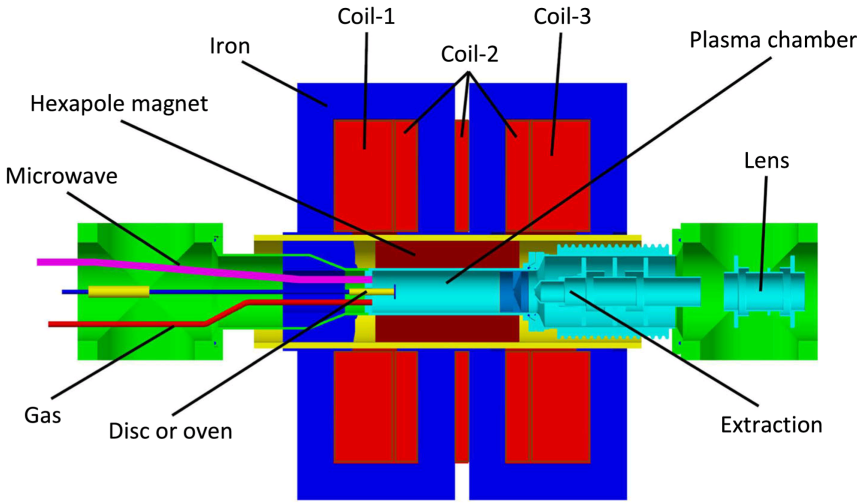


Figure 4.2: A drawing of the cross-section of the Atomki-ECRIS. **Credit:** Reproduced from Biri et al. (2021), Fig. 3 [3], CC BY 4.0.

The ECR ion source generates ions by heating plasma with 14 GHz microwaves, confined within a hexapole magnetic trap and solenoidal coils (Figure 4.2). Neutral gas is injected into the chamber, where collisions with energetic electrons ionise the atoms. The ions are then extracted electrostatically, focused by an einzel lens system, and directed into the beam transport line, to give a beam energy of:

$$E_{beam} = qV_{ext} \tag{4.1}$$

where E_{beam} is the kinetic energy of the ion source (eV), q is the charge-state of the projectile ion, and V_{ext} is the extraction voltage (V). The magnetic trap configuration allows stable production of singly and multiply charged ions relevant to astrophysical irradiation experiments [3]. The facility operates across a broad energy range (50 eV - 900 keV), providing singly and multiply charged ions such as H^+, O^{n+}, and S^{n+}, which are directly relevant to the Jovian environment [3, 4].

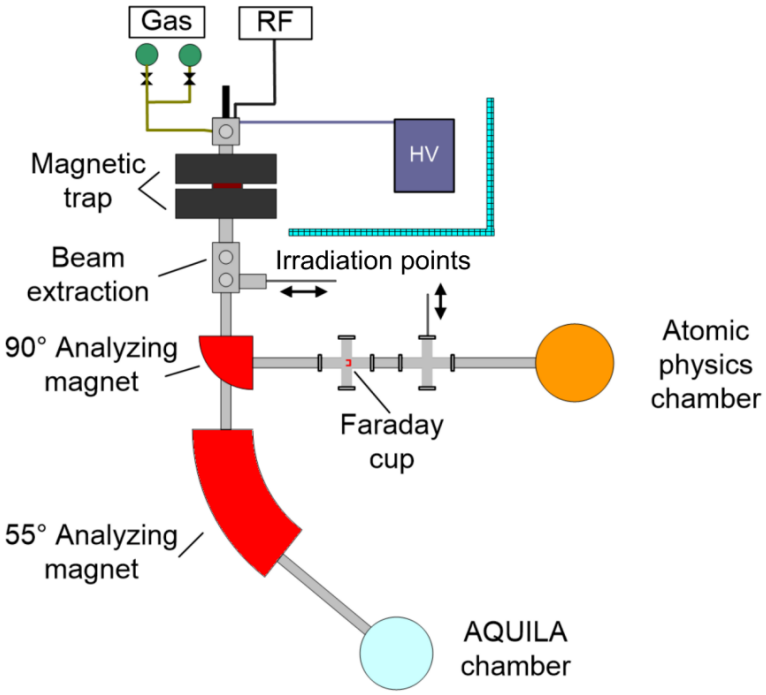


Figure 4.3: A drawing depicting the top-down view of the beamlines from the Atomki ECR ion source. **Credit:** Reprinted from R. Rácz et al., AQUILA: A laboratory facility for the irradiation of astrochemical ice analogs by keV ions, *Rev. Sci. Instrum.* 95, 095105 (2024), with the permission of AIP Publishing, [4].

The ECR ion source feeds into two beamlines (Figure 4.3). The 55° analysing line was used for the present experiments, delivering the beam into the AQUILA cryogenic chamber. The transport line includes bending magnets, collimators, einzel lenses, and deflector plates that together focus, collimate, and steer the beam. These elements ensure that the current density is homogeneous and that the beam spot is well-defined on the ice substrate.

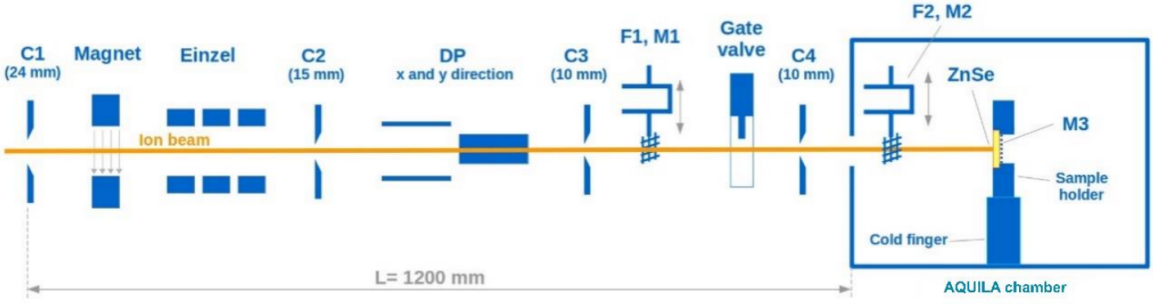


Figure 4.4: Schematic of the ion beam transport line from the 55° bending magnet to the AQUILA chamber. **Credit:** Reprinted from R. Rácz et al., AQUILA: A laboratory facility for the irradiation of astrochemical ice analogs by keV ions, *Rev. Sci. Instrum.* 95, 095105 (2024), with the permission of AIP Publishing, [4].

Diagnostics are provided along the transport line in the form of Faraday cups and

meshes (F1/M1 before the chamber, F2/M2 inside; see Figure 4.4). When inserted, the Faraday cups measure absolute beam current, while meshes transmit ∼90% of the beam, enabling monitoring of the ion beam without interrupting irradiation. Deflector plates upstream allow fine steering in the x-y directions to maintain alignment. These diagnostics ensured reproducibility of fluence and allowed dose control during experiments.

In Figure 4.4, 'F1' and 'M1' represent the Faraday cup and mesh, respectively, situated immediately beyond the third collimator. When the Faraday cup is inserted into the path of the ion beam, the current can be quantitatively determined. After the current has been determined, the mesh is inserted into the ion beam path, allowing for 90% of the beam transmission to minimise the effect of secondary electrons. The actual ultra-high-vacuum (UHV) AQUILA chamber is separated from the beamline vacuum systems by a pneumatic gate valve. In between the gate valve and the entrance to the chamber is a fourth and final collimator - labelled as 'C4' in Figure 4.4 - used to ensure none of the scattered ions irradiate the substrate. Once the beam has finally entered the chamber, there is another Faraday cup and mesh, labelled 'F2' and 'M2' respectively, used to measure the ion beam current and profile within the chamber. These two components behave the same as their earlier counterparts.

The transport line ends at the AQUILA cryogenic chamber, a stainless-steel ultra-high-vacuum (UHV) vessel (Figures 4.4 and 4.5). The chamber is evacuated using a turbomolecular pump backed by a dry scroll pump, with a separate roughing line used for initial pump-down from the atmosphere. Under typical operating conditions, the base pressure reaches $\sim 10^{-9}$ mBar after bake-out, and is maintained in the 10^{-8}-10^{-9} mBar range during ice growth and irradiation. The chamber pressure is monitored using a combination of Pirani and cold-cathode gauges mounted on the main volume. A pneumatic gate valve separates the AQUILA chamber from the upstream beamline vacuum (Figure 4.4), allowing the cryogenic region to be isolated without venting the entire transport line. Immediately downstream of this valve, a fourth and final collimator (C4 in Figure 4.4) defines the ion beam spot at the chamber entrance and reduces scattering onto the chamber walls.

At the centre of the chamber is a copper sample holder mounted on the cold finger of the cryogenic stage (Figure 4.9) onto which the NaCl and ZnSe substrates are fixed. The holder is surrounded by a removable copper heat shield, which reduces radiative heating from the chamber walls and helps to maintain a uniform substrate temperature; both configurations are shown in Figure 4.6. The heat shield also limits line-of-sight deposition onto non-sample surfaces, reducing uneven condensation during irradiation. Multiple optical ports, equipped with ZnSe windows, provide access for the FTIR beam and for the laser interferometry system used to determine ice thickness (Section 4.3.4). A top-down schematic of the chamber layout, including the ion beam, IR beam path, and sample holder geometry, is shown in Figure 4.5.

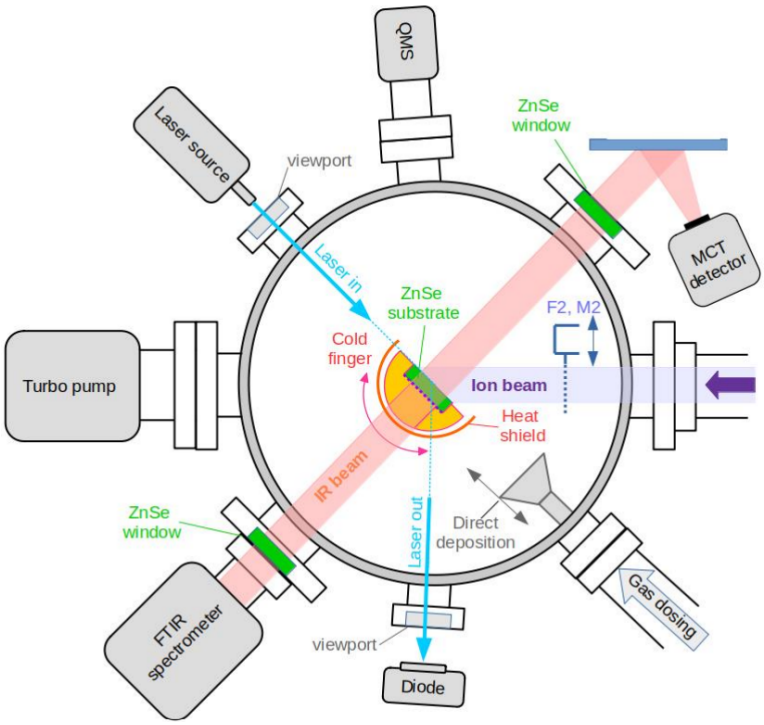
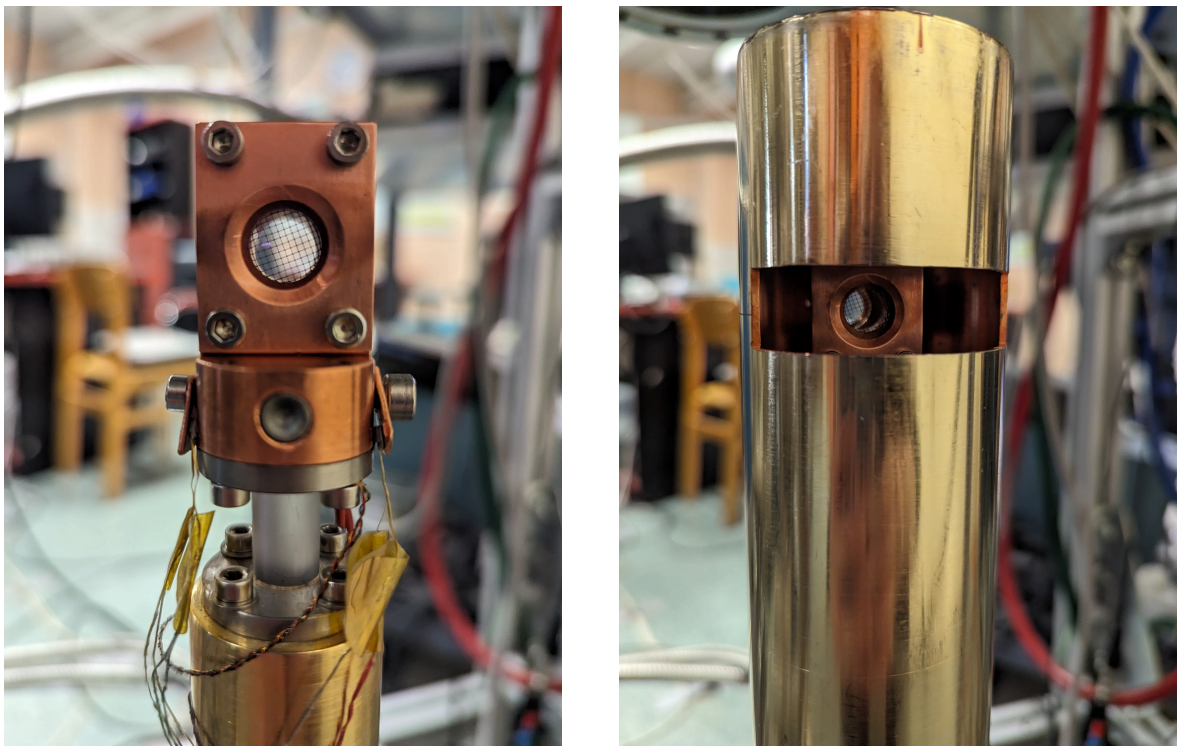


Figure 4.5: A top-down schematic of the AQUILA chamber, arranged for transmission absorption mid-infrared spectroscopy. Its rotatable sample holder and heat shielding facilitate ion beam irradiation, with the infrared beam aligned orthogonally to the deposition surface. When rotated, the sample holder also allows for laser interferometry[1] to measure ice thickness by reflecting the incident laser beam into the photodiode. **Credit:** Reprinted from R. Rácz et al., AQUILA: A laboratory facility for the irradiation of astrochemical ice analogs by keV ions, *Rev. Sci. Instrum.* 95, 095105 (2024), with the permission of AIP Publishing, [4].

Inside the AQUILA chamber itself (Figure 4.5), samples were grown on either NaCl or ZnSe substrates mounted on a cold finger cooled to ∼90 K. Ices were deposited via

[1]Multiple optical ports, equipped with ZnSe windows, provide access for the FTIR beam and for the laser interferometry system used to determine ice thickness (Section 4.2.1).

background dosing, forming films of order 200-300 nm in thickness, a range determined from FTIR band integrals (Equation 4.2) and chosen to ensure full energy deposition by O^{2+} and S^{5+} ions whilst avoiding spectral saturation, as established from SRIM penetration depth simulations (see Section 5.1). Here, 'background deposition' refers to admitting the gaseous formamide-water vapour mixture - produced by heating liquid formamide and water to generate sufficient vapour pressure for controlled dosing - into the main chamber volume so that molecules condense from the isotropic background vapour onto all line-of-sight surfaces. This approach ensured that the molecules mixed homogeneously, rather than forming distinct layers. In contrast, "direct deposition" refers to a collimated gas inlet aimed directly at the substrate, producing a more localised flux and preferential growth on the front surface. The chamber is maintained under ultra-high vacuum conditions (10^{-8}-10^{-9} mbar) and has multiple optical ports, including ZnSe windows for Fourier transform infrared spectroscopy (FTIR). This geometry enables in-situ spectroscopic monitoring: the ion beam bombards the ice, and at selected fluence steps, the ion beam is temporarily interrupted while the IR beam passes through the sample, allowing vibrational changes to be followed throughout the irradiation sequence.



(a) **(b)**

Figure 4.6: Images of the sample holder with a NaCl window mounted. **(a)** is the sample holder outside of the cryogenic chamber, and **(b)** is the sample holder outside of the cryogenic chamber with its heat shield cover.

4.2.1 FTIR Spectroscopy and Ice Thickness Determination

At the Atomki-ECRIS facility, Fourier Transform Infrared Spectroscopy (FTIR) was employed as an in-situ tool to monitor molecular changes during ion-surface interactions. FTIR monitors changes in the deposited ice during ion irradiation by tracking the growth and decay of specific vibrational bands as a function of fluence, providing detailed information on chemical groups and bonding structures, and allowing the underlying reaction dynamics to be inferred (see Section 3.1.1.1). This enabled real-time observation of the destruction of formamide and the appearance of radiolysis products during irradiation.

The AQUILA setup is equipped with a Bruker Vertex V70v spectrophotometer, which allows for IR spectra to be recorded over the range 4000-650 cm^{-1}. For these experiments, spectra were acquired at a resolution of 1 cm^{-1}. Although the spectrometer is capable of 0.1 cm^{-1} resolution, the vibrational bands of amorphous formamide-water ices are broad (tens of cm^{-1}), so finer resolution would not significantly change

the integrated band areas used here, while increasing acquisition time and reducing the signal-to-noise ratio.

Ice thickness was determined from FTIR spectra by converting integrated band absorbances into column densities using an integrated form of the Beer-Lambert law:

$$\begin{aligned} N &= ln(10)\frac{S}{A_\nu} \\ d &= 10^4\frac{m}{\rho N_A} \\ &= 10^4 ln(10)\frac{mS}{\rho N_A A_\nu} \end{aligned} \tag{4.2}$$

where, N is the column density (molecules cm^{-2}), S is the integrated absorbance of a known band (cm^{-1}), A_ν is the band strength (cm molecule^{-1}), m is the molar mass (g mol^{-1}), ρ is the density of the ice (g cm^{-3}), and N_A is Avogadro's constant (6.02×10^{23} mol^{-1}). In the case of mixed formamide-water ices, the thickness was approximated by applying the last calculation in Equation 4.2 to each component separately and then averaging the results. The method is subject to large uncertainties, potentially up to 50% [5, 6], primarily due to uncertainties in band strengths and assumptions about mixture density. This reflects a combination of factors: (i) band strengths for formamide and for mixed ices are only known to within ∼20-30%, (ii) the density of the amorphous mixture is not precisely constrained and must be approximated from pure-component values, (iii) baseline placement and integration limits for the IR bands introduce additional systematic errors, especially in thin films with fringes and overlapping water features, and (iv) a further ∼10% correction is applied to account for ice deposited on the rear face of the substrate during background dosing. Taken together in quadrature, these contributions lead to an overall thickness uncertainty of order 40-50%.

In the ion irradiation experiments, penetration depths were quantified using SRIM[2] for 15 keV H^+, 30 keV O^{2+}, and 60 keV S^{5+} in a 50:50 formamide-water ice, assuming a bulk density of ∼0.94 g cm^{-3}. The SRIM simulations yielded maximum projected

[2]SRIM, "Stopping and Range of Ions in Matter", is a software package primarily used to calculate the interactions of ions with matter [7].

ranges of ∼200 nm for O^{2+} and S^{5+}, and ∼390-400 nm for H^+ in the mixed ice. When compared with the experimental film thicknesses (200-300 nm; Table 4.2), this implies that O^{2+} and S^{5+} deposit essentially all of their kinetic energy within the ice layer, whereas 15 keV protons partially transmit through the film and therefore deposit only a fraction of their energy. The chosen thickness range thus represents a compromise: sufficiently thick to capture the full energy deposition of the heavier ions, while avoiding the much larger thicknesses required to fully stop H^+, which would have led to severe FTIR spectral saturation and loss of quantitative accuracy.

The ice thicknesses were estimated using the ∼3.0 μm (∼3,333 cm^{-1}) IR peak after subtracting a straight baseline. To obtain realistic error bars, the area measurement was recalculated with the baseline windows offset. It included the effect of random noise in a quiet part of the spectrum, which provides the data-driven component of the uncertainty. To quantify the systematic uncertainty from reasonable baseline placement in thin-film IR spectra, where shallow background slopes, fringes, and broad band wings bias the 3 μm area, the baseline windows were deliberately shifted ($\pm$50 cm^{-1}) and the spread of re-integrated areas was taken as the baseline-selection error. Finally, the two small "known unknowns" from the literature, [4] - a ∼10% uncertainty in the peak's band strength and a ∼0.16% uncertainty in the ice density - were all combined to give the final error.

The thickness determination in AQUILA relies on the same basic principle as standard two-beam optical interferometry. Light from a coherent source is split into a reference arm and a measurement arm, reflected from a reference surface and the sample, and then recombined. Differences in optical path length between the two arms generate bright and dark interference fringes (Figure 4.7). Each fringe corresponds to a change of approximately $\lambda/2$ in the optical path, so counting fringes during ice growth provides a direct measure of the increase in film thickness.

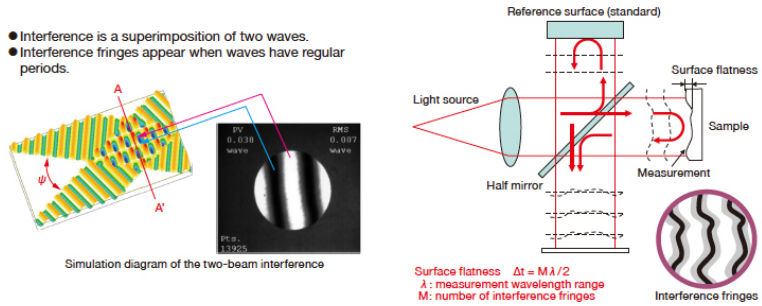


Figure 4.7: Schematic illustration of two-beam optical interferometry. A reference surface and a sample surface form an interferometer, and the superposition of the reflected beams produces interference fringes whose spacing encodes differences in optical path length. **Credit:** Reproduced with permission from OptoSigma, 'Principle of Interferometer', [8]

In addition to the band-strength method, the AQUILA chamber is equipped with a laser interferometry system that provides an independent, in-situ measure of ice thickness. A collimated laser beam (He-Ne, $\lambda = 632.8$ nm) is directed through one of the ZnSe viewports onto the substrate at near-normal incidence. As the ice grows on the substrate, reflections from the vacuum-ice and ice-substrate interfaces interfere, producing an oscillatory intensity pattern (interference fringes) in the reflected beam, which is detected by a photodiode mounted on the opposite viewport.

The thickness d of the ice layer is related to the number of fringes N observed during deposition by:

$$d = \frac{N\lambda}{2n\cos\theta}, \tag{4.3}$$

where λ is the laser wavelength, n is the fundamental part of the refractive index of the ice at λ, and θ is the incidence angle (here $\theta \approx 0$). Assuming a constant n for a given composition, each full fringe corresponds to an increment of $\lambda/(2n)$ in film thickness. In the experiments presented in this thesis, the interferometry data were used as a consistency check on FTIR-derived thicknesses, confirming that the target range of 200-300 nm was achieved within the quoted uncertainties.

4.2.2 Experimental Methodology

For irradiation experiments, cryogenic ices were deposited on NaCl and ZnSe windows (15 × 3 mm, Crystran). NaCl was selected because chloride-bearing salts are thought to be present on Europa's surface and in its subsurface ocean, making NaCl a plausible

analogue material for Europan surface composition (see Section 2.3.1). In particular, spectral observations and modelling suggest that irradiated chloride salts may contribute to the non-ice components on Europa's trailing hemisphere, consistent with exchange between a salty ocean and the surface [9, 10]. Using NaCl as the substrate, therefore, allows us to test whether a reactive, halide-rich surface can modify the radiolysis chemistry of the overlying formamide-water ice. ZnSe, by contrast, was chosen as an IR-transparent but chemically more inert substrate, providing a reference case in which the underlying surface is not expected to participate strongly in the chemistry. Any systematic differences between NaCl- and ZnSe-supported ices can therefore be interpreted as substrate-driven effects, thereby isolating the role of a Europan-like salty surface. After mounting the substrates on the sample holder, the chamber was pumped down to a pressure of 10^{-8}–10^{-9} mBar and cooled to 90 K.

Formamide-water ices were prepared by background deposition at 90 K. This meant the molecules mixed homogeneously as opposed to creating distinct layers. Figure 4.8 shows typical post-irradiation residues on NaCl and ZnSe windows. To avoid cross-contamination, windows were replaced between irradiation experiments.



(a) **(b)**

Figure 4.8: Post-irradiation photographs of the substrates, showing residual deposits on (**a**) a NaCl window and (**b**) a ZnSe window. Each substrate was replaced between experiments to avoid contamination from prior runs.

Inside the chamber, samples were mounted on a rotatable cold finger, as shown in Figure 4.6. Panel (a) shows the cold finger inside the chamber, while panel (b)

shows the deposition needle aligned with the substrate for ice growth. Background deposition results in ice coating both the front and rear sides of the substrate. Only the front side was exposed to irradiation, while the rear contributed to the apparent FTIR absorbance. To correct for this, column densities were adjusted downward by ∼10% to account for back-surface ice. This correction factor is based on the assumption that, under background deposition conditions, the rear face of the substrate receives a smaller flux than the front face due to partial shadowing by the mounting hardware and asymmetric gas flow dynamics within the chamber; a 10% contribution from the rear surface is a standard conservative estimate adopted in laboratory astrochemistry studies using this geometry [4].

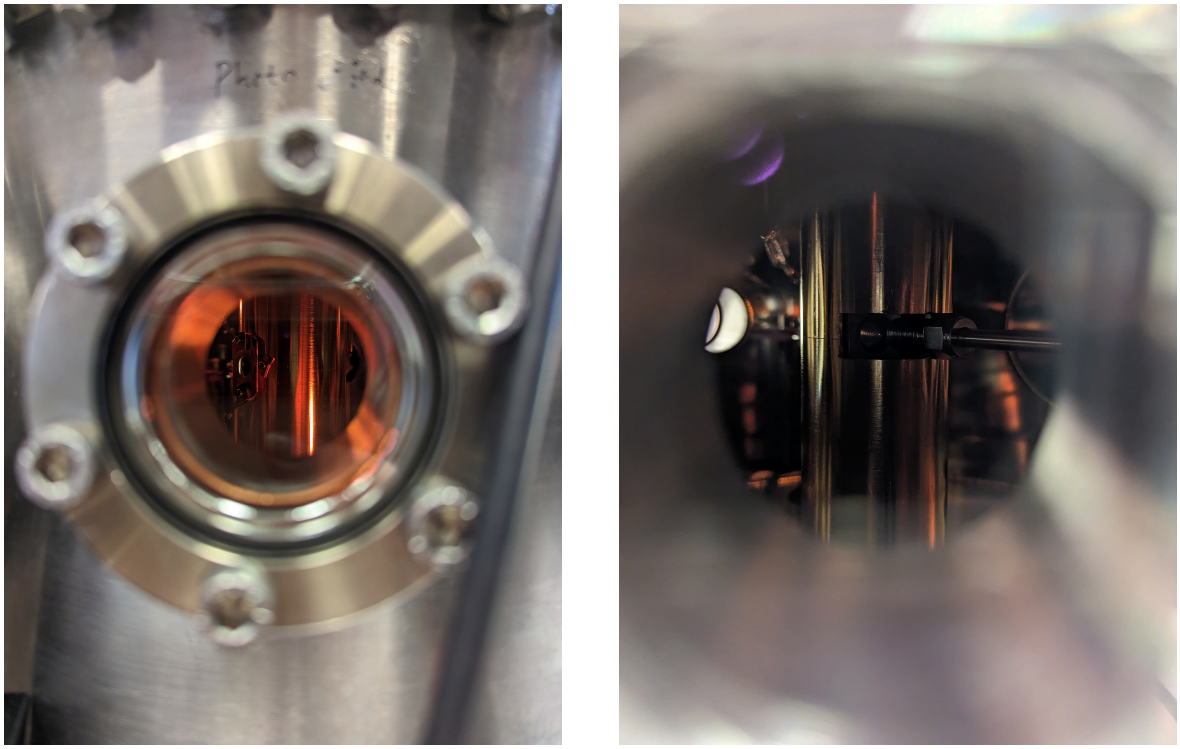
Deposition thickness was monitored in real time by observing the pressure rise within the chamber during dosing and by timing the duration for which the deposition needle was open. This provided a qualitative check that the gas flux and deposition conditions were consistent between runs. However, chamber pressure alone is only an approximate proxy for deposited thickness, as it depends on factors such as the molecules' sticking coefficient, local gas flow dynamics, and pumping speed. Consequently, the ice thicknesses reported in this work were derived from FTIR band integrals using Equation 4.2, with pressure monitoring serving only as a guide during deposition rather than as a primary thickness calibration.

To illustrate the consistency between the FTIR-derived thicknesses and the background-pressure estimate, one representative ion-irradiation run was analysed using both methods. For the 30 keV O^{2+} experiment on a NaCl substrate (Table 4.2), the FTIR band-strength method (Equation 4.2) was applied to the 3.0 μm OH-stretch band to obtain a column density N_{FTIR} and corresponding film thickness $d_{\mathrm{FTIR}} \approx 220$ nm. Independently, the average background pressure during dosing, P, together with the gas temperature T and the dosing time t, was inserted into the kinetic-theory expression for the molecular flux:

$$F = \frac{P}{\sqrt{2\pi m k_{\mathrm{B}} T}},$$

This is assuming a sticking coefficient of unity. The resulting column density $N_P = Ft$ was converted to a thickness $d_P = N_P m/(\rho N_{\mathrm{A}})$, giving $d_P \approx 250$ nm for the same run.

Given the uncertainties in P, the sticking coefficient, the mixture density, and the IR band strength, the agreement between d_{FTIR} and d_P is well within the expected 40-50% error. On this basis, FTIR-derived thicknesses are adopted as the primary values reported in this thesis, with pressure-based estimates serving only as a qualitative cross-check on deposition reproducibility between runs.



(a) **(b)**

Figure 4.9: Cold finger and substrate inside the cryogenic chamber. **(a)** shows the cold finger with mounted substrate as viewed through a window; **(b)** shows the cold finger with deposition needle aligned for background dosing of the formamide-water ice.

During irradiation, samples were exposed in a series of fluence steps: the ion beam was applied for a fixed interval, then temporarily switched off while an FTIR spectrum was recorded. Irradiation was continued until the integrated areas of the diagnostic formamide bands no longer decreased significantly with further fluence, i.e. their destruction curves reached a plateau within the experimental uncertainty. Spectra were recorded at each fluence step to monitor the chemical evolution throughout the irradiation sequence. Table 4.2 summarises the experimental parameters.

The ice compositions listed in Table 4.2 were derived from the pre-irradiation FTIR spectra. Diagnostic bands for water and formamide were integrated and converted to

Table 4.2: Experimental parameters for ion irradiation of cryogenic formamide-water ices on NaCl and ZnSe windows at 90 K. Ice composition is given as the molar ratio of formamide to water. Energies correspond to the incident ion kinetic energy delivered by the Atomki-ECRIS.

Ion	Window	Energy (keV)	Ice Comp.[a]	Ice Thick. (nm)	Temp. (K)	Fluence (cm^{-2})
H^+		15	52:48	237 ± 30	90	1.10×10^{16}
O^{2+}	NaCl	30	45:55	223 ± 28	90	1.92×10^{15}
S^{5+}		60	49.6:50.3	226 ± 28	90	9.65×10^{14}
H^+		15	46:54	278 ± 29	90	1.94×10^{17}
O^{2+}	ZnSe	30	47:53	210 ± 23	90	3.16×10^{15}
S^{5+}		60	47:53	222 ± 24	90	1.08×10^{15}

[a] Molar ratio of formamide to water.

column densities using the band-strength method in Equation 4.2. For each experiment, the molar fraction of formamide was then calculated as:

$$R_{\mathrm{FA}} = \frac{N_{\mathrm{FA}}}{N_{\mathrm{FA}} + N_{\mathrm{H_2O}}}, \tag{4.4}$$

Where N_{FA} and $N_{\mathrm{H_2O}}$ are the column densities of formamide and water, respectively. The resulting R_{FA} values are reported in Table 4.2 as two-component proportions ("xx:yy", FA:H_2O), rounded to the nearest integer.

The primary sources of uncertainty in these ratios are the adopted band strengths for formamide and water, baseline placement and band overlap in the 3 μm region, and the assumption that pure-ice densities are representative of the mixed formamide-water films. These effects introduce non-negligible uncertainties in the absolute column densities, but several systematic contributions cancel when forming the FA:H_2O ratio. For this reason, explicit error bars are not quoted on the compositions in Table 4.2; the ratios should be interpreted as approximately 50:50 mixtures with small run-to-run deviations, sufficient for the comparative analysis presented in 4.

Finally, after irradiation, temperature-programmed desorption (TPD) runs were performed. The sample holder was heated using a resistive heater element mounted on the cryogenic cold finger and controlled by a feedback temperature controller. The temperature was ramped at 5 K min^{-1}, and at every 30 K interval the ramp was paused to allow the substrate temperature to stabilise before acquiring an FTIR spectrum. These TPD measurements provided qualitative information on the desorption behaviour of

volatile products, but were not used in the subsequent quantitative analysis.

Monitoring Spectral Changes with Fluence

To track the chemical evolution of the irradiated ices, FTIR spectra were acquired at incremental fluence steps during ion and electron experiments. As irradiation progressed, changes in the area under key vibrational bands were monitored to assess the destruction of initial molecular species and the formation of new products.

When the signal-to-noise ratio permitted, the integrated absorbance of selected bands was measured as a function of fluence. This approach enabled semi-quantitative tracking of species abundance. For instance, the gradual decrease in the C=O stretching band of formamide with increasing fluence indicated progressive molecular degradation. In contrast, the emergence and growth of new bands (e.g. associated with isocyanic acid or other photoproducts) reflected reaction pathways triggered by energy deposition.

Where full integration was not feasible, relative peak intensities were compared qualitatively between fluence steps. This method, although less precise, still provided valuable insight into the fluence-dependent chemistry occurring within the ice.

4.3 NSRRC Synchrotron (TLS)

The Taiwan Light Source (TLS) is a third-generation synchrotron light source located at the National Synchrotron Radiation Research Centre (NSRRC) in Hsinchu, Taiwan. It was one of the first facilities of its kind in Asia, beginning operations in 1994. The TLS operates with a beam energy of 1.5 GeV and has a 120-meter circumference storage ring. It is primarily used to produce intense beams of ultraviolet (UV) and soft X-ray radiation, which are crucial for research in various fields, including physics, materials science, and biology.

The facility features about 22 beamlines that support numerous experimental techniques, including X-ray absorption spectroscopy, protein crystallography, and nanostructure analysis. Researchers utilise the TLS for advanced studies on materials,

biomolecules, and chemical reactions, among other topics. The TLS's complementary resource, the Taiwan Photon Source (TPS), provides higher-energy X-rays, expanding the scope of research even further into areas such as biomedical and nanotechnology research [11–13].

4.3.1 U90 Endstation (Electron Irradiation)

The U90 endstation at the Taiwan Light Source (TLS, NSRRC) was used to simulate the bombardment of Europa's surface by magnetospheric electrons (see Section 3.2.1.2). Electrons form a significant component of Jupiter's radiation environment and contribute significantly to the surface dose on Europa [14, 15]. Laboratory irradiation with electrons, therefore, complements the ion-irradiation experiments at AQUILA, allowing a systematic comparison of how high-LET heavy ions and low-LET electrons affect the chemistry of formamide-water ices.

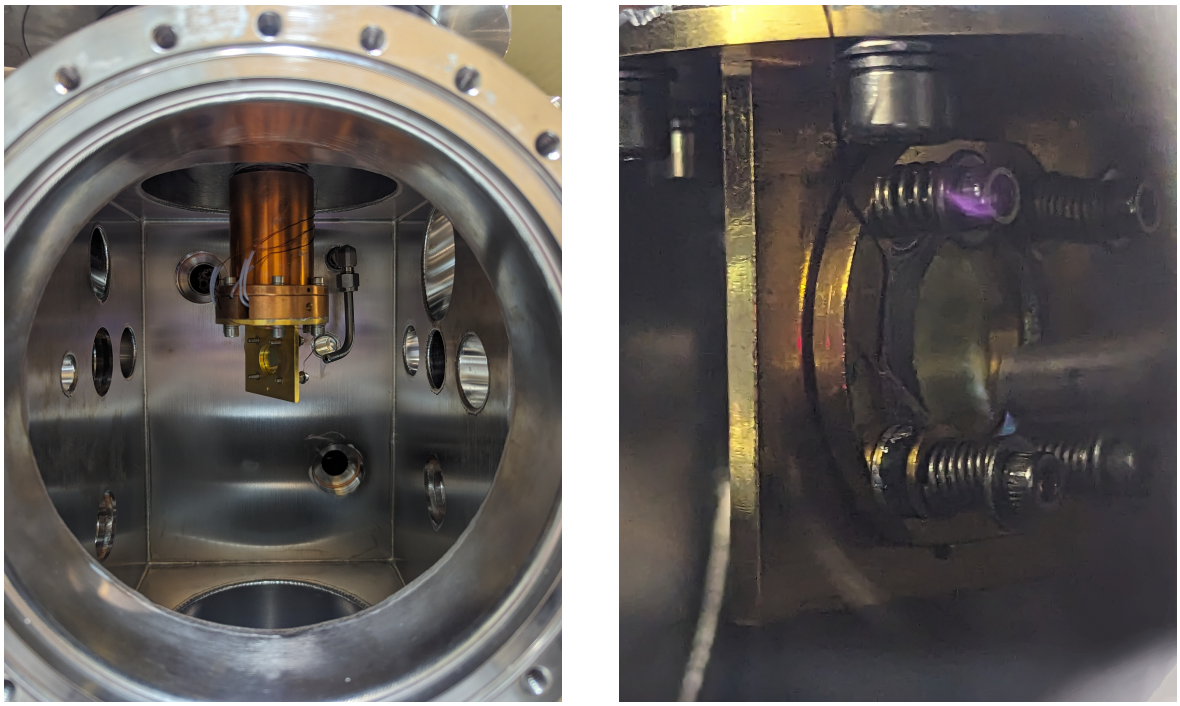
The U90 chamber, an ultra-high-vacuum (UHV) system referred to as the 'Electron-Bombardment Matrix Isolation Endstation', is designed for astrochemistry experiments [16, 17]. Whilst the U90 endstation is part of the 03A1 beamline[3], the electron irradiation is conducted using a dedicated chamber that does not use the synchrotron light of the TLS: instead the endstation uses an internal electron gun for electron irradiation.

The U90 endstation chamber houses a closed-cycle helium cryostat capable of reaching temperatures as low as ∼3-4 K, though samples were maintained at 90 K to reproduce Europa-like surface temperatures. NaCl and ZnSe windows (25 mm diameter, 2 mm thickness, Crystran) were mounted on the cryostat cold head. The chamber base pressure was typically 10^{-7}-10^{-8} Torr, maintained using turbomolecular pumps backed by dry pumps. A rotatable sample holder allowed the substrate to be positioned alternately for irradiation or infrared analysis without breaking the vacuum.

Electron irradiation was performed using a Kimball Physics EFG-7 electron gun, capable of delivering electrons in the few-hundred eV to keV range [19]. For these experiments, a beam of 2 keV electrons was directed at the ice samples, representing the

[3]The 03A1 beamline is a high-flux, high resolution beamline that hosts photons of energies ranging from 4-40 eV, [18].

low-energy secondary electrons and magnetospheric electrons most relevant to Europa's surface [20]. The source is a thermionic emitter with integrated electrostatic optics and deflection plates, enabling beam focusing to a mm-scale spot and precise steering onto the sample substrate. Beam stability and flux were monitored with a Faraday cup located at the entrance of the chamber.



(a) **(b)**

Figure 4.10: Images of the U90 station where **(a)** is the sample holder inside the chamber, and **(b)** is an image taken through a window of the deposition needle pointed at the sample holder.

4.3.2 FTIR and Ice Thickness Determination

Ices were grown by background deposition of a 50:50 formamide-water mixture at 90 K. Deposition thicknesses were first estimated in real time from chamber pressure changes and dosing times, and subsequently refined from IR spectra (see Section 4.2.1). The FTIR system coupled to U90 is a Bomem DA8 spectrometer, covering 4300-700 cm^{-1} [21], with a working resolution of 1 cm^{-1}. Due to interference from secondary radiation produced by the electron beam (UV, X-rays), spectra could only be collected before and after irradiation, rather than continuously. For each run, the initial ice thickness was obtained from the integrated 3.0 μm OH-stretch band using the band-strength

method:

$$N_0 = \ln(10)\,\frac{S_0}{A_\nu}, \qquad d = 10^4\,\frac{mN_0}{\rho N_\mathrm{A}}, \tag{4.5}$$

Where S_0 is the pre-irradiation band area, A_ν the adopted band strength, m the molar mass, ρ the ice density, and N_A Avogadro's constant (cf. Equation 4.2). After irradiation to a total fluence F, the post-irradiation spectrum provided a final column density $N(F)$, from which the destruction efficiency was defined as:

$$D(F) = 1 - \frac{N(F)}{N_0}. \tag{4.6}$$

Since only pre- and post-irradiation spectra were available at U90, $D(F)$ could be determined at the final fluence for each experiment. Hence, full G-values and dose-dependent survivabilities could not be derived for the electron runs.

Monte-Carlo simulations with CASINO v3.3[4] [22], predicted an effective stopping range of ∼179 nm for two keV electrons in 50:50 formamide-water ice (ρ = 0.9355 g cm^{-3}). The ZnSe-supported film (183 ± 19 nm) closely matched this target, ensuring near-complete energy deposition. In contrast, the NaCl-supported film was thicker (420 ± 44 nm), spreading the energy deposition over a larger column. This discrepancy arose from an operational issue during dosing, in which an initial under-deposition of formamide was corrected by extended dosing, leading to excess thickness. Differences in behaviour between the two substrates, therefore, reflect both thickness effects and substrate chemistry.

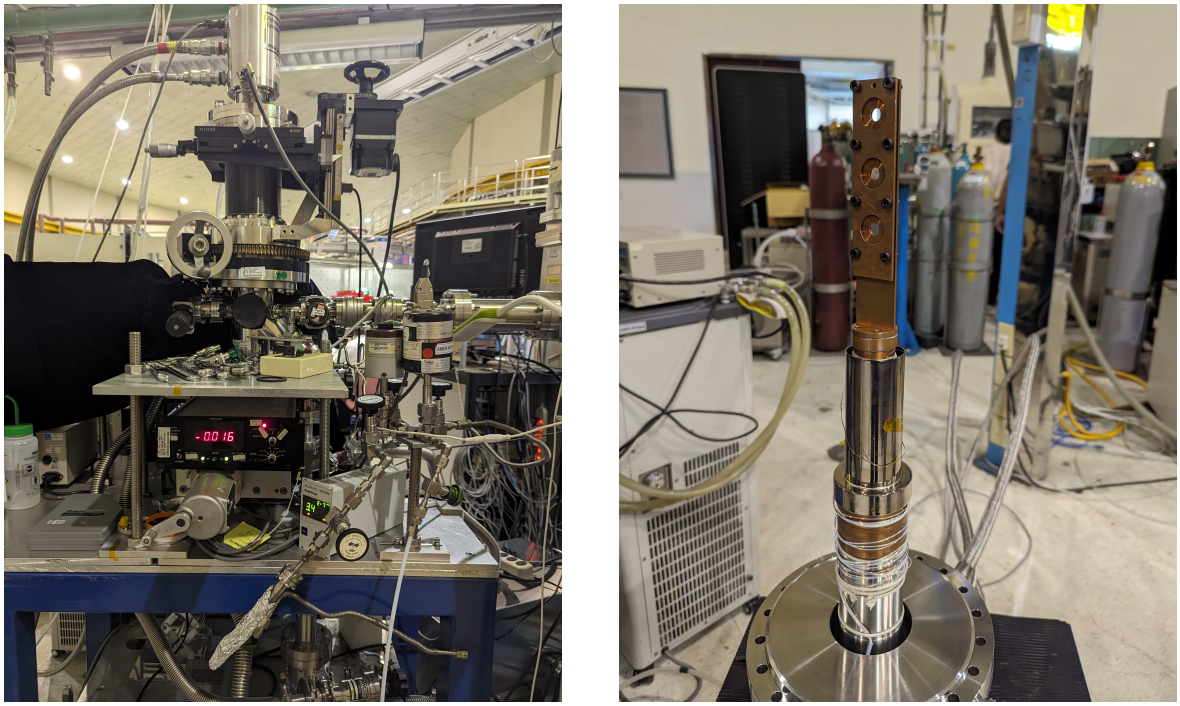
Table 4.3: Summary of electron irradiation experiments (2 keV) through NaCl and ZnSe windows. All runs were performed at 90 K. Total fluence and ice thickness values are also provided.

Window	Irradiation Type	Energy (keV)	Temp. (K)	Ice Thick. (nm)	Fluence (cm^{-2})
NaCl	Electron	2	90	420 ± 44	3.37×10^{19}
ZnSe	Electron	2	90	183 ± 19	3.37×10^{19}

[4]CASINO ("monte CArlo SImulation of electroN trajectory in sOlids") is a Monte-Carlo code for electron transport and energy-deposition in solids, [22]

4.3.3 BL03 Endstation (VUV Irradiation)

At the TLS, a series of experiments were conducted that allowed for the Vacuum-ultraviolet (VUV) "white light" irradiation of a Europan ocean analogue. The BL03 endstation, shown in Figure 4.11, was built for the purpose of inducing and monitoring the photochemistry of solids/ices under UHV conditions. At the end station, VUV irradiation was used to simulate the effects of magnetospheric photons on an Europan ocean analogue. A mixture of formamide-water ice was deposited onto NaCl substrates and irradiated with 9 eV photons at temperatures between 10 and 130 K. Several experiments were carried out to test the temperature dependence of VUV-driven chemistry; one served as a control at 10 K to assess changes at very low temperatures.



(a) **(b)**

Figure 4.11: Images of the BL03 station where **(a)** is the BL03 endstation, and **(b)** is the sample holder.

The BL03 beamline is designed for photochemistry under UHV conditions. It extracts ∼50 mrad bending-magnet radiation from the TLS, monochromatised with a 6 m cylindrical grating monochromator to deliver photons in the 4-40 eV range [23]. Typical photon fluxes are on the order of 10^{11}-10^{12} photons s^{-1}. The beam was focused to ∼0.5 × 0.2 mm at the sample, although in certain experiments it may be defocused to ∼8 × 5 mm to ensure uniform coverage of the ice film. The photon flux was monitored

using a gold mesh photocurrent detector, read out with a Keithley electrometer [24]. A simplified schematic of the full BL03 optical layout is shown in Figure 4.12, illustrating the path of synchrotron radiation from the source through the monochromator and refocusing optics to the endstation. This layout enables precise energy selection and beam shaping, allowing for stable, tunable VUV irradiation across the experimental range.

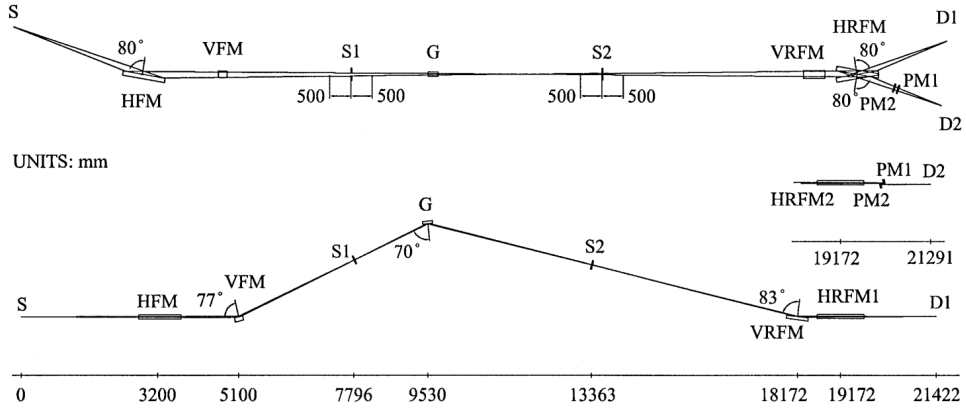


Figure 4.12: Schematic layout of the BL03 (03A1) beamline at the Taiwan Light Source. The synchrotron source (S) is followed by a series of optical components: horizontal and vertical focusing mirrors (HFM, VFM), slits (S1, S2), a cylindrical grating monochromator (G), and vertical/horizontal refocusing mirrors (VRFM, HRFM), leading to two possible detector paths (D1 and D2). All distances are in mm. **Credit:** Reprinted from Nuclear Instruments and Methods in Physics Research Section A: Accelerators, Spectrometers, Detectors and Associated Equipment, Vol. 467, Y. F. Song et al., Performance of a novel VUV bending magnet beamline, Pages 569–572, Copyright (2001), with permission from Elsevier, [25]

The irradiation chamber is UHV-compatible, achieving pressures of 10^{-8}–10^{-9} mbar with turbomolecular and backing pumps. At its centre is a rotatable cold-head cryostat (APD HC-DE204S), capable of cooling samples to ∼10 K while maintaining good thermal contact [24, 26]. Samples were prepared by background deposition of mixed formamide–water vapour, giving homogeneously mixed ices on NaCl substrates. ZnSe windows were not used in this campaign due to time constraints; instead, the focus was on varying the deposition temperature.

Table 4.4 summarises the parameters for the experiments performed on the BL03 endstation at the NSRRC. As discussed in Section 2.3.1, Europa's surface temperature can vary between ∼50-130 K, providing a series of temperatures to irradiate the samples at to simulate the Europan surface ice. At its lowest the BL03 chamber can reach ∼10

Table 4.4: Summary of experimental irradiation conditions for Sets 1 and 2. Both sets used photon irradiation (9 eV) through a NaCl window; the only variable was the sample temperature, as listed.

Experiment	Irradiation Type	Energy (eV)	Window	Temp. (K)	Fluence (cm^{-2})
Set 1	Photon	9	NaCl	10 50 90	$(2.4 \pm 1.3)\times10^{19}$
Set 2	Photon	9	NaCl	10 50 90 110 130	$(2.4 \pm 1.3)\times10^{19}$

K, this provided a good control temperature to ensure that any chemical changes occurring in the ice were as a result of a temperature change. Due to time restrictions and faults in the equipment, the first set of experiments, as illustrated in Table 4.4, capped at a top temperature of 90 K, whereas the second set of experiments reached a top temperature of 130 K. This means that whilst repeats were performed to ensure that the experiments were repeatable and to be confident of the reason for chemical changes within the ice, 110 and 130 K do not have repeats and have been taken at face value.

Unlike the ion and electron experiments, which used mid-IR vibrational bands to track destruction and product formation, BL03 studies focused on electronic absorption features in the VUV range. At 9 eV (∼137 nm), absorption is dominated by electronic excitations such as $n \rightarrow \pi^*$ transitions of the formamide C=O group and water excitations, rather than vibrational bands. Consequently, FTIR monitoring of column densities was not possible. Ice thickness and composition could therefore only be estimated indirectly, using chamber pressure changes and dosing time as guides. This introduces larger uncertainties than for the ion and electron datasets, making the results qualitative in terms of absolute ice column density.

VUV photons interact with matter via electronic excitation within the first tens of nanometers of the ice, their behaviour therefore differs fundamentally from that of ions or electrons, which deposit energy stochastically along their paths. The BL03 experiments were therefore not treated as complementary to the AQUILA or BL21A2 datasets, but rather as a separate study of the temperature dependence of VUV-driven

chemistry in formamide-water ices.

4.3.4 Ice Preparation and Thickness Estimation at BL03

At the BL03 endstation, ice films were characterised using VUV transmission spectroscopy rather than FTIR. Transmitted VUV light passing through the ice was detected using a solar-blind photomultiplier tube (PMT) operating in photon-counting mode, while the incident intensity, $I_0(\lambda)$, was monitored using a calibrated gold or Ni mesh photocurrent detector [24]. Absorbance was then calculated using the Beer-Lambert relation,

$$A(\lambda) = \ln\left(\frac{I_0(\lambda)}{I(\lambda)}\right), \tag{4.7}$$

where $I(\lambda)$ is the transmitted intensity through the ice-coated substrate at each wavelength.

Since BL03 is configured for VUV spectroscopy and lacks MIR detection, it was not possible to determine ice thickness or composition from vibrational band integrals as in the ion and electron irradiation experiments. The incident photons at 9 eV ($\sim$137 nm) probe broad electronic excitations (e.g. $n \rightarrow \pi^*$ transitions associated with the formamide carbonyl and water-related electronic states) rather than narrow vibrational modes [25]. In condensed-phase mixtures these VUV features are typically broad, overlapping, and not associated with well-constrained integrated band strengths, making them unsuitable for quantitative column density determination in the same way as MIR bands.

Ice deposition during the BL03 experiments was therefore monitored indirectly using the chamber pressure rise during dosing and the deposition time. This provided a practical, run-to-run consistency check on the gas flux and deposition conditions, but it should be treated as a first-order proxy rather than an absolute thickness calibration, since it depends on the effective sticking coefficient, local flow geometry, and pumping speed. As a result, BL03 thickness and composition estimates are considered semi-quantitative, and the VUV dataset is interpreted primarily in terms of relative spectral evolution and temperature-dependent photochemistry rather than absolute, dose-normalised yields.

Finally, it is worth emphasising that VUV irradiation differs fundamentally from ion or electron irradiation in how energy is deposited. At 9 eV, photons drive chemistry via discrete photoabsorption events and electronic excitation within the upper tens to hundreds of nanometres of the ice, rather than via continuous collision cascades along a charged-particle track. This difference in energy-deposition geometry is an additional reason why the BL03 experiments are treated as a separate, temperature-dependent VUV study, complementary in mechanism but not directly comparable in a strictly quantitative sense to the AQUILA or U90 irradiation datasets.

4.3.5 Experimental Methodology

For both sets of experiments conducted at the two end stations at the NSRRC, ice was deposited onto a NaCl window (25 x 2 mm) to more closely simulate Europa's surface. In the electron irradiation experiments, a ZnSe window was also used as a more chemically inert window with which to compare the NaCl results. Once the sample windows were mounted onto their respective sample holders, the chambers were evacuated to pressures of $\sim 10^{-7}$-10^{-8} mBar, to prevent chamber contamination and aid in temperature reduction. For the electron irradiation experiments, illustrated in Table 4.3, the substrate temperature was reduced to 90 K and maintained at that temperature until the irradiation was concluded. As demonstrated in Table 4.4, for the photon experiments performed on the BL03 endstation, temperatures ranging between 10-130 K were used, providing a control experiment, followed by a range of temperatures corresponding to the extremes experienced on Europa.

As discussed previously, formamide-water ices were prepared via background deposition on both end chambers. This made sure that molecules mixed homogeneously and did not form distinct layers. The target composition was 50:50 formamide:water with a deposition thickness of $\sim$180 nm for the electron irradiation and $\lesssim$300 nm for the photon irradiation experiments.

Inside the chambers, samples were mounted on a rotatable cold finger, as shown in Figure 4.10. Like the experiments performed at Atomki, background deposition resulted in ice coating both the front and rear sides of the substrate. Although only the

front side was irradiated, the rear side contributed to the apparent FTIR absorbance. To correct for this, column densities were reduced by approximately 10% to account for ice on the back surface.

During deposition at the NSRRC endstations, the pressure rise in the chamber and the dosing duration were used as a real-time guide to keep the gas flux consistent between runs. Where MIR spectra were available (U90 electron experiments), the reported ice thicknesses were derived from FTIR band integrals (Section 4.3.2), with pressure/time monitoring used only as an operational check rather than a calibrated thickness measure.

4.3.6 Effects of Temperature

As illustrated in Table 4.4, the BL03 experiments explored how varying the sample temperature influences VUV-driven chemistry in formamide–water ices. These temperatures spanned from 10 K, used as a control to mimic the coldest regions of Europa, up to 130 K, near the maximum daytime surface temperature of the moon.

At the lowest temperatures (10-50 K), photodissociation products generated by VUV photons tend to remain trapped within the rigid ice matrix, limiting their diffusion and therefore reducing the extent of secondary or recombinational chemistry. This leads to the build-up of radicals or unstable intermediates within the ice [27].

As the temperature increases to the 50-130 K range, the thermal mobility of radicals, atoms, and small molecules improves, facilitating radical-radical recombination, rearrangement, and the formation of more stable photoproducts [28, 29]. These effects have been observed in a range of VUV and electron irradiation studies on astrophysical ices, where moderate warming leads to both enhanced chemical complexity and structural reorganisation of the ice matrix.

At temperatures above 130 K, the volatile components of the ice - particularly water and formamide - begin to desorb more rapidly under vacuum conditions [30]. As a result, irradiation effects can be masked or diminished due to the loss of target material, and the lifetimes of reactive species are significantly reduced. However, these higher temperatures may still be relevant to endogenic activity or transient heating events

(e.g., plumes or impact sites) on Europa or other icy bodies, where short-term exposure to elevated temperatures may trigger rapid chemical reactions before desorption dominates.

This temperature dependence highlights the complex interplay between energy input and thermal environment in determining both the fate of organic molecules and the potential for prebiotic synthesis on icy worlds like Europa.

4.4 Data Acquisition and Processing

4.4.1 FTIR Spectroscopy

The FTIR spectra collected across all ion, electron, and photon experiments were processed consistently to extract quantitative information on molecular destruction and product formation. As outlined in Sections 4.2.1, 4.3.2, and 4.3.4, the AQUILA ion experiments provided spectra at intermediate fluence steps, whereas the U90 electron and BL03 photon experiments yielded only pre- and post-irradiation spectra.

All spectra were manually baseline-corrected over the 3750-650 cm^{-1} range following the procedures described in Section 4.2.1. Where necessary, broad water features were removed (by subtraction or deconvolution) to isolate formamide-specific bands. No spectral smoothing was applied to preserve weak but potentially diagnostic features.

For the ion and electron datasets, particular attention was given to formamide diagnostic bands and the most prominent radiolysis products. In practice, this meant tracking the formamide CH-bending and CN-stretch modes near 1388 and 1328 cm^{-1}, together with strong product bands such as CO_2 (2340 cm^{-1}), OCN^- (2165 cm^{-1}), and CO (2135 cm^{-1}), provided they remained unsaturated and free from severe overlap (see Sections 4.2.1 and 4.3.2 for the facility-specific details).

Integrated band areas $S(F)$ were then converted into column densities $N(F)$ using the Beer-Lambert relation already introduced in Section 4.2.1, with the appropriate band strengths A_ν adopted from the literature. The resulting column densities were plotted as a function of fluence or absorbed dose to obtain destruction curves for formamide and growth curves for radiolysis products. Dose-response quantities such

as destruction efficiencies, G-values, and survivabilities are defined and discussed in more detail in Section 3.3.3 (see Appendix A for the full column density and G-value calculation procedure).

4.4.2 Summary of Film Thickness Estimates

Ice thicknesses used throughout this thesis were determined differently depending on facility constraints. For the AQUILA ion and U90 electron campaigns, film thicknesses were derived from FTIR band integrals using the band-strength method (Equation 4.2); the full procedure and uncertainty sources are described in Sections 4.2.1 and 4.3.2. The resulting thicknesses carry uncertainties of order 40-50%, dominated by band-strength systematics, baseline placement, mixture-density assumptions, and the $\sim$10% correction for back-side deposition during background dosing.

As a consistency check, the AQUILA thicknesses were compared with SRIM-derived ion ranges (Section 4.2.1), confirming that O^{2+} and S^{5+} deposit essentially all of their energy within the 200-300 nm films, while 15 keV H^{+} partially transmits. For the U90 electron runs, FTIR-derived thicknesses were compared with CASINO stopping-range simulations (Section 4.3.2), indicating near-complete energy deposition for the ZnSe-supported film.

For the BL03 VUV experiments, MIR thickness determination was not available; thickness was therefore estimated only semi-quantitatively from dosing conditions (Section 4.3.4) and is used to support relative comparisons within that dataset rather than absolute, dose-normalised yields.

4.4.3 Fluence Calculations

Fluence values were obtained differently at the three facilities, reflecting the available diagnostics and beamline designs.

At the Atomki-ECRIS facility, ion fluences were recorded directly during irradiation. Each incremental dose step was provided by the beam diagnostics (Faraday cups and meshes along the transport line; see Section 4.2), and the total fluence was obtained by summing these contributions. Since the fluence is measured in-situ within the chamber,

these values are considered the most accurate particle-dose measurements in this work.

At the NSRRC U90 endstation, there was no direct fluence readout at the sample position, so electron fluences had to be reconstructed from beam parameters. For each run, the total charge Q (C) delivered to the sample is:

$$Q = I \cdot \eta \cdot t, \tag{4.8}$$

where I is the measured beam current (A), η is the transmission efficiency of the beamline (for example, losses at meshes and apertures), and t is the irradiation time (s). The total number of incident electrons is then

$$N_e = \frac{Q}{e}, \tag{4.9}$$

where $e = 1.602 \times 10^{-19}$ C. The particle fluence, Φ (electrons cm^{-2}), is obtained by dividing by the irradiated spot area A (cm^2):

$$\Phi = \frac{N_e}{A}. \tag{4.10}$$

For the 3 hour irradiations at 2 keV, this procedure yielded a total fluence of 3.37×10^{19} electrons cm^{-2} for both NaCl and ZnSe substrates (Table 4.3).

For the BL03 VUV experiments, the photon flux at the sample was not monitored continuously during the runs. Instead, the flux $\dot{N}$ (photons s^{-1}) was estimated from beamline specifications and periodic calibration measurements [24, 31]. The photon fluence density is

$$\Phi_\gamma = \frac{\dot{N}}{A}, \tag{4.11}$$

and the total photon fluence is

$$F_\gamma = \Phi_\gamma \cdot t, \tag{4.12}$$

where A is the illuminated area and t is the exposure time. Using a conservative flux estimate of $\dot{N} \approx 2 \times 10^{12}$ photons s^{-1} and the experimental irradiation times, the total photon fluence was estimated as $(2.4 \pm 1.3) \times 10^{19}$ photons cm^{-2} for each BL03 run (Table 4.4). As this estimate relies on assumed flux values and indirect deposition

monitoring, these photon fluences are treated as order-of-magnitude values: sufficient for internal comparisons within the VUV dataset, but not used for strict quantitative comparison with the ion and electron fluences.

In summary, ion fluences at AQUILA were directly measured by beamline diagnostics, whereas electron and photon fluences at the NSRRC endstations were reconstructed from beam currents, transmission factors, exposure times, and estimated fluxes. The resulting uncertainties are therefore smallest for the ion experiments and largest for the VUV experiments, an important caveat when comparing dose–response trends across the different irradiation sources.

4.4.4 Temperature-Programmed Desorption (TPD)

Temperature-programmed desorption (TPD) was used as a post-irradiation diagnostic to track the thermal release of volatile species and to assess trapping within the ice matrix. In this work, TPD is treated as a qualitative tool: it provides a consistency check on volatile retention and ice restructuring during warm-up, but it is not used for kinetic modelling or for quantitative yield extraction.

After irradiation, the sample holder was heated using a resistive heater mounted on the cryogenic cold finger and controlled by a feedback temperature controller. The temperature was ramped at a constant linear rate of 5 K min^{-1}. During the warm-up, the ramp was paused at regular temperature intervals to allow stabilisation before acquiring spectra. For the FTIR-based experiments, spectra were recorded at 30 K intervals. For the VUV-based experiments (BL03), an analogous stepped warm-up protocol was followed (see Section 7.3.1.1 for more details), but spectra were acquired in the VUV transmission configuration at each temperature step, so the thermal evolution was tracked via changes in the VUV absorbance rather than MIR vibrational band intensities.

Since desorption temperatures depend on the heating rate, the onset and apparent maxima observed during warm-up correspond specifically to the 5 K min^{-1} ramp used in the experiments discussed in this thesis. The TPD results are therefore interpreted primarily in terms of relative trends between experiments performed under identical

heating conditions (e.g. retention vs loss, and evidence for restructuring), rather than absolute desorption temperatures.

Bibliography

[1] Kovac J. Foundations of Spectroscopy (Oxford Chemistry Primers No. 78) (Duckett, Simon; Gilbert, Bruce). Journal of Chemical Education. 2003;80(9):1006.

[2] Cooper JF, Johnson RE, Mauk BH, Garrett HB, Gehrels N. Energetic Ion and Electron Irradiation of the Icy Galilean Satellites. Icarus. 2001;149(1):133-59.

[3] Biri S, Vajda IK, Hajdu P, Rácz R, Csík A, Kormány Z, et al. The Atomki Accelerator Centre. The European Physical Journal Plus. 2021 Feb;136(2).

[4] Rácz R, Kovács STS, Lakatos G, Rahul KK, Mifsud DV, Herczku P, et al. AQUILA: A laboratory facility for the irradiation of astrochemical ice analogs by keV ions. Review of Scientific Instruments. 2024 09;95(9):095105.

[5] Ding JJ, Boduch P, Domaracka A, Guillous S, Langlinay T, Lv XY, et al. Implantation of multiply charged sulfur ions in water ice. Icarus. 2013.

[6] Pilling S, Duarte ES, Domaracka A, Rothard H, Boduch P, da Silveira EF. Radiolysis of astrophysical ice analogs by energetic ions: the effect of projectile mass and ice temperature. Physical chemistry chemical physics : PCCP. 2011;13 35:15755-65.

[7] Ziegler JF, Ziegler MD, Biersack JP. SRIM – The Stopping and Range of Ions in Matter; 2010. Version SRIM-2013. `http://www.srim.org/`.

[8] Principle of Interferometer — optosigma.com;. [Accessed 29-11-2025]. `https://www.optosigma.com/uk_en/support/tutorial/interferometers/principle-of-interferometers?___store=uk_en&___from_store=eu_en`.

[9] Trumbo S, Brown M, Hand K. Sodium chloride on the surface of Europa. Science Advances. 2019;5.

[10] Hand K, Carlson RW. Europa's surface color suggests an ocean rich with sodium chloride. Geophysical Research Letters. 2015;42:3174 3178.

[11] TLS and TPS at National Synchrotron Radiation Research Center (NSRRC); 2017. Available from: https://lightsources.org/lightsources-of-the-world/asia-oceania/national-synchrotron-radiation-research-center/.

[12] Taiwan Light Source Beamlines — tls.nsrrc.org.tw;. [Accessed 07-10-2024]. https://tls.nsrrc.org.tw/index.aspx?lang=en.

[13] Taiwan Light Source Beamlines — tls.nsrrc.org.tw;. [Accessed 07-10-2024]. https://tls.nsrrc.org.tw/page.aspx?pid=161&lang=en.

[14] Paranicas C, Ratliff JM, Mauk B, Cohen C, Johnson RE. The ion environment near Europa and its role in surface energetics. Geophysical Research Letters. 2002;29.

[15] Nordheim T, Jasinski J, Hand K. Galactic Cosmic-Ray Bombardment of Europa's Surface. The Astrophysical Journal Letters. 2019;881.

[16] Taiwan Light Source Beamlines — tls.nsrrc.org.tw;. [Accessed 03-09-2025]. https://tls.nsrrc.org.tw/bd_page.aspx?lang=en&pid=1352&port=21A2#:~:text=part%2C%20the%20Bomem%20DA%208ME,8%7D%20Torr.

[17] Bahou M, Wu YJ, Lee Y. A new method for investigating infrared spectra of protonated benzene (C6H7+) and cyclohexadienyl radical (c-C6H7) using para-hydrogen. The Journal of chemical physics. 2012;136 15:154304.

[18] Taiwan Light Source Beamlines — tls.nsrrc.org.tw;. [Accessed 04-09-2025]. https://tls.nsrrc.org.tw/bd_page.aspx?lang=en&port=03A1&pid=1188.

[19] EFG-7 / EGPS-2017 Low Energy Electron Gun System — kimballphysics.com;. [Accessed 04-09-2025]. https://www.kimballphysics.com/product/efg-7-egps-2017-90/.

[20] Wu YJ, Chen HF, Chuang SJ, Huang TP. UV and IR Spectra to Determine Simulated Astrophysical Species. Astrophysical Journal. 2013.

[21] Yamanouchi S, Conway S, Strong K, Colebatch O, Lutsch E, Roche S, et al. Network for the Detection of Atmospheric Composition Change (NDACC) Fourier transform infrared (FTIR) trace gas measurements at the University of Toronto Atmospheric Observatory from 2002 to 2020. Earth System Science Data. 2023.

[22] Drouin D, Couture AR, Joly D, Tastet X, Aimez V, Gauvin R. CASINO V2.42: a fast and easy-to-use modeling tool for scanning electron microscopy and microanalysis users. Scanning. 2007;29 3:92-101.

[23] Taiwan Light Source Beamlines — tls.nsrrc.org.tw;. [Accessed 05-09-2025]. https://tls.nsrrc.org.tw/bd_page.aspx?lang=en&pid=1189&port=03A1#:~:text=Focusing%20Mirror%3AN%2FA.

[24] Lo J, Ghosh R, Lu HC, Hung W, Cheng B. Vacuum-Ultraviolet Absorption Spectra of Icy C2H4 at 13–60 K. 2021;8.

[25] Song Y, Ma CI, Hsieh T, Huang LR, Chung S, Cheng N, et al. Performance of a novel VUV bending magnet beamline. Nuclear Instruments & Methods in Physics Research Section A-accelerators Spectrometers Detectors and Associated Equipment. 2001;467:569-72.

[26] Pavithraa S, Lo J, Rahul KK, Sekhar BN, Cheng B, Mason NJ, et al. Vacuum ultraviolet photoabsorption of prime ice analogues of Pluto and Charon. Spectrochimica acta Part A, Molecular and biomolecular spectroscopy. 2018;190:172-6.

[27] Holtom P, Bennett C, Osamura Y, Mason N, Kaiser R. A Combined Experimental and Theoretical Study on the Formation of the Amino Acid Glycine (NH2CH2COOH) and Its Isomer (CH3NHCOOH) in Extraterrestrial Ices. The Astrophysical Journal. 2005;626:940 952.

[28] Bennett C, Jamieson C, Mebel A, Kaiser R. Untangling the formation of the cyclic carbon trioxide isomer in low temperature carbon dioxide ices. Physical Chemistry Chemical Physics. 2004;6:735-46.

[29] Mason N, Dawes A, Holtom P, Mukerji R, Davis MP, Sivaraman B, et al. VUV spectroscopy and photo-processing of astrochemical ices: an experimental study. Faraday Discussions. 2006;133:311-29; discussion 347-74, 449-52.

[30] Collings M, Anderson MR, Chen R, Dever JW, Viti S, Williams DA, et al. A laboratory survey of the thermal desorption of astrophysically relevant molecules. Monthly Notices of the Royal Astronomical Society. 2004;354:1133-40.

[31] Taiwan Light Source Beamlines — tls.nsrrc.org.tw;. [Accessed 05-09-2025]. https://tls.nsrrc.org.tw/bd_page.aspx?lang=en&pid=1193&port=03A1#:~:text=Vertical%20Refocusing.

Chapter 5

Ion Irradiation of Formamide and Water Ice Mixture

5.1 Experimental Overview and Irradiation Parameters

In this Chapter, the experimental parameters and conditions for the ion irradiation of formamide-water ices are discussed. As discussed in Section 4.2.2, NaCl and ZnSe windows were both tested as suitable substrates. There is significant evidence that suggests sodium chloride is present in Europa's ocean, particularly in the chaos terrains [1], making the salt an ideal surface for depositing formamide-water ice to mimic the Europan surface. ZnSe windows were also tested for the irradiation experiments, as zinc selenide provides a more mechanically robust material that is less likely to degrade due to moisture sensitivity [2, 3], compared to NaCl, which is more susceptible to degradation in humid environments. Furthermore, the ZnSe windows provided complementary data sets to the NaCl windows, ensuring that any observed chemical changes or phenomena could be attributed either to the window type or to robust phenomena [4, 5]. Moreover, as shown in Table 5.1, both the NaCl and ZnSe windows span broad spectral ranges, encompassing the MIR. This is crucial, as it is the range in which the in-situ FTIR equipment at Atomki operates, enabling consistent spectral monitoring of chemical changes.

Table 5.1: Experimental conditions for ion irradiation of formamide–water ices at 90 K on NaCl and ZnSe substrates.

Ion	Win.	Ice Comp.[a]	Ice Thick. (nm)[b]	Temp. (K)	Fluence (cm^{-2})
H^+	NaCl	52:48	237	90	1.10×10^{16}
O^{2+}		45:55	223	90	1.92×10^{15}
S^{5+}		49.6:50.3	226	90	9.65×10^{14}
H^+	ZnSe	46:54	278	90	1.94×10^{17}
O^{2+}		47:53	210	90	3.16×10^{15}
S^{5+}		47:53	222	90	1.08×10^{15}

[a] Molar ratio (FA:H_2O) from pre-irradiation FTIR; typical uncertainty ∼15% per component for near-1:1 mixtures (not shown).
[b] Thickness from FTIR band integrals; typical systematic uncertainty ∼40-50% (not shown).

The uncertainties on the formamide:water mixing ratios follow directly from the FTIR band-strength method outlined in Section 4.4. For mixed formamide-water ices, the dominant contributions arise from the literature band strengths for the individual

vibrational modes (typically ±20-30%), together with baseline placement and minor assumptions regarding the density of the mixed films. The statistical uncertainty associated with spectral noise is comparatively small, generally below the 10% level. Taken together, these factors result in an overall relative uncertainty of roughly 30% on the molar compositions, corresponding to approximately ±15% for mixtures close to 1:1. This uncertainty has therefore been applied uniformly to the ice compositions reported in Table 5.1.

The aim when depositing ice onto the substrates was always to achieve as close to a 50:50 ratio of formamide to water as possible, but the actual ratios are shown in Table 5.1. The formamide-water ice ratio in the experiments varied slightly between 46:54 and 52:48 due to the incremental deposition procedure. Deposition was monitored using chamber pressure changes as a guide, with in-situ FTIR measurements used after each step to determine the ice thickness and composition. While this approach allowed reasonable accuracy in quantifying the ratio, exact control was not possible. Additionally, due to limitations on maximum ice thickness (to avoid exceeding ion penetration depths and prevent spectral saturation), it was not always feasible to precisely match the composition to a 50:50 ratio.

Similarly, it was not possible to set the ice thickness precisely; the target ice thickness was ∼250 nm per experiment, although achieving a near 50:50 formamide-water ratio was prioritised over thickness, which resulted in some variation. Using the software SRIM, [6], the penetration depths of 15 keV H^+, 30 keV O^{2+}, and 60 keV S^{5+} ions in a 50:50 formamide-water ice were determined. SRIM simulations showed maximum penetration depths of ∼200 nm for O^{2+} and S^{5+}, and a range of ∼390-400 nm for H^+. Figure 3.9 in Section 3.2.1 demonstrates that hydrogen penetrates significantly further into water ice than oxygen and sulphur. With this information in mind, it was decided that 250 nm was a suitable thickness as this was sufficient to absorb the majority of the energy from oxygen and sulphur ions. Creating an ice thick enough to absorb the full energy deposition from hydrogen irradiation would have required excessive thickness, leading to spectral saturation. In FTIR spectroscopy, spectral saturation occurs when the absorbance is sufficiently strong that the detector response becomes nonlinear,

leading to quantitative inaccuracies, distorted band shapes, obscured minor features, and baseline distortion, [7, 8]. All of these issues would mean that the chemical changes in formamide and water during irradiation of the ices would not be accurately monitored. Therefore, it was decided that it would be better to have an ice thickness that was appropriate for the energetic deposition of sulphur and oxygen, and to forgo full energetic deposition of hydrogen to maintain accurate FTIR monitoring of the ices.

Section 4.2.2 demonstrated that the ice was deposited onto the substrates using background deposition, as opposed to direct deposition. This was to ensure that instead of having layered ices, the formamide and water were mixed as homogeneously as possible. Additionally, background deposition was used to better approximate the likely molecular mixing in extraterrestrial ices observed on comets and Europa. In comets, in particular, ice often coexists with various organics, composed of multimolecular ices [9]. Furthermore, the formamide found on comet 67P, discussed in Section 2.4.1, was at an abundance of roughly 0.004% relative to H_2O such that that if formamide were delivered to an icy body, such as Europa, it would be mixed into a pre-existing water-ice matrix as opposed to forming a layer on top of the ice, [10]. As discussed in Section 3.2.1.1, H^+, O^{2+}, and S^{5+} were selected for this study as they represent the most astrophysically relevant ion species in Europa's radiation environment, originating primarily from Jupiter's magnetosphere and the volcanic activity of Io. Protons, produced in Jupiter's ionosphere and from other secondary sources, are the lightest and most mobile charged particles, penetrating deeply into the ice and enabling subsurface radiolysis. Oxygen ions, generated mainly through the ionisation of SO_2 from Io's volcanism, have shorter penetration depths but higher linear energy transfer (LET), driving concentrated chemical processing in near-surface ice layers. Sulphur ions, also derived from Io, are among the heaviest species present, depositing energy over extremely short distances and creating dense ionisation tracks that promote intense surface chemistry. Together, these ions span a representative range of penetration depths and LET values, enabling the simulation of both deep and surface-localised radiolytic effects relevant to formamide-water ices on Europa.

5.2 Evolution of IR Spectra and Radiolysis Products

Prior to irradiation, after the deposition of the formamide-water ice, a reference IR spectrum was obtained using in-situ FTIR. This pre-irradiation spectrum served as the baseline for tracking chemical and structural changes in the ice upon exposure to ionising radiation. The primary objective was to monitor both the destruction of formamide and the formation of new radiolytic products, which was achieved by tracking several key vibrational features in the mid-IR region. These features are illustrated in Figure 5.1. The vibrational spectrum of unirradiated ice is dominated by formamide-specific absorption bands superimposed on the broad water-ice profile. The CH stretching mode ($\sim$2730 cm^{-1}), a strong C=O stretching mode ($\sim$1690 cm^{-1}), NH_2 scissoring ($\sim$1630 cm^{-1}), CH bending ($\sim$1388 cm^{-1}), and CN stretching ($\sim$1328 cm^{-1}) are all clearly distinguishable. Upon irradiation, these diagnostic formamide bands decrease while new features assigned to radiolysis products emerge, such as CO (C$\equiv$O stretching; $\sim$2135 cm^{-1}), OCN^- (C$\equiv$N stretching; $\sim$2165 cm^{-1}), and CO_2 (asymmetric stretching; $\sim$2340 cm^{-1}). The irradiation-specific evolution of these features is discussed in the following subsections for each projectile and substrate.

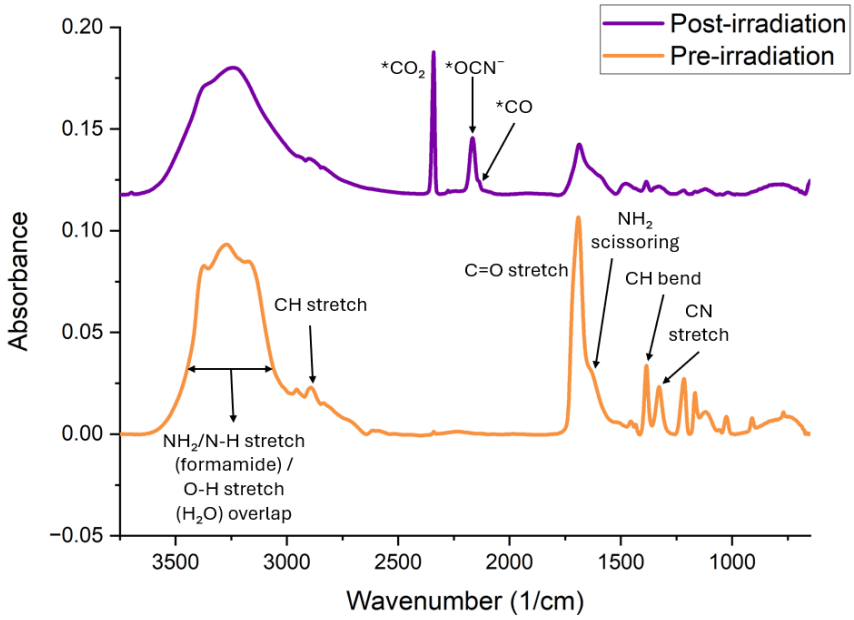


Figure 5.1: Infrared spectra of a cryogenic 50:50 (molar) formamide-water ice mixture deposited onto an NaCl window and maintained at 90 K, from pre-irradiation (spectrum 1, yellow) to post-final irradiation (spectrum 10, dark purple), with each number in between representing the fluence increment number, with 15 keV H^+ ions. Key vibrational modes of formamide are labelled, including CH stretch (∼2730 cm^{-1}), C=O stretch (∼1690 cm^{-1}), NH_2 scissoring (∼1630 cm^{-1}), CH bending (∼1388 cm^{-1}), CN stretching (∼1328 cm^{-1}), and a broad region near 3200-3400 cm^{-1} representing the overlapping N-H/O-H stretches of formamide and water. The post-irradiation spectrum shows significant changes in peak intensity and the appearance of new features, including CO (C≡O stretching; ∼2135 cm^{-1}), OCN^- (C≡N stretching; ∼2165 cm^{-1}), and CO_2 (asymmetric stretching; ∼2340 cm^{-1}), marked with asterisks. Spectra have been vertically offset for clarity.

In addition to the diagnostic formamide and product bands discussed above, a less resolved structure is also present below ∼1300 cm^{-1} (Figure 5.1). This low-wavenumber region is inherently congested, because it contains overlapping bending/deformation modes of NH_2CHO as well as contributions from the H_2O-rich ice matrix (including librational/lattice-related absorption in amorphous solid water). Irradiation-induced changes in this region are therefore likely to reflect a combination of matrix restructuring and the build-up of minor radiolysis products whose strongest absorptions occur at lower wavenumber. Given the degree of overlap and the comparatively low signal-to-noise in this part of the spectrum, these features are treated qualitatively here and are not used for the quantitative yield analysis.

5.2.1 Proton Irradiation

To investigate the radiolytic evolution of the formamide-water ice under proton irradiation, the ice mixture was exposed incrementally to 15 keV H^+ ions, with FTIR spectra recorded between fluence steps to track the dose dependence of parent destruction and product growth. The choice of 15 keV represents a compromise between achieving meaningful energy deposition within the typical film thickness used here (∼237 nm; Table 5.1) and avoiding excessive sputtering or strong-band saturation effects that would compromise quantitative FTIR analysis. It is also within the Europa-relevant energy regime for magnetospheric protons [11] and matches the practical upper limit for singly charged protons at Atomki-ECRIS: the available ion energy is set by $E = qV$, giving a maximum of ∼15 keV for $q = 1$ under the laboratory-accessible voltage/charge-state configuration [12].

As this was one of the first experiments in the series, the initial fluence steps were deliberately kept low to resolve early-stage chemical evolution and to avoid overwhelming the FTIR signal. In total, twelve irradiation steps were performed, with individual step fluences ranging from 6.3×10^{13} to 2.1×10^{15} ions cm^{-2} (Table 5.2). Irradiation was continued to a final cumulative fluence of $\sim 1.1 \times 10^{16}$ ions cm^{-2}, at which point the decrease in the diagnostic formamide bands approached a plateau, indicating diminishing additional chemical change within the experimental sensitivity.

Table 5.2: Cumulative ion fluences corresponding to the spectrum indices used in Figures 5.2-5.12.

Spectrum index	H^+ / NaCl	H^+ / ZnSe	O^{2+} / NaCl	O^{2+} / ZnSe	S^{5+} / NaCl	S^{5+} / ZnSe
	Cumulative fluence [ions cm^{-2}]					
1	0	0	0	0	0	0
2	6.28×10^{13}	2.52×10^{13}	6.70×10^{13}	1.22×10^{13}	6.07×10^{12}	9.81×10^{12}
3	1.31×10^{14}	5.05×10^{13}	1.31×10^{14}	2.23×10^{13}	1.37×10^{13}	2.48×10^{13}
4	2.56×10^{14}	8.13×10^{13}	2.53×10^{14}	4.86×10^{13}	2.87×10^{13}	4.99×10^{13}
5	5.06×10^{14}	2.39×10^{14}	4.96×10^{14}	1.24×10^{14}	5.09×10^{13}	1.00×10^{14}
6	8.70×10^{14}	4.77×10^{14}	8.54×10^{14}	3.75×10^{14}	9.52×10^{13}	2.00×10^{14}
7	9.72×10^{14}	9.97×10^{14}	1.21×10^{15}	4.98×10^{14}	2.26×10^{14}	3.00×10^{14}
8	1.69×10^{15}	2.48×10^{15}	1.92×10^{15}	7.49×10^{14}	3.53×10^{14}	1.08×10^{15}
9	2.40×10^{15}	4.99×10^{15}	…	1.33×10^{15}	5.61×10^{14}	…
10	4.49×10^{15}	9.99×10^{15}	…	3.16×10^{15}	9.65×10^{14}	…
11	6.59×10^{15}	2.50×10^{16}	…	…	…	…
12	8.90×10^{15}	5.00×10^{16}	…	…	…	…
13	1.10×10^{16}	1.00×10^{17}	…	…	…	…
14	…	1.94×10^{17}	…	…	…	…

The twelve irradiation steps correspond to spectra 2-13 in Figure 5.2 and 2-14 in Figure 5.4; the cumulative fluence associated with each spectrum is listed in Table 5.2.

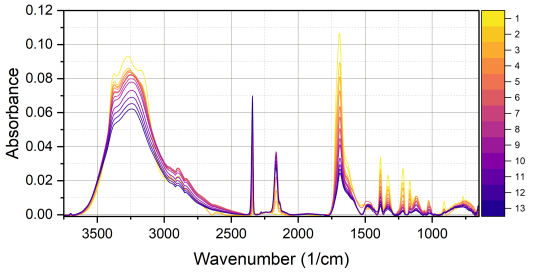
For example, spectra 4 and 5 on NaCl using H^+ ions correspond to $F \approx 2.6 \times 10^{14}$ and 5.1×10^{14} ions cm^{-2}, respectively.

5.2.1.1 NaCl Window Experiments

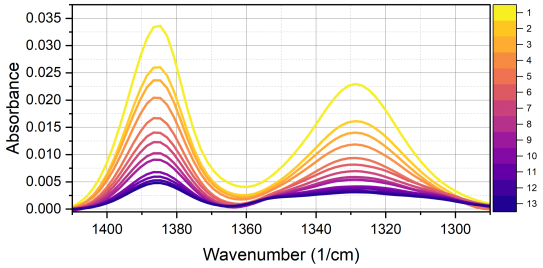
For this set of experiments, a proton irradiation energy of 15 keV was chosen as a representative energy for magnetospheric protons on Europa, based on modelling of surface-interacting populations [11]. Due to initial uncertainties regarding how rapidly formamide would degrade under proton irradiation, a stepwise irradiation approach was used. The fluence values started low, and once the chemical changes were observed via FTIR, the situation was assessed, and the next fluence value was determined. This strategy avoided overwhelming the signal at early stages and enabled monitoring of the early-stage radiolysis and damage effects.

At 15 keV, protons have a calculated penetration depth between roughly 390 and 400 nm. For this experiment, the ice thickness was ∼237 nm, see Table 5.1. As the penetration depth of 15 keV protons exceeds the thickness of the ice for this particular set of experiments, only partial energy deposition occurs. This still provides a useful analogue for subsurface interactions on Europa, where deeper penetration is expected due to thin surface layers and variable porosity. SRIM implies that this corresponds to an energy deposition of approximately 12.6 keV per particle.

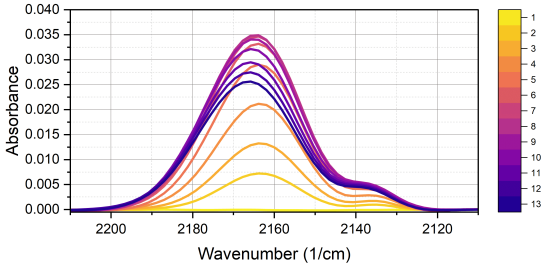
This partial deposition influenced the distribution and intensity of radiation-driven chemical changes within the ice. As a result, the evolving infrared features reflect both the depth-dependent energy delivery and the progressive molecular degradation associated with proton irradiation. As the fluence increased, characteristic formamide peaks, including those at 1388 and 1328 cm^{-1}, progressively diminished, indicating radiolytic destruction of the parent molecule. In parallel, new features corresponding to CO, CO_2, and OCN^- emerged and intensified, reflecting the formation of small radiolysis products and new chemical species. It should be noted that the OCN^- feature appeared as a shoulder on the CO band, requiring careful spectral deconvolution.



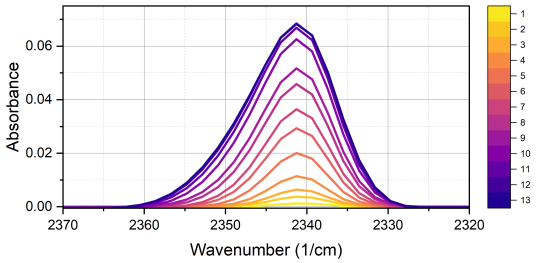
(a) Evolution of the full mid-IR spectrum of formamide-water ice.



(b) Close-up of the 1388 cm^{-1} and 1328 cm^{-1} features attributed to formamide's CH bending and CN stretching vibrations, respectively.



(c) Evolution of the 2165 cm^{-1} band assigned to OCN^-, with the shoulder at 2135 cm^{-1} corresponding to CO. These features appear post-irradiation and increase with fluence.



(d) Formation of CO_2 at 2340 cm^{-1}, showing its growth with increasing proton fluence.

Figure 5.2: Evolution of infrared spectral features for a 50:50 formamide-water ice mixture deposited on a NaCl window and irradiated with 15 keV H^+ ions at 90 K. (a) Full mid-infrared spectrum across all fluences. (b) Formamide degradation tracked via CH and NH_2 bending modes. (c) Emergence of CO and OCN^- features post-irradiation. (d) Progressive formation of CO_2 with fluence. All spectra are colour-coded by increasing ion fluence, from pre-irradiation (spectrum 1, yellow) to post-final irradiation (spectrum 13, dark purple), with each number in between representing the fluence increment number.

A closer inspection of Figure 5.2b shows that the formamide bands decrease rapidly during the earliest fluence increments, whereas at higher fluence the rate of decrease slows and approaches a plateau. As fluence increases, the formamide bands at 1388 and 1328 cm^{-1} decrease steadily; on NaCl they fall rapidly up to spectra 5-6 ($F \sim$ (5-9) $\times 10^{14}$ ions cm^{-2}) and then begin to plateau at higher doses. This plateau was used as an indicator to terminate irradiation, suggesting that any remaining formamide may have been embedded deeper in the ice or shielded by radiolysis products. Water ice can be an active component of radiation chemistry when being irradiated. It

produces H/OH via radiolysis, and the hydrogen-bond network enables rapid proton transfer (Grotthuss hopping[1]), so water-rich ices can re-form formamide from common precursors during and after processing [15, 16]. Hydrogenated water-ice surfaces also open low-barrier routes from isocyanates to formamide, consistent with replenishment rather than complete loss [17]. Additionally, formamide is retained: when formamide is deposited on a compact layer of amorphous water ice, $> 95\%$ sinks through the ice and sticks to the surface underneath, [18]. In water-bearing ices, any proton-driven destruction of formamide is countered by water-mediated reformation and matrix trapping, [19], so destruction of the formamide plateauing is expected.

Figures 5.2c and 5.2d show the development of three key radiolysis products: OCN^- ($\sim$2165 cm^{-1}), CO ($\sim$2135 cm^{-1}), and CO_2 ($\sim$2340 cm^{-1}). OCN^- and CO form relatively quickly in the early fluence steps, with their bands increasing in intensity until they begin to plateau. In the proton/NaCl experiment, OCN^- and CO continue to grow up to at least spectrum 7 ($F \sim 1.7 \times 10^{15}$ ions cm^{-2}) before showing signs of saturation and decline, whereas CO_2 increases monotonically over the full fluence range explored ($F \leq 1.1 \times 10^{16}$ ions cm^{-2}). In the later stages of irradiation, OCN^- begins to show signs of degradation, and CO follows a similar trend.

This behaviour suggests that while OCN^- and CO are stable in the short term, they are not indefinitely resistant to radiolytic breakdown. Their eventual decline may be due to continued energy input driving secondary processing, such as fragmentation or further chemical reaction within the matrix. This behaviour is consistent with dynamic radiation-driven chemistry, in which products are both formed and subsequently destroyed as the dose increases. In addition, CO and OCN^- are comparatively reactive (and, in many ice-radiolysis systems, can behave as intermediate products), whereas CO_2 is a lower-energy, more thermodynamically stable end product. As a result, continued irradiation may not only destroy CO and OCN^- at high fluence but also drive net conversion into CO_2 via ongoing oxidation chemistry (e.g. OH/O-atom pathways, potentially proceeding through HOCO-type intermediates), [20–24].

[1]Grotthuss hopping refers to rapid proton transfer through a hydrogen-bonded network, where the proton effectively moves by successive bond rearrangements rather than by physical diffusion of a single hydronium ion. This mechanism enables extremely fast proton mobility in water and water ice [13, 14].

CO_2, on the other hand, as shown in Figure 5.2d, forms consistently throughout the experiment. In contrast to OCN^- and CO, CO_2 shows no signs of degradation, and its final absorbance surpasses that of the other two products. This suggests that CO_2 is a more radiolytically stable product in this system, or that its formation is continually favoured as fluence increases. A small CO_2 peak is already present in the pre-irradiation spectrum, likely due to minor contamination during deposition. However, the clear trend in band growth indicates genuine radiolytic production, with the pre-existing contribution considered negligible.

The observed behaviour of the radiolysis products can be linked to the LET and penetration depth of the protons used in the irradiation. As discussed in Section 3.2.1, 15 keV protons have a relatively low LET and a moderate penetration depth of approximately 390-400 nm in H_2O-rich ice. In this experiment, the ice was $\sim$237 nm thick, indicating that the protons partially deposited their energy within the ice layer, resulting in a more distributed, subsurface energy input compared to that of heavier ions.

This energy-delivery profile can help explain the trends in induced chemistry observed in the spectra. The continued formation of CO_2 throughout irradiation, without apparent signs of degradation, suggests that CO_2 is a stable radiolytic product under these conditions. Its persistence may reflect its production in deeper ice layers, where energy is delivered more diffusely - but not as significantly as what would perhaps be seen in oxygen and sulphur ion irradiation due to their higher LET values - and where the molecular environment may shield it from immediate secondary breakdown. Conversely, OCN^- and CO are more susceptible to accumulated dose effects near the ice surface, where the energy deposition is concentrated over a shorter distance. Their plateauing behaviour, followed by signs of degradation at higher fluences, is consistent with the kind of secondary processing expected in near-surface regions.

Furthermore, CO_2 is a thermodynamically stable molecule with strong C=O bonds and no labile H atoms, which reduces the number of accessible reaction channels once it is formed in the ice. This suggests that CO_2 is less likely to undergo further decomposition under continued radiolysis than more reactive carbon-bearing intermediates [25].

In addition, the continued increase of the CO_2 band is most naturally interpreted as net accumulation, in which CO_2 formation continues to outpace its destruction over the fluence range explored. In H_2O-rich ices this is consistent with ongoing oxidation chemistry, where radiolysis-generated oxidising fragments (e.g. OH/O) can convert carbon-bearing species into CO_2 via transient intermediates such as HOCO. Quantum chemical studies have shown how CO_2 forms in water-dominated ices:

$$\mathrm{CO} + \cdot\mathrm{OH} \xrightarrow{\mathrm{H^+}} \mathrm{HOCO}\cdot \quad (1)$$

$$\mathrm{HOCO}\cdot \xrightarrow{\mathrm{H^+}} \mathrm{CO_2} + \mathrm{H}\cdot \quad (2)$$

Scheme 5.1: Suggested reaction pathways for CO_2 formation in irradiated H_2O-rich ices. CO is initially formed and is subsequently oxidised by OH radicals to produce the HOCO· radical intermediate. Unimolecular decomposition of HOCO· yields CO_2 and a hydrogen radical. H^+ above the arrow denotes proton irradiation as the initiating energy source that generates the reactive radicals driving these steps. This pathway is consistent with previous laboratory and theoretical studies of radiation-driven surface chemistry in astrophysical ices [26][2].

The same cannot be said for OCN^- and CO, which are more prone to secondary reactions. They also require more complex formation mechanisms (as illustrated in Schemes 5.2 and 5.3), which are more sensitive to local energy density and, in the case of CO, the availability of less commonly formed radical species. Furthermore, studies suggest that OCN^- is likely to form early in irradiation but can be susceptible to secondary degradation or structural transformation [27]. Additionally, OCN^- generally forms via multi-step reaction pathways, making it more prone to reduction after irradiation [28]. However, OCN^- does have a potentially kinetically dominant chemical pathway that is simpler than those of the multi-step pathways; see Scheme 5.2. Whilst it is possible that the OCN^- observed in the IR spectra could have been produced via first-order processes, the rise-then-decline behaviour is more consistent with OCN^- acting as a transient species: it accumulates at early fluence but is subsequently processed (e.g. converted into other products and/or neutralised via recombination), leading to a reduction in the OCN^- band intensity at higher doses [27, 28].

[2]Although reactions are labelled with H^+ to indicate ion irradiation, the actual bond-breaking and radical formation is primarily initiated by secondary electrons produced via ionisation events. These electrons drive most of the subsequent radiation chemistry.

$$HCONH_2 \xrightarrow{H^+} OCN^- + H_2 + H^+ \quad (1)$$

$$NH_2CHO \xrightarrow{H^+} HNCO + H_2 \quad (2)$$

$$HNCO + H_2O \xrightarrow{H^+} OCN^- + H_3O^+ \quad (3)$$

Scheme 5.2: Suggested reaction pathways for OCN^- formation in irradiated formamide-water. Chemical pathway (1) is known to occur as a result of the direct photodissociation of formamide. (2) and (3) are the two steps of a multi-step pathway to form OCN^-, occurring when the radiation fragments of formamide combine to form HNCO, which subsequently undergoes deprotonation. These pathways are consistent with previous laboratory and theoretical studies of radiation-driven surface chemistry in astrophysical ices [26].

The emergence of CO during proton irradiation of the formamide-water ice at 90 K is a notable phenomenon, as CO is known to desorb at a much lower temperature. CO desorbs at around 20-30 K in a high vacuum, [29–31]. Even CO, loosely bound to water-rich ice, primarily sublimes at ∼50-70 K [30]. However, CO is a known and common radiolysis product of formamide [27]; the formation of CO from the 1:1 NH_2CHO:H_2O ice matrix under 15 keV H^+ irradiation likely proceeds via several competing radical pathways, facilitated by energy deposition and subsequent radical mobility. While precise reaction intermediates are difficult to isolate, Scheme 5.3 represents plausible mechanisms based on known radical and photolytic chemistry, [19, 25, 27, 32]. Dawley et al. (2014) [27], discussed how the presence of water may catalyse CO production if formamide is ionised by irradiation. They suggested that the barrier to formamide dissociation is significantly reduced when two water molecules couple to a formamide molecule. Although some CO is retained by microporosity and matrix trapping, retention at 90 K is surprising and implies unusually efficient trapping in this mixed system.

$$\mathrm{HCONH_2} \xrightarrow{\mathrm{H^+}} \mathrm{CO + NH_3} \quad (1)$$

$$\mathrm{NH_2CHO} \xrightarrow{\mathrm{H^+}} \mathrm{HCO\cdot + NH_2\cdot} \quad (2)$$

$$\mathrm{HCO\cdot} \xrightarrow{\mathrm{H^+}} \mathrm{CO + .H} \quad (3)$$

$$\mathrm{NH_2CHO} \xrightarrow{\mathrm{H^+}} \mathrm{HNCO + H_2} \quad (4)$$

$$\mathrm{HNCO + \cdot H} \xrightarrow{\mathrm{H^+}} \mathrm{NH_2\cdot + CO} \quad (5)$$

$$\mathrm{HNCO + \cdot H} \xrightarrow{\mathrm{H^+}} \mathrm{NH_2CO\cdot} \quad (6)$$

$$\mathrm{NH_2CO\cdot} \xrightarrow{\mathrm{H^+}} \mathrm{NH_2\cdot + CO} \quad (7)$$

Scheme 5.3: Suggested reaction pathways for CO formation in irradiated formamide-water. Chemical pathway (1) occurs by the decarboxylation of formamide. Chemical pathway (2) is the direct dissociation of formamide, leading to chemical pathway (3), where HCO· is unstable and dissociates to CO. (4) is the dehydrogenation of formamide via H-abstraction, leading to (5), which is a radical-driven transformation common in warm or irradiated ices. Chemical pathway (6) involves radical capture followed by rearrangement, leading to chemical pathway (7), which involves the fragmentation of the carbonyl radical into CO and an amine fragment. These pathways are consistent with previous laboratory and theoretical studies of radiation-driven surface chemistry in astrophysical ices, [19, 25, 27, 32]. Here, "H^+" denotes proton irradiation as the initiating energy source that generates reactive radicals/intermediates; it does not imply that each subsequent transformation requires direct H^+ impact, and several steps represent radical chemistry that can proceed once these reactive fragments are present in the ice.

Taken together, the trends in the product bands and the simplified mechanisms in Schemes 5.1-5.3 provide a consistent picture of the underlying chemistry. The proposed reactions are not unique or exhaustive: radiolysis in mixed molecular ices is governed by stochastic, multi-step processes involving primary ionisation and numerous secondary interactions such as radical recombination, proton abstraction, and dissociative electron attachment. However, since many intermediates are IR inactive or spectrally blended, the actual formation mechanisms remain partially unresolved. Nevertheless, these schemes serve as plausible net pathways by which formamide can yield CO, CO_2, and OCN^- under ionising radiation, and are consistent with previous laboratory and theoretical studies [19, 26, 27, 32].

5.2.1.2 ZnSe Window Experiments

A complementary set of experiments was performed using a ZnSe window to test whether the chemical trends observed on NaCl were substrate-driven artefacts or intrinsic to the irradiated formamide-water ice. Since ZnSe is a less reactive material, this provided complementary data for comparative validation.

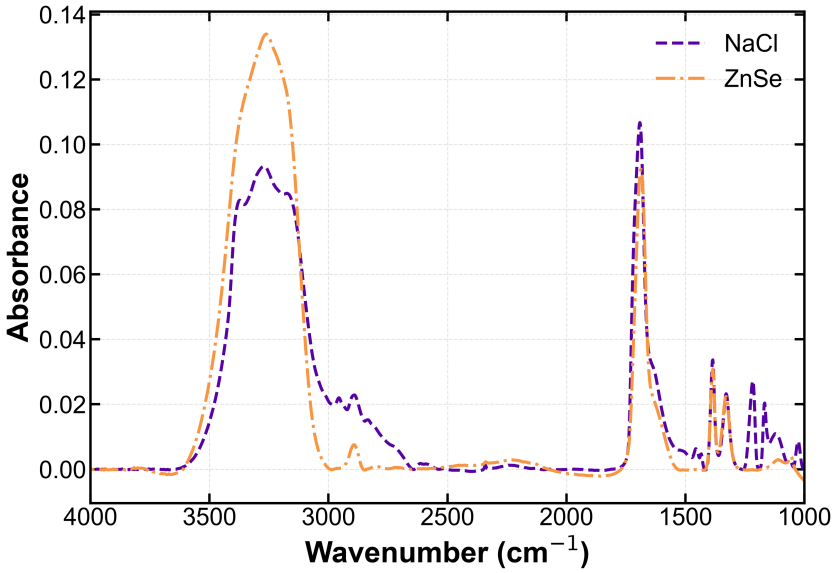
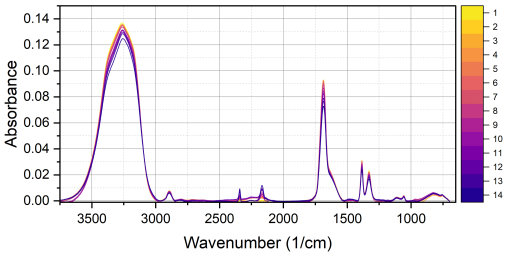
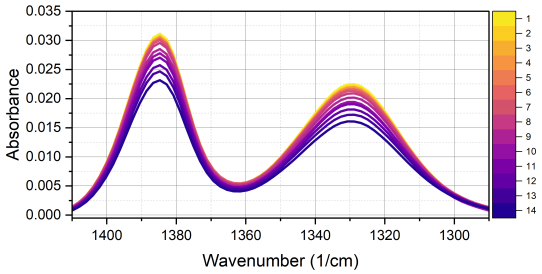


Figure 5.3: Comparison of infrared spectra of formamide-water ice deposited on NaCl (dashed line) and ZnSe (dash-dot line) substrates under equivalent deposition conditions at 90 K, before proton irradiation. The close agreement in band positions and relative intensities of the key formamide features (CH bend at ∼1388 cm^{-1}, CN stretch at ∼1328 cm^{-1}, C=O stretch at ∼1690 cm^{-1}) supports that the two ices are chemically equivalent prior to irradiation, and that any subsequent differences in spectral evolution can be attributed to substrate effects rather than differences in initial ice composition.

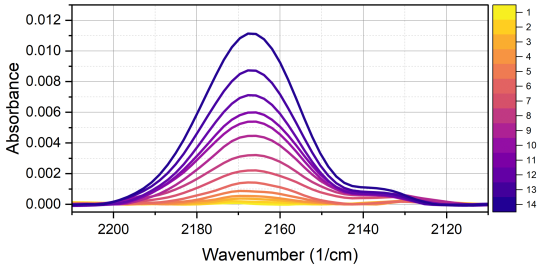
Since these experiments were meant to parallel each other, the same parameters were used: 15 keV proton irradiation, 90 K consistent temperature, and irradiating until the destruction of formamide plateaus (equating to a total fluence of 1.9×10^{17} ions cm^{-2}, over an order of magnitude larger than the total fluence for the NaCl window proton irradiation). The pre-irradiation spectra supports that chemically equivalent ices were deposited on both substrates prior to irradiation (Figure 5.3).



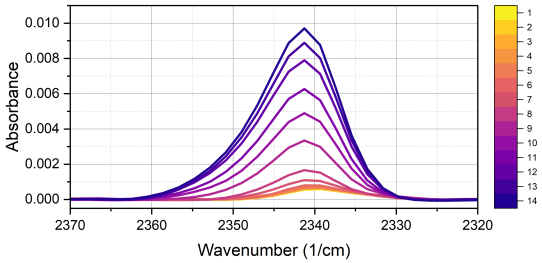
(a) Evolution of the full mid-IR spectrum of formamide-water ice.



(b) Close-up of the 1388 cm^{-1} and 1328 cm^{-1} features attributed to formamide's CH bending and CN stretching vibrations, respectively.



(c) Evolution of the 2165 cm^{-1} band assigned to OCN^-, with the shoulder at 2135 cm^{-1} corresponding to CO. These features appear post-irradiation and increase with fluence.



(d) Formation of CO_2 at 2340 cm^{-1}, showing its growth with increasing proton fluence.

Figure 5.4: Evolution of infrared spectral features for a 50:50 formamide-water ice mixture deposited on a ZnSe window and irradiated with 15 keV H^+ ions at 90 K. (a) Full mid-infrared spectrum across all fluences. (b) Formamide degradation tracked via CH and NH_2 bending modes. (c) Emergence of CO and OCN^- features post-irradiation. (d) Progressive formation of CO_2 with fluence. All spectra are colour-coded by increasing ion fluence, from pre-irradiation (spectrum 1, yellow) to post-final irradiation (spectrum 14, dark purple), with each number in between representing the fluence increment number.

When comparing Figures 5.2 and 5.4, there are notable differences between the two sets of experiments that can be observed from the spectra. The first can be seen in the full mid-IR spectra, Figures 5.2a and 5.4a. The most apparent difference between the NaCl and ZnSe spectra are the widths of the O-H stretch overlapped with NH_2/N-H stretch (∼3300 cm^{-1}) bands, and the much weaker set of features between 1500-1000 cm^{-1} on the ZnSe window compared to the NaCl window (though faint bands persist near ∼1100 cm^{-1} on ZnSe and differ from those observed on NaCl). This region commonly contains C–O stretching modes and other skeletal/deformation vibrations in

oxygen-bearing species, but the low intensity and overlap in the ZnSe spectra preclude confident assignment here. Furthermore, NaCl exhibits a larger overall evolution with dose, as evidenced by the ∼3300 cm^{-1} and ∼1690 cm^{-1} features, where the decrease in absorbance is more pronounced on the NaCl window. This result is unexpected given the order-of-magnitude difference in the total fluence values between the NaCl and ZnSe experiments; under such conditions, greater destruction of formamide features would typically be anticipated on the ZnSe window. Overall, the full mid-IR spectra in Figure 5.4a show a flatter baseline and reduced spectral artefacts (e.g. less fringing and baseline drift between successive scans), which more likely reflects differences in optical interference effects and measurement stability between the two substrate configurations rather than a difference in ice thickness. Indeed, Table 5.1 shows that the ZnSe film was not thinner than the NaCl film, but slightly thicker (278 nm vs 237 nm).

The formamide bands (∼1388 cm^{-1} and ∼1328 cm^{-1}) in Figures 5.2b and 5.4b display a more pronounced decrease with dose on the NaCl window; quantitatively, the absorbance of formamide bands decreased by ∼86% on NaCl compared to 31% on ZnSe, despite lower fluence, indicating significantly more efficient destruction on NaCl.

Figures 5.2c and 5.4c display the evolution of the 2165 cm^{-1} band assigned to OCN^-, with the shoulder at 2135 cm^{-1} corresponding to CO. Figure 5.4c shows that the CO band persists throughout irradiation, despite the ice temperature being 90 K. This reinforces the conclusion that CO was trapped within the water matrix, likely due to microporosity and hydrogen-bond site interactions, as previously discussed. The absorbance of both OCN^- and CO on the ZnSe window was markedly lower than on the NaCl window (∼0.001 vs ∼0.005, respectively), a factor-of-five difference that implies the production of these two by-products was more efficient, by dose, on the NaCl window. These values represent single experimental runs and have not been subject to formal statistical testing; the difference is therefore described in observational rather than statistical terms. Furthermore, where the spectra in Figure 5.2c indicate that OCN^- and CO started to degrade before the total irradiation was finished - showing a mid-dose maximum/plateau -, there is no sign of this in Figure 5.4c. Compared with the NaCl window, OCN^- and CO on ZnSe form very slowly initially, and then the

formation rate increases significantly at the end of irradiation.

A similar trend can be seen with the CO_2 bands pictured in Figures 5.2d and 5.4d. NaCl reaches absorbance ∼0.070 A whereas ZnSe reaches absorbance of ∼0.010 A. This indicates that CO_2 was produced less efficiently on the ZnSe window. Like NaCl, the ZnSe window shows some mild CO_2 contamination before irradiation begins; however, this will have had a negligible effect on the radiolytic production of CO_2.

To determine whether the observed chemical behaviour was substrate-dependent, the same irradiation protocol was applied to ZnSe windows, enabling a direct comparison of spectral trends and validating the reproducibility of radiolytic product formation across substrates. Any spectral differences between the NaCl and ZnSe datasets are therefore interpreted as arising from subtle variations in ice morphology or substrate-ice interactions, rather than fundamental chemical effects within the ices. In particular, hygroscopic substrates such as NaCl can develop thin, ion-rich interfacial water films under ambient handling, which can plausibly modify interfacial chemistry and the trapping/stabilisation of radiolysis products, as discussed below. As a result, substrate-specific interfacial effects provide a plausible explanation for the small differences observed between the NaCl and ZnSe spectra, without implying a fundamental change in the bulk ice chemistry [33–36].

NaCl windows are both hygroscopic and hydrophilic, meaning that under ambient handling, they can absorb moisture from the atmosphere and develop a thin water film on their surface [33]. This occurs due to the deliquescence of atmospheric H_2O, which forms an ion-rich surface brine layer even before the window enters the vacuum chamber [34]. Although measures were taken to minimise exposure (see Section 4.2.2), it was unavoidable that the NaCl windows would briefly contact atmospheric conditions before pumping and cooling. In such conditions, surface brines are known to readily absorb CO_2 from ambient air, with carbonate and bicarbonate species forming through routine interactions between CO_2 and NaCl in humid environments [35]. During irradiation, radiolytically generated radicals such as ·OH and carbonate radicals can recombine - through intermediates like peroxymonocarbonate - to liberate CO_2 from surface-bound carbonates, consistent with mechanisms observed in pulse radiol-

ysis studies of carbonate solutions, [36]. This provides a plausible pathway for trace CO_2 contamination in the early stages of the experiment, and could help to explain the slightly elevated baseline and increased CO_2 absorbance observed on the NaCl windows compared to ZnSe.

Furthermore, the presence of an ionic, water-rich interfacial layer helps to retain products such as OCN^-. As discussed in Section 5.2.1.1, Scheme 5.2 shows how OCN^- primarily forms via a multi-step reaction. When the radiolysis of the formamide-water ice produces the molecular intermediates of the aforementioned chemical pathways, the anion OCN^- is more readily stabilised due to the presence of counter-ions (Na^+) [37, 38]. OCN^- becomes ion-paired and remains in the ice as $NH_4^+OCN^-$, [39]. This process likely boosted the absorbance of the $\sim$2165 cm^{-1} band on the NaCl window, as is seen in Figure 5.4c.

Another way the aforementioned NaCl film can aid in the retention of radiolysis products is that a hydrated/ionic interface tends to produce a more compact, higher-density set of molecular layers between the window and the ice as a result of better wetting[3]. Water binds to ionic sites on NaCl and forms an ordered, tightly bound first layer [40–42]. Additionally, the thin film picked up from atmospheric contamination, discussed in previous paragraphs, can act as a compact base layer if it is present before or early in ice deposition [41, 42]. Furthermore, the ionic surface created by NaCl organises water into oscillatory, high-density hydration layers, as illustrated schematically in Figure 5.5. The water in contact with NaCl forms tightly bound, ordered hydration layers because the lattice ions strongly orient and immobilise the first few monolayers. This produces a compact interfacial region with reduced porosity and fewer molecular escape pathways, allowing volatile radiolysis products such as CO and CO_2 to remain trapped at 90 K. In contrast, ZnSe lacks charged binding sites and instead forms a more open, weakly interacting interface, leading to poorer retention. Trapped products then accumulate to higher steady-state column densities, as seen by the larger CO/CO_2 absorbance in Figures 5.2c and 5.2d. In comparison, ZnSe is more hydrophobic and therefore wets poorly; it does not develop the same dense interfacial

[3]Here 'better wetting' simply means that water spreads out and forms a compact film on the surface, rather than growing as a fluffy, porous layer.

layers at the ice-substrate boundary.

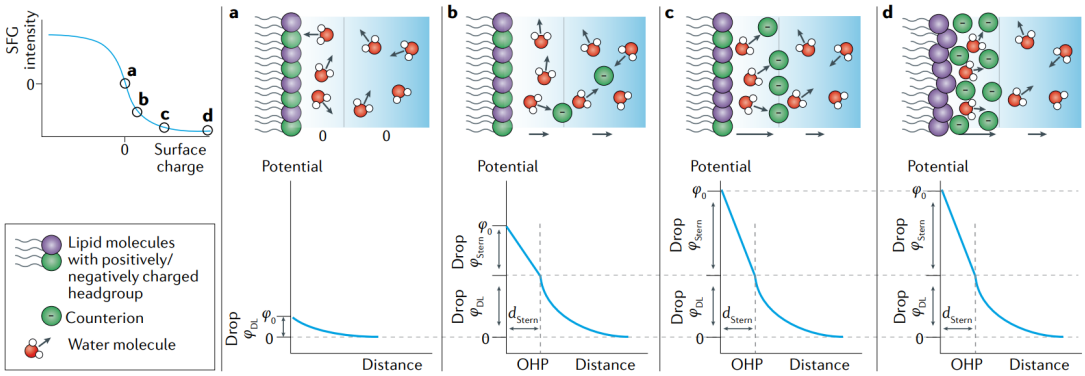


Figure 5.5: Schematic illustration of how interfacial water structure depends on surface charge. Increasing the surface charge draws counterions and water molecules into the interface, forming tightly bound hydration layers and a pronounced potential drop across the Stern and diffuse regions. In the context of this work, an ionic substrate such as NaCl behaves similarly to panels (b-d), forming a compact, ordered interfacial region that can retain volatile radiolysis products more effectively. A weakly interacting surface, such as ZnSe, resembles panel (a), showing minimal hydration layering. **Credit:** Reproduced with permission from Springer Nature: G. Gonella et al., Water at charged interfaces, *Nature Reviews Chemistry*, vol. 5, pp. 466–485, 2021, Springer Nature, [43].

Another contributing factor to the notable differences in window-type spectra is the refractive indices of the windows. A higher refractive index window reflects more light back into the ice-window interface owing to Fresnel reflection[4] [47]. The measured absorbance of a thin ice film is affected not only by molecular absorption but also by optical boundary effects. At the ice-window interface, Fresnel reflection is stronger for ZnSe than for NaCl, owing to the larger mismatch in refractive index. For the windows used in this experiment, the ZnSe windows had a refractive index of 2.4028, and the NaCl windows had a refractive index of 1.49065 [48, 49]. As a result, less light couples into the film and the standing-wave field is suppressed, so the apparent absorbance of IR bands on ZnSe substrates is reduced relative to NaCl.

Additionally, the ZnSe windows and the NaCl windows had different thermal conductivities (∼18 W m^{-1} K^{-1} at 298 K, and ∼6.5 W m^{-1} K^{-1} at 273 K, respectively [48, 49]). As ZnSe is just under three times more thermally conductive than NaCl, it is a better heat sink; ZnSe would have kept the ice slightly colder under-irradiation. The radiolysis products discussed here require molecular mobility to follow

[4]Fresnel reflection is a phenomenon whereby light, at a boundary between two materials with different refractive indices, is partially reflected, [44–46].

their proposed chemical pathways, and maintaining a cooler temperature can hinder this process. There is a chance this could have suppressed diffusion-assisted product growth. Still, it is likely it would not have had as significant an effect as the justifications stated above for the major differences between spectra.

It might be expected that heavier substrates such as ZnSe would enhance radiolysis through stronger backscattering and secondary particle production [50]. However, the results instead show the opposite trend, with ZnSe yielding smaller product bands. This indicates that backscatter is not the dominant effect under these conditions, and instead, interfacial chemistry with the windows, film morphology, and apparent absorbance provide more consistent explanations.

The ZnSe results confirm that the observed chemistry is irradiation-driven, while the NaCl substrate strongly modulates the apparent efficiency and retention (and thus the band intensities) of the radiolysis products. However, it is essential to note that a significantly higher fluence was required to achieve comparable levels of formamide destruction on the ZnSe window, and overall product formation was markedly lower. Moreover, additional mid-IR features between 1000-1500 cm^{-1} are observed in the NaCl experiments but are absent or diminished on ZnSe. These differences suggest that while the dominant radiolysis pathways are consistent across substrates (i.e. formamide destruction accompanied by the formation of CO, CO_2, and OCN^-), the relative yields and spectral prominence of individual products are influenced by substrate-ice interactions, potentially behaving in a catalytic manner by modifying the local interfacial environment and thereby favouring particular reaction pathways [51, 52]. However, confirming true catalysis (i.e. specific lowering of activation barriers and catalyst regeneration) would require dedicated mechanistic experiments and is beyond the scope of this thesis.

5.2.2 Oxygen Ion Irradiation

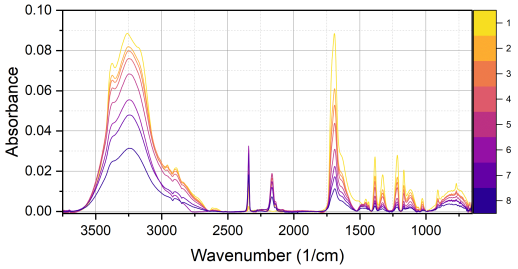
5.2.2.1 NaCl Window Experiments

To investigate the effect of heavier, higher-LET ions on the formamide-water ice mixture, additional experiments were carried out using 30 keV O^{2+} ions. As discussed in

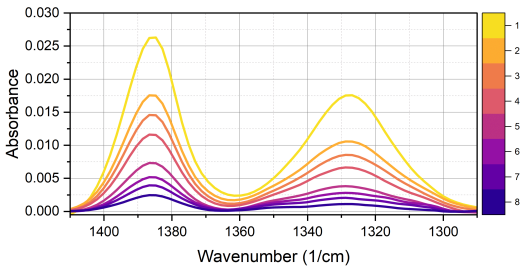
Section 3.2.1 and illustrated in Figure 3.9, SRIM calculations show that oxygen ions at these energies have projected ranges of order ∼100 nm in H_2O ice, significantly shorter than the film thicknesses used here (∼230-280 nm; Table 5.1). Unlike the proton case, where ions only partially stop within the ice, the 30 keV oxygen ions deposit essentially their full kinetic energy inside the formamide-water film. This makes the oxygen experiments a closer analogue for shallow implantation of magnetospheric O^+/O^{2+} at Europa, where tens-of-keV ions are expected to process the uppermost ∼100 nm of the surface [11].

Oxygen has a much higher electronic stopping power than hydrogen at comparable energies, such that the chemical evolution is compressed into lower fluences. The same qualitative sequence is still present as in the proton data: (i) initial destruction of formamide, accompanied by the growth of OCN^-, CO and CO_2; (ii) a plateau in the parent and product bands; and in some cases (iii) a late-stage regime where products begin to decline. However, the transition between these stages occurs at fluences that are typically a few times lower than for protons.

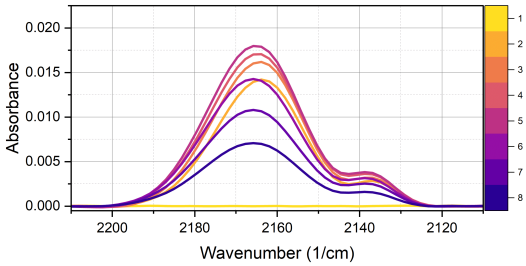
A summary of the cumulative fluence steps and their mapping to the spectrum numbers in Figures 5.6 and 5.9 is given in Table 5.2. As a reference point for cross-comparison, on NaCl a cumulative fluence of $\sim 3 \times 10^{14}$ ions cm^{-2} falls between spectra 4 and 5 in the O_2^+ dataset (Figure 5.6a), and it also falls between spectra 4 and 5 in the H^+ NaCl dataset (Figure 5.2a). Throughout this section, whenever specific fluence values are quoted, the corresponding spectrum numbers are given alongside them to make comparisons between figures unambiguous.



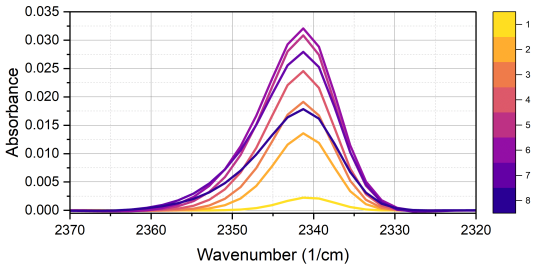
(a) Evolution of the full mid-IR spectrum of formamide-water ice.



(b) Close-up of the 1388 cm^{-1} and 1328 cm^{-1} features attributed to formamide's CH bending and CN stretching vibrations, respectively.



(c) Emergence and subsequent evolution of the OCN^- band at ~2165 cm^{-1}, with the shoulder at ~2135 cm^{-1} corresponding to CO, as a function of ion fluence.



(d) Evolution of the CO_2 band at ~2340 cm^{-1} as a function of ion fluence.

Figure 5.6: Evolution of infrared spectral features for a 50:50 formamide-water ice mixture deposited on a NaCl window and irradiated with 30 keV O^{2+} ions at 90 K. (a) Full mid-infrared spectrum across all fluences. (b) Formamide degradation tracked via CH and NH_2 bending modes. (c) Emergence of CO and OCN^- features post-irradiation. (d) Progressive evolution and subsequent decay of CO_2 with fluence. All spectra are colour-coded by increasing ion fluence, from pre-irradiation (spectrum 1, yellow) to post-final irradiation (spectrum 8, dark purple), with each number in between representing the fluence increment number.

The full spectra in Figure 5.6a show that the O-H/N-H stretching complex near 3300 cm^{-1} exhibits a more structured, shouldered profile under oxygen irradiation compared to the smoother single-band envelope seen under proton irradiation (Figure 5.7), though the substantially lower O^{2+} fluence relative to H^+ means this difference cannot be attributed to ion type alone. The band wings become more extended and the peak maximum shifts slightly, indicating a higher degree of lattice disorder and hydrogen-bond rearrangement. The H_2O bending mode around 1690 cm^{-1} similarly decreases and broadens with fluence. These changes are consistent with dense ion tracks that locally amorphise and compact the ice, in line with the higher stopping power of O^{2+}.

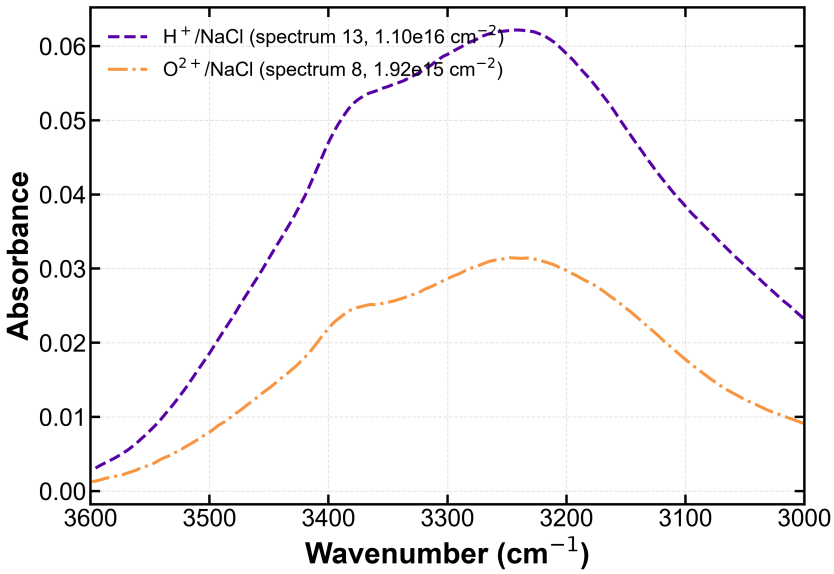


Figure 5.7: Comparison of the O-H/N-H stretching region (∼3000–3600 cm^{-1}) for formamide-water ice irradiated with 15 keV H^+ ions (dashed line) and 30 keV O^{2+} ions (dash-dot line), shown at the final spectrum of each run (H^+: 1.10×10^{16} cm^{-2}; O^{2+}: 1.92×10^{15} cm^{-2}).

Focusing on the formamide modes (Figure 5.6b), both the 1388 cm^{-1} (CH bend) and 1328 cm^{-1} (CN stretch) bands show a rapid, almost monotonic decrease with fluence. On NaCl, the formamide bands have already lost a substantial fraction of their initial absorbance by spectrum 4 (cumulative fluence $\sim 2.5 \times 10^{14}$ ions cm^{-2}), and approach a shallow plateau by spectra 7-8 (cumulative fluence $\gtrsim 10^{15}$ ions cm^{-2}). Compared to the proton experiment on NaCl, where similar degrees of destruction only occur at much higher cumulative fluence (spectra 8-10 in Figure 5.2b), this confirms that oxygen removes formamide more efficiently per ion.

The CO/OCN^- region (Figure 5.6c) follows the same general pattern as in the hydrogen case, but compressed in fluence. OCN^- at ∼2165 cm^{-1} and the CO shoulder at ∼2135 cm^{-1} become clearly visible by spectrum 3 (cumulative fluence of order 10^{14} ions cm^{-2}). Both bands grow steadily up to around spectrum 5 (cumulative fluence $\sim 5 \times 10^{14}$ ions cm^{-2}), after which the peak heights begin to level off and then decline slightly by spectrum 8 (final cumulative fluence $\sim 2 \times 10^{15}$ ions cm^{-2}). The mid-dose maximum is therefore reached at substantially lower fluence than in the proton NaCl experiment, where OCN^- and CO only start to decline at much higher cumulative doses (spectra 7-9 in Figure 5.2c). This suggests that the high local energy

density of oxygen tracks not only accelerates formation of these products, but also their secondary processing and eventual destruction.

CO_2 at ~2340 cm^{-1} (Figure 5.6d) behaves similarly to CO and OCN^-, but its decline is more subtle. The CO_2 band grows rapidly between spectra 2 and 5, then flattens, with only a modest reduction in peak absorbance, in comparison to CO and OCN^-, between spectra 7 and 8. Within the signal-to-noise of the spectra, CO_2 is best described as reaching a late plateau, with a downturn at the penultimate irradiation. Importantly, there is no evidence that CO_2 starts to be destroyed earlier than CO; if anything, CO shows a slightly more pronounced decrease than CO_2 in the final spectra. Overall, oxygen on NaCl therefore produces a familiar product suite (OCN^-, CO, CO_2) but drives both their formation and their self-destruction at significantly lower fluences than protons.

5.2.2.2 ZnSe Window Experiments

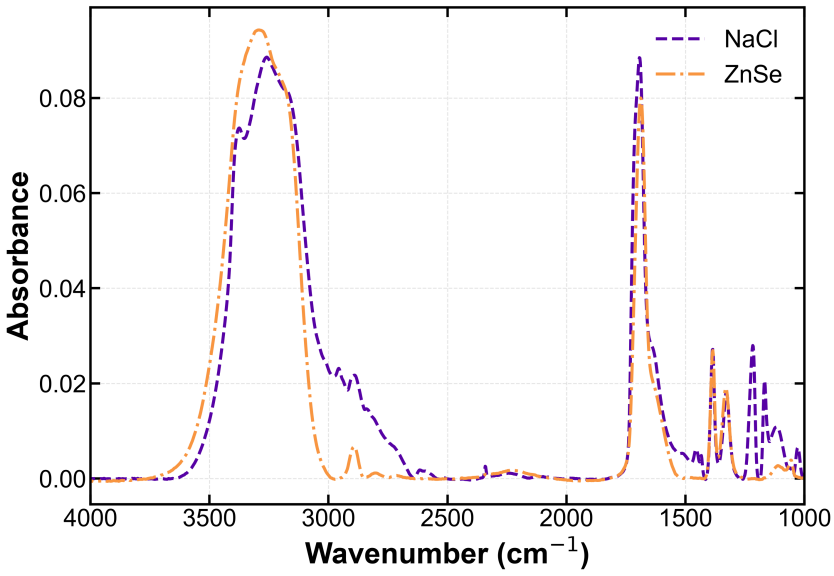
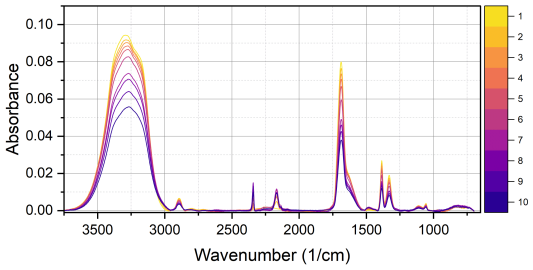
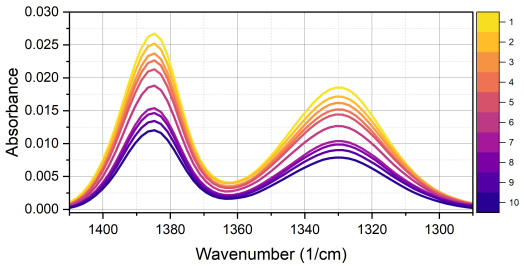


Figure 5.8: Comparison of the infrared spectra of formamide-water ice deposited on NaCl (dashed line) and ZnSe (dash-dot line) substrates under equivalent deposition conditions at 90 K, before oxygen irradiation. The close agreement in band positions and relative intensities of the key formamide features (CH bend at ~1388 cm^{-1}, CN stretch at ~1328 cm^{-1}, C=O stretch at ~1690 cm^{-1}) supports that the two ices are chemically equivalent prior to irradiation, and that any subsequent differences in spectral evolution can be attributed to substrate effects rather than differences in initial ice composition.

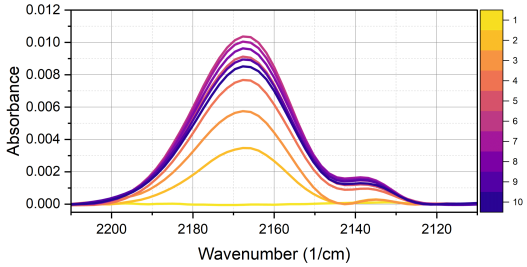
As with the proton experiments, ZnSe serves primarily as a control substrate to distinguish intrinsic ice chemistry from NaCl-induced interfacial effects (Sections 4.2.2 and 5.2.1.2). The pre-irradiation spectra collected on both substrates confirm that chemically equivalent formamide-water ices were deposited prior to irradiation, as shown in Figure 5.8. The full spectra in Figure 5.9a show that under oxygen irradiation, the O-H/N-H stretch and H_2O bending bands still broaden and decrease, but the overall evolution with fluence is gentler than on NaCl (Figure 5.6a). The absence of additional small features between 1500 and 1000 cm^{-1} again suggests a cleaner, less reactive interface on ZnSe.



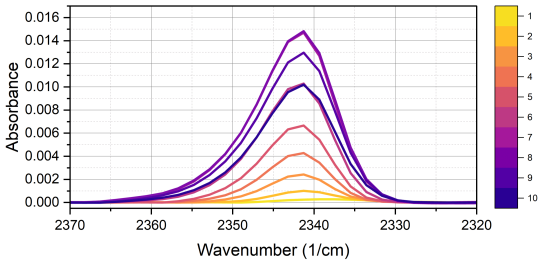
(a) Evolution of the full mid-IR spectrum of formamide-water ice.



(b) Close-up of the 1388 cm^{-1} and 1328 cm^{-1} features attributed to formamide's CH bending and CN stretching vibrations, respectively.



(c) Emergence and subsequent evolution of the OCN^- band at ~2165 cm^{-1}, with the shoulder at ~2135 cm^{-1} corresponding to CO, as a function of ion fluence.



(d) Evolution of the CO_2 band at ~2340 cm^{-1} as a function of ion fluence.

Figure 5.9: Evolution of infrared spectral features for a 50:50 formamide-water ice mixture deposited on a ZnSe window and irradiated with 30 keV O^{2+} ions at 90 K. (a) Full mid-infrared spectrum across all fluences. (b) Formamide degradation tracked via CH and NH_2 bending modes. (c) Emergence of CO and OCN^- features post-irradiation. (d) Progressive evolution and subsequent decay of CO_2 with fluence. All spectra are colour-coded by increasing ion fluence, from pre-irradiation (spectrum 1, yellow) to post-final irradiation (spectrum 10, dark purple), with each number in between representing the fluence increment number.

In Figure 5.9b, the 1388 and 1328 cm^{-1} formamide bands decrease steadily with dose, but remain clearly visible even by spectrum 10 (final cumulative fluence $\sim 3 \times 10^{15}$ ions cm^{-2}). The two bands track each other closely throughout; any asymmetry between them is modest and can be attributed to slightly different sensitivity to local matrix changes. Compared to NaCl, considerably more fluence is required to reach a similar fractional loss of formamide, reinforcing the idea that the ionic, hydrated NaCl interface both enhances destruction and traps radiolysis products.

The CO/OCN^- complex on ZnSe (Figure 5.9c) also displays a smoother evolution than on NaCl. OCN^- and CO emerge by spectrum 3 (cumulative fluence of order 10^{13} ions cm^{-2}) and continue to grow until spectra 7-8 (cumulative fluence of a few $\times 10^{14}$ ions cm^{-2}), beyond this point, the band strengths largely plateau: any decline by spectra 9-10 is small compared with the NaCl case. In qualitative terms, ZnSe exhibits the same growth to saturation sequence as NaCl, but the onset of any self-destruction is clearly shifted to higher fluence and is much less pronounced.

CO_2 at 2340 cm^{-1} (Figure 5.9d) grows monotonically over the entire irradiation series, from spectrum 2 up to spectrum 8, and does not show a downturn as sharp as NaCl, within the explored fluence range. Its peak absorbance remains significantly smaller than on NaCl at comparable fluence, consistent with both reduced total destruction of formamide and less efficient trapping of CO_2 near the interface. Taken together, the ZnSe results confirm that oxygen drives the same basic chemistry as protons, but the window material strongly modulates both the apparent destruction rate and the steady-state column densities of OCN^-, CO, and CO_2.

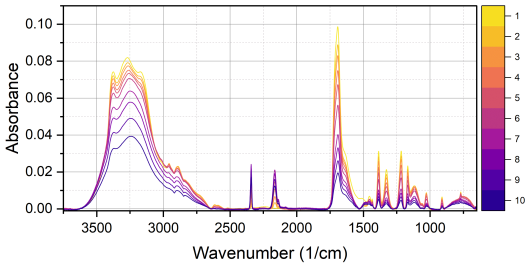
5.2.3 Sulphur Ion Irradiation

Sulphur ion irradiation represents the highest-LET end of the ion series studied here. Experiments were carried out with 60 keV S^{5+}, chosen both for practical reasons (matching the available charge-state/voltage combinations at Atomki-ECRIS) and because keV/amu sulphur ions are a key component of Europa's magnetospheric environment, supplied mainly by Io's plasma torus [11]. SRIM calculations show that at these energies S^{5+} has a projected range that is even shorter than oxygen, tens of nanome-

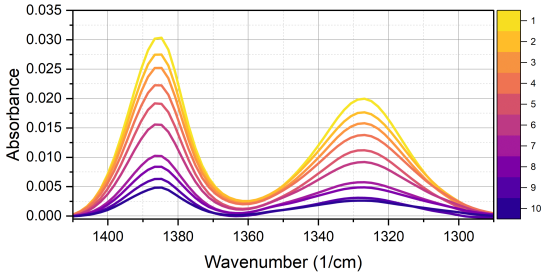
tres in pure water ice. Thus, essentially all energy is deposited in a very shallow layer near the vacuum interface and the chemistry is strongly confined to near-surface layers rather than being distributed throughout the bulk.

The sulphur experiments again show the same qualitative pattern as hydrogen and oxygen: destruction of formamide, growth of OCN^-, CO, and CO_2, and, in some cases, a subsequent flattening or decline of product bands at the highest fluences. However, both the characteristic fluence scales and the relative importance of NaCl vs ZnSe effects are pushed to more extreme values. As before, the mapping between spectrum index and cumulative fluence is given in Table 5.2. For sulphur on NaCl, the lowest fluence step corresponds to $\sim 6 \times 10^{12}$ ions cm^{-2} (spectrum 2 in Figure 5.10a), and the final spectrum (spectrum 10) reaches cumulative fluences of the order of 10^{15} ions cm^{-2} (see Table 5.2). On ZnSe, the corresponding range spans from $\sim 10^{13}$ ions cm^{-2} (spectrum 2) up to cumulative fluences also approaching $\sim 10^{15}$ ions cm^{-2} (spectrum 8).

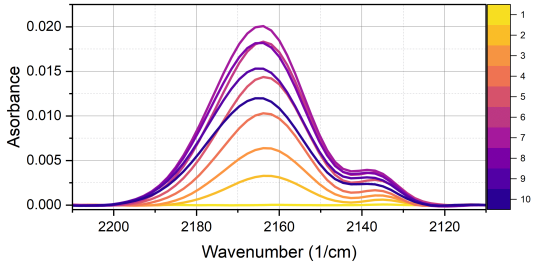
5.2.3.1 NaCl Window Experiments



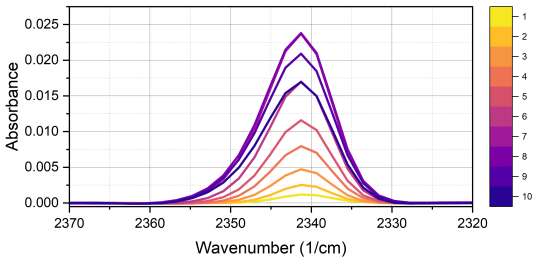
(a) Evolution of the full mid-IR spectrum of formamide-water ice.



(b) Close-up of the 1388 cm^{-1} and 1328 cm^{-1} features attributed to formamide's CH bending and CN stretching vibrations, respectively.



(c) Evolution of the 2165 cm^{-1} band assigned to OCN^-, with the shoulder at 2135 cm^{-1} corresponding to CO. These features appear post-irradiation and increase with fluence.



(d) Formation of CO_2 at 2340 cm^{-1}, showing its growth with increasing proton fluence.

Figure 5.10: Evolution of infrared spectral features for a 50:50 formamide-water ice mixture deposited on a NaCl window and irradiated with 60 keV S^{5+} ions at 90 K. (a) Full mid-infrared spectrum across all fluences. (b) Formamide degradation tracked via CH and NH_2 bending modes. (c) Emergence of CO and OCN^- features post-irradiation. (d) Progressive formation of CO_2 with fluence. All spectra are colour-coded by increasing ion fluence, from pre-irradiation (spectrum 1, yellow) to post-final irradiation (spectrum 10, dark purple), with each number in between representing the fluence increment number.

The full spectra in Figure 5.10a show that sulphur produces clear changes even at the lowest fluence steps. The O-H/N-H stretch and H_2O bending bands decrease noticeably with each increment, and additional broadening on the low-frequency side of the stretch band suggests the formation of more strongly hydrogen-bonded and/or more complex, less-volatile material (potentially including cross-linked or oligomeric products) within the track cores. The per-step evolution is at least as strong as in the oxygen experiment, but not so extreme as to erase all volatile signatures; the spectrum retains recognisable

water and formamide features throughout the series.

The formamide bands at 1388 and 1328 cm^{-1} (Figure 5.10b) decline steadily with fluence but do not vanish completely within the explored range. By spectrum 5 (cumulative fluence of order 5^{13} ions cm^{-2}; see Table 5.2) both bands have dropped noticeably, and by spectrum 10 ($\sim 1 \times 10^{15}$ ions cm^{-2}) their peak absorbances are reduced by roughly a factor of 2-3 relative to the pre-irradiation spectrum. This is faster destruction per ion than in the proton-NaCl case, and broadly comparable to, or slightly faster than, oxygen on NaCl, but not so extreme that the bands are fully extinguished. Hence Sulphur drives efficient but not instantaneous removal of formamide from the NaCl-supported ice.

The OCN^-/CO complex (Figure 5.10c) shows a pronounced growth phase followed by a mild late-stage decline. OCN^- at 2165 cm^{-1} and CO at 2135 cm^{-1} are clearly present by spectrum 3 (cumulative fluence of order 10^{13} ions cm^{-2}) and reach their maximum strengths around spectra 6-7 ($\sim 10^{14}$ ions cm^{-2}). CO formation is already efficient in the earliest sulphur fluence steps, and by $F \sim (3–6) \times 10^{14}$ ions cm^{-2} the CO and CO_2 bands are comparable in strength to those obtained with oxygen at similar fluence. Within the probed range, oxygen appears at least as effective as sulphur at depleting the formamide bands on NaCl, despite sulphur's higher stopping power. They do not clearly exceed the proton yields. Beyond the maximum, the bands decrease modestly towards spectrum 10, indicating that self-destruction sets in once the accumulated dose in the near-surface region becomes large. However, the downturn is less dramatic than in the oxygen case, where the CO/OCN^- bands on NaCl show a clearer late-fluence collapse.

CO_2 on NaCl (Figure 5.10d) again behaves very similarly under oxygen and sulphur. The 2340 cm^{-1} band grows steadily from spectrum 2 through to approximately spectrum 6-7, then flattens and shows at most a modest decrease by spectrum 10. Within the uncertainties, the growth and destruction timescales for CO_2 under sulphur on NaCl are comparable to those seen for oxygen on NaCl, rather than being dramatically shorter or steeper. Thus, sulphur can be viewed as a somewhat more forceful version of oxygen on this substrate: the same products are formed, with similar peak yields

and similar onset of late-stage processing, but at slightly lower cumulative fluence and with somewhat stronger matrix disruption.

5.2.3.2 ZnSe Window Experiments

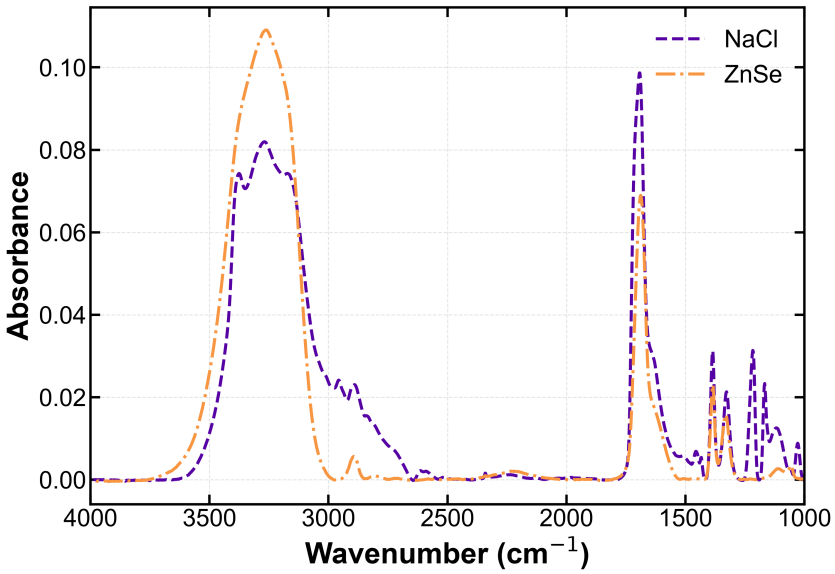
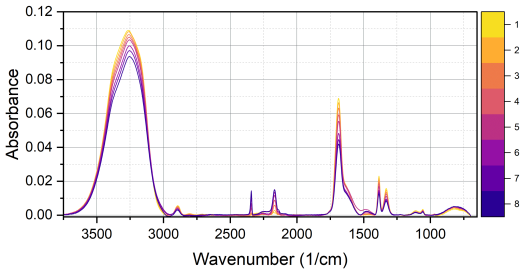
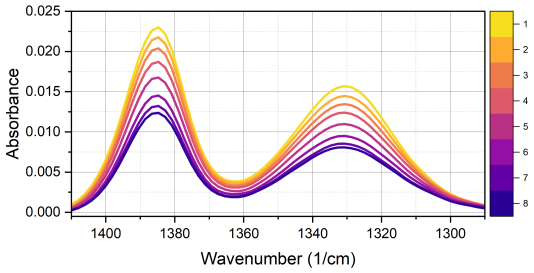


Figure 5.11: Comparison of the infrared spectra of formamide-water ice deposited on NaCl (dashed line) and ZnSe (dash-dot line) substrates under equivalent deposition conditions at 90 K, before sulphur irradiation. The close agreement in band positions and relative intensities of the key formamide features (CH bend at ∼1388 cm^{-1}, CN stretch at ∼1328 cm^{-1}, C=O stretch at ∼1690 cm^{-1}) supports that the two ices are chemically equivalent prior to irradiation, and that any subsequent differences in spectral evolution can be attributed to substrate effects rather than differences in initial ice composition.

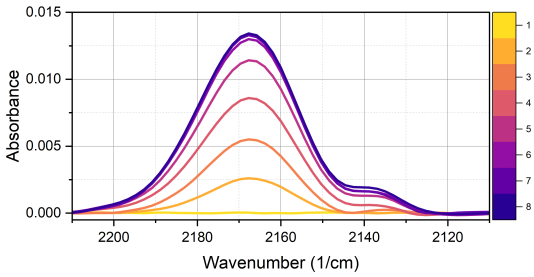
The pre-irradiation spectra collected on both substrates confirm that chemically equivalent formamide-water ices were deposited prior to irradiation, as shown in Figure 5.11. On ZnSe, the full spectra in Figure 5.12a again show a milder evolution than on NaCl. The O-H/N-H stretch band decreases with fluence, but retains a relatively symmetric shape; there is less evidence for strong additional broadening or for the growth of mid-IR features associated with complex surface chemistry. This is consistent with sulphur delivering energy into a thin near-surface region that is less strongly confined than on NaCl, allowing radicals and volatile fragments to escape more readily.



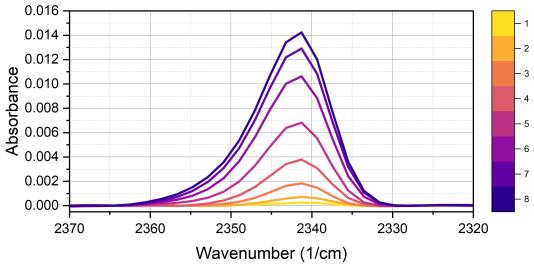
(a) Evolution of the full mid-IR spectrum of formamide-water ice.



(b) Close-up of the 1388 cm^{-1} and 1328 cm^{-1} features attributed to formamide's CH bending and CN stretching vibrations, respectively.



(c) Evolution of the 2165 cm^{-1} band assigned to OCN^-, with the shoulder at 2135 cm^{-1} corresponding to CO. These features appear post-irradiation and increase with fluence.



(d) Formation of CO_2 at 2340 cm^{-1}, showing its growth with increasing proton fluence.

Figure 5.12: Evolution of infrared spectral features for a 50:50 formamide-water ice mixture deposited on a ZnSe window and irradiated with 60 keV S^{5+} ions at 90 K. (a) Full mid-infrared spectrum across all fluences. (b) Formamide degradation tracked via CH and NH_2 bending modes. (c) Emergence of CO and OCN^- features post-irradiation. (d) Progressive formation of CO_2 with fluence. All spectra are colour-coded by increasing ion fluence, from pre-irradiation (spectrum 1, yellow) to post-final irradiation (spectrum 8, dark purple), with each number in between representing the fluence increment number.

The formamide bands in Figure 5.12b decrease approximately linearly over the irradiation sequence. On ZnSe, the formamide bands decrease more gradually with sulphur fluence and begin to show a gentle plateau at intermediate doses (spectra 5-7, $F \sim (4\text{in-situ-}11) \times 10^{14}$ ions cm^{-2}). The plateau occurs at a higher residual absorbance than in the NaCl experiment, but still indicates that a fraction of the formamide population becomes resistant to further destruction under continued irradiation. An alternative explanation is geometric rather than chemical. Since S^{5+} deposits energy within only the uppermost tens of nanometres, the FTIR signal (which averages over

the full film) can appear to plateau once the surface layer is heavily processed. This is a noticeably slower destruction than on NaCl for the same cumulative fluence, mirroring the trend already seen for protons and oxygen. Of all the ion/substrate combinations, sulphur on ZnSe shows some of the most persistent formamide signatures.

OCN^- and CO on ZnSe (Figure 5.12c) grow steadily with fluence and then approach a plateau at the highest fluence steps. There is no strong evidence for a late-stage downturn analogous to that seen on NaCl: by spectrum 8, the 2165/2135 cm^{-1} complex has essentially saturated but has not yet clearly begun to decline. On ZnSe, the CO, CO_2, and OCN^- bands produced by sulphur irradiation exhibit peak absorbances similar to or slightly higher than those in the corresponding oxygen and proton experiments at comparable fluence. However, their growth is more gradual, and the subsequent decline is gentler, consistent with the ZnSe interface moderating secondary destruction even for high-LET projectiles.

The CO_2 band on ZnSe (Figure 5.12d) grows monotonically across the full fluence range explored. As with oxygen on ZnSe, there is no convincing sign of CO_2 destruction; any changes in peak height between the last few spectra are small compared to the overall growth. The absolute CO_2 yield remains modest compared to NaCl for the same projectile, and is comparable to or lower than the oxygen ZnSe experiment. Thus, sulphur on ZnSe is best described as producing relatively low but steadily increasing amounts of CO_2 without entering a strong destructive regime within the accessible fluences.

In summary, oxygen and sulphur irradiation both reproduce the basic chemistry established under proton bombardment - destruction of formamide and formation of OCN^-, CO and CO_2 - but compress it into progressively lower fluence ranges as the projectile mass and stopping power increase. On NaCl, higher-LET ions (oxygen and especially sulphur) drive earlier onset of product saturation and modest late-stage destruction, while on ZnSe the same products grow more slowly, achieve lower peak abundances, and either plateau or continue to increase over the available fluence range. Comparing ions at similar cumulative fluence, formamide survives best under hydrogen, whereas oxygen and sulphur both remove it more efficiently, with broadly comparable

destruction levels that vary slightly with substrate. The NaCl vs ZnSe contrast is strongest for the heavier ions, reflecting the combined influence of high-LET tracks and interfacial chemistry on radiolytic outcomes. This ordering is fully consistent with the LET hierarchy (H < O < S) and emphasises that both projectile type and interfacial chemistry jointly control the radiolytic outcomes in formamide-water ices relevant to Europa's surface.

A direct comparison with previous laboratory irradiation studies shows that the overall behaviour observed here is consistent with the established picture for irradiated organic-containing ices. Comparable radiolysis products to those observed in this work (including CO, CO_2, and OCN^-) have been reported previously for proton irradiation of pure solid formamide [32]. More broadly, ion-irradiation studies of astrophysical ice analogues consistently show that increasing stopping power (higher LET) increases the chemical change per incident particle, such that qualitatively similar product sets can appear at lower cumulative fluence and product bands often reach plateaus earlier as precursors are depleted and/or secondary processing becomes important [53, 54]. Importantly, the present experiments use mixed water:formamide ices, so the product distribution and growth behaviour are not expected to match pure-formamide studies one-to-one: H_2O radiolysis supplies additional oxidising fragments (e.g. OH/O and related products) and the hydrogen-bonded matrix modifies trapping, diffusion, and condensed-phase band profiles [27, 55, 56]. Accordingly, agreement is assessed primarily in terms of the dominant product identities (CO, CO_2, and OCN^-) and the qualitative LET-ordering, rather than exact peak abundances, which can vary with mixture composition, temperature, thickness, and analysis choices (e.g. band strengths and integration limits) [27, 28, 32].

5.3 Radiation Chemical Yields (G-values) for Destruction and Formation

To quantify the efficiency of ion-induced chemistry, radiation chemical yields (G-values) were determined for both the destruction of formamide and the formation of CO, CO_2, and OCN^-. G-values are defined as the number of molecules produced or destroyed per

100 eV of energy deposited, and were calculated using the dose-dependent band area evolution, as described in detail in Section 3.3.3 and Appendix A. The G-values were calculated by integrating FTIR absorbance bands, converting the column densities to molecular yields per 100 eV using known band strengths, plotting the column densities against cumulative energy fluence, and extracting the initial linear slope.

$$G = \pm 100 \times \left(\frac{dN}{dE}\right) \tag{5.1}$$

Equation 5.1 shows the overarching relationship used to calculate G-values. Here, N is the molecular column density (molecules/cm^2), determined from integrated FTIR band areas and known band strengths, and E is the cumulative energy fluence (eV/cm^2). The slope $\frac{dN}{dE}$ of the initial linear dose-response gives the yield expressed as the number of molecules formed or destroyed per 100 eV of absorbed energy. Positive values denote product formation ($G(+P)$), while negative values denote precursor destruction ($G(-M)$). This "overarching" equation summarises the calculation without detailing intermediate steps, such as the integration of FTIR bands or the conversion to column densities. The intermediate steps are detailed in Section 3.3.3.

Table 5.3 presents the radiolysis yields (G-values) for the destruction of formamide and the formation of key products (CO, CO_2, OCN^-) on NaCl and ZnSe windows under ion irradiation. This comparison is important because it highlights not only the efficiency of formamide destruction and product formation, but also the influence of the underlying substrate and ion species on the observed chemistry - a critical factor when extrapolating to planetary surface conditions.

In general, oxygen ions produced the highest formation yields, particularly for OCN^- and CO, consistent with their relatively high LET and moderate penetration depth. On NaCl, sulphur ions give formation yields that are of the same order of magnitude, though typically slightly lower than oxygen. On ZnSe, the contrast is stronger: oxygen clearly dominates OCN^- and CO production, while sulphur yields are noticeably smaller. Proton yields are lower and require higher fluences to achieve similar degradation levels, particularly on ZnSe.

On NaCl windows, the formamide destruction yields ($G(-M)$) for all ions are con-

Table 5.3: Radiolysis yields (G-values) for formamide on NaCl and ZnSe windows under ion irradiation. Listed are destruction yields $G(-M)$ and product formation yields $G(+P)$ (molecules per 100 eV) for the main infrared absorption bands. Uncertainties are quoted with two significant figures; central values are rounded consistently. A dash indicates not applicable.

Ion	Window	Fluence (particles cm^{-2})	Bands (cm^{-1})	Assignment	$G(-M)$ (molecules/100 eV)	$G(+P)$ (molecules/100 eV)
			1388	NH_2CHO	$(3.36 \pm 0.06) \times 10^{0}$	—
			1328	NH_2CHO	$(3.71 \pm 0.09) \times 10^{0}$	—
H^+	NaCl	1.10×10^{16}	2340	CO_2	—	$(5.58 \pm 0.011) \times 10^{-2}$
			2165	OCN^-	—	$(2.78 \pm 0.035) \times 10^{-1}$
			2135	CO	—	$(2.53 \pm 0.040) \times 10^{-1}$
			1388	NH_2CHO	$(3.56 \pm 0.22) \times 10^{0}$	—
			1328	NH_2CHO	$(3.57 \pm 0.18) \times 10^{0}$	—
O^{2+}	NaCl	1.92×10^{15}	2340	CO_2	—	$(9.71 \pm 0.13) \times 10^{-2}$
			2165	OCN^-	—	$(2.93 \pm 0.18) \times 10^{-1}$
			2135	CO	—	$(2.72 \pm 0.081) \times 10^{-1}$
			1388	NH_2CHO	$(2.96 \pm 0.02) \times 10^{0}$	—
			1328	NH_2CHO	$(2.40 \pm 0.01) \times 10^{0}$	—
S^{5+}	NaCl	9.65×10^{14}	2340	CO_2	—	$(5.68 \pm 0.010) \times 10^{-2}$
			2165	OCN^-	—	$(2.06 \pm 0.0082) \times 10^{-1}$
			2135	CO	—	$(2.59 \pm 0.011) \times 10^{-1}$
			1388	NH_2CHO	$(4.49)^{\dagger} \times 10^{-2}$	—
			1328	NH_2CHO	$(5.30)^{\dagger} \times 10^{-2}$	—
H^+	ZnSe	1.94×10^{17}	2340	CO_2	—	$(1.18)^{\dagger} \times 10^{-3}$
			2165	OCN^-	—	$(8.92)^{\dagger} \times 10^{-3}$
			2135	CO	—	$(1.47)^{\dagger} \times 10^{-2}$
			1388	NH_2CHO	$(4.75 \pm 0.03) \times 10^{0}$	—
			1328	NH_2CHO	$(2.74 \pm 0.01) \times 10^{0}$	—
O^{2+}	ZnSe	3.16×10^{15}	2340	CO_2	—	$(5.54 \pm 0.0042) \times 10^{-2}$
			2165	OCN^-	—	$(6.29 \pm 0.049) \times 10^{-1}$
			2135	CO	—	$(3.41 \pm 0.017) \times 10^{-1}$
			1388	NH_2CHO	$(1.69 \pm 0.04) \times 10^{0}$	—
			1328	NH_2CHO	$(1.85 \pm 0.06) \times 10^{0}$	—
S^{5+}	ZnSe	1.08×10^{15}	2340	CO_2	—	$(1.56 \pm 0.0019) \times 10^{-2}$
			2165	OCN^-	—	$(1.60 \pm 0.049) \times 10^{-1}$
			2135	CO	—	$(4.24 \pm 0.0097) \times 10^{-2}$

Notes: Uncertainties represent the statistical error on the linear fit to the initial dose-response slope.

† Uncertainty not quoted. The exceptionally high fluence used in the H^+/ZnSe experiment (1.94×10^{17} particles cm^{-2}) results in a very large number of data points over which the initial linear slope is fitted, driving the statistical uncertainty on the fit to near zero. This does not reflect the true uncertainty on the G-value, which is dominated by systematic contributions from band strength uncertainties, ice thickness determination, and baseline placement, estimated to be of order 20-30% and vastly exceeding the statistical errors. Central values for H^+/ZnSe should therefore be treated as order-of-magnitude estimates only.

sistently in the range of ∼2.4-3.7 molecules/100 eV. The narrow spread of values here shows that the energetic destruction from H^+, O^{2+}, and S^{5+} all lead to comparably efficient formamide destruction. However, on ZnSe windows, the destruction of formamide is less efficient. Despite most total fluences for ZnSe windows being roughly an order of magnitude larger than those used on the NaCl windows, the G-values for H^+ irradiation are orders of magnitude lower on the ZnSe windows, in comparison. For O^{2+} and S^{5+} irradiation of the ZnSe windows, the G-values are much more comparable, closer to the range of ∼1.7-4.8 molecules/100 eV. Similarly to what was discussed in Section 5.2.1.2, this observation suggests there was a strong substrate effect, particularly for the H^+/ZnSe case. These trends reinforce that LET and substrate properties jointly influence radiolytic outcomes, rather than just the ion species alone.

On the NaCl window, OCN^- and CO have the highest yields (∼0.2-0.3 molecules/100 eV), which is relatively consistent for the different ions used during radiolysis. This result is somewhat unexpected, particularly because in every instance of irradiation type, CO_2 consistently exhibited a higher final absorbance than OCN^- and CO (see Figures 5.2, 5.6, and 5.10 for spectral examples of this). Although CO_2 showed the largest final absorbance, this does not equate to the highest G-value. Its band at 2340 cm^{-1} is intrinsically strong [27, 57], so fewer molecules produce a stronger peak. Since G-values are derived from the initial slope of formation (not total end absorbance), the higher early-time yields of OCN^- and CO explain their larger G-values. Given CO_2 tends to form secondarily, as shown in Scheme 5.1, the initial slope may be lower even when its cumulative band appears larger. Finally, end absorbance values depend upon the specific parameters of the experiment; final peak integrated areas reflect total fluence, ice thickness, and matrix effects, not just intrinsic productivity per unit energy. In summary, despite CO_2 ending with a larger absorbance, this outcome is still consistent with OCN^- and CO having higher initial formation efficiency per energy deposited.

In comparison, on the ZnSe windows the H^+ product yields are substantially lower than on NaCl, typically by factors of ∼20-50 (i.e. ∼1-2 orders of magnitude; Table 5.3). By contrast, the O^{2+} and S^{5+} product yields on ZnSe are broadly comparable to those

on NaCl for most bands, differing only by factors of order unity to a few (Table 5.3). The same suppression patterns for H^+ ion irradiation are observed in the destruction of formamide, but the substrate hinders secondary-product chemistry. For the heavier ions, however, products are observed on both substrates at similar efficiencies. On NaCl, heavy ions (O^{2+}, S^{5+}) and protons all yield similar $G(-M)$ values in the range ∼2.4-3.7 molecules/100 eV. This suggests that, once normalised to deposited energy, formamide destruction is relatively insensitive to the specific projectile species under these conditions and is instead primarily governed by the total local energy density delivered to the ice. Despite this, the substrate effect is more dramatic than the ion effect, especially when comparing H^+/NaCl vs H^+/ZnSe. This is interesting as irradiation chemistry is usually interpreted in terms of the projectile (ion type/LET/energy deposition), but here the results show that the substrate can dominate the outcome. This observation is unusual, as in several previous irradiation experiments of astrophysical ice analogues, the infrared-transparent substrate (e.g. KBr, CsI, NaCl, ZnSe) has been treated as an inert support, with the assumption that they have no influence on the observed radiochemistry [58–61]. The present results, however, suggest that this assumption may not always hold, particularly for NaCl. Furthermore, on NaCl, H^+ irradiation produces destruction and product yields comparable to those of heavier ions, whereas on ZnSe the same irradiation yields minimal observable chemistry. This indicates that NaCl does not behave as a passive substrate under these conditions: substrate-ice interactions (e.g. ionic surface effects and/or irradiation-induced charge trapping at the interface) may plausibly enhance the local production and/or retention of radiolysis products such as OCN^- and CO. However, since radical or charge-centre populations were not measured directly in this work, this is treated as a plausible interpretation of the substrate dependence rather than a confirmed mechanistic explanation.

Given these results, it is strongly implied that the NaCl windows actively participated in, or facilitated, radiolysis chemistry.

5.4 Estimation of Mean Survival Times under Europa-like Irradiation

While G-values provide insight into the relative efficiencies of molecular destruction and product formation, they do not reveal how long these molecules might persist in Europa's radiation environment. To assess the chemical longevity of formamide and its radiolysis products, it is necessary to estimate their mean survival times (chemical survivability) under simulated Jovian irradiation conditions.

Survivability was calculated as the ratio of the initial number of formamide molecules in the irradiated sample to their radiation-induced destruction rate, yielding a mean lifetime (τ) in seconds, which was also expressed in years for comparison. The intermediate steps are detailed in Section 3.3.5. These survival estimates assume a Europan surface dose rate derived from the average flux and energy-deposition profiles of H^+, O^{2+}, and S^{5+} ions, as discussed in Section 3.2.1. Energy deposition was assumed to occur uniformly across the ice depth, with dose rates scaled accordingly: these are depth-averaged lifetimes over the full film.

$$\tau = \frac{N_0}{R} \tag{5.2}$$

Equation 5.2 shows the overarching relationship used to calculate the characteristic survivability (mean lifetime) of formamide in ice under Europan surface dose rates. Here, N_0 is the initial number of formamide molecules in the irradiated sample, determined from the sample geometry, composition, and density, and R is the radiation-induced destruction rate (molecules/s), obtained from the experimentally determined G-value and the depth-dependent dose rate. The resulting lifetime τ is reported in seconds and converted to years for comparison with geologic and astrobiological timescales. This equation provides the summary expression for survivability, while intermediate steps (e.g. conversion of dose rate to eV/g·s, and scaling by mass) are omitted here.

Table 5.4 shows the mean survival times of formamide under Europa irradiation, derived from the decay of its 1388 and 1328 cm^{-1} bands on both NaCl and ZnSe win-

Table 5.4: Mean survival times of formamide under irradiation, averaged across H^+, O^{2+}, and S^{5+} projectiles, for the 1388 and 1328 cm^{-1} bands on NaCl and ZnSe windows. Values are reported as mean ± uncertainty ($CL = 95\%$), in years.

Window	1388 cm^{-1} Mean ± uncertainty (years)	1328 cm^{-1} Mean ± uncertainty (years)
NaCl	$(1.26 \pm 0.06) \times 10^5$	$(1.30 \pm 0.06) \times 10^5$
ZnSe	$(1.95 \pm 0.03) \times 10^5$	$(2.67 \pm 0.07) \times 10^5$

Notes: Uncertainties are half-widths of the 95% confidence interval ($CL = 95\%$) derived from Monte Carlo error propagation (10^4 iterations). Standard deviations: NaCl 1388 cm^{-1}: 2.74×10^3 yr; NaCl 1328 cm^{-1}: 2.70×10^3 yr; ZnSe 1388 cm^{-1}: 1.61×10^3 yr; ZnSe 1328 cm^{-1}: 3.53×10^3 yr.

dows. These values provide a quantitative estimate of the molecular lifetime against energetic processing and allow direct comparison of stability across substrates. It is important to note that the estimated lifetimes reported here assume homogeneous, planar ices of known composition under steady irradiation. In realistic environments such as Europa's surface or cometary grains, porosity, regolith shielding, and temperature-dependent diffusion may increase or decrease actual survival times. Furthermore, radiolytic products such as CO and OCN^- may undergo migration, trapping, or secondary reactions that redistribute or transform them over time, complicating their detectability in natural settings. Similar processes are in principle possible during laboratory experiments, but the comparatively short irradiation timescales and cryogenic conditions strongly limit long-range diffusion, making such effects less significant than they may be on Europa.

Additionally, these survivability estimates assume a steady-state flux, in which the radiation environment on Europa remains constant over time. The calculation also assumes uniform energy deposition across the irradiated ice thickness and does not account for several important physical processes, specifically, thermal evolution of the ice, such as diffusion or desorption of volatile products, and sputtering losses due to energetic ions, which are not included in this model. These processes can shorten the actual residence time of molecules like formamide in natural settings. As such, the calculated values likely represent an upper-limit approximation of molecular stability under idealised irradiation conditions.

Formamide survival times in these experiments are of order 10^5 years, which is broadly consistent with laboratory studies of simple organics in ices exposed to ion

irradiation. For example, J. Brucato et al. (2006) [32] reported that frozen formamide exposed to energetic ions could retain a significant fraction of molecules on timescales up to 10^8 years in dense cloud environments, while other laboratory irradiations of methanol and CO-rich ices suggest destruction lifetimes ranging from 10^4-10^6 years depending on flux and composition [62, 63]. These comparisons highlight that formamide, while susceptible to radiolysis, is not unusually fragile under energetic processing, and the surrounding matrix and substrate strongly modulate its apparent stability. Notably, the results show shorter survival times on NaCl than on ZnSe, suggesting that salt-rich surfaces, such as those found on Europa, may promote more rapid molecular degradation than inert mineral substrates, with direct implications for the detectability of prebiotic species in outer Solar System ices.

The close agreement between the lifetimes derived from the 1388 and 1328 cm^{-1} bands indicates that both vibrational modes respond similarly to irradiation. In an ideal, homogeneous bulk sample, both the 1388 and 1328 cm^{-1} bands would yield identical column densities because each vibrational mode probes the same underlying molecular abundance. However, in thin mixed ices, the two bands acquire small mode-specific systematic offsets. These arise from: (i) matrix- and temperature-dependent variations in the literature band strengths (A-values), (ii) differing amounts of spectral overlap and baseline structure (the 1388 cm^{-1} region is notably more crowded), (iii) frequency-dependent thin-film interference and local-field effects, which are more pronounced on ZnSe, and (iv) minor saturation effects affecting the stronger of the two bands. Together, these factors produce a band-to-band spread of only a few per cent. We therefore treat the difference between the two bands as a systematic effect rather than an error in the method, and the close agreement between the derived lifetimes reflects the underlying consistency of the measurements.

Experiments on ZnSe windows consistently yielded longer formamide lifetimes than those of the experiments done on NaCl windows. This further reinforces that substrate effects extend beyond G-values into estimated molecular survival lifetimes. The substrate effect mirrors the G-value findings: NaCl promotes faster destruction (shorter lifetimes), whereas ZnSe appears to preserve formamide for longer. If the substrate is

chemically active, then this implies that the presence of NaCl on Europa (or comets/interstellar grains) will have an impact on the degradation of prebiotically relevant simple molecules and their radiolysis by-products. In other words, formamide might persist much longer in an inert or mineral-like environment (ZnSe-like) than on salt-rich surfaces (NaCl-like), which could directly affect predictions for detectability and abundance in space.

5.5 Comparative Analysis and Implications for Europa's Surface Chemistry

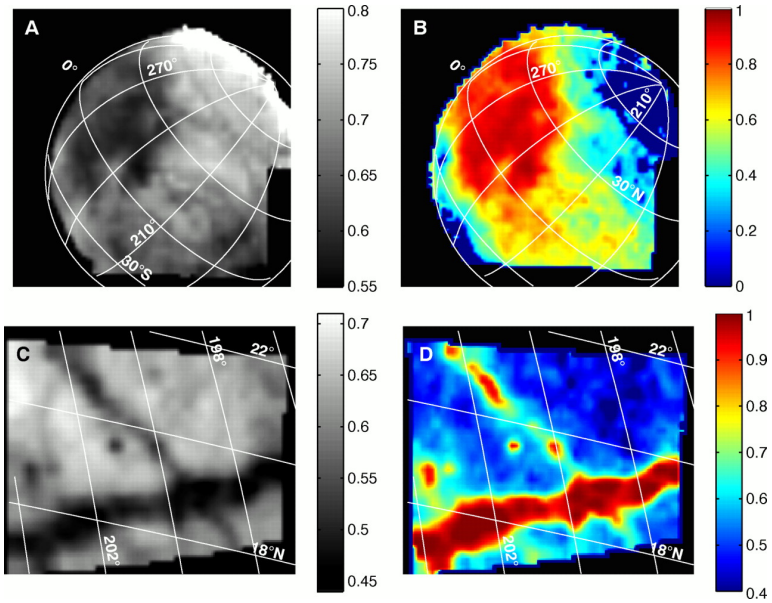


Figure 5.13: Near-infrared observations of Europa's surface from Galileo/NIMS, showing the distribution of non-ice components interpreted as hydrated salts. Panel (A) presents a near-hemispheric albedo map, while (B) and (D) highlight concentrations of non-ice material (red shading) associated with darker terrains, including chaos regions and lineae. The association of salts with these geologic units supports their identification as evaporite-like deposits, likely formed by briny fluids reaching the surface. **Credit:** Reproduced from T. B. McCord et al., *Science*, doi:10.1126/science.280.5367.1242 (1998), AAAS, [64].

The experimental results in this section show two consistent outcomes, discussed here in the context of Europa's chemically complex surface (Figure 5.13). First, formamide is radiolytically destroyed on timescales of $\sim 10^5$ years under Europa-like irradiation. These lifetimes are short compared with Europa's surface renewal timescales (10^6-10^7 years), meaning that organics at the surface cannot persist over geological periods without replenishment. However, they are still long compared with human and mission

timescales, so freshly delivered or recently exposed formamide could remain detectable for tens of thousands of years. This distinction is important: detection of NH_2CHO at Europa's surface would imply either continuous resupply (endogenic activity, plume fallout, impact gardening) or recent deposition, rather than long-term stability.

Second, the G-values show that early irradiation favours the rapid formation of small, stable products such as CO and OCN^-, with CO_2 building up more gradually but eventually reaching the largest column densities. The apparent discrepancy between early-time yields and final abundances can be explained by the strong band strength of the CO_2 feature and by its continued formation via secondary radical pathways (e.g. HOCO-mediated oxidation). In practical terms, this means CO and OCN^- act as early-stage tracers of radiation processing, while CO_2 is more consistent with longer-term accumulation as an oxidised sink for carbon in the ice, potentially fed by multiple carbon-bearing intermediates rather than exclusively by direct destruction of formamide. OCN^- is especially valuable because its abundance depends not only on cumulative dose but also on the surrounding matrix chemistry: stabilisation by ions such as Na^+ or NH_4^+ enhances its retention, so the presence or absence of its 2165 cm^{-1} feature carries information about both radiation history and local environment.

The substrate results reinforce this point. On NaCl, formamide was destroyed more efficiently, and product yields were higher than on ZnSe, despite lower fluences. This indicates that NaCl is not chemically inert: the presence of Na^+ ions and surface hydration layers likely promote radiolysis and stabilise products such as OCN^-. In contrast, ZnSe behaved more like an inert substrate, with slower parent destruction, suppressed yields, and longer survival times. Translated to Europa, this suggests that salt-rich terrains such as the chaos regions will be chemically more "active" than ice-rich areas, with faster turnover of prebiotic molecules and enhanced production of radiolysis products.

Beyond Europa, these results scale to other outer Solar System and interstellar environments. On comets and interstellar grains, radiation dose rates are far lower, so the same G-values imply much longer survival times (10^6-10^8 years). In those settings, formamide can persist as a reservoir and be released episodically, while CO_2 gradually

accumulates as the most robust long-lived product. CO and OCN^- are still produced efficiently per unit energy, but at lower doses they remain at modest abundances and are easily redistributed by thermal cycling or outgassing. This matches astronomical observations: CO_2 is often detected as a major component of cometary and interstellar ices, whereas CO and OCN^- detections are more variable [61, 65, 66].

Taken together, these findings show that it is not only the ion flux and LET that determine radiation chemistry, but also the chemical environment of the ice. For Europa, salt-rich regions should drive more aggressive radiation-induced processing than previously assumed, shortening the lifetimes of prebiotic molecules like formamide and biasing the detectable inventory toward robust products such as CO_2. For comets and dense cloud ices, much lower fluxes allow formamide to act as a long-term prebiotic reservoir, with radiation chemistry shaping the balance of small products that may later be delivered to planetary surfaces.

5.5.1 Local Implications for Ion-Driven Chemistry

The results presented in this chapter show that the relative LET and penetration depths of H^+, O^{2+}, and S^{5+} govern both the rate of formamide destruction and the identity of the major radiolysis products. CO_2 is consistently produced across all irradiation conditions and remains radiolytically stable, whereas CO and OCN^- form rapidly before undergoing secondary processing at higher doses. These trends reflect the balance between primary ionisation events and subsequent radical-radical chemistry, which is strongly modulated by near-surface energy deposition.

The comparison between NaCl and ZnSe windows also highlights the importance of interfacial structure: ionic surfaces create compact hydration layers that retain volatile radiolysis products more efficiently, leading to higher steady-state column densities for CO and CO_2 in NaCl experiments. This indicates that the interfacial molecular environment can significantly modulate the observed chemistry, even when the bulk ice composition is the same.

Across all experiments, the three ion species follow a consistent hierarchy. Protons, with the lowest LET and deepest penetration depths, drive the slowest apparent de-

struction: formamide bands persist to the highest fluences, and product bands such as CO, CO_2, and OCN^- grow gradually before saturating. Oxygen ions, with higher LET and shallower ranges, compress the same chemistry into lower fluence windows: formamide is removed more efficiently per ion, and the growth-plateau-decline sequence of the product bands is shifted to earlier doses. Sulphur lies at the high-LET end: on NaCl, it behaves as a higher-LET analogue of oxygen, producing similar peak yields and product suites but with more pronounced matrix disruption and a slightly earlier onset of track-driven restructuring. On ZnSe, sulphur still forms the same products but with comparatively modest yields and no clear destructive downturn within the accessible fluence range. In all cases, NaCl enhances both destruction and product retention relative to ZnSe, so the projectile hierarchy ($H < O \sim S$ in effectiveness) is continuously modulated by the substrate.

One additional consideration is that the substrate contrast appears less pronounced for H^+ irradiation on ZnSe than for the heavier ions, plausibly because low-LET protons generate reactive events more sparsely and may therefore be less sensitive to interfacial effects than dense high-LET ion tracks. This interpretation is plausible given the strong water-ion interactions expected on ionic NaCl surfaces, but it is not directly isolated here; targeted tests (e.g. controlled hydration/handling and thickness-dependence) would be required to confirm it.

Taken together, these findings provide a consistent picture in which ion mass and charge state, LET, ice thickness, and interfacial structure jointly determine the chemical evolution of formamide-water ices under ion irradiation.

Bibliography

[1] Trumbo S, Becker T, Brown M, Denman W, Molyneux P, Hendrix A, et al. A New UV Spectral Feature on Europa: Confirmation of NaCl in Leading-hemisphere Chaos Terrain. The Planetary Science Journal. 2022;3.

[2] Niu G, Wang Z, Xue Y, Yan J, Dutta A, Chen X, et al. Pencil-on-Paper Humidity Sensor Treated with NaCl Solution for Health Monitoring and Skin Characterization. Nano letters. 2022.

[3] Cho M, Kim IS, Kim MJ, Hyun D, Koo SM, Sohn H, et al. NaCl Ionization-Based Moisture Sensor Prepared by Aerosol Deposition for Monitoring Respiratory Patterns. Sensors (Basel, Switzerland). 2022;22.

[4] Tashmetov M, Madaminov B. Influence of high-fluence electron irradiation on the band gap, Raman spectra, and microhardness of ZnSe. Physica Scripta. 2025;100.

[5] Ushiki T, Imazawa R, Kitazawa SI, Ishikawa M, Murakami H, Shimizu K, et al. Effects of Gamma-ray and neutron irradiation on infrared optical properties of ZnSe and ZnS for ITER divertor thermography. Journal of Nuclear Materials. 2024.

[6] Ziegler JF, Ziegler MD, Biersack JP. SRIM – The Stopping and Range of Ions in Matter; 2010. Version SRIM-2013. `http://www.srim.org/`.

[7] Brandt J, Mattsson K, Hassellöv M. Deep Learning for Reconstructing Low-Quality FTIR and Raman Spectra—A Case Study in Microplastic Analyses. Analytical Chemistry. 2021;93:16360 16368.

[8] Santalices D, Meléndez J, Briz S. Analysis of periodic temporal changes in the spectral signature of IR sources by modeling of spectral artifacts in FTIR systems. Journal of Quantitative Spectroscopy and Radiative Transfer. 2025.

[9] Gálvez O, Ortega IK, Maté B, Moreno MA, Martín-Llorente B, Herrero VJ, et al. A study of the interaction of CO{2} with water ice. Astronomy & Astrophysics. 2007 Sep;472(2):691-8.

[10] Slavicinska, K , Rachid, M G , Rocha, W R M , Chuang, K -J , van Dishoeck, E F , Linnartz, H . The hunt for formamide in interstellar ices - A toolkit of laboratory infrared spectra in astronomically relevant ice mixtures and comparisons to ISO, Spitzer, and JWST observations. A&A. 2023;677:A13.

[11] Paranicas C, Ratliff JM, Mauk B, Cohen C, Johnson RE. The ion environment near Europa and its role in surface energetics. Geophysical Research Letters. 2002;29.

[12] TA2 Facility 12 - Atomki ECRIS Laboratory: Atomki-Queen's University Uce Laboratory for Astrochemistry (AQUILA) - Europlanet — europlanet.org;. [Accessed 14-08-2025]. https://www.europlanet.org/europlanet-2024-ri/ta2-dplf/ta2-facility-12-atomki-ecris-laboratory/.

[13] Marx D. Proton transfer 200 years after von Grotthuss: insights from ab initio simulations. Chemphyschem : a European journal of chemical physics and physical chemistry. 2006;7 9:1848-70.

[14] Agmon N. The Grotthuss mechanism. Chemical Physics Letters. 1995;244(5):456-62.

[15] Rimola A, Skouteris D, Balucani N, Ceccarelli C, Enrique-Romero J, Taquet V, et al. Can Formamide Be Formed on Interstellar Ice? An Atomistic Perspective. ACS Earth and Space Chemistry. 2018.

[16] Boland M, Chaquin P, Volatron F, Markovits A. Formamide synthesis in the interstellar mediumcatalyzed by damaged water ice. Astronomy & Astrophysics. 2023.

[17] Tieppo N, Redondo P, Pauzat F, Parisel O, Guillemin J, Ellinger Y. Building formamide and N-substituted formamides from isocyanates on hydrogenated water ices. Astronomy & Astrophysics. 2025.

[18] Chaabouni H, Diana S, Nguyen T. Thermal desorption of formamide and methylamine from graphite and amorphous water ice surfaces. Proceedings of the International Astronomical Union. 2017;15:370 371.

[19] Jones B, Bennett C, Kaiser R. Mechanistical studies on the production of formamide (H2NCHO) within interstellar ice analogs. The Astrophysical Journal. 2011;734.

[20] Hudson RL, Moore MH. Radiation chemical alterations in solar system ices: An overview. Journal of Geophysical Research. 2001.

[21] Oba Y, Watanabe N, Kouchi A, Hama T, Pirronello V. Experimental Study Of CO2 Formation By Surface Reactions Of Non-Energetic OH Radicals With CO Molecules. The Astrophysical Journal Letters. 2010.

[22] Qasim D, Lamberts T, He J, Chuang K, Fedoseev G, Ioppolo S, et al. Extension of the HCOOH and CO2 solid-state reaction network during the CO freeze-out stage: inclusion of H2CO. Astronomy & Astrophysics. 2019.

[23] Broekhuizen FV, Keane J, Raymond W, for Astrophysics BSL, Observatory L, Center TNNR, et al. A quantitative analysis of OCNformation in interstellar ice analogs. 2003.

[24] Hudson RL, Moore MH. New experiments and interpretations concerning the "XCN" band in interstellar ice analogues. Astronomy & Astrophysics. 2000.

[25] Gerakines P, Hudson R. The radiation stability of glycine in solid CO2 – In situ laboratory measurements with applications to Mars. Icarus. 2015;252:466-72.

[26] Molpeceres G, Enrique-Romero J, Aikawa Y. Cracking the puzzle of CO2 formation on interstellar ices. Quantum chemical and kinetic study of the CO + OH -> CO2 + H reaction. Astronomy & Astrophysics. 2023.

[27] Dawley MM, Pirim C, Orlando T. Radiation processing of formamide and formamide:water ices on silicate grain analogue. The journal of physical chemistry A. 2014;118 7:1228-36.

[28] Sivaraman B, Sekhar BN, Nair B, Hatode V, Mason NJ. Infrared spectrum of formamide in the solid phase. Spectrochimica acta Part A, Molecular and biomolecular spectroscopy. 2013;105:238-44.

[29] Noble JA, Congiu E, Dulieu F, Fraser HJ. Thermal desorption characteristics of CO, O_2 and CO_2 on non-porous water, crystalline water and silicate surfaces at submonolayer and multilayer coverages. Monthly Notices of the Royal Astronomical Society. 2012;421:768-79.

[30] Martín-Doménech R, Muñoz Caro GM, Bueno J, Goesmann F. Thermal desorption of circumstellar and cometary ice analogs. Astronomy & Astrophysics. 2014;564:A8.

[31] Bisschop SE, Fraser HJ, Öberg KI, van Dishoeck EF, Schlemmer S. Desorption rates and sticking coefficients for CO and N_2 interstellar ices. Astronomy & Astrophysics. 2006;449:1297-309.

[32] Brucato J, Baratta G, Strazzulla G. An infrared study of pure and ion irradiated frozen formamide. Astronomy & Astrophysics. 2006;455:395-9.

[33] Sodium Chloride Windows | Edmund Optics — edmundoptics.com;. [Accessed 21-08-2025]. https://www.edmundoptics.com/f/sodium-chloride-nacl-windows/14170/?srsltid=AfmBOopd9hLoFx0gL-c60nWnhlEi-KO3HO6kO2Iu_IH1iu6LVPWnmBn1&utm_.

[34] Abdulsattar MA, Khalid A, Abdul-Hussein YM. Structural, Vibrational and Thermodynamic Characteristics of Nacl Single-Molecule Dissolution in Water: A DFT Study. Journal of Physics: Conference Series. 2021;1818.

[35] Vandenborre J, Truche L, Costagliola A, Craff E, Blain G, Baty V, et al. Carboxylate anion generation in aqueous solution from carbonate radiolysis, a potential

route for abiotic organic acid synthesis on Earth and beyond. Earth and Planetary Science Letters. 2021;564:116892.

[36] Haygarth K, Marin TW, Janik I, Kanjana K, Stanisky CM, Bartels D. Carbonate radical formation in radiolysis of sodium carbonate and bicarbonate solutions up to 250 degrees C and the mechanism of its second order decay. The journal of physical chemistry A. 2010;114 5:2142-50.

[37] Hudson RL, Moore MH, Gerakines PA. The Fromation Of Cyanate Ion (OCN−) In Interstellar Ice Analogs. The Astrophysical Journal. 2001.

[38] Theulé P, Duvernay F, Ilmane A, Hasegawa T, Morata O, Coussan S, et al. Kinetics of the OCN− and HOCN formation from the HNCO + H2O thermal reaction in interstellar ice analogs. Astronomy & Astrophysics. 2011;530.

[39] Raunier S, Chiavassa T, Marinelli F, Allouche A, Aycard JP. Reactivity of HNCO with NH3 at low temperature monitored by FTIR spectroscopy: formation of NH4+OCN−. Chemical Physics Letters. 2003.

[40] Yang Y, Meng S, Wang EG. Water adsorption on a NaCl (001) surface: A density functional theory study. Physical Review B. 2006.

[41] Ewing GE. Thin Film Water. The Journal of Physical Chemistry B. 2004.

[42] Tang M, Chan CK, Li YJ, Su H, Ma Q, Wu Z, et al. A review of experimental techniques for aerosol hygroscopicity studies. Atmospheric Chemistry and Physics Discussions. 2019.

[43] Gonella G, Backus EHG, Nagata Y, Bonthuis DJ, Loche P, Schlaich A, et al. Water at charged interfaces. Nature Reviews Chemistry. 2021.

[44] Judd DB. Fresnel reflection of diffusely incident light. Journal of research of the National Bureau of Standards. 1942;29:329.

[45] Gershun A. Fresnel Reflection of Diffusely Incident Light. Journal of the Optical Society of America. 1945;35:162-3.

[46] Tsai T, Lee ZC, Tsao HX, Lin ST. Minimization of Fresnel reflection by anti-reflection fiber Bragg grating inscribed at the fiber ends. Optics express. 2019;27 8:11510-5.

[47] Pasanen HP, Khan R, Odutola JA, Tkachenko NV. Transient Absorption Spectroscopy of Films: Impact of Refractive Index. The Journal of Physical Chemistry C, Nanomaterials and Interfaces. 2024;128:6167 6179.

[48] Zinc Selenide ZnSe Optical Material | Crystran — crystran.com;. [Accessed 21-08-2025]. https://www.crystran.com/optical-materials/zinc-selenide-znse.

[49] Sodium Chloride NaCl Optical Material | Crystran — crystran.com;. [Accessed 21-08-2025]. https://www.crystran.com/optical-materials/sodium-chloride-nacl.

[50] Mitchell S. Rutherford Backscattering Spectrometry (RBS) Tutorial — eag.com;. [Accessed 22-08-2025]. https://www.eag.com/app-note/rutherford-backscattering-spectrometry-rbs-tutorial/?.com.

[51] An LY, Dai Z, Di B, li Xu L. Advances in Cryochemistry: Mechanisms, Reactions and Applications. Molecules. 2021.

[52] Takenaka N, Tanaka M, Okitsu K, Bandow H. Rise in the pH of an unfrozen solution in ice due to the presence of NaCl and promotion of decomposition of gallic acids owing to a change in the pH. The journal of physical chemistry A. 2006.

[53] Barros ALF, Boduch P, Domaracka A, Rothard H, Silveira F. Radiolysis of astrophysical ices by heavy ion irradiation: Destruction cross section measurement. Low Temperature Physics. 2012;38:759-65.

[54] Barros ALF, Domaracka A, Andrade D, Boduch P, Rothard H, Silveira F. Radiolysis of frozen methanol by heavy cosmic ray and energetic solar particle analogues. Monthly Notices of the Royal Astronomical Society. 2011.

[55] Cooper PD, Moore MH, Hudson RL. O atom production in water ice: Implications for O2 formation on icy satellites. Journal of Geophysical Research. 2010.

[56] Das S. Critical Review of Water Radiolysis Processes, Dissociation Products, and Possible Impacts on the Local Environment: A Geochemist. Australian Journal of Chemistry. 2013;66:522-9.

[57] Gerakines P, Schutte W, Greenberg J, Dishoeck EF. The Infrared Band Strengths of H2O, CO and CO2 in Laboratory Simulations of Astrophysical Ice Mixtures. arXiv: Astrophysics. 1994.

[58] Mifsud D, Kaňuchová Z, Herczku P, Ioppolo S, Juhász Z, Kovács S, et al. Sulfur Ice Astrochemistry: A Review of Laboratory Studies. Space Science Reviews. 2021;217.

[59] Pilling S, Duarte ES, Domaracka A, Rothard H, Boduch P, Silveira ÊF. Radiolysis of H2O:CO2 ices by heavy energetic cosmic ray analogs. Astronomy & Astrophysics. 2010;523.

[60] Gerakines PA, Moore MH, Hudson RL. Ultraviolet photolysis and proton irradiation of astrophysical ice analogs containing hydrogen cyanide. Icarus. 2004.

[61] Öberg K. Photochemistry and Astrochemistry: Photochemical Pathways to Interstellar Complex Organic Molecules. Chemical reviews. 2016;116 17:9631-63.

[62] Hudson RL, Moore MH. Infrared Spectra and Radiation Stability of H2O2 Ices Relevant to Europa. Astrobiology. 2006.

[63] Moore MH, Hudson RL, Carlson RW. The radiolysis of SO2 and H2S in water ice: Implications for the icy jovian satellites. Icarus. 2007.

[64] McCord TB, Hansen GB, Fanale FP, Carlson RW, Matson DL, Johnson TV, et al. Salts on Europa's Surface Detected by Galileo's Near Infrared Mapping Spectrometer. Science. 1998.

[65] Bockelée-Morvan D, Crovisier J, Mumma M, Weaver H. The composition of cometary volatiles. 2004:391.

[66] Altwegg K, Balsiger H, Fuselier S. Cometary Chemistry and the Origin of Icy Solar System Bodies: The View After Rosetta. Annual Review of Astronomy & Astrophysics. 2019.

Chapter 6

Electron Irradiation of Formamide and Water Ice Mixture

Building on the ion-irradiation experiments presented in Chapter 5, this Chapter examines how low-energy electrons process the same formamide-water ices under Europa-like conditions. While high-LET ions dominate the dense energy deposition that drives bulk radiolysis in Europa's trailing hemisphere, Jupiter's magnetosphere also contains a substantial population of keV-MeV electrons (Section 2.3.1) that continuously bombard the upper layers of the ice shell. These electrons are expected to play a key role in near-surface chemistry, controlling volatile loss, gentle pre-processing of organics, and the evolution of salt-rich terrains such as chaos regions and lineae. To investigate this regime, 2 keV electron irradiations were carried out at the U90 endstation of the Taiwan Light Source, using NaCl and ZnSe substrates to mirror the ion experiments and to disentangle any catalytic behaviour of salt-rich surfaces from the intrinsic electron-driven chemistry. In Section 6.1, the experimental geometry and irradiation conditions are outlined. Section 6.2 then presents the evolution of the IR spectra on NaCl and ZnSe, while Section 6.4 quantifies destruction efficiencies and approximate G-values derived from these measurements. Section 6.5 compares the electron data directly with the ion-irradiation experiments from Chapter 5, and the implications for Europa's surface chemistry are briefly summarised before being developed in more detail in the overall Conclusions Chapter.

6.1 Experimental Overview and Irradiation Parameters

As discussed in Sections 4.2.2 and 5.1, NaCl and ZnSe were specifically chosen for their chemical composition. NaCl is strongly inferred to be present in Europa's ocean [1], based on HST detections of irradiated NaCl in chaos terrains interpreted as upwelled oceanic material, and is therefore a suitable medium to use for mimicking the surface on which ice may be grown. In comparison, ZnSe is chemically inert and acts as a reference to determine what observations are as a result of NaCl behaving as a catalyst and what observations are as a result of electron irradiation. ZnSe is much less likely to degrade in the presence of water and is less susceptible to humid environments. Furthermore, ZnSe provides a complementary data set to the NaCl experiment. In

all experiments presented in this Chapter, formamide is the sole source of nitrogen; any N-bearing radicals and products therefore originate from its amide group. Table 6.1 in Section 6.3 summarises the experimental parameters used for the experiments discussed in this Chapter.

Similarly to the ion experiments discussed in the previous Chapter, the aim was to deposit a 50:50 ratio of formamide-water ice onto the substrates and to maintain a thickness of the ice $\lesssim$180 nm. True ice compositions and ice thicknesses are displayed in Table 6.1 in Section 6.3. This target ice thickness would ensure that the full energy of the electrons would be deposited in the ice. The software CASINO was used to calculate the penetration depth of 2 keV electrons in a 50:50 formamide-water ice (see Section 4.3.2 for a more detailed explanation), and it was determined that ∼99% of the electrons' energy would be deposited into ice as thick as 180 nm.

As discussed in Section 4.3.2 and as shown in Table 6.1, the actual ice composition and thickness of the ice grown on both windows (particularly NaCl) are far from these aims. The ices were thicker than the suggested ice thickness; the NaCl-grown ice was ∼2.6× thicker than the ice on the ZnSe window, which falls within a more reasonable ∼20% margin of the intended ice thickness, spreading the energy deposition over a larger column. Due to time constraints and operational issues during dosing, this could not be corrected for. Therefore, it should be noted that this thickness difference will have a notable impact on both the physical processing and the resulting chemistry: thicker ices provide greater self-shielding from incoming radiation and may favour different radical diffusion and recombination pathways compared to thinner samples [2]. Consequently, direct comparisons of product yields and destruction efficiencies between NaCl and ZnSe experiments must account for thickness-related effects. This caveat was taken into account throughout the subsequent analysis and interpretation of the experimental results.

Although the target during deposition was to produce mixed formamide-water ices at an equimolar 50:50 ratio with a nominal thickness of ∼180nm, the resulting films were significantly more water-rich. This discrepancy arose from practical constraints: the formamide delivery line suffered from variable flow. At the same time, the higher

volatility of water and limited control over cryogenic pumping made it difficult to maintain precise co-deposition rates. Due to strict time constraints during the assigned beamtime, it was not possible to iteratively adjust the deposition conditions to achieve the intended stoichiometry. Instead, the actual composition was quantified post-deposition from the infrared spectra. While this outcome differed from the original design, it resulted in ices that are more representative of those expected on icy outer Solar System bodies, where water is overwhelmingly dominant, and formamide would plausibly occur only as a trace component. This makes the experiments especially relevant to evaluating the survivability and chemical evolution of formamide under realistic planetary ice conditions, directly supporting the broader aim of assessing its potential prebiotic role in such environments.

Similar to the ion irradiation experiments performed at Atomki (see Section 5.1), the ice was deposited onto the windows using background deposition. This ensured that the molecules within the ice were homogeneously mixed, more closely approximating the likely molecular mixture in extraterrestrial ices. Furthermore, the chemistry for layered ices and mixed ices differs significantly. For layered ices, the majority of the chemistry of significance occurs at the interface between the two ice types, preserving chemical zoning. However, mixed ices allow for the continuous interactions throughout the ice matrix, creating bulk chemical reactions [3]. These differences in chemistry drastically affect the reaction network and the evolution of ice morphology in the ice mantle.

When investigating Europa, electrons are imperative to consider due to their importance in the role of near-surface ice chemistry [4]. As discussed in Section 3.2.1.2, electron irradiation was chosen due to its ubiquitous presence in Europa's radiation environment, originating primarily from Io's volcanic activity, solar winds, and sputtering from other Galilean moons. The electrons in Jupiter's magnetosphere typically have energies ranging from a few keV to several MeV; hence, the decision to use 2 keV electrons in these experiments. Furthermore, electrons have a lower LET than the heavy ions used at Atomki, leading to more diffuse energy deposition; as a result, electrons are less efficient than heavy ions for bulk processing but are less likely to form

dense ionisation tracks.

6.2 Evolution of IR Spectra and Radiolysis Products

After ice deposition and before irradiation began, an initial FTIR spectrum was collected as a reference. A second spectrum was obtained only after the samples were fully irradiated. As discussed in Section 4.3.2, the electron gun filament was operated at high temperature and emitted strong broadband infrared radiation into the beamline; this secondary optical radiation saturated the FTIR detector when the beam was on, so it was not possible to collect incremental spectra during irradiation. As a result, destruction efficiencies were analysed instead of G-values. For completeness, G-values were also estimated for this dataset using a simplified calculation method. This approach, although quick, assumes complete energy deposition and averages over all chemistry, resulting in a significant underestimation of the actual initial depletion yields. Accordingly, these G-values are included in the analysis only as reference values, not for direct comparison with the ion irradiation data. Due to the lack of appearance of weaker features in the electron experiment spectra, only major vibrational features were used to track the evolution of the spectra: the O-H/N-H stretch (∼3200-3500 cm^{-1}), the formamide C=O band (near ∼1700 cm^{-1}), and the H_2O band (near ∼1640 cm^{-1}). The fingerprint region (∼1500-1000 cm^{-1}) shows only weak, poorly resolved features.

6.2.1 NaCl Window

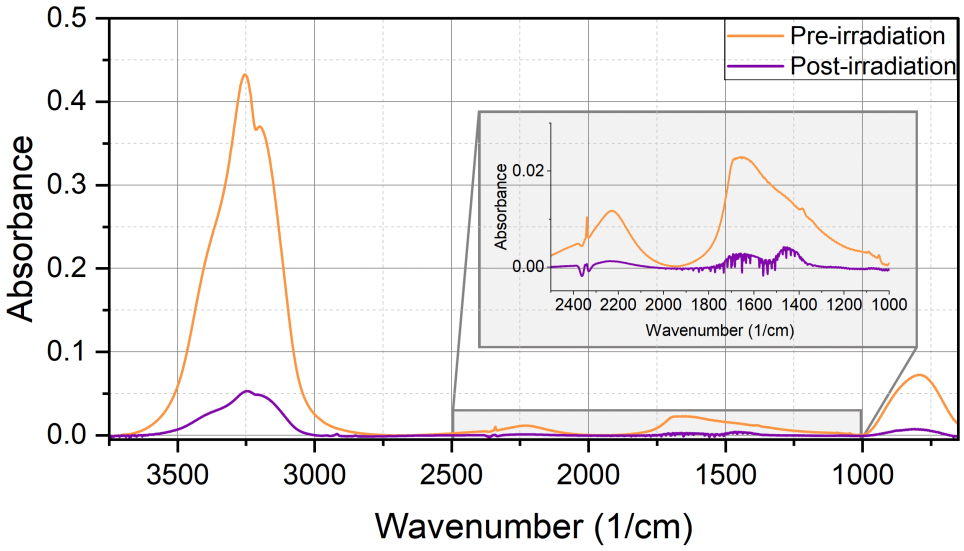


Figure 6.1: Evolution of infrared spectral features for a 50:50 formamide-water ice mixture deposited onto a NaCl window, at 90 K, and irradiated with 2 keV electrons. These spectra display the pre-irradiation spectrum (yellow) and the post-irradiation spectrum (dark purple).

The first observations from these spectra, in Figure 6.1, is that there are not as many noticeable spectroscopic features as observed in the ion irradiation in Figure 5.1, in Section 5.2. Due to the thicker ice present on the NaCl window, the overall absorbance of the ice grown is nearly three times larger than that of the ion irradiation experiment. This larger absorbance in itself can mask finer structures. As this trend is observed both before and after irradiation, it is safe to assume that the differences in fingerprints between the ion and electron experiments are primarily due to instrumental and/or sample-preparation differences. Furthermore, due to the thickness of the ice, it is highly likely that the spectra are partially saturated; see Section 3.2.1. This partial saturation has led to strong bands being too intense, causing band flattening/clipping at the top, apparent broadening, and loss of weaker neighbouring peaks in the fingerprint region. This means that whilst the O-H/N-H band is extreme, the spectral features expected to be seen around ~2500-1000 cm^{-1} are incredibly weak or non-existent. Even if the thickness of the ice were the same, small changes in deposition rate/angle, or beam footprint can result in a pathlength difference of between 2 and 4 times. Since the

equipment used at the NSRRC was in a different configuration and featured different models, it is entirely possible that this was the case.

After electron irradiation, the spectrum is significantly flattened. This is evident in the almost complete loss of the O-H/N-H and C=O bands, whose peak intensities decrease to near the baseline. It should be noted that in the pre-irradiation spectrum, see Figure 6.1, there is evidence of minor CO_2 contamination at ∼2340 cm^{-1}, similar to the contamination seen in the heavy ion experiments, discussed in Section 5.2.1.1. However, much like the O-H/N-H bands, the CO_2 is completely depleted post-irradiation. This disappearance of CO_2 is consistent with electron-stimulated desorption (and/or rapid conversion to more minor volatiles that also don't accumulate). Electron-stimulated desorption (ESD) is the process where an incoming electron of energies ranging between eV to keV interacts with a solid surface or ice, transferring enough energy to break chemical bonds and cause atoms, radicals, or molecules to desorb from the surface [5, 6]. This happens as a result of the ionisation and electronic excitation of the molecules via electron penetration. The secondary electrons deposit the energy locally, destabilising bonds. This destabilisation can lead to bond cleavage or to an Auger-like process[1] where the energy is used for nuclear motion, and the molecule is desorbed from the ice surface into the vacuum. Furthermore, weakly bound CO_2 tends to desorb between the temperatures of ∼70-110 K [9, 10], meaning that at 90 K CO_2 is only marginally retained and therefore is susceptible to any non-thermal excitation. Additionally, radiation chemistry also consumes CO_2, as secondary electrons and radicals (H· and OH· analogues in ice) reduce or fragment to CO_2, see Scheme 6.1, converting it to CO, formate, carbonic acid, etc [11].

[1]The Auger process is when an inner-shell hole is filled, the released energy ejects another electron (Auger electron) instead of a photon. In solids, this can localise energy and drive desorption/fragmentation [7, 8].

$$CO_2 \xrightarrow{e^-} CO_2{}^- \quad (1)$$

$$CO_2{}^- \longrightarrow CO + O^- \quad (2)$$

$$CO_2 \xrightarrow{e^-} CO + O\cdot \quad (3)$$

$$CO_2(s) \xrightarrow{e^-} CO_2(g) \quad (4)$$

$$H_2O \xrightarrow{e^-} H\cdot + OH\cdot \quad (5)$$

$$CO + OH\cdot \rightleftharpoons HOCO\cdot \quad (6)$$

$$CO_2 + H_2O \longrightarrow H_2CO_3 \quad (7)$$

Scheme 6.1: Representative chemical reactions showing possible pathways for the destruction and subsequent conversion of CO_2 during irradiation of formamide-water ice. These are simplified and do not account for secondary processes such as radical recombination.

Scheme 6.1 shows the potential chemical pathways that would lead to the destruction of CO_2. Chemical pathway **(1)** shows electron attachment to CO_2 forming the CO_2^- radical anion; in protic media, this anion is rapidly protonated to form formate, $CO_2{}^-\cdot + H^+ \longrightarrow HCO_2\cdot$ (formyloxy radical) [12]. Chemical pathway **(2)** then illustrates the unimolecular dissociation of CO_2^- into CO and O^-, while chemical pathway **(3)** represents an alternative channel in which direct electron impact on neutral CO_2 produces CO and O [13]. Chemical pathway **(4)** shows electron-stimulated desorption of CO_2, in which electronic excitation leads to the ejection of CO_2 from the ice into the gas phase [13, 14]. Taken together, chemical pathways **(1)**-**(4)** represent direct electron or secondary-electron interactions with CO_2. In contrast, chemical pathways **(5)**-**(7)** are part of the radiolysis-radical network in H_2O ice. Chemical pathway **(5)** depicts the primary radiolysis step of water, producing H· and OH·. Chemical pathway **(6)** illustrates the formation of the HOCO intermediate, as detailed in Section 5.2.1.1, which can subsequently form formic acid [11]. Chemical pathway **(7)** is the formation of carbonic acid from carbon dioxide and water [15, 16]. To summarise, in the formamide-water ice, the electrons start a cascade of secondary electrons that, through excitations, both eject and chemically consume the CO_2. Weakly bound CO_2 will have been desorbed from the surface layer, whilst the remaining CO_2 would have been depleted through dissociative electron attachment[2] (DEA) and electron-impact

dissociation.

Unlike the ion irradiation experiment, the typical product markers for OCN^- ($\sim$2165 cm^{-1}), CO ($\sim$2135 cm^{-1}), and CO_2 ($\sim$2340 cm^{-1}) do not rise above the noise in the post-irradiation spectrum. In this mixed ice, nitrogen is supplied exclusively by formamide, so any N-bearing fragments and products must originate from the breakdown of the NH_2CHO group, as sketched in Scheme 6.1. This strongly suggests that the supported pathways are dominated by fragmentation and volatile loss, rather than the build-up of IR-active products, consistent with low-LET electron processing that generates cascades of low-energy secondary electrons driving dissociative attachment/ionisation and bond cleavage [18, 19]. As a result, the electron beam breaks parent molecules into small fragments (H, H_2, CO, CO_2) and N-bearing radicals such as $NH_2\cdot$ and $NH\cdot$ derived from formamide; many of these species are weakly IR-active in the condensed phase and/or are efficiently removed by ESD, so they do not accumulate as sharp product bands [5, 20, 21].

By contrast, under ion irradiation (high-LET tracks), radiolysis fragments readily recombine or rearrange in the ice to form stable condensed species with strong dipole transitions, classically including OCN^- and carbon oxides, so new, well-defined IR features appear [18, 22]. Overall, the electron-track chemistry in these experiments tends to remove oscillator strength from dipole-active modes (such as O-H, N-H, or C=O) by depleting intact functional groups without leaving intense, narrow product bands, whereas heavy-ion tracks more often reassemble fragments into IR-visible residues [22]. This behaviour is typical for water-baseline levels, eV electron energies, where the chemistry is mediated by abundant low-energy secondaries and accompanied by the desorption of small products [21, 23].

The large, smooth O-H/N-H band before irradiation and the lack of crisp structure are consistent with a water-rich, thicker film on NaCl. A high H_2O fraction produces a broad hydrogen-bonded stretch that red-shifts and broadens with stronger H-bonding, masking sharper modes from minor components such as formamide [24, 25]. In very thick films, intense bands can depart from Beer-Lambert linearity (apparent "flatten-

[2]Dissociative electron attachment (DEA) is when a low-energy electron attaches to a molecule, temporarily giving it a negative charge. The ion then quickly breaks apart, typically into smaller ion fragments and neutral molecules [17].

ing" or saturation), which further hides weaker fingerprint peaks [26]. Moreover, NaCl windows are hygroscopic/hydrophilic, as discussed in Section 5.2.1.2, so during dosing the near-substrate region is water-rich (and can even become brine-like at the interface), biasing the spectrum toward a broader O-H/N-H envelope and promoting rapid water uptake/cryopumping [27–29]. After electron irradiation, all significant features are reduced to near-baseline levels, and no prominent new product bands appear, again supporting a fragmentation-and-desorption pathway rather than residue build-up. The complete disappearance of CO_2 is consistent with electron-stimulated desorption and mild beam heating removing weakly bound CO_2 from water-rich interfaces [21, 30]. Any apparent "increase" in the N-H contribution after irradiation is therefore interpreted as a relative effect: electrons and mild beam heating preferentially deplete and compact the water-rich component, so the residual O-H/N-H envelope becomes slightly more N-H weighted even though the overall integrated intensity of the band decreases.

6.2.2 ZnSe Window

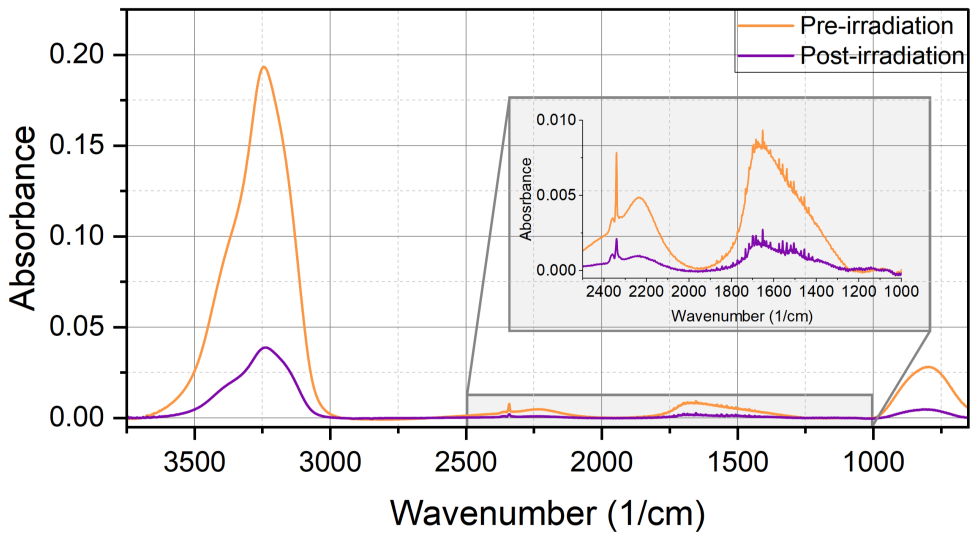


Figure 6.2: Evolution of infrared spectral features for a 50:50 formamide-water ice mixture deposited onto a ZnSe window, at 90 K, and irradiated with 2 keV electrons. These spectra display the pre-irradiation spectrum (yellow) and the post-irradiation spectrum (dark purple).

Consistent with both the ion-irradiation results in Chapter 5 and the composition estimates in Table 6.1, the spectra shown in Figure 6.2 for the ZnSe electron irradiation

experiment indicate a smaller ratio of water in the ice compared with the film grown on the NaCl window. In the ion experiments, NaCl-supported ices were systematically thicker and more water-rich than those on ZnSe because NaCl is hygroscopic and tends to build up a hydrated, brine-like interfacial layer that preferentially takes up water, whereas ZnSe remains comparatively dry with less wetting (see Section 5.2.1.2). The electron-irradiation films follow the same pattern: the ZnSe spectrum showing a cleaner fingerprint region and a broad O-H/N-H band at ∼3300–3200 cm^{-1} that is lower and narrower than the corresponding band in the NaCl spectrum (Figure 6.1), consistent with a lower H_2O fraction. Additionally, on top of the reduced ratio of water in the ice, ZnSe is chemically inert in comparison to NaCl and therefore does not start with a pre-hydrated film. Similarly to the contamination on the NaCl window, ZnSe begins with a small CO_2 peak. Whilst the CO_2 was completely destroyed on the NaCl window, the reduction in CO_2 post-irradiation vs pre-irradiation is marginal on the ZnSe window.

Much like on NaCl, the O-H/N-H/C=O bands on ZnSe are strongly diminished after electron irradiation, and no sharp new product bands emerge. This suggests extensive fragmentation and volatile losses, with little condensed-phase product build-up under 2 keV electrons. The trend is consistent with the ion-irradiation results, Chapter 5: on NaCl, CO_2 often rises early and then declines, whereas on ZnSe it tends to grow more slowly and rarely reaches the subsequent destruction regime. A plausible contributor is the substrate: NaCl is hydrophilic and hygroscopic, so under ambient handling it readily acquires a thin, ion-rich water film (pre-wetting; see Section 5.2.1.2), which strongly alters near-surface transport and desorption pathways [31]. In ESD, the ejection probability is highly surface-biased, governed by energy deposition in the top few nanometers to (at most) a few tens of nanometers via secondary electrons, so species located in this interfacial region are preferentially purged [32].

By contrast, ZnSe is non-hygroscopic and does not form brine films; water ices grown on less-wetting substrates are typically more porous at low temperatures, which enhances volatile trapping in pore networks [33]. Substrate wetting affects island growth and pore topology at 90 K, which biases volatile trapping. Thus, CO_2 produced in the ZnSe films is more likely to remain sequestered, whereas on NaCl it

partitions into and diffuses through the pre-wetted interfacial layer, where ESD efficiently removes it. Additionally, electrolytes in the NaCl brine layer "salt out" CO_2 (lowering its solubility in liquid water), biasing it toward the gas phase and further aiding loss to vacuum.

Film thickness also matters and cannot be discounted when considering observational analysis. ESD efficiency drops rapidly with depth, so thicker ices tend to retain CO_2 formed below the ESD-active zone [32]. Moreover, low-temperature amorphous solid water (ASW) is highly porous; porosity (and therefore volatile capacity) generally increases in thicker films at deposition temperatures $\lesssim$120 K and then collapses, i.e. pores compact and volatile-containing cavities close, on warming or energetic processing [34, 35]. Irradiation can also compact pores, which may re-trap or immobilise volatiles depending on the timing and dose [36, 37]. Taken together, while thickness differences are likely to have contributed to the NaCl-ZnSe contrast, the dominant control here is the substrate: NaCl's pre-wetted, electrolyte-rich interface promotes near-surface availability and efficient ESD-driven CO_2 loss, whereas ZnSe favours retention in a more porous, less-wetted ice [31–33].

Despite the differences in thickness, composition, and substrate properties, the overall spectral shapes for the NaCl and ZnSe experiments are very similar: both show broad O-H/N-H stretching envelopes, comparable formamide C=O features, and the same general pattern of band depletion after electron irradiation (Figures 6.1 and 6.2). This indicates that the underlying electron-driven chemistry in the mixed formamide-water ice is qualitatively the same on both substrates, and that the NaCl-ZnSe contrast mainly reflects differences in ice thickness, porosity, and interfacial processing efficiency rather than fundamentally different reaction networks. Having established the qualitative spectral behaviour on both substrates, the next step is to quantify the initial ice composition and thickness from the pre-irradiation spectra and to use these as a basis for comparing destruction efficiencies.

Table 6.1: Summary of experimental irradiation conditions for electron irradiation experiments, and the transmission range of the windows. Samples were irradiated at 2 keV through different windows, with varied ice compositions and thicknesses.

Window	Energy (keV)	Ice Comp.[a]	Ice Thick. (nm)[b]	Temp. (K)	Fluence (cm^{-2})	Range (cm^{-1})
NaCl	2	12:88	587	90	3.37×10^{19}	625-40000
ZnSe	2	8:92	225	90	3.37×10^{19}	476-16667

[a] Molar ratio of formamide to water.

[b] Ice composition and thickness are from pre-irradiation FTIR band integrals; typical systematic uncertainty ∼30% (up to ∼50%).

6.3 Determination of ice composition and thickness

The relative abundances of water and formamide in the ice mixtures were determined from their integrated infrared absorbance bands, following the procedure described in Section 4.3.2. For each pre-irradiation spectrum, which had already been manually baseline-corrected, only a constant residual offset was removed using adjacent side-bands. The resulting pre-irradiation ice compositions and thicknesses for each window, derived from this procedure, are summarised in Table 6.1. The following bands and literature band strengths were used:

- H_2O: O-H stretching band (3700-3000 cm^{-1}), with band strength $A_{H_2O} = 3.07 \times 10^{-16}$ cm molecule^{-1} at ∼90 K [38].
- NH_2CHO: deconvolved N-H stretching component (3170-3150 cm^{-1})[3], with band strength $A_{FA} = 1.349 \times 10^{-16}$ cm molecule^{-1} (this work, based on independent calibrations of pure formamide ice at comparable temperatures).

For each band, the integrated absorbance S (in cm^{-1}) was computed as:

$$S = \int_{\nu_1}^{\nu_2} A(\nu)\, d\nu, \tag{6.1}$$

where $A(\nu)$ is the baseline-corrected absorbance at wavenumber ν. These values were converted to optical depth as $\tau(\nu) = A(\nu)\ln(10)$ before integration.

The column density N (molecules cm^{-2}) was then obtained from the integrated absorbance S using the band-strength method, assuming the selected feature remained

[3]It should be noted that there is significant overlap with the water O-H band and the formamide N-H bands. Additionally, the N-H band from formamide can shift/broaden the O-H band from water, increasing uncertainty.

in the linear (unsaturated) regime:

$$N = \frac{S}{A}, \tag{6.2}$$

where A is the temperature-appropriate band strength for the chosen vibrational mode. If a band showed partial saturation, the resulting N would be underestimated; such cases were therefore avoided by selecting weaker, unsaturated features for quantification.

The column densities were converted to physical thickness d (in nm) using:

$$d = \frac{10^7\, M\, N}{\rho\, N_A}, \tag{6.3}$$

Where M is the molar mass ($\mathrm{g\,mol^{-1}}$), ρ the bulk density ($\mathrm{g\,cm^{-3}}$), and N_A Avogadro's number. The densities adopted were $\rho = 0.934\,\mathrm{g\,cm^{-3}}$ for amorphous H_2O ice and $\rho = 0.937\,\mathrm{g\,cm^{-3}}$ for formamide ice, values consistent with literature measurements of these ices at cryogenic temperatures [39, 40].

The relative molecular composition was expressed as the molar ratio:

$$R = \frac{N_{\mathrm{FA}}}{N_{\mathrm{H_2O}} + N_{\mathrm{FA}}} \times 100\%, \tag{6.4}$$

This is reported as a two-component proportion "$xx : yy$", representing formamide:water. For example, a measured ratio $N_{\mathrm{FA}}/N_{\mathrm{H_2O}} = 0.12$ corresponds to $\approx 12 : 88$ (FA:H_2O) in molecular terms.

6.3.1 Assumptions and Uncertainties

The following assumptions were made:

1. Band strengths are transferable from literature values or prior calibration, and are temperature-appropriate for the ice mixtures used.

2. The chosen bands are representative and minimally overlapped by other species; residual offsets are small and handled by constant subtraction.

3. If a band becomes optically thick, Beer–Lambert deviates from linearity and N

from S/A is underestimated.

4. Densities of pure condensed phases apply to thin mixed ices.

5. Instrumental noise and digitisation of spectra introduce a ∼10-15% uncertainty in integrated areas.

Taking into account uncertainties in A values (typically ±10-20%), residual baseline placement, and digitisation, the overall uncertainty was conservatively assigned to be ∼30-50% (depending on band crowding: here 30% is adopted) on absolute thicknesses and compositional ratios. The ice compositions and thicknesses are displayed in Table 6.1.

These derived column densities and thicknesses provide the baseline needed to interpret the electron-induced changes in terms of destruction efficiencies and G-values, which are discussed in the following section.

6.4 Destruction Efficiency

In radiation chemistry, quantitative yields are traditionally reported as G-values (molecules per 100 eV of absorbed energy; see Section 5.3), which provide an energy-normalised measure for comparison across radiation types and energies [41]. By contrast, the destruction efficiency η (Equation 6.5) is a per-particle metric (molecules per electron). It expresses the mean number of precursor molecules removed by each incident primary electron. For thin films, η is directly related to the destruction cross-section σ in the low-fluence limit, where $N(F) = N_0 \exp(-\sigma F)$ and $\eta \approx \sigma N_0$ [42, 43]. η is not normalised to energy, it is sensitive to electron energy and stopping power and therefore it is most useful as an experiment-specific metric for quantifying molecular loss per incident electron and for linking to σ, while G-values are preferred for cross-comparison across radiation fields.

For the electron-irradiation experiments, only pre- and post-irradiation FTIR spectra were collected. Without incremental dose points, the initial linear slope required for a proper G-value could not be measured. Endpoint estimates of $G(-M)$ can be reported for completeness; however, these conflate depletion and secondary chemistry,

thereby carrying larger systematic uncertainties. Therefore, destruction efficiencies (η) are emphasised here as the most faithful summary of the electron-beam data. By contrast, the ion-irradiation experiments (AQUILA) included incremental spectra, allowing true G-values to be determined from early-dose slopes.

$$\eta \equiv \frac{N_0 - N}{F} \tag{6.5}$$

Here N_0 and N are the initial and final column densities (molecules cm^{-2}), and F is the total fluence (electrons cm^{-2}). η thus has units of molecules per electron.

Table 6.2: Summary of fluence, $G(-M)$ values, and destruction efficiency for electron irradiation experiments at 2 keV through different windows.

Window	Fluence (particles cm^{-2})	$G(-M)$ (molecules/100 eV)	Destruction Efficiency (molecules electron^{-1})
NaCl	3.37×10^{19}	$(3.62 \pm 0.22) \times 10^{-2}$	$(8.18 \pm 0.41) \times 10^{-3}$
ZnSe	3.37×10^{19}	$(3.74 \pm 0.74) \times 10^{-3}$	$(2.34 \pm 0.12) \times 10^{-3}$

Table 6.2 reports the calculated destruction efficiencies and G-values. The NaCl-supported film shows a destruction efficiency ∼3.5× higher than ZnSe. Since both films exceeded the ∼180 nm penetration depth of 2 keV electrons in 50:50 formamide-water ice [44], this difference cannot be attributed to incomplete stopping of the beam. Instead, the substrate properties are implicated. ZnSe (Zn=30, Se=34) has a much higher atomic number than NaCl (Na=11, Cl=17), which leads to stronger electron backscattering [45, 46]. Backscattered electrons (BSEs) reduce net energy deposition in the overlying ice, but can redistribute a fraction of the energy near the film-substrate interface. The NaCl films, being thicker, confine essentially all primaries, whereas the thinner ZnSe film (see Table 6.1) was close to the electron range, allowing some primary and BSE contributions at the interface. This likely accounts for the lower net destruction efficiency observed on ZnSe. Although most primaries stop within the film, substrate-dependent BSE and secondary-electron spectra still modulate interfacial energy delivery.

A useful way to reconcile η and $G(-M)$ is through the mean energy deposited per electron:

$$E_{\mathrm{dep/e^-}} \;=\; 100 \text{ eV} \, \frac{\eta}{G(-M)}. \tag{6.6}$$

Numerically,

$$E_{\mathrm{dep/e^-}}(\mathrm{NaCl}) \approx 22.6 \text{ eV/e}^-, \tag{6.7}$$

$$E_{\mathrm{dep/e^-}}(\mathrm{ZnSe}) \approx 62.5 \text{ eV/e}^-. \tag{6.8}$$

Thus, while fewer molecules are destroyed per electron on ZnSe, the ratio of η to $G(-M)$ implies a higher effective deposition per electron. This highlights the strong role of substrate-dependent scattering in shaping energy delivery to the ice, consistent with the Z-scaling of electron backscatter coefficients [47]. It should be noted that the values derived from $\eta/G(-M)$ are illustrative only; because the reported electron G-values are endpoint estimates (not initial-slope G), they are subject to dose and chemistry biases and should not be interpreted as quantitative film-dose without a transport model.

It is most likely that due to the hydrophilic and hygroscopic nature of NaCl, the chemistry occurring at the interfacial layer of NaCl that results in the higher destruction efficiency. The substrate effects mirror the destruction efficiency findings: NaCl promotes faster destruction, whereas ZnSe tends to preserve formamide for longer. Whilst no by-products were observed after irradiation, these results do agree with what was discussed in the heavy ion irradiation experiments, in Chapter 5.

Assumptions and uncertainties

The destruction efficiencies and $G(-M)$ values derived from the electron-irradiation experiments are based on several simplifying assumptions. First, only pre- and post-irradiation spectra were available, so both η and $G(-M)$ are based on endpoint differences in column density rather than on true initial slopes. This means that any curvature in the dose-response (e.g. due to secondary chemistry or saturation at high dose) is folded into the reported values. Second, the column densities themselves inherit the uncertainties from the ice-quantification procedure in Section 6.3, including band-strength uncertainties (∼10-20%), baseline placement, and partial saturation of strong bands in the thick NaCl film; these contribute ∼30% systematic uncertainty on absolute N_0 and N. Third, the fluence was taken from the beamline diagnostics and

assumed to be spatially uniform over the IR footprint; any non-uniformity in the beam profile or time-dependent drift would introduce an additional ∼10-20% uncertainty in the effective fluence.

Taken together, these effects imply that the absolute values of η and $G(-M)$ carry an order 30-50% systematic uncertainty. However, the relative trends between NaCl and ZnSe, and between electrons and ions, are more robust, since many of the systematic contributions (e.g. band strengths and calibration of the IR response) cancel out in ratios. Accordingly, the electron $G(-M)$ values are used here as illustrative, order-of-magnitude estimates, while the destruction efficiencies and cross-comparisons are emphasised for the interpretation.

While these destruction efficiencies and endpoint $G(-M)$ values are specific to the 2 keV electron experiments, they are most informative when set alongside the corresponding ion-irradiation data. The following section, therefore, places the electron results in direct comparison with the heavy-ion experiments from Chapter 5.

6.5 Electrons vs Ions: A Comparative Analysis

A striking difference emerges when comparing the overall effectiveness of electrons and ions at destroying formamide. The electron irradiations, Table 6.2, required fluences on the order of 10^{19} particles cm^{-2}, yet only achieved destruction efficiencies of 8.18×10^{-3} and 2.34×10^{-3} molecules per electron on NaCl and ZnSe, respectively. In contrast, ion irradiations required fluences several orders of magnitude lower (10^{14}-10^{17} particles cm^{-2}) to achieve comparable or greater destruction, with $G(-M)$ values typically between 2 and 4 molecules per 100 eV. This difference is consistent with the expected behaviour of low-LET versus high-LET radiation: electrons deposit their energy more diffusely, producing relatively sparse molecular damage, while ions (especially heavier and more highly charged species) deliver energy in dense tracks, leading to far more extensive radiolytic destruction per particle.

The choice of substrate had a substantial effect on the radiation chemistry. Both electrons and ions produced substantial destruction when samples were deposited on NaCl windows, but this behaviour was markedly suppressed on ZnSe. For electron

irradiation, the destruction of ZnSe was approximately 3.5 times lower than on NaCl, despite identical fluences. An even more pronounced effect was observed for protons: $G(-M)$ values on NaCl were ∼3.5, whereas on ZnSe they dropped to only ∼0.05. In contrast, heavier ions (O^{2+} and S^{5+}) remained relatively effective on ZnSe, although with somewhat lower $G(-M)$ values than on NaCl. This pattern suggests that the NaCl substrate enhances radiation-driven destruction pathways relative to the more inert ZnSe case, particularly for low-LET projectiles like electrons and protons.

Low-LET projectiles, such as electrons, dissipate their energy diffusely, producing sparse ionisations and excitations distributed across the ice matrix. The result is many isolated fragments or radicals that either desorb via electron-stimulated desorption (ESD) or remain too dilute to recombine efficiently into stable condensed-phase products. In contrast, high-LET ions (especially O^{2+} and S^{5+}) deposit energy along dense tracks only a few nanometres wide. Within these track cores, the radical density is high enough that recombination pathways are strongly favoured, producing robust condensed-phase species such as OCN^-, CO, and CO_2 with well-defined IR bands [22, 42, 48]. This difference explains why ion irradiations typically show new, sharp IR product features, whereas electron irradiations are dominated by precursor band depletion without significant product accumulation.

Overall, these results indicate that the efficiency of radiolytic destruction is governed not only by the energy and type of the projectile but also by the physical properties of the underlying substrate. The markedly lower destruction on ZnSe may reflect its higher density and stopping power, which could reduce the generation or escape depth of secondary electrons, thereby limiting the cascade of damage events that typically follow primary energy deposition. In simple terms, ZnSe contains a heavier, doubly charged cation (Zn^{2+}) compared with the singly charged Na^+ in NaCl, and both Zn and Se carry more bound electrons than Na and Cl. The different bond charges and partial charge distribution in Zn-Se relative to Na-Cl, together with the higher effective atomic number of ZnSe, enhance electron scattering and backscattering, and modify the surface potential and secondary-electron yield. This further reduces the number of secondaries that can propagate into the ice and drive chemistry near the interface.

This effect appears most severe for low-LET radiation, which relies heavily on secondary electron production to drive chemistry. In contrast, high-LET ions can still cause substantial molecular disruption in ZnSe despite this suppression. The combination of these findings demonstrates that low-energy electrons are inherently much less efficient than high-energy ions on a per-particle basis, and that the chemical outcome of radiolysis experiments can depend sensitively on the choice of substrate.

In summary, the electron data and ion data tell a consistent story: low-LET electrons primarily deplete precursors through diffuse energy deposition and ESD-biased loss with little condensed-phase product build-up, whereas high-LET ions create dense track cores that favour recombination chemistry and the emergence of IR-visible residues (e.g., CO, CO_2, OCN^-). Substrate choice modulates both regimes; NaCl amplifies near-surface processing and volatile escape, while ZnSe tends to retain products, so any cross-comparison of radiolysis efficiencies must account for interfacial physics as well as LET. Practically, this means electrons are less efficient per particle and more sensitive to surface/wetting conditions, while ions remain comparatively robust drivers of bulk chemical change across substrates.

6.6 Implications for Europa's Near-Surface Chemistry

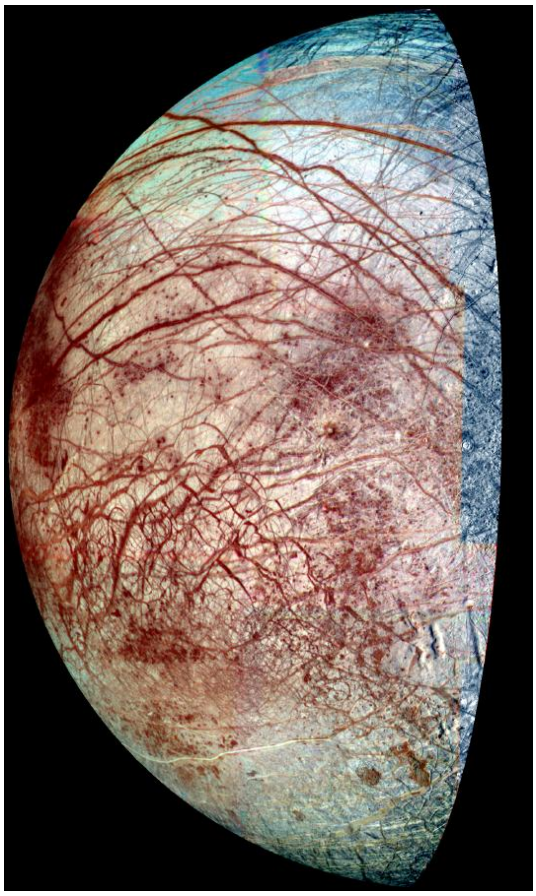


Figure 6.3: Enhanced colour image of Europa where the reddish linear features show cracks and ridges, the "chaos terrain". The red material at the ridges and chaos terrains is a non-ice contaminant, likely salts brought to the surface from the ocean. Sourced: NASA/JPL/University of Arizona.

The electron irradiation experiments show that 2 keV electrons are comparatively inefficient at driving bulk destruction of formamide in water-rich ices, but highly effective at depleting and desorbing volatiles in the near-surface region. On NaCl, the combination of hygroscopic, salt-rich interfaces and abundant low-energy secondary electrons promotes faster destruction and volatile loss than on ZnSe, where an inert, less-wetting substrate favours volatile retention in a more porous ice. This is particularly relevant to Europa's chaos terrain (Figure 6.3), where salt-rich material brought to the surface from the subsurface ocean is expected to dominate the interfacial chemistry. These substrate dependencies mirror, and help to explain, the trends seen in the ion-irradiation

experiments in Chapter 5.

In the context of Europa, this suggests that electron irradiation will primarily control the chemistry and volatile inventory of the uppermost ice layers, especially in salt-rich terrains where pre-wetted, brine-like interfaces are likely. A more detailed synthesis of how the electron and ion results combine to shape Europa's surface chemistry, and of the implications for the survivability and detectability of formamide and related species, is presented in the overall Conclusions and Future Work Chapter (Chapter 8).

Bibliography

[1] Trumbo S, Becker T, Brown M, Denman W, Molyneux P, Hendrix A, et al. A New UV Spectral Feature on Europa: Confirmation of NaCl in Leading-hemisphere Chaos Terrain. The Planetary Science Journal. 2022;3.

[2] Mifsud DV, Hailey PA, Herczku P, Juhász Z, Kovács STS, Sulik B, et al. Laboratory Experiments on the Radiation Astrochemistry of Water Ice Phases. The Astrophysical Journal. 2023.

[3] Müller B, Giuliano B, Goto M, Caselli P. Spectroscopic measurements of CH3OH in layered and mixed interstellar ice analogues. Astronomy & Astrophysics. 2021.

[4] Szalay J, Allegrini F, Ebert R, Bagenal F, Bolton S, Fatemi S, et al. Oxygen production from dissociation of Europa's water-ice surface. Nature Astronomy. 2024;8:567 576.

[5] Madey TE, John T Yates J. Electron-Stimulated Desorption as a Tool for Studies of Chemisorption: A Review. Journal of Vacuum Science and Technology. 1971.

[6] Redhead PA. The first 50 years of electron stimulated desorption (1918-1968). Vacuum. 1997.

[7] Auger effect | Auger electron, electron emission, atomic transitions | Britannica — britannica.com;. [Accessed 09-09-2025]. `https://www.britannica.com/science/Auger-effect`.

[8] Knotek ML, Feibelman PJ. Ion Desorption by Core-Hole Auger Decay. Physical Review Letters. 1978.

[9] Gálvez O, Ortega IK, Maté B, Moreno MA, Martín-Llorente B, Herrero VJ, et al. A study of the interaction of CO2 with water ice. Astronomy & Astrophysics. 2007.

[10] Kruczkiewicz F, Dulieu F, Ivlev A, Caselli P, Giuliano BM, Ceccarelli C, et al. Comprehensive laboratory constraints on thermal desorption of interstellar ice analogues. Astronomy & Astrophysics. 2024.

[11] Qasim D, Lamberts T, He J, Chuang KJ, Fedoseev G, Ioppolo S, et al. Extension of the HCOOH and CO2 solid-state reaction network during the CO freeze-out stage: inclusion of H2CO. Astronomy & Astrophysics. 2021.

[12] Grills DC, Lymar SV. Radiolytic formation of the carbon dioxide radical anion in acetonitrile revealed by transient IR spectroscopy. Physical Chemistry Chemical Physics. 2018.

[13] Wang XD, Gao XF, Xuan CJ, Tian SX. Dissociative electron attachment to CO2 produces molecular oxygen. Nature Chemistry. 2016.

[14] Itikawa Y. Cross Sections for Electron Collisions With Carbon Dioxide. 2002.

[15] Ioppolo S, Kanuchov'a Z, James R, Dawes A, Ryabov A, Dezalay J, et al. Vacuum ultraviolet photoabsorption spectroscopy of space-related ices: formation and destruction of solid carbonic acid upon 1 keV electron irradiation. Astronomy & Astrophysics. 2020.

[16] Gerakines P, Moore M, Hudson R. Carbonic acid production in H_2O:CO_2 ices. UV photolysis vs. proton bombardment. 2000;357:793-800.

[17] Fabrikant I. Recent progress in the theory of dissociative electron attachment: from diatomics to biomolecules. 2011.

[18] Jay-Gerin J. Fundamentals of Water Radiolysis. Encyclopedia. 2025.

[19] Sanche L. Low energy electron-driven damage in biomolecules. The European Physical Journal D - Atomic, Molecular, Optical and Plasma Physics. 2005;35:367-90.

[20] Herring-Captain J, Grieves GA, Alexandrov A, Sieger MT, Chen H, Orlando TM. Low-energy (5–250 eV) electron-stimulated desorption of H+, H2+, and H+(H2O)n from low-temperature water ice surfaces. Physical Review B. 2005.

[21] Abdulgalil AGM, Rosu-Finsen A, Marchione D, Thrower JD, Collings MP, McCoustra MRS. Electron-Promoted Desorption from Water Ice Surfaces: Neutral Gas-Phase Products. ACS Earth and Space Chemistry. 2017.

[22] Pilling S, Duarte ES, Silveira ÊF, Balanzat E, Rothard H, Domaracka A, et al. Radiolysis of ammonia-containing ices by energetic, heavy, and highly charged ions inside dense astrophysical environments. Astronomy & Astrophysics. 2009.

[23] Zheng W, Jewitt D, Kaiser RI. Electron irradiation of crystalline and amorphous D 2O ice. Chemical Physics Letters. 2007.

[24] Ikemoto Y, Harada Y, Tanaka M, Nishimura S, Murakami D, Kurahashi N, et al. Infrared Spectra and Hydrogen-Bond Configurations of Water Molecules at the Interface of Water-Insoluble Polymers under Humidified Conditions. The Journal of Physical Chemistry B. 2022.

[25] Zelent B, Vanderkooi JM. Infrared spectroscopy used to study ice formation: the effect of trehalose, maltose and glucose on melting. Analytical Biochemistry. 2009.

[26] Chalmers JM. Mid-infrared Spectroscopy: Anomalies, Artifacts and Common Errors. Handbook of Vibrational Spectroscopy. 2006.

[27] Sodium Chloride Windows | Edmund Optics — edmundoptics.com;. [Accessed 10-09-2025]. https://www.edmundoptics.com/f/sodium-chloride-nacl-windows/14170/?srsltid=AfmBOorTwk6rVCpXxTuZMzjLlK3U9esKTWfr1KItCg3W_0Ck3ZqK6DgY&.

[28] Baglin V. Cryopumping and Vacuum Systems. Proceedings of the 2017 CERN–Accelerator–School course on Vacuum for Particle Accelerators. 2017.

[29] Arsić J, Kamiński D, Radenović N, Poodt P, Graswinckel WS, Cuppen H, et al. Thickness-dependent ordering of water layers at the NaCl(100) surface. The Journal of chemical physics. 2004.

[30] Šiller L, Sieger M, Orlando T. Electron-stimulated desorption of D2O coadsorbed with CO2 ice at VUV and EUV energies. Journal of Chemical Physics. 2003.

[31] Souda R. Nanoconfinement Effects of Water on Hydrophilic and Hydrophobic Substrates at Cryogenic Temperatures. The Journal of Physical Chemistry C. 2012.

[32] Mitchell EH, Raut U, Teolis BD, Baragiola RA. Porosity effects on crystallization kinetics of amorphous solid water: Implications for cold icy objects in the outer solar system. Icarus. 2017.

[33] Raut U, Fama M, Teolis B, Baragiola R. Characterization of porosity in vapor-deposited amorphous solid water from methane adsorption. The Journal of chemical physics. 2007;127 20:204713.

[34] He J, Clements AR, Emtiaz S, Toriello F, Garrod RT, Vidali G. The effective surface area of amorphous solid water measured by the infrared absorption of carbon monoxide. Submitted to ApJ. 2019.

[35] Burghaus U. Adsorption of water on epitaxial graphene. Journal of Materials Research. 2020;36:129 139.

[36] Accolla M, Congiu E, Dulieu F, Manicò G, Chaabouni H, Matar E, et al. Changes in the morphology of interstellar ice analogues after hydrogen atom exposure. Physical chemistry chemical physics : PCCP. 2010;13 17:8037-45.

[37] Dohnálek Z, Kimmel G, Ayotte P, Smith RS, Kay BD. The deposition angle-dependent density of amorphous solid water films. Journal of Chemical Physics. 2003;118:364-72.

[38] Escribano B, del Burgo Olivares C, Carrascosa H, Martín-Doménech R, Gómez PC, Caro GMM. Estimating the infrared band strengths of amorphous interstellar ice analogues using density functional theory. Astronomy & Astrophysics. 2025.

[39] Brucato J, Baratta G, Strazzulla G. An infrared study of pure and ion irradiated frozen formamide. Astronomy & Astrophysics. 2006;455:395-9.

[40] Loerting T, Bauer M, Kohl I, Watschinger K, Winkel K, Mayer E. Cryoflotation: densities of amorphous and crystalline ices. The journal of physical chemistry B. 2011;115 48:14167-75.

[41] Garrett BC, Dixon DA, Camaioni DM, Chipman DM, Johnson MA, Jonah CD, et al. Role of Water in Electron-Initiated Processes and Radical Chemistry: Issues and Scientific Advances. Chemical Reviews. 2004.

[42] Dartois E, Dartois E, Augé B, Augé B, Augé B, Boduch P, et al. Heavy ion irradiation of crystalline water ice. arXiv: Astrophysics of Galaxies. 2015.

[43] Barros ALF, Barros ALF, Andrade D, Silveira ÊF, Alcantara KF, Boduch P, et al. Chemical reactions in the nitrogen–acetone ice induced by cosmic ray analogues: relevance for the Solar system. Monthly Notices of the Royal Astronomical Society. 2017;474:1469-81.

[44] Meesungnoen J, Jay-Gerin J, Filali-Mouhim A, Mankhetkorn S. Low-Energy Electron Penetration Range in Liquid Water. 2002;158:657 660.

[45] Assa'd AMD, Gomati MME. Backscattering coefficients for low energy electrons. Scanning Microscopy. 1998.

[46] Gomati MME, Walker CGH, Assa'd AMD, Zadrazil M. Theory Experiment Comparison of the Electron Backscattering Factor from Solids at Low Electron Energy (250–5,000 eV). Scanning. 2008.

[47] Schröder S, Rammelkamp K, Vogt DS, Gasnault O, Hübers HW. Contribution of a martian atmosphere to laser-induced breakdown spectroscopy (LIBS) data and testing its emission characteristics for normalization applications. Icarus. 2019.

[48] Spinks JWT, Woods RJ. An introduction to radiation chemistry. New York, NY (USA); John Wiley and Sons Inc.; 1989.

Chapter 7

VUV Irradiation of Formamide and Water Ice Mixture

Europa's surface is continually processed by both energetic charged particles and solar vacuum-ultraviolet (VUV) photons. In Chapters 5 and 6, the effects of ion and electron irradiation on formamide-water ices were investigated as analogues for radiolysis driven by Jupiter's magnetosphere. Those studies considered how energetic particles can restructure the ice and drive the formation and destruction of simple, potentially prebiotic species at depth. However, in the uppermost layers of the ice, where photons dominate the energy input, solar VUV irradiation is expected to play a key role in controlling the chemistry and desorption of volatiles on Europa's surface.

In this Chapter, the results of the VUV irradiation of formamide-water ices on NaCl windows are presented. These experiments aimed to simulate solar VUV irradiation of Europa's surface ice. NaCl windows were used to simulate a saline surface analogous to that expected on Europa, thereby reproducing the potential chemical evolution occurring on a salt-rich substrate.

7.1 Introduction

VUV irradiation experiments were performed at the NSRRC TLS in Taiwan. These experiments studied formamide-water ices deposited on NaCl substrates at temperatures between 10 and 130 K, chosen for their relation to the surface temperature of Europa; see Section 2.3.1. Each sample was irradiated with 9 eV photons under high-vacuum conditions to simulate astrochemical photochemistry in cold environments. Post-irradiation, both VUV absorption spectra and TPD (temperature-programmed desorption) spectra - see Section 7.3.1.1 for more details - were collected to characterise photochemical and thermal evolution.

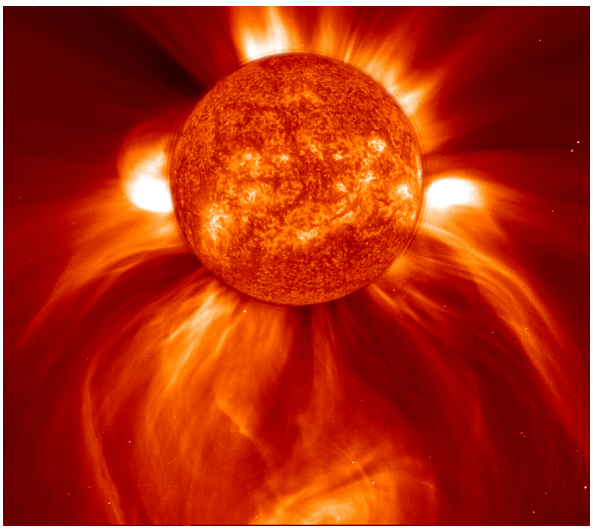


Figure 7.1: An image acquired by the LASCO C2 coronagraph instrument on the ESA-NASA SOHO spacecraft showing a widely spreading coronal mass ejection (CME), taken in January 2002. Such eruptions contribute strongly to the Sun's vacuum-ultraviolet (VUV) output, which in turn irradiates the surfaces of outer Solar System bodies, including Europa [1]. **Credit:** ESA/NASA/Soho.

The Sun is the dominant source of VUV photons in the Jovian system. An example of such VUV-emitting solar activity is shown in Figure 7.1, which presents a coronal mass ejection observed in the VUV by the SOHO spacecraft. Although Europa orbits far from the Sun, this radiation field provides the primary VUV photon flux incident on its surface. VUV irradiation was therefore chosen to reproduce the solar vacuum-UV flux at Europa's surface. Because Europa's atmosphere is extremely tenuous, solar photons reach the surface with minimal attenuation and penetrate only the upper hundreds of nanometres [2], where they induce electronic excitations that can break molecular bonds or eject volatiles [3, 4].

VUV experiments were performed in two runs: Experimental Run 1 explored early-stage irradiation and desorption between 10-90 K, while Experimental Run 2 extended this temperature range to 130 K to investigate additional thermal processing effects. See Section 4.3.3 for a more detailed explanation of the methodology. These temperatures, excluding 10 K, which was used as a control temperature, are representative of the surface temperatures Europa experiences. At its lowest, near the poles, Europa can reach temperatures as low as 50 K, and at its equator, Europa can reach highs of 130 K, with a mean annual surface temperature of ∼90 K, [5]. A more detailed description of the conditions experienced at Europa can be found in Section 2.3.1.

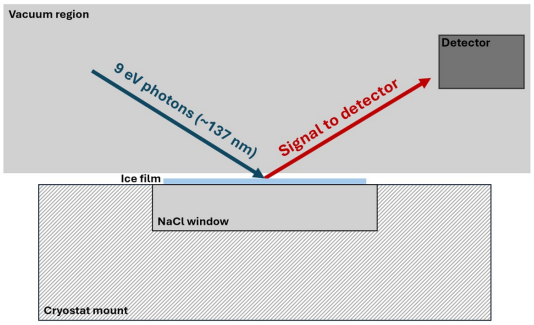


Figure 7.2: Schematic of the experimental geometry for VUV irradiation of formamide-water ices on NaCl substrates. The VUV beam is incident from the vacuum side, ensuring that absorption arises only from the condensed film and not from the NaCl substrate.

In this beamline setup, both VUV irradiation and UV/VUV spectral acquisition were performed with the photons incident on the ice from the vacuum side. During UV/VUV spectral acquisition, the cryostat was rotated such that both the light source and detector were positioned on the vacuum side of the sample (see Figure 7.2). In this configuration, the detector collects the emergent signal from photons that have interacted with the ice film, while the NaCl window remains outside the optical path. Although NaCl is transparent in the infrared, it becomes strongly absorbing below ~150 nm, including at 137 nm (9 eV). This geometry, therefore, avoids absorption by the substrate and ensures that the recorded spectra reflect only the electronic transitions of the mixed formamide-water ice. The wavelength-dependent changes in signal intensity are interpreted as absorption within the ice, which in this energy range is dominated by broad electronic transitions characteristic of VUV excitation.

Table 7.1: Summary of experimental irradiation conditions for Experimental Runs 1 and 2. Both runs used photon irradiation (9 eV); the VUV beam impinged from the vacuum side. Ice thicknesses here are displayed as estimates only. The same fluence applies to all temperatures.

Experiment	Irradiation Type	Energy (eV)	Temp. (K)	Ice Thickness (nm)[a]	Fluence (cm^{-2})
Experimental Run 1	Photon	9	10	99.58	$(2.4 \pm 1.3)\times10^{19}$
			50	75.71	
			90	57.26	
Experimental Run 2	Photon	9	10	225.80	$(2.4 \pm 1.3)\times10^{19}$
			50	58.12	
			90	77.84	
			110	30.73	
			130	40.05	

[a] Ice thicknesses are dosing/attenuation-based estimates (pressure-time/Hertz-Knudsen style) and should be treated as semi-quantitative; fluence uncertainty is shown explicitly.

Table 7.1 summarises the irradiation conditions for Experimental Runs 1 and 2.

In these VUV experiments, the primary variable of interest was temperature, so the substrate material was not varied: only NaCl substrates were used. This contrasts with the heavy-ion and electron irradiation studies in earlier chapters, where both NaCl and ZnSe were compared, and ensures that all VUV measurements in this Chapter are directly comparable across the temperature series.

Ice thicknesses in Table 7.1 are pressure-time estimates (Hertz-Knudsen) and should be treated as semi-quantitative; the method and associated uncertainties are described in Section 7.2.1 (Ice Thickness Determination).

7.2 Experimental Parameters and Methodology

The VUV experiments described in this Chapter share a common set of preparation, irradiation, and diagnostic conditions. Mixed formamide-water ices were deposited onto NaCl windows under high-vacuum, irradiated with 9 eV photons, and subsequently characterised using UV/VUV spectroscopy and temperature-programmed desorption (TPD). The key experimental parameters, including deposition temperature, estimated ice thickness, and photon fluence, are summarised in Table 7.1. The following subsections outline the approach used to estimate ice thicknesses from the deposition conditions and describe the irradiation and heating protocols adopted for Experimental Runs 1 and 2.

7.2.1 Ice Thickness Determination

The estimated ice thicknesses in Table 7.1 follow from these Hertz-Knudsen calculations based on the deposition conditions, rather than from direct optical measurements. VUV spectroscopy is a powerful technique for probing electronic transitions in astrophysical ice analogues, but it does not readily yield quantitative information on film thickness or composition. Accurate thickness measurements require well-characterised absorption cross-sections in the solid phase, which exist for water ice [3] but are not well quantified for solid formamide. Solid-phase VUV spectra of formamide have been reported, but reliable absolute absorption cross-sections are not yet available. Furthermore, molecular interactions and hydrogen bonding within binary ices lead to

non-linear mixing behaviour, causing band shifts and intensity changes that prevent straightforward deconvolution into separate component spectra.

This limitation arises because, in practice, the Beer-Lambert law cannot be applied directly to condensed, mixed ices. Absorbance follows the Beer-Lambert law (see Equation 7.2.1 below), but in these condensed, mixed ices the variables are not separable. Increasing either the film thickness (l) or the formamide concentration (c) similarly raises the total absorbance, so changes in thickness and composition are effectively indistinguishable in the VUV spectra. In addition, real cryogenic ices are not optically smooth or uniform: their porosity and surface roughness introduce diffuse optical losses and internal reflections, breaking the assumptions of the Beer-Lambert law, which requires a clear, homogeneous, purely absorbing medium.

$$A(\lambda) = \varepsilon(\lambda)cl, \tag{7.1}$$

where $A(\lambda)$ is the absorbance, $\varepsilon(\lambda)$ is the molar absorptivity, c is the molar concentration, and l is the optical path length.

During irradiation, the ice film undergoes both chemical changes and compaction: new species form, overlapping the parent spectrum, and density changes alter the optical path. Accordingly, the VUV spectra were interpreted qualitatively, and relative deposition was estimated indirectly from chamber pressure changes and dosing time rather than by absolute quantification. This limitation is particularly pronounced in the VUV, where electronic transitions are broad, overlapping, and sensitive to local structure, and solid-phase absorption cross-sections are poorly constrained.

Despite these experimental limitations, it was still necessary to estimate the minimum ice thickness required for the majority of the incident photon energy to be absorbed. This was done by calculating the VUV penetration depth of a 50:50 formamide-water ice using the Beer-Lambert absorption formalism [3, 6]. Laboratory photoabsorption cross-sections for solid formamide at 30 K [7], together with the molecular number density of the ice (calculated from its bulk density and molar mass), were used to determine an estimate for the absorption coefficient - that is, the probability per unit thickness that a photon will be absorbed. Combining this value with the equivalent

for water ice gave a penetration depth of roughly 22 nm for the 50:50 mixture when irradiated with 9 eV photons. This means that the photon intensity falls by a factor of e over 22 nm, with about two-thirds of photons absorbed within that distance. To absorb $\geq$95 % of photons, the ice would need to be at least $\sim$67 nm thick.

Based on these estimated thicknesses (Table 7.1), most of the deposited ices meet or exceed this threshold, although some films are thinner and therefore absorbed a smaller fraction of the incident radiation; an effect that has been considered in the interpretation of their VUV spectra. Conversely, in Experimental Run 2, the 10 K ice was substantially thicker than this limit. The estimated ice thicknesses show a trend with deposition temperature within Experimental Run 1, decreasing as the substrate becomes warmer; Experimental Run 2 shows more variable thicknesses across temperature, likely reflecting run-to-run differences in sticking efficiency and deposition conditions at the beamline. This behaviour is expected: at higher temperatures, molecules striking the surface are more likely to re-evaporate rather than stick, reducing the net condensation rate and resulting in thinner films. Similar temperature-dependent variations in sticking efficiency and desorption rate have been reported for water and mixed molecular ices under high-vacuum conditions, [8, 9].

Finally, because mid-infrared vibrational bands were not accessible at BL03, the formamide:H_2O mixing ratio for these VUV experiments could not be measured directly. The ices are therefore treated as approximately equimolar ($\sim$50:50 formamide:H_2O), consistent with the intended deposition conditions. This composition should be regarded as nominal rather than a quantitatively constrained experimental value, and is used to provide a reasonable basis for the penetration-depth estimates and qualitative comparison of the VUV results.

Ice thicknesses themselves were estimated using pressure- and time-based calculations derived from the Hertz-Knudsen equation, which relate chamber pressure changes and dosing time to molecular flux:

$$Z = \frac{P}{\sqrt{2\pi m k_B T}}, \tag{7.2}$$

where Z is the molecular flux in molecules cm^{-2} s^{-1}, P is the gas pressure in Pascals,

m is the molecular mass in kg molecule^{-1}, k_B is the Boltzmann constant in J K^{-1}, and T is the gas temperature in Kelvin. Assuming full sticking ($s = 1$), the resulting mass flux (sZm) was converted to a film thickness using the ice's bulk density and the valve-open time. As these estimates rely on several simplifying assumptions - including uniform chamber pressure, complete sticking, and an approximate density - they should be regarded as semi-quantitative indicators rather than absolute measurements of film thickness.

As in the heavy-ion and electron irradiation experiments (Sections 4.3.4 and 5.1), the ice films were grown by background deposition rather than direct line-of-sight deposition. This method produced homogeneously mixed ices, which are more representative of astrophysical and planetary environments where molecules accrete simultaneously from the gas phase. Mixed ices also allow bulk chemical reactions throughout the film, unlike layered ices, where chemistry is confined mainly to the interfaces [10–12].

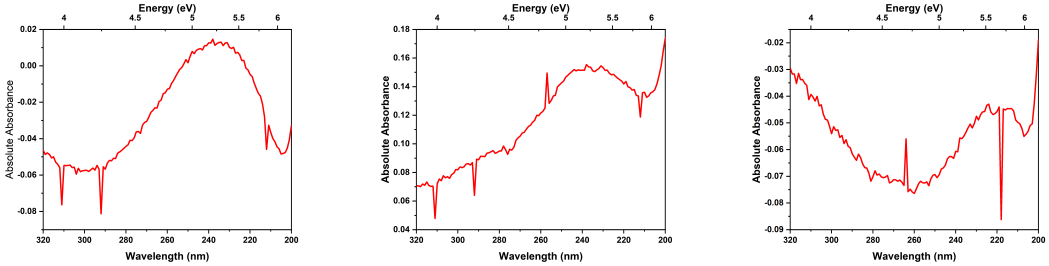
7.3 Electronic Spectra and Spectral Evolution

7.3.1 Experimental Run 1: Spectral Evolution from 10-90 K

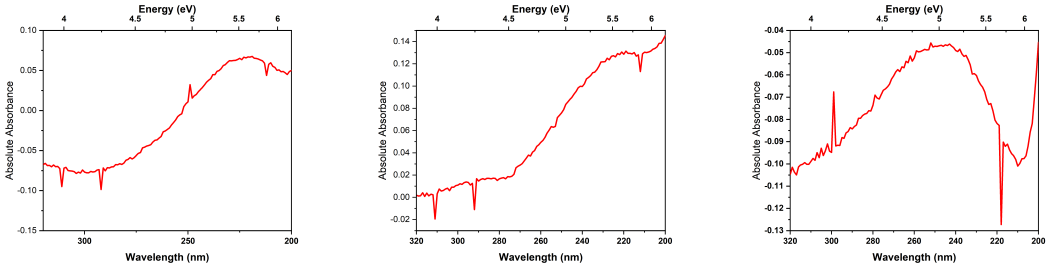
The "Experimental Run 1" experiments were performed at temperatures of 10, 50, and 90 K. These temperatures sample the range of surface conditions expected on Europa (see Section 2.3.1). Experimental Run 1 was designed to investigate early-stage irradiation and desorption between 10 and 90 K. The 10 K photon-irradiation experiments provided a baseline for interpreting the behaviour of mixed formamide-water ices at higher temperatures, as both thermal diffusion and radical mobility are strongly suppressed at this temperature, allowing the intrinsic photochemical effects of the VUV irradiation on the ices to be isolated [13]. For a detailed description of the experimental parameters, see Section 4.3.3.

The chosen photon energy, 9 eV, lies within the vacuum-ultraviolet range and provides sufficient enough energy to excite $\pi \rightarrow \pi^*$ and $n \rightarrow \pi^*$ electronic transitions in both formamide and its photoproducts, [3, 14]. See Section 3.2.1.3 for an in-depth explanation about formamide in the VUV and its transition states.

Figure 7.3 shows both the pre- and post-irradiation spectra for 10 K, 50 K, and 90 K. Figure 7.4 displays the subtraction spectra (post- subtract pre-irradiation) for a visual guide on the differences in absorbance between the two runs of spectra.

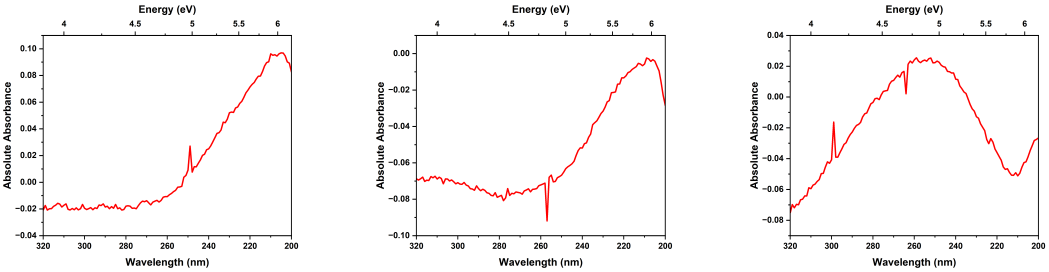


(a) 10 K: Pre-irradiation **(b)** 50 K: Pre-irradiation **(c)** 90 K: Pre-irradiation



(d) 10 K: Post-irradiation **(e)** 50 K: Post-irradiation **(f)** 90 K: Post-irradiation

Figure 7.3: VUV absorption spectra of formamide-water ices collected pre- and post-irradiation at 10, 50, and 90 K for **Experimental Run 1**. All experiments used NaCl substrates and 9 eV photon irradiation. Sharp vertical features ('spikes') that appear at fixed energies are instrumental artefacts (e.g. detector noise or residual lamp structure) and do not correspond to molecular absorption bands.



(a) 10 K **(b)** 50 K **(c)** 90 K

Figure 7.4: Subtraction spectra (post- subtract pre-irradiation) of formamide-water ices deposited on NaCl substrates at 10, 50, and 90 K for **Experimental Run 1**. The differential absorbance isolates photochemically induced changes.

As shown in Figure 7.3, the pre- and post-irradiation spectra share a broadly similar overall shape. Before irradiation, all three samples exhibit a single, broad absorption band centred around 5-6 eV. Following exposure to 9 eV photons, this feature becomes smoother and less structured, shifts slightly to higher energy (blue-shifts) - bar

90 K, which slightly red-shifts and broadens markedly (Figure 7.5) -, and shows an overall increase in absorbance. The subtraction spectra in Figure 7.4 isolate these irradiation-induced changes, revealing a redistribution of oscillator strength and the appearance of overlapping electronic transitions arising from photoproducts. Here, oscillator strength describes the probability or intensity of an electronic transition - how strongly a molecule absorbs light at a given energy - while overlapping transitions occur when multiple species absorb within the same spectral region, producing blended rather than distinct peaks. The resulting subtraction spectra display clear positive features near 5-6 eV, consistent with an enhancement of the amide $n \rightarrow \pi^*$ "W" transition of formamide (see Section 7.3.1, page 276), typically centred near 5.3 eV in the condensed phase, [14–16].

In comparison to the 10 K spectra, the 50 K spectra exhibited a less well-defined and broader W-band near 5.0-5.6 eV, with a less distinct valley around 210 nm ($\sim$6 eV). Additionally, the pre-irradiation baseline rose more steadily between 4-5.5 eV, consistent with a more structurally relaxed and optically uniform film. After irradiation, the 50 K spectrum becomes smoother and less structured, indicating a loss of intensity and increased homogeneity (Figure 7.5) due to enhanced hydrogen-bond rearrangement and inhomogeneous mixing. At 50 K, partial molecular mobility allows dipoles to reorient and mixtures to interdiffuse on experimental timescales, increasing environmental heterogeneity and broadening the electronic transitions [13, 17], see Section 4.3.6 for more detail.

Compared to 10 and 50 K, the broad peak at 90 K is even less well-defined and broader (Figure 7.5). The pre-irradiation spectrum displayed a broad absorption maximum near 5.6 eV, with a more pronounced red tail than observed at 10 K and 50 K. The valley at 6 eV became less distinct, suggesting a greater degree of inhomogeneous broadening within the ice. This broadening is characteristic of partially annealed amorphous[1] mixtures where local hydrogen-bond geometries vary widely [17, 20]. Fol-

[1]Amorphous ice has a disordered, porous structure that traps molecules and radicals in random sites, while crystalline ice is denser and has a regular hydrogen-bond network. The transition from amorphous to crystalline water ice occurs near $\sim$130-150 K for pure H_2O, and at $\sim$150-170 K for pure $HCONH_2$, but is suppressed in mixed ices like formamide-water, where formamide disrupts hydrogen bonding. These structural differences influence how light interacts with the ice and how radiation-driven chemistry proceeds [18, 19]. For a more detailed description regarding amorphous and crystalline ices, see Section 3.1.3.

lowing irradiation, the overall absorbance of the 90 K ice increased slightly, and the long-wavelength slope steepened, but unlike the 10 and 50 K spectra, after irradiation, the broad peak red-shifts slightly. This can be confirmed by observing the subtraction spectrum, which shows that the main difference feature lies slightly to the red side of the pre-irradiation maximum, in contrast to the blue-shifted difference features seen at 10 K and 50 K. No discrete new peaks emerged, only weak shoulders consistent with overlapping bands. The changes, therefore, reflect a redistribution of oscillator strength rather than the formation of distinct photoproduct bands. At 90 K, radicals and small fragments created by photon absorption have sufficient mobility to recombine or relax within the matrix, mitigating the accumulation of condensed-phase product features [13, 14].

The blue-shifts observed at 10 and 50 K mainly arise from matrix compaction, which increases the local density and refractive indices of the ice. These shifts are driven primarily by irradiation-induced changes in the ice matrix - such as increased density and refractive index (i.e. a modified local dielectric environment) - which alter the effective local electric field experienced by the absorbing group and thus the apparent position of the band, without requiring a change in the underlying electronic state of the parent species. At the same time, irradiation produces high-energy photoproducts that add absorption on the short-wavelength side of the spectrum. These additional features steepen the high-energy slope and can accentuate the appearance of a blueward shift - that is, an apparent movement of the absorption band maximum toward shorter wavelengths (higher photon energies) - even though they do not shift the parent transition itself. The implication is that the observed blueward shift in the post-irradiation VUV spectra at 10 and 50 K is a composite effect: a genuine matrix-induced shift of the W-band superimposed on additional short-wavelength absorption from photoproducts, both of which contribute to the overall band moving toward higher energies. By contrast, the slight red-shift at 90 K reflects the onset of thermal relaxation and matrix annealing, which reduces the local disorder introduced at lower temperatures and lowers the average excitation energy as the ice approaches structural equilibrium.

The persistent narrow dips in all spectra were instrument-related artefacts, likely caused by normalisation imperfections or beamline optical interference, as their energies remained fixed regardless of irradiation. Narrow features that seem to disappear after irradiation, as can be seen in Figure 7.3, are attributed to thin-film interference/normalisation rather than a molecular transition. The ice/NaCl stack can produce weak Fabry-Pérot fringes[2], see more about Fabry-Pérot in Section 7.3.2; irradiation compacts and slightly thins the film, shifting or damping the fringe so the local bump disappears, while the genuine, broader electronic bands remain at fixed energies [23, 24]. The corresponding subtraction spectra do not reveal distinct product bands at this energy, further indicating an optical artefact rather than new chemistry.

Electronic Transition Assignment

In all the spectra presented in Figure 7.3, there is a broad absorption feature ascribed to an electronic transition, with the present electronic transition centred around ∼5.3 eV. This is attributed to the amide $n \rightarrow \pi^*$ transition (the "W" band) of formamide (see more in Section 3.1.2.3, page 101) [15, 16]. In condensed ices, this transition is known to broaden and blue-shift relative to the gas-phase position near ∼219 nm, further supporting the chosen assignment. Generally, water absorption is weak above 180 nm [3], so the observed features between 200-320 nm are primarily attributed to formamide and its photoproducts rather than the water matrix.

Post-irradiation, the W-band broadened and blue-shifted, with an overall increase in absorption. This broadening and blue-shifting indicated modification of the electronic environment within the ice and is consistent with photochemical processing and/or matrix compaction. If irradiation only changed the abundance of the parent species (i.e. the formamide column density) without producing additional VUV-absorbing species, the W-band would be expected to retain approximately the same position and overall shape, with the dominant effect being a change in intensity. The observed band broadening and shift therefore imply changes beyond simple scaling, consistent with matrix

[2]Fabry-Pérot fringes are periodic interference patterns that occur when light reflects multiple times between two parallel surfaces. Constructive and destructive interference between these reflections produce narrow oscillations in transmitted or reflected intensity [21, 22].

reorganisation (e.g. compaction) and/or additional overlapping absorption from photoproducts [6, 25]. Combined with known product bands in the 4.5-6.5 eV region [6, 25], the spectra are consistent with the presence of species such as HNCO, CO, CO_2, and HCN, although VUV alone cannot isolate their contributions. In this energy range, electronic transitions are intrinsically broad and strongly overlapping for many small molecules, so VUV spectroscopy does not provide unique vibrational "fingerprints" and cannot be used to identify individual photoproducts from these bands alone unambiguously.

To quantify these qualitative trends, Figure 7.5 presents the FWHM of the formamide W-band across the Experimental Run 1 series, fitted over a 210-280 nm window selected as the widest range for which the pre- and post-irradiation fits at all three temperatures remain well-constrained. Following irradiation, the band narrows between 10 K and 50 K before broadening sharply at 90 K, confirming quantitatively that the pronounced red-tail broadening described above is concentrated at this temperature rather than developing gradually across the series. The 90 K pre-irradiation point (hollow marker) could not be reliably constrained: the band is too weak and ill-defined at this temperature to fit reliably, consistent with its description above as "less well-defined," and this value should not be compared numerically with the other points, but used to easily visualise the changes in overall peak.

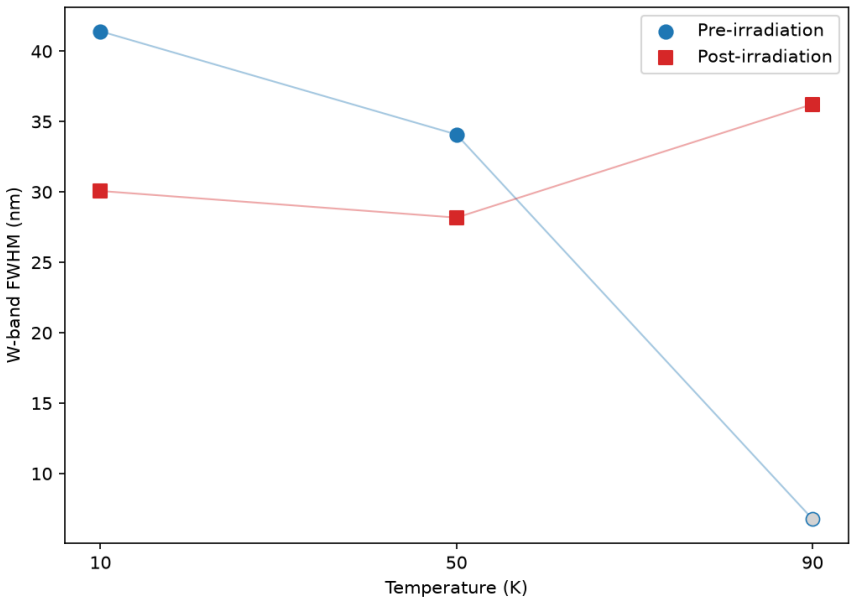


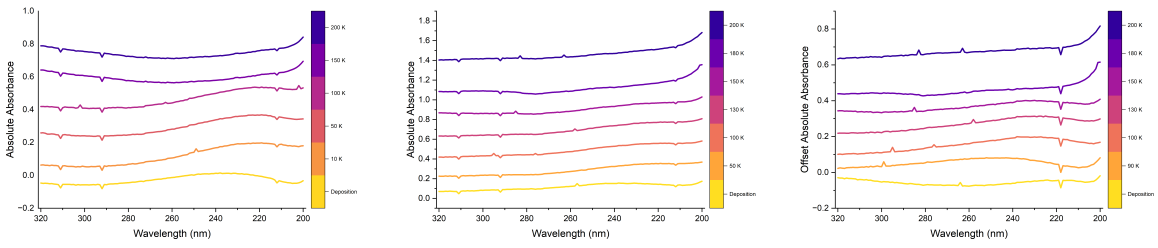
Figure 7.5: Full width at half maximum (FWHM) of the formamide W-band as a function of temperature for Experimental Run 1, fitted over a common 210-280 nm window. Pre-irradiation values are shown as filled circles and post-irradiation values as filled squares; the hollow marker denotes a low-confidence fit (see discussion on p. 277).

7.3.1.1 TPD Heating Trends

Temperature-programmed desorption (TPD) is a technique used to monitor the release of volatile species from ice as it is gradually warmed. As the temperature increases at a controlled rate, molecules trapped in the film desorb at characteristic temperatures that depend on their binding energies and interactions with the surrounding matrix. By recording the desorption profile, TPD reveals information about molecular volatility, trapping efficiency, and ice morphology. For example, TPD can help to determine whether species are weakly adsorbed on the surface or embedded within the bulk. In the present work, TPD spectra complement the VUV measurements by showing how irradiation products and parent molecules evolve or are released during thermal processing, linking spectroscopic changes to physical desorption behaviour. In this work, 'TPD spectra' refer to VUV absorption spectra recorded at successive temperatures during the warm-up, so changes in band shape reflect both volatile loss and matrix restructuring. In practice, the TPD profiles indicated that the changes observed upon warm-up were dominated by physical restructuring/compaction. However, they remain consistent with some photoproducts formed during irradiation at low tempera-

ture. TPD therefore provides a cross-check that ties the optical behaviour to thermal stability and volatile release. The TPD spectra for Experimental Run 1 are shown in Figure 7.6.

In all experiments, the warm-up phase was performed at a constant linear heating rate of 5 K min^{-1}. This relatively rapid ramp rate represents a compromise between experimental duration and spectral resolution, and was found to produce smooth desorption profiles without inducing obvious cracking or catastrophic outgassing of the ice films. The peak desorption temperature in TPD depends on the heating rate β, so the absolute temperatures reported for the onset and maxima of desorption features correspond specifically to $\beta = 5$ K min^{-1}. A slower ramp (e.g. 0.5-1 K min^{-1}, commonly used in laboratory astrochemistry experiments) would shift these peaks to somewhat lower temperatures, typically by an order of 5-10 K for desorption-limited processes. The analysis in this Chapter, therefore, emphasises relative trends between experiments performed at the same ramp rate, rather than absolute desorption temperatures or detailed kinetic modelling. The relatively fast warm-up also implies that weakly bound photoproducts may desorb on similar temperature scales to the main water/formamide features, so any quoted desorption temperatures for such species should be regarded as approximate and potentially blended with the dominant matrix loss. Since multiple photoproducts absorb within the same 4.5-7 eV region as formamide, their appearance and subsequent desorption primarily manifest as subtle changes in the overall band shape during TPD, rather than as isolated features.



(a) TPD evolution from 10 K. **(b)** TPD evolution from 50 K. **(c)** TPD evolution from 90 K.

Figure 7.6: TPD spectra for **Experimental Run 1** experiments showing the thermal evolution of irradiated formamide-water ices from initial deposition temperatures to 200 K.

At 10 and 50 K, the TPD spectra retain the same overall shape throughout heating

to 200 K, but the contrast between valleys and crests gradually increases. The broad mid-UV minimum (∼315-280 nm) remains stationary, while the short-wavelength curvature strengthens as temperature rises. At 150 K and above, this develops into a pronounced trough with a steep rise beginning just shy of ∼190 nm (≥6.5 eV), corresponding to the low-energy onset of the $\pi \rightarrow \pi^*$ valence transition. The progressive smoothing of the spectra with increasing temperature is attributed to structural relaxation and pore collapse within the amorphous ice, which reduces light scattering and increases molecular uniformity [17, 20]. The steady reweighting of intensity toward higher energies, without the appearance of new bands, confirms that these spectral changes arise from physical restructuring rather than the formation of any new chemical species.

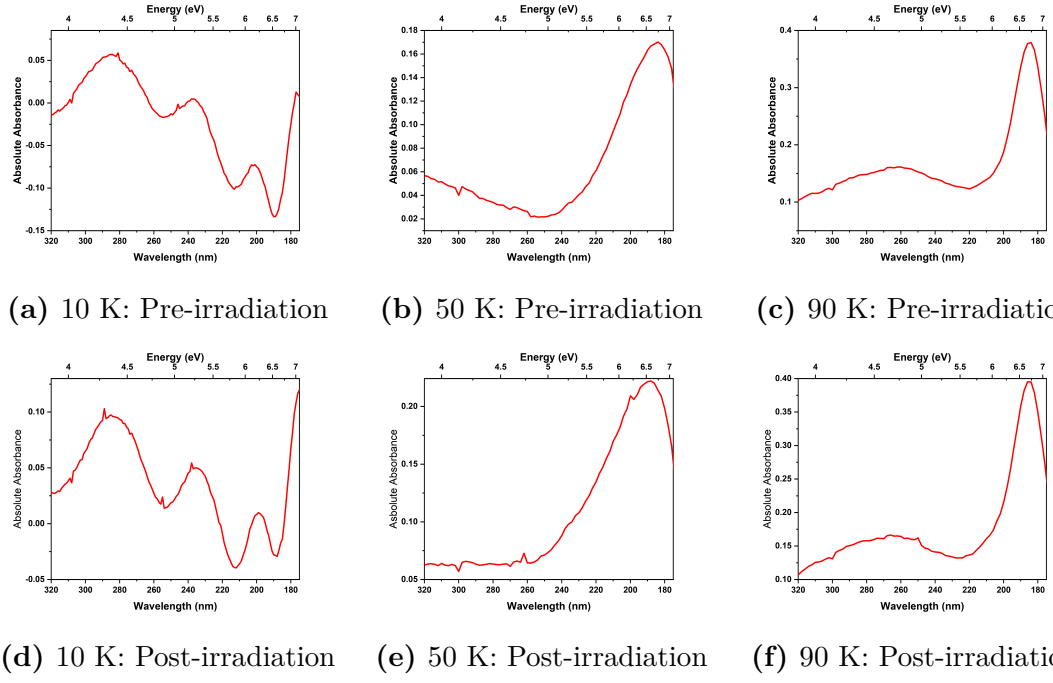
The 90 K TPD spectra exhibit a similar trend, with gradual intensity reweighting toward shorter wavelengths during heating. The broad mid-UV envelope remains largely constant up to 150 K, beyond which the short-wavelength side becomes dominant as ice thins through desorption. No new electronic transitions appear during heating, indicating that photoproducts either desorb concurrently with water or remain spectroscopically silent in the VUV region. This behaviour supports the conclusion that photochemistry at 90 K was limited to low-yield fragmentation and matrix relaxation rather than the accumulation of stable condensed-phase products.

7.3.2 Experimental Run 2: Spectral Evolution from 10-130 K

10K - 90 K

At temperatures between 10 and 90 K, Experimental Run 2 reproduced the previous Experimental Run 1 experiments under identical conditions. As with most synchrotron measurements, minor variations in photon flux, beam footprint, and ice deposition introduced subtle differences in signal-to-noise and spectral contrast. These differences were within expected experimental uncertainty. These experiments, again, investigated early-stage irradiation and desorption between 10 and 90 K. They were performed to simulate the VUV irradiation of surface-level ice at Europa, with 10 K used as a baseline

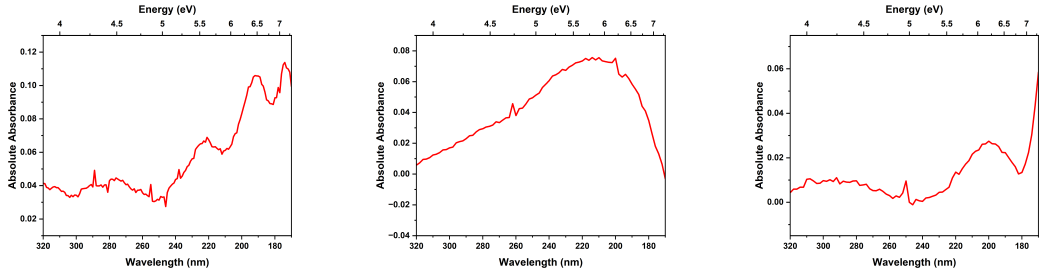
for interpreting the behaviour of formamide-water ices at higher temperatures. Pre- and post-irradiation spectra are shown in Figure 7.7, and the corresponding subtraction spectra are shown in Figure 7.8.



(a) 10 K: Pre-irradiation **(b)** 50 K: Pre-irradiation **(c)** 90 K: Pre-irradiation

(d) 10 K: Post-irradiation **(e)** 50 K: Post-irradiation **(f)** 90 K: Post-irradiation

Figure 7.7: VUV absorption spectra of formamide-water ices collected pre- and post-irradiation at 10, 50, and 90 K for **Experimental Run 2**. Sharp vertical features ('spikes') that appear at fixed energies are instrumental artefacts (e.g. detector noise or residual lamp structure) and do not correspond to molecular absorption bands.



(a) 10 K **(b)** 50 K **(c)** 90 K

Figure 7.8: Subtraction spectra (post- subtract pre-irradiation) of formamide-water ices deposited on NaCl substrates at 10, 50, and 90 K for **Experimental Run 2**.

In contrast to the earlier dataset, the 10 K pre- and post-irradiation spectra in Experimental Run 2 display three partially resolved features between 4.0 and 6.5 eV, along with a more apparent rise toward shorter wavelengths (Figure 7.7). The overall profile is smoother and has a better signal-to-noise ratio, which allows subtle shoulders to appear that were not evident in the corresponding Experimental Run 1 spectrum.

The differences between the Experimental Run 1 (Figure 7.3) and Experimental Run 2 (Figure 7.7) spectra arise primarily from optical-path effects associated with the greater ice thickness in Experimental Run 2, rather than from any change in chemical composition. The Experimental Run 2 film was estimated to be a little over twice as thick as the Experimental Run 1 film deposit, and this increase in thickness affects both the contrast and the apparent fine structure of the VUV absorption profile.

In thin films, the vacuum/ice/NaCl arrangement acts as a weak Fabry-Pérot etalon (see Equation 7.3 below), where multiple internal reflections generate low-amplitude interference ripples whose spacing varies approximately as $\Delta\lambda \propto 1/d$ (or $\Delta E \propto 1/d$ in energy space). This behaviour is well established in thin-film optics [21, 22] and has been explicitly documented in laboratory ice spectroscopy [26, 27]. A thicker film, therefore, exhibits more closely spaced fringes, and these can coincide with the intrinsic shoulders of the broad "W" band. As a result, the structure that is optically blended into a single broad maximum in the thinner Experimental Run 1 film becomes resolved as multiple peaks in the thicker Experimental Run 2 spectrum.

$$2nd\cos\theta = m\lambda \tag{7.3}$$

where n is the refractive index, d is the film thickness, θ is the internal angle of incidence, m is the interference order as an integer, and λ is the wavelength. At normal incidence, this equation simplifies to $2nd = m\lambda$.

Additionally, as absorbance scales roughly linearly with path length ($A \propto d$) away from saturation, the thicker Experimental Run 2 film naturally exhibits greater contrast and improved visibility of weaker spectral shoulders. The similarity of the band positions between datasets, and the absence of any new discrete transitions further confirm that the apparent "extra peaks" in Experimental Run 2 arise from thickness-dependent interference and optical effects, not from chemical differences or enhanced photoproduct formation.

Although this fringing gives the 10 K spectrum in Figure 7.7 a visibly different appearance from the other temperatures in this series, the panel is retained here rather than removed: the multi-peak structure is a well-understood optical artefact rather

than an unexplained anomaly, and omitting it would obscure a real methodological limitation rather than resolve one. It is, however, excluded from the quantitative FWHM comparison in Figure 7.11, since a single-Gaussian description does not meaningfully represent a band resolved into multiple partially overlapping features by interference - the same reasoning that ruled out multi-Gaussian deconvolution for the OCN^-/CO doublet in Chapter 5. The 50-130 K spectra, which retain a single broad W-band envelope, are treated quantitatively in that comparison instead.

The 10 K post-irradiation spectrum shows a very slight blue-shift of the main peak and its accompanying shoulders, along with a noticeable increase in absorbance on the high-energy (short-wavelength) side. These effects point to two processes that dominate ice behaviour at this temperature. First, matrix compaction occurs efficiently at 10 K, as energetic photons collapse micropores and reduce structural disorder. This increase in density subsequently increases the local refractive index and strengthens intermolecular interactions, both of which tend to shift broad electronic transitions to slightly higher energies. Second, irradiation produces high-energy photoproducts, whose electronic transitions appear primarily on the short-wavelength side of the parent band. These new absorptions do not shift the parent band directly; instead, they add intensity to the high-energy slope, accentuating the apparent blue-shift produced by compaction. The combination of a small intrinsic blue-shift of the matrix and additional high-energy absorption from photoproducts yields the overall post-irradiation profile observed at 10 K.

Following irradiation, the main maximum became slightly sharper, and the low-energy scattering was suppressed, implying a modest increase in density or compaction of the amorphous matrix. Photon-induced rearrangement of the hydrogen-bond network at 10 K has been reported in other mixed ices, where secondary electrons and local heating collapse micro-pores and increase optical homogeneity [17, 20]. Such compaction increases the effective refractive index and can produce apparent band sharpening without necessarily changing chemical composition.

At 50 K, before irradiation, the spectrum shows a dominant band centred at ∼6.7 eV. After exposure to 9 eV photons, the peak subtly red-shifts in contrast to the Ex-

perimental Run 1 50 K spectra. The sign of the small post-irradiation shift differs from that of the Experimental Run 1 50 K spectra (which subtly blue-shifts after irradiation) because the spectra reflect a balance between true matrix changes and thickness-dependent optical effects. As shown in Table 7.1, in Experiment Run 2 the ice is somewhat thinner (by approximately 18 nm), which places the underlying Fabry-Pérot interference in a different phase relative to the broad W-band. The Fabry-Pérot phase is the optical phase shift $\delta = 4\pi nd/\lambda$ accumulated as light traverses the film, which determines whether reflections interfere constructively or destructively. Small changes in n or d therefore shift this phase and move the fringe pattern [21, 22]. Upon irradiation, compaction changes nd (see Equation 7.3) and moves the fringe phase; in a thinner film, this phase shift can introduce a slight red-shift in the apparent band position, whereas in the thicker Experimental Run 1 film, the same effect introduces a slight blue-shift. In addition, the thinner film experiences a higher dose per molecule (less attenuation of the incident 9 eV photons), allowing mild relaxation during exposure at 50 K, which also favours a small redward drift. The opposite signs arise from differences in optical path/phase and dose profile rather than from different chemistry.

Additionally, the high-energy side of the main peak increased in intensity, and the inter-band valley near ∼5.0 eV deepened. These changes reflect a small redistribution of oscillator strength toward higher-energy transitions, which occurs when irradiation produces VUV-active photoproducts with electronic bands in the 6-8 eV region. Species such as HNCO, CO, and CO_2 contribute weak but distinct absorption on the short-wavelength side, effectively steepening the high-energy slope and lowering the apparent minimum between bands [14, 25]. This shoulder is quantitatively too weak to constrain via single-Gaussian fitting at 50 K, unlike at 90 K where the same feature is more pronounced (Figure 7.11). The increase in high-energy absorbance is consistent with the creation of small VUV-active photoproducts - most plausibly HNCO, CO, and CO_2 - whose $\pi \rightarrow \pi^*$ transitions overlap the formamide W-band envelope [14, 25]. The relative invariance of the main band position indicated that the electronic structure of the parent molecule remained largely intact. At the same time, the added absorbance originated from weakly bound fragments and radicals formed through N-H, C-N, and

C=O bond cleavage. These species either recombined rapidly or remained trapped in the water matrix without forming distinct new condensed-phase bands.

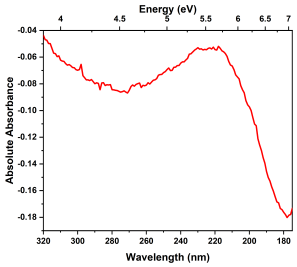
The spectra from Experimental Run 2 at 90 K reproduced the overall shape of the first dataset but displayed a much sharper contrast and a better-defined trough near 5.8 eV. A shallow pre-peak around 4.7 eV, visible in both the pre- and post-irradiation trace, was interpreted as a minor optical interference effect rather than a true molecular band; it is absent or phase-shifted in other runs and does not evolve systematically with irradiation or during the TPD warm-up in the way a genuine molecular absorption feature would. After irradiation, the higher-energy side of the main band (6.7-7.0 eV) intensified, again suggesting the presence of overlapping photoproduct transitions. The slight broadening of this region, consistent with the increase in FWHM shown in Figure 7.11, reflects an increase in inhomogeneity following photon-induced compaction and radical recombination [6, 17]. As with the 90 K post-irradiation spectrum, in Experimental Run 1, the spectrum is slightly red-shifted after irradiation, indicating that the dominant process at 90 K is thermal relaxation and matrix annealing.

Compared with the Experimental Run 1, the Experimental Run 2 spectra exhibited a smoother baseline, higher contrast, and reduced instrumental spiking, consistent with cleaner optical alignment and a more uniform film thickness. These factors allowed the inter-band valley near 7 eV and the short-wavelength rise to appear more distinctly, improving confidence in the band assignments.

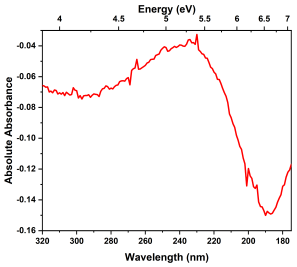
110K & 130 K

Experiments at 110 K and 130 K were only performed in Experimental Run 2 due to time constraints and beam availability. These temperatures represent the upper range of Europa's equatorial surface, where the ice is expected to be metastable and close to the amorphous-to-crystalline transition threshold [28]. The onset of this structural transition is consistent with independent constraints from the infrared measurements discussed in Chapter 3, Section 3.1.3. In those experiments, pure H_2O ice was found to undergo an amorphous-to-crystalline transition between ∼130-150 K, while pure $HCONH_2$ crystallised over a slightly higher range of ∼150-170 K under compa-

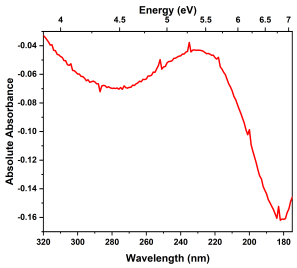
rable vacuum and heating conditions. In mixed formamide-water ices, the presence of formamide disrupts the hydrogen-bond network of water, broadening and partially suppressing the transition so that the ice remains structurally disordered to higher temperatures. At 110-130 K, VUV-driven chemistry therefore interacts strongly with thermal annealing and desorption, and the red-shifting, smoothing, and loss of contrast observed in the VUV spectra (Figure 7.9) are consistent with thermally driven restructuring and incipient crystallisation inferred from the IR data, providing insight into the final stages of near-surface processing. The corresponding subtraction spectra are shown in Figure 7.10.



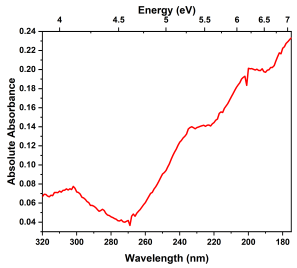
(a) 110 K: Pre-irradiation



(b) 130 K: Pre-irradiation

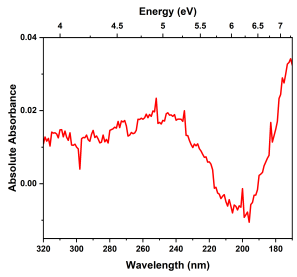


(c) 110 K: Post-irradiation

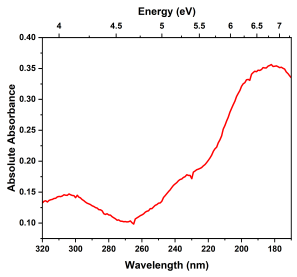


(d) 130 K: Post-irradiation

Figure 7.9: VUV absorption spectra of formamide-water ices collected pre- and post-irradiation at 110 and 130 K for '**Experimental Run 2**. Sharp vertical features ('spikes') that appear at fixed energies are instrumental artefacts (e.g. detector noise or residual lamp structure) and do not correspond to molecular absorption bands.



(a) 110 K



(b) 130 K

Figure 7.10: Subtraction spectra (post- subtract pre-irradiation) of formamide-water ices deposited on NaCl substrates at 110 and 130 K for **Experimental Run 2**.

At 110 K, both the pre- and post-irradiation spectra retain the broad ∼5.3 eV W-band with a shallow minimum near 6.5 eV and the characteristic short-wavelength rise. After irradiation, the spectrum shows a marginal red-shift of the band maximum, a change in curvature around 205-210 nm (∼6.0 eV) that is more pronounced than the shift in band centre alone would suggest (Figure 7.11), and a slight reduction of the extreme high-energy tail. This pattern points to thermally assisted relaxation/annealing and partial reorganisation of the matrix processes that lower the average excitation energy and smooth the profile as the ice becomes more ordered and begins to crystallise. Compared with 10-90 K, the 110 K spectra display weaker product-related structure and lower contrast, consistent with increased molecular mobility, reduced retention of VUV-induced photoproducts, and the growing dominance of thermal reorganisation over irradiation-driven compaction.

At 130 K, the pre-irradiation spectrum retains a broad W-band envelope centred near ∼5.3 eV, followed by a shallow inter-band valley approaching ∼6.2-6.4 eV. After irradiation, the overall shape of the band changes markedly: the central maximum broadens and flattens (Figure 7.11), the inter-band valley largely disappears but remains centred at the same energy, and the high-energy shoulder near 200-210 nm becomes more pronounced. The fixed valley position indicates that the electronic structure of the primary absorber remains largely unaltered, while the loss of contrast and smoothing of the profile reflect matrix reorganisation and the partial loss of material through desorption and increase in density (physical film thinning) rather than purely optical effects, as opposed to new transitions.

To quantify these trends across the extended temperature range, Figure 7.11 presents the equivalent FWHM analysis for Experimental Run 2. Two fit windows were used - 230-300 nm for 50 K and 90 K, and 210-280 nm for 110 K and 130 K - reflecting the differing spectral position of the resolvable feature at each pair of temperatures. The 10 K spectrum is excluded from this comparison, as the greater film thickness at this temperature resolves the W-band into three partially overlapping components via Fabry-Pérot interference (Equation 7.3), for which a single-Gaussian FWHM carries no clear physical meaning. The band width is comparable between the pre- and post-

irradiation spectra at 90 K, while 110 K shows a substantial post-irradiation increase, larger than the change in curvature alone might suggest; the accompanying red-shift of the band centre is well supported, though the full magnitude of the width change should be treated with some caution. The 50 K points (hollow markers) are shown but unresolved: the same high-energy shoulder resolved at 90 K is present here too, but at roughly one-fifth the relative amplitude, and could not be reliably constrained at any window tested, so the points are retained rather than omitted. The 130 K post-irradiation value (also a hollow marker) is not directly comparable to the others: the fit is well-constrained, but by this temperature, the pre-irradiation peak has dissolved into a continuous, monotonic slope following irradiation, so the fitted value describes a residual feature rather than a comparable peak width.

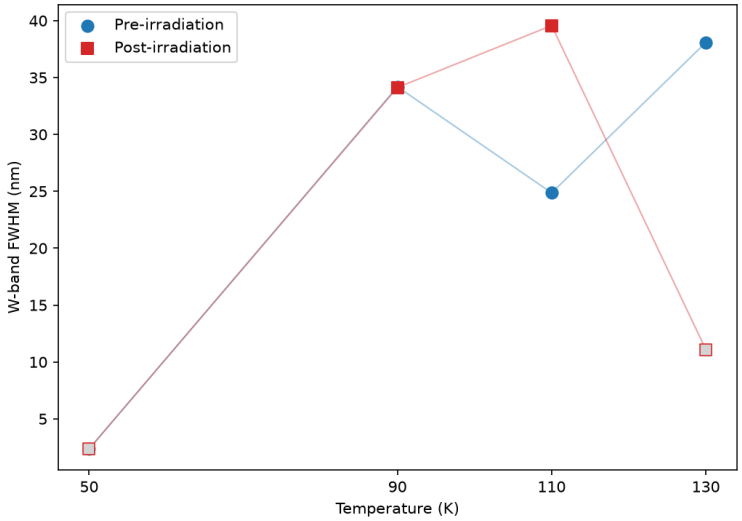
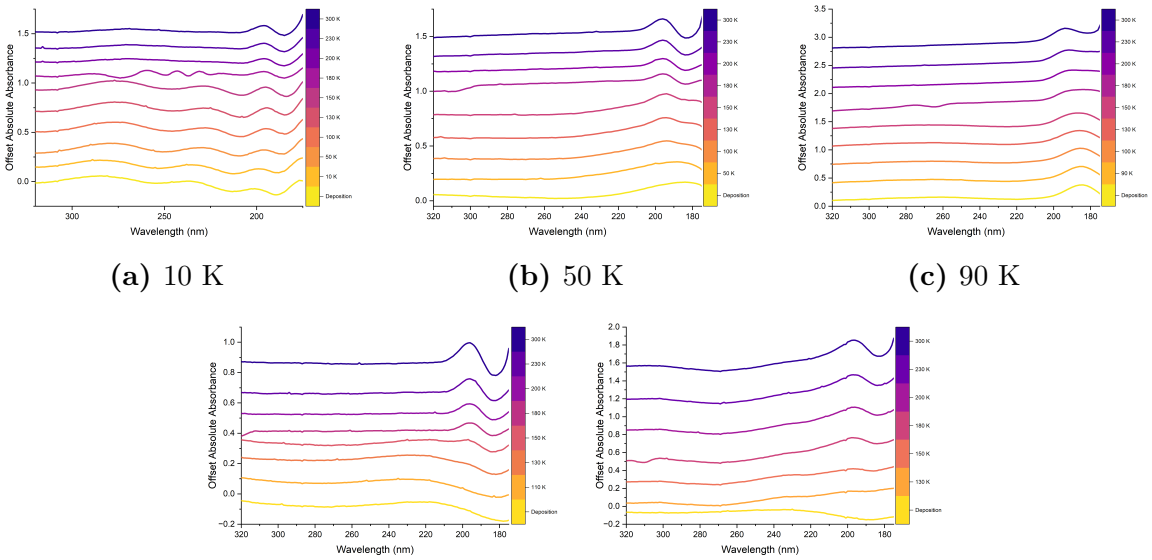


Figure 7.11: Full width at half maximum (FWHM) of the formamide W-band as a function of temperature for Experimental Run 2, fitted over 230–300 nm (50 K, 90 K) and 210-280 nm (110 K, 130 K). Pre-irradiation values are shown as filled circles and post-irradiation values as filled squares; hollow markers denote low-confidence fits (see discussion on p. 287). The 10 K spectrum is excluded (see discussion on p. 287).

7.3.2.1 TPD Heating Trends



(a) 10 K **(b)** 50 K **(c)** 90 K

(d) 110 K **(e)** 130 K

Figure 7.12: TPD spectra for Experimental Run 2 experiments, showing the thermal evolution of irradiated formamide-water ices from initial temperatures to 300 K.

The TPD spectra for Experimental Run 2 are shown in Figure 7.12. The extended TPD run (10-300 K, using the same linear heating rate of 5 K min^{-1} as in Experimental Run 1) provided complementary information on how irradiation-induced species and matrix structure evolved during heating. The overall spectral shape remained consistent from 10 K up to 180 K, but intensity was progressively reweighted toward the short-wavelength side. This behaviour corresponds to the thermally driven relaxation and compaction of the amorphous film, accompanied by the desorption of the most weakly bound volatiles below 120 K. Between 150 and 220 K, desorption of water and formamide led to a rapid decrease in absorbance, followed by substrate-dominated interference effects above 230 K. The persistence of the 5.0-5.6 eV feature up to the onset of water sublimation implies that most photoproducts remained trapped until the bulk matrix began to desorb. At the same time, the absence of distinct new bands at higher temperatures does not imply a lack of photochemistry. Rather, many low-binding-energy products desorb before they can build up to detectable column densities or remain spectrally resolved beneath the broad W-band as their contributions are gradually removed during warm-up.

Similarly, during TPD heating of the 50 K ice, the spectra maintained the same overall shape but progressively reweighted intensity toward shorter wavelengths. Between 50 K and 150 K, the mid-UV region remained stable while the short-wavelength edge steepened, suggesting continued compaction and slight pore collapse. At 180 K and above, the spectra became dominated by the rising wing near 6.5 eV as water began to desorb; by 230-250 K, both H_2O and formamide had largely sublimed, and residual signals arose primarily from optical interference effects of the thinning film [29]. The absence of new narrow features through the heating sequence confirmed that the observed variations were governed by physical restructuring rather than new photochemical pathways.

TPD evolution at 90 K mirrored its Experimental Run 1 counterpart: intensity redistributed toward shorter wavelengths with increasing temperature, but no new bands formed. The smooth, monotonic trends indicated that the film underwent a gradual increase in density and thinning rather than chemical transformation. The onset of steep absorbance decline above 180 K corresponded to water sublimation, with formamide desorbing slightly later [29].

At 110 K, the TPD spectra retained their geometry up to 150 K. Above this temperature, water desorption shortened the optical path, leading to a gradual loss of contrast. No additional electronic bands were resolved, supporting the interpretation that VUV-induced chemistry at 110 K remained limited to structural reorganisation and thermally induced annealing.

At 130 K, the high-energy rise below 190 nm became dominant as the temperature increased, marking the leading edge of the $\pi \rightarrow \pi^*$ band that lies outside the plotted range. The smooth evolution of this slope during the TPD sequence indicated that the spectral changes were dominated by physical restructuring rather than new chemistry. The loss of overall absorbance above 180 K confirmed progressive desorption of both water and formamide, leaving only the NaCl substrate contribution.

No new resolved bands appeared during the warm-up, only weak shoulders consistent with overlapping $\pi \rightarrow \pi^*$ from small products, indicating that the observed spectral evolution was physical (density, refractive index, and optical-path changes)

rather than the formation of additional condensed-phase products. In practice, any VUV-active photoproducts formed during irradiation are expected to contribute only subtle modifications to the broad W-band envelope rather than discrete, easily identifiable peaks. Their electronic transitions lie within the same 4.5-7 eV range as the parent formamide absorption, so additional species effectively remain "hidden" beneath the dominant band and manifest primarily as small changes in band shape, contrast, or slope. As the ice warms, the most volatile products desorb first, progressively reducing their contribution to the composite absorption profile. This early loss alters the detailed shape of the band without generating new, narrow features. Very volatile species, especially CO in analogous ice systems, are expected to leave the ice at relatively low temperatures, so their contribution to the composite W-band envelope is removed early in the TPD ramp, subtly reshaping the band even though no new narrow feature appears. Consequently, many photoproducts inferred from the irradiation conditions and from the ion/electron experiments in Chapters 5 and 6 are unlikely to accumulate as long-lived condensed-phase bands in the VUV spectra, even though similar molecular families are plausibly formed. A small increase in smoothness and contrast at higher temperatures also reflected the transition from a highly porous amorphous ice to a compacted, partially crystalline film, consistent with the behaviour of mixed water-dominated ices reported by [29].

7.4 Temperature Dependence of Photochemistry

Table 7.2: Summary of dominant physical and spectral processes observed during VUV irradiation of formamide-water ices across the investigated temperature range.

Temp. (K)	Dominant Processes	Spectral Behaviour
10	Photon-induced compaction and early photoproduct formation	Slight blue-shift; steepening of short-wavelength slope
50	Partial relaxation; interference-phase effects	Minor apparent shift (red or blue) depending on thickness
90	Onset of annealing	Smoothing and weak red-shift
110	Thermally assisted compaction and reorganisation	Marginal red-shift; lower contrast
130	Strong thermal restructuring and desorption	Flattened, slope-dominated band; valley disappears; no energy shift

A comparative analysis of the 10-130 K experiments reveals a systematic, temperature-dependent evolution in both the physical structure of the mixed formamide-water ice and its photochemical response. Across all datasets, absorption begins to rise toward shorter wavelengths from around 250 nm, corresponding to the onset of the amide

$n \rightarrow \pi^*$ ("W") manifold, confirming that the fundamental electronic structure of formamide is preserved throughout irradiation. Although the centre of absorption of the W transition remains approximately consistent across the series, its shape, contrast, and fine structure vary strongly with temperature, reflecting progressive matrix reorganisation and the changing efficiency of photoproduct retention.

At 10 K, the W-band is relatively broad and high-contrast (Figure 7.5), occasionally modulated by low-amplitude interference ripples characteristic of a rigid, porous amorphous film. The limited mobility of the matrix confines photoproducts and excitations locally, producing only minor redistribution of absorption. By 50 K, the envelope becomes narrower and smoother (Figure 7.5), consistent with the onset of limited molecular motion and partial hydrogen-bond rearrangement; interference-phase effects and small differences in film thickness occasionally modify the apparent shift direction between datasets. At 90 K, annealing becomes significant; the post-irradiation band broadens sharply - the largest such change observed across either series (Figure 7.5) - while weak shoulders merge and a modest reweighting toward the high-energy side appears, suggesting the early stages of compaction and structural relaxation.

At 110 K, the spectrum shows a marginal red-shift and reduced contrast, alongside a further post-irradiation broadening of the band (Figure 7.11), indicating thermally assisted increased density and the beginning of partial crystallisation. At 130 K, the W-band transforms into a broad, asymmetric slope (Figure 7.11) in which the inter-band valley largely disappears while remaining centred at the same energy, and the high-energy shoulder near 200-210 nm becomes more pronounced. This transition reflects major matrix restructuring, film thinning through desorption, and the optical blending of residual parent and weak photoproduct absorption rather than the emergence of new transitions. Together, these spectra chart a continuous evolution from a defect-rich amorphous solid at 10 K to a compact, partially ordered film at 130 K.

The irradiation-induced spectral changes mirror the physical evolution of the ice. The slight blue-shifts and steepening of the high-energy slope observed at the lowest temperatures arise from irradiation-driven compaction and the formation of a small population of high-energy photoproducts (e.g., CO, CO_2, HNCO) whose $\pi \rightarrow \pi^*$ ab-

sorptions add intensity on the short-wavelength side [14, 25]. As temperature increases, enhanced molecular mobility allows transient radicals to recombine or diffuse, reducing the accumulation of identifiable stable products - as they revert back to the parent molecule or to unreactive species - and smoothing the overall profile. Beyond 110 K, thermal annealing dominates: the parent band transforms into a broad, flattened slope as structural relaxation and desorption redistribute oscillator strength, diminishing the contrast of any overlapping product features. The near-constant position of the W-band centroid across 90-130 K confirms that the underlying electronic structure of formamide remains intact despite these morphological changes.

Temperature-programmed desorption (TPD) measurements corroborate this interpretation. Progressive smoothing and the absence of new absorption features upon heating indicate that rising temperature primarily drives physical reorganisation, compaction, and volatile loss, not further chemical transformation. The simultaneous desorption of water and formamide at their characteristic temperatures limits the retention of photoproducts, reinforcing that photochemistry in these mixed ices is strongly constrained by matrix volatility.

Overall, the temperature series demonstrates that VUV-induced chemistry in formamide-water ices is governed by the balance between radiation-driven bond cleavage and thermally driven structural evolution. At low temperatures, photolysis generates confined excitations within an amorphous network, yielding limited fragmentation but high product trapping. With increasing temperature, greater molecular mobility promotes recombination and outgassing, reducing the net yield of identifiable products. By 130 K, radiation continues to produce new fragments[3], but these are quickly rearranged, recombined, or lost as the ice reorganises and desorbs. In this regime, temperature and radiation reach a balance: mobility enhances short-term chemistry, but volatility prevents long-term retention of new molecules. The implications of this temperature dependence for Europa are discussed in Section 7.5.1.

[3]The specific photoproducts are not directly identified from the VUV spectra. Their presence is inferred from subtle intensity redistribution and comparison with known absorption bands of likely fragments (e.g., CO, CO_2, HNCO) reported in prior VUV studies [14, 25].

7.5 Conclusions and Implications for Europa's Surface Chemistry

The VUV irradiation experiments presented in this Chapter examined how 9 eV photons modify mixed formamide-water ices on NaCl across a temperature range of 10-130 K, under conditions approximating Europa's near-surface environment. Throughout all experiments, the core electronic signature of formamide - the broad amide $n \rightarrow \pi^*$ "W" band centred near ∼5.3 eV - remained present before and after irradiation, indicating that the parent molecule is not catastrophically destroyed under the VUV fluences employed. Instead, irradiation produced comparatively subtle spectral changes: modest blue- or red-shifts, band broadening, sharpening or loss of contrast, and small modifications to the high-energy slope. These effects were strongest at low temperature and became progressively muted as the ice approached the onset of thermally driven restructuring and desorption.

The spectral evolution is best interpreted as a combination of matrix compaction, restructuring, and the formation of small VUV-active photoproducts whose electronic transitions are superimposed on the dominant W-band envelope. At 10 K, photon-induced collapse of micropores and strengthening of the hydrogen-bond network increased the local density and refractive index of the ice, producing slight blue-shifts and enhanced high-energy absorption. At 50 K, partial molecular mobility narrowed and smoothed the spectra, while at 90 K annealing produced the most pronounced post-irradiation broadening observed across either series, with weak red-shifts consistent with thermally assisted matrix relaxation. At 110 K, restructuring and desorption drove a further, substantial broadening of the band while it remained a discrete feature; by 130 K, the W-band instead flattened into a slope-like profile, the inter-band valley losing contrast while remaining at fixed energy, and no new discrete bands emerged. Across the full temperature series, the broad, overlapping nature of the electronic transitions prevented unambiguous identification of individual photoproducts; VUV spectroscopy here therefore traces overall electronic excitation and matrix evolution rather than providing molecular fingerprints.

The accompanying TPD sequences demonstrated that the warm-up behaviour of the irradiated films is governed primarily by physical processes - compaction, pore collapse, and progressive desorption of water and formamide - rather than by additional photochemistry during heating. Using a constant heating rate of 5 K min^{-1}, the TPD spectra showed smooth reweighting of intensity toward shorter wavelengths and eventual loss of absorbance as the ice sublimed, with residual structure increasingly dominated by interference effects from the thinning film. The relatively rapid ramp implies that weakly bound, volatile photoproducts are likely to desorb near, or blend with, the main water/formamide desorption features, so their individual contributions to the VUV spectra remain difficult to isolate. As a result, the quantitative desorption temperatures reported for different components should be regarded as specific to this ramp rate, and the analysis in this Chapter has focused on relative trends rather than detailed kinetic modelling.

Taken together, these experiments show that 9 eV VUV photons primarily process the upper optical skin depth (tens of nanometres) of formamide-water ices, with efficiency that depends sensitively on temperature. At low temperatures (10-50 K), products and structural changes are efficiently trapped, leading to detectable but still modest spectral modifications superimposed on a persistent parent band. At intermediate temperatures (90-110 K), increased molecular mobility promotes annealing, redistribution of oscillator strength, and partial loss of trapped fragments, while leaving the underlying electronic structure of formamide largely intact. At the highest temperatures studied (130 K), thermal restructuring and desorption dominate, erasing most evidence of VUV-induced chemistry and producing spectrally flattened, slope-dominated profiles. In all regimes, the absence of new, sharp bands and the retention of the W-band centroid indicate that VUV irradiation under these conditions favours gentle restructuring and limited fragmentation rather than wholesale conversion into a distinct product suite.

The broader implications for Europa, and how these VUV results sit alongside the ion and electron irradiation experiments, are discussed in Section 7.5.1.

7.5.1 Implications for Europa's Surface Chemistry

These laboratory results suggest that similar processes may occur on Europa. In the colder polar regions ($\leq$ 80 K), VUV irradiation would promote the accumulation of trapped photoproducts within an amorphous matrix, preserving them over geologic timescales. Toward warmer equatorial regions ($\sim$120-130 K), increased molecular mobility would enhance radical recombination and desorption, limiting the persistence of complex organics in the surface ice. Consequently, the chemical inventory detectable at Europa's surface is likely to vary with latitude, reflecting the balance between radiation-driven formation and temperature-driven loss of photochemical species.

Placed alongside the ion and electron results from Chapters 5 and 6, the VUV experiments support a picture in which Europa's surface chemistry is vertically stratified and controlled by the interplay between penetration depth, energy-deposition density, and temperature. High-LET ions drive efficient radiolysis in the shallow subsurface, generating stable residues such as CO_2 and OCN^-; low-LET electrons provide deeper, more diffuse processing and dominate near-surface volatile loss; and VUV photons act only on the outermost nanometres, subtly reshaping the optical skin without fully erasing the electronic signature of formamide.

Bibliography

[1] Russano G, Andretta V, Leo YD, Teriaca L, Uslenghi M, Giordano S, et al. Eruptive events with exceptionally bright emission in H-alpha observed by the Metis coronagraph. Astronomy & Astrophysics. 2024.

[2] Bagenal F, Dols V. The Space Environment of Io and Europa. JGR Space Physics. 2023.

[3] Cruz-Diaz GA, Caro GMM, Chen YJ, Yih TS. Vacuum-UV spectroscopy of interstellar ice analogs II. Absorption cross-sections of nonpolar ice molecules. Astronomy & Astrophysics. 2014.

[4] Gudipati MS, Henderson BL, Fleury B, Carrasco N, Rivas N, Couturier-Tamburelli I, et al. Radiation-induced near-surface atmospheres of Europa and Titan. EPSC Abstracts, European Planetary Science Congress 2015. 2015.

[5] Ashkenazy Y. The surface temperature of Europa. Heliyon. 2016;5.

[6] Cruz-Diaz G, Caro GMM, Chen YJ, Yih T. Vacuum-UV spectroscopy of interstellar ice analogs - I. Absorption cross-sections of polar-ice molecules. Astronomy & Astrophysics. 2014;562.

[7] Sivaraman B, Nair B, Sekhar B, Jones N, Hoffmann S, Mason N. Electron impact dissociation and VUV photoabsorption of frozen formamide. Chemical Physics Letters. 2014;608:404-7.

[8] Bisschop SE, Fraser HJ, Öberg KI, van Dishoeck EF, Schlemmer S. Desorption rates and sticking coefficients for CO and N2 interstellar ices. Astronomy & Astrophysics. 2006.

[9] Hama T, Watanabe N. Surface processes on interstellar amorphous solid water: adsorption, diffusion, tunneling reactions, and nuclear-spin conversion. Chemical reviews. 2013;113 12:8783-839.

[10] Oberg K, Dishoeck E, Linnartz H. Photodesorption of ices I: CO, N , and CO . Astronomy & Astrophysics. 2008;496:281-93.

[11] Fuchs GW, Acharyya K, Bisschop S, Oberg K, van Broekhuizen FV, Fraser HJ, et al. Comparative studies of O2 and N2 in pure, mixed and layered CO ices. Faraday Discussions. 2006;133:331-45; discussion 347-74, 449-52.

[12] Cuppen H, Walsh C, Walsh C, Lamberts T, Lamberts T, Semenov D, et al. Grain Surface Models and Data for Astrochemistry. Space Science Reviews. 2017;212:1 58.

[13] Oberg K. Photochemistry and astrochemistry: photochemical pathways to interstellar complex organic molecules. 2016.

[14] Sivaraman B, Sekhar BNR, Jones NC, Hoffmann SV, Mason NJ. VUV spectroscopy of formamide ices. Chemical Physics Letters. 2012.

[15] Gingell J, Mason NJ, Zhao H, Walker I, Siggel M. VUV optical-absorption and electron-energy-loss spectroscopy of formamide. Chemical Physics. 1997;220:191-205.

[16] Lundell J, Krajewska M, Rasanen M. Matrix Isolation Fourier Transform Infrared and Ab Initio Studies of the 193-nm-Induced Photodecomposition of Formamide. The Journal of Physical Chemistry A. 1998.

[17] He J, Clements AR, Emtiaz S, Toriello F, Garrod RT, Vidali G. The effective surface area of amorphous solid water measured by the infrared absorption of carbon monoxide. Submitted to ApJ. 2019.

[18] Jenniskens P, Blake DF. Crystallization Of Amorphous Water Ice In The Solar System. The Astrophysical Journal. 1996.

[19] Mastrapa R, Grundy W, Gudipati M. Amorphous and Crystalline H 2 O-Ice. 2013;356:371-408.

[20] Minissale M, Aikawa Y, Bergin E, Bertin M, Brown WA, Cazaux S, et al. Thermal desorption of interstellar ices: A review on the controlling parameters and their implications from snowlines to chemical complexity. Chemical Reviews. 2022.

[21] Heavens OS. Optical properties of thin films. Reports on Progress in Physics. 1960;23:1 65.

[22] Macleod H, Macleod H. Thin-Film Optical Filters, Fourth Edition. 2010.

[23] Teolis B, Loeffler M, Raut U, Fama M, Baragiola R. Infrared reflectance spectroscopy on thin films: Interference effects. Icarus. 2007;190:274-9.

[24] Hudson R, Yarnall Y. Infrared spectra and optical constants of astronomical ices: IV. Benzene and pyridine. Icarus. 2022.

[25] Ramachandran R, Pavithraa S, Meka JK, Rahul KK, Lo JI, Chou SL, et al. Vacuum Ultraviolet Photoabsorption Spectra of Icy Isoprene and its Oligomers. arXiv (astro-phGA). 2025.

[26] Swanepoel R. Determination of the thickness and optical constants of amorphous silicon. Journal of Physics E: Scientific Instruments. 1983;16:1214-22.

[27] Manifacier J, Gasiot J, Fillard J. A simple method for the determination of the optical constants n, k and the thickness of a weakly absorbing thin film. Journal of Physics E: Scientific Instruments. 1976;9:1002-4.

[28] Ashkenazy Y. The surface temperature of Europa. Heliyon. 2019.

[29] Chaabouni H, Diana S, Nguyen T, Dulieu F. Thermal desorption of formamide and methylamine from graphite and amorphous water ice surfaces. Astronomy & Astrophysics. 2020.

Chapter 8

Conclusions and Solar System Relevance

This thesis has examined the radiation-driven chemistry of formamide-water ices under conditions relevant to Europa and other icy bodies, combining ion, electron, and vacuum-ultraviolet (VUV) irradiation experiments to explore how different energy sources influence prebiotic molecular evolution in cold environments. Through a series of controlled laboratory studies, the work characterised how formamide degrades, what photoproducts emerge, and how these outcomes depend on irradiation type, energy deposition depth, substrate material, and temperature. By integrating vibrational (IR) and electronic (VUV) spectroscopy with radiation chemical yield analysis, the thesis provides a comparative understanding of how each radiation regime alters formamide's stability and reactivity in water-rich ices. Together, these results build a coherent picture of the chemical pathways accessible on Europa's surface and offer experimental constraints that can support the interpretation of upcoming observations from JUICE and Europa Clipper (see Chapter 2).

8.1 Thesis Summary

Europa and its sibling icy moons are central to discussions of prebiotic chemistry. As outlined in Chapter 2, Europa is one of the most promising locations for life beyond Earth, containing several of the essential ingredients: liquid water beneath a thick icy shell; CO_2 concentrated in young terrains; sulphur-bearing species supplied by Io; and expected nitrogen and phosphorus inputs from the interior, Io-derived material, and cometary delivery. Taken together, these factors indicate that none of the key elements required for life are missing. In addition, the intense fluxes of energetic electrons, protons, and heavy ions supplied by Jupiter's magnetosphere drive extensive surface radiolysis, breaking down water and other volatiles to generate oxidants and reactive molecules that continually modify the moon's surface chemistry. Coupled with a potentially communicating subsurface ocean, these processes establish Europa as an environment where radiation-induced chemistry may play a significant role in prebiotic molecular evolution.

Formamide (NH_2CHO) is a central molecule in this context, as it contains four key biogenic elements (C, H, N, and O) and acts as a C_1 building block enabling a wide

range of chemical transformations. As discussed in Chapter 2, with sufficient energy, formamide can chemically evolve into nucleobases, nucleotides, amino acids, sugars, and other bioessential molecules. It is stable in both the gas and aqueous phases, allowing it to act as a chemical hub and to produce a suite of prebiotically relevant molecules while overcoming limitations of water, such as the hydrolysis of key bonds. Furthermore, formamide is abundant in astrophysical environments, making it an ideal molecule for simulating prebiotic processes. The results presented in Chapters 5 through 7 therefore focus on formamide-water mixtures, which better represent the conditions expected in the outer Solar System, where water is the dominant volatile. Any formamide present on these bodies is likely to be embedded within water-rich ices, consistent with observations of interstellar and cometary ices in which formamide-water systems have been detected alongside other volatiles. Importantly, water is not a passive matrix: under irradiation it produces reactive species such as OH· and H·, which can significantly alter formamide's degradation pathways. These considerations motivated our studies of formamide-water mixtures when assessing radiation-driven chemistry relevant to icy moons.

In the research described in this thesis, we aimed to determine not only whether formamide survives in water-rich ices under outer Solar System conditions, but also how it breaks apart, what it turns into, and how those processes depend on the type of radiation involved. As discussed in Chapter 1, simulating ion, electron, and VUV irradiation at cryogenic temperatures, tracking the loss of formamide alongside the emergence of new IR and VUV spectral features, and quantifying these changes through radiation chemical yields provides a coherent picture of the early-stage radiolysis and photolysis pathways operating in realistic icy environments. Ultimately, these experiments supply the first systematic dataset for mixed formamide-water ices under conditions relevant to Europa, Ganymede, and Enceladus, offering a foundation for interpreting future spectral observations and constraining how long prebiotic molecules may persist on irradiated icy surfaces.

8.2 Summary of Results Using Different Types of Radiation

Chapter 5 presents the results of irradiating ∼50:50 formamide-water ices at 90 K with 15 keV H^+, 30 keV O^{2+}, and 60 keV S^{5+} ions. Across all ion types, formamide exhibited rapid early destruction followed by a fluence-dependent plateau, behaviour consistent with matrix trapping, partial reformation via water-derived radicals, and shielding by accumulated radiolysis products. CO and OCN^- formed early and then stabilised or declined at high fluence, indicating secondary processing. At the same time, CO_2 grew continuously and was not subsequently destroyed, making it the most radiolytically stable end product. The chemistry, therefore, followed a fragmentation → recombination → secondary-loss sequence driven by dense energy deposition.

G-values showed that formamide destruction increased with LET, with O^{2+} and S^{5+} producing the highest yields. Substrate dependence was pronounced: taking ZnSe as the more inert reference surface, NaCl enhanced both formamide destruction and product formation, such that comparable levels of chemical change were reached at substantially lower fluence on NaCl. Although CO_2 accumulated most strongly, CO and OCN^- had the largest G-values, reflecting efficient low-dose formation. Normalising by LET indicated that energy density, not ion identity, governed the chemistry. Overall, radiolysis was controlled primarily by LET and substrate, with ion species playing a secondary role.

These results are directly relevant to Europa, where high-LET ion irradiation dominates the trailing hemisphere. Efficient bulk radiolysis implies that surface-exposed organics are short-lived, undergoing chemical transformation rather than simple removal. CO_2 stability and transient OCN^- persistence point to detectable radiolysis signatures for JUICE and Europa Clipper. Substrate effects suggest that salt-rich terrains will be highly reactive, with shorter molecular lifetimes and higher yields of oxidised products. Survivability estimates of $\sim 10^5$ years for formamide (modulated by salt content) indicate that detection would imply recent delivery or exposure, not long-term preservation. Europa's surface therefore behaves as a dynamic chemical reactor,

with rapid turnover shaping both its prebiotic inventory and the signatures accessible to spacecraft.

Chapter 6 describes the 2 keV electron irradiation of formamide-water ices at 90 K on NaCl and ZnSe. These low-LET electrons deposited energy diffusely, producing sparse ionisations and cascades of low-energy secondaries rather than dense ionisation tracks. As a result, electron-driven chemistry was far less efficient than ion-induced chemistry: fragmentation and volatile loss dominated, and little residue accumulated. The IR spectra were correspondingly less structured, showing only major modes and lacking the characteristic OCN^-, CO, and CO_2 features seen in the ion experiments. Approximate G-values from endpoint estimates confirmed the relatively weak destructive power of electrons. Substrate effects persisted, with ZnSe showing $\sim$3.5 times lower destruction than NaCl.

Despite their low per-particle efficiency, electrons remain crucial for Europa, where their flux far exceeds that of ions. Their diffuse energy deposition suggests they control near-surface volatile depletion and desorption. Salt-rich terrains, analogous to NaCl, likely experience more aggressive electron-driven turnover, while purer water-ice regions (ZnSe-like) preserve trace organics longer but in forms less accessible to remote sensing. The high magnetospheric electron flux means that electron-driven chemistry significantly shapes the uppermost layers of Europa's surface.

Chapter 7 presents the results of 9 eV VUV irradiation of formamide-water ices between 10 and 130 K. VUV photons penetrate only the upper tens of nanometres, restricting chemistry to the optical skin depth. The response was strongly temperature-dependent: at 10 K, irradiation compacted micropores and strengthened hydrogen bonding, producing sharper features and enhanced high-energy absorption; at 50 K, partial mobility broadened bands; at 90 K, annealing produced red-shifts and smoothing of the W-band; and above 110 K, desorption and restructuring dominated, suppressing photoproduct retention. Across all temperatures, no new discrete electronic bands formed. Instead, spectral changes arose from subtle shoulders and slope modifications associated with small fragments (CO, CO_2, HNCO, radicals) superimposed on the broad W-band.

VUV processing was most efficient at low temperatures, where products remained trapped, and progressively weaker at higher temperatures, where radicals recombined or desorbed. These results suggest that VUV photons primarily influence Europa's uppermost surface layers, especially in cold regions where small photoproducts can accumulate. Warmer terrains undergo rapid reorganisation, erasing VUV-generated features. Combined with the ion and electron results, the VUV data show that Europa's chemistry is vertically stratified: high-LET ions dominate dense-track radiolysis in the near-surface bulk; electrons, with their deeper and more diffuse penetration, contribute to extended bulk processing while governing near-surface volatile loss; and VUV photons reshape only the optical skin. Substrate effects reinforce that salt-rich terrains are chemically active but poor at preserving organics.

Across the three irradiation regimes, the dominant differences arise from penetration depth, energy-deposition density, and resulting chemical pathways. VUV photons affect only the upper nanometres; electrons penetrate more deeply but deposit energy diffusely; and heavy ions deliver dense tracks that strongly drive radiolysis. These differences yield distinct product distributions and destruction efficiencies (ions $\gg$ electrons $\gg$ VUV). Formamide is most stable under VUV irradiation, more vulnerable to electrons, and most efficiently destroyed by ions. Together, the regimes approximate Europa's complete radiation environment and highlight the depth dependence of organic survival.

Substrate effects play an important role. NaCl acted as a chemically active interface promoting destruction and product formation, while ZnSe behaved more inertly. Optical coupling, thermal conductivity, and hygroscopicity contributed to these differences, resulting in systematically higher yields on NaCl. Salt-rich terrains on Europa are therefore predicted to be chemically dynamic but poor at preserving organics, while purer ice regions may act as longer-lived reservoirs.

Taken together, these findings show that Europa's surface is likely to be a highly dynamic chemical interface. Radiation-driven destruction and generation compete continuously, product distributions vary with temperature and local geology, and only a narrow vertical interval within the ice is favourable for preserving prebiotic molecules.

These results provide a framework for interpreting forthcoming data from JUICE and Europa Clipper, guiding expectations for where organics may be detectable and how radiation processing shapes the observable chemical landscape.

8.3 Implications for Detectability on Europa

Building on the comparative results in Section 8.2, this section focuses on how depth, substrate, and temperature affect what is spectroscopically observable on Europa. The implications for Europa Clipper and JUICE are that surface spectra will not directly reflect bulk composition. VUV- and electron-dominated chemistry continually modifies the optically thin uppermost layers, which become chemically depleted, reorganised, and spectrally flattened, meaning remote observations are likely to under-represent deeper or less volatile organics. Instead, the most stable radiolytic residue, CO_2, together with relatively long-lived species such as OCN^- and other oxidised products generated efficiently in ion tracks, is expected to dominate IR signatures and contribute only broadly to VUV absorption. Salt-rich terrains will appear more chemically "active" due to faster turnover of prebiotically relevant molecules, enhanced CO_2 and OCN^- production, and distinct spectral baselines driven by hydration and morphology. This behaviour is likely to inform the interpretation of chaos regions, lineae, and brine-rich patches.

Temperature further modulates detectability. Cold polar regions ($\lesssim$ 80 K) can retain both VUV-generated fragments and surviving parent molecules, thereby producing stronger, more chemically diagnostic spectral features. In contrast, warmer equatorial terrains will appear spectrally "clean" because fragments do not accumulate: desorption dominates, and bands flatten. Without accounting for depth-dependent processing, such regions could be misinterpreted as chemically inactive. Remote sensing must therefore consider that different radiation components interact with different depths: VUV photons shape the observable optical skin, electrons both drive near-surface volatile loss and process material throughout the upper ice column, and ions generate dense-track products in the shallow subsurface that are detectable only when exposed by geological activity or impact gardening. This sets realistic expectations

for band strengths, product ratios, and geographic variability in Europa Clipper and JUICE observations.

8.3.1 Assumptions and Limitations

Several limitations must be considered when interpreting these results. The laboratory ice films used here - hundreds of nanometres for IR and even thinner for VUV - are far smaller and more uniform than Europa's complex, porous, multi-grain surface ices. Real regolith contains grain boundaries, voids, salts, clathrates, and thermal gradients that alter radical mobility and trapping in ways not captured by a uniform thin film. Energy deposition, compaction, and desorption in thin films approximate local microphysics, but cannot reproduce Europa's centimetre- to metre-scale stratigraphy.

Secondly, accelerated fluxes of ions, electrons, and photons were required to produce measurable changes on experiment timescales. Europa's radiation environment operates at far lower fluxes over years to millennia, influencing radical recombination, thermal relaxation, and burial. The experiments, therefore, capture underlying mechanisms rather than literal exposure timescales.

Thirdly, the chemistry investigated here focused on binary formamide-water mixtures without co-deposited species such as CO, NH_3, CH_3OH, SO_2, or additional salts. Europa's surface contains a complex mixture of volatiles from Io-derived sulphur implantation, subsurface-ocean salts, and carbon-bearing ices, all of which can modify reaction pathways. The results thus reflect isolated formamide chemistry rather than the complete reactive network expected on Europa.

A related limitation is the intentionally high formamide concentration used. The 50:50 formamide-water mixture enables measurable chemical and spectral changes within feasible irradiation times and within IR/VUV detection limits. In reality, Europa's surface is water-dominated, with organics likely present at ppm-percent levels. The mixture used here therefore samples high-density formamide chemistry rather than the dilute grain-boundary chemistry expected on Europa. While this captures intrinsic radiolysis pathways and parent/product band behaviour, it may overestimate absolute product yields, destruction efficiencies, and IR feature visibility.

Spectral interpretation also carries uncertainties. Overlapping bands, baseline structure, film-thickness effects, noise, and interference fringes - particularly on ZnSe and in VUV-normalised spectra - limit detection of weak or transient species. Some radicals and photoproducts likely formed but remained below detection thresholds or appeared only as blended shoulders. G-values, therefore, quantify detectable products rather than the complete chemical inventory.

Finally, the experiments isolated irradiation types by using ions, electrons, and photons separately. Real icy surfaces are simultaneously exposed to these components, and synergistic effects (such as electron-stimulated desorption during ion radiolysis, photon-induced radical mobility, or ion-driven restructuring that affects VUV absorption) are not captured. The study therefore characterises first-order behaviours but not the complete multi-component radiation chemistry of the Jovian system.

8.4 Future Work

Future work arising from this thesis should bridge the gap between the simplified laboratory analogues used here and the far more complex chemical environments expected on Europa's surface and within its subsurface ocean. As discussed throughout this study, the actual composition, salinity, and volatile inventory of Europa's ice shell remain uncertain and will only become clearer with forthcoming observations from JUICE and Europa Clipper. The experiments performed in this thesis isolated individual radiation components. They focused on binary formamide-water ices, enabling the underlying mechanisms of radiolysis and photolysis to be identified, but necessarily omitted the wider reactive network present in realistic icy environments. Future investigations should therefore move toward geochemically and compositionally faithful systems, incorporating aqueous formamide-salt solutions, mixed-volatile ices, and combined irradiation regimes. Such studies will help determine how Europan salts influence prebiotic chemistry, how complex organics evolve under more realistic fluence-time conditions, and whether irradiation of brine-rich analogues can drive the formation of biomolecules relevant to astrobiology and detectable by next-generation spacecraft.

8.4.1 Aqueous Formamide-Salt Irradiation Experiments

A key extension of this work will be to investigate the irradiation of aqueous formamide-salt systems that more closely resemble the chemistry expected in Europa's subsurface ocean. Although preliminary plans for such experiments were developed during this project, time constraints, equipment failures, and sample-preparation challenges prevented their completion. Future studies should therefore adopt a systematic "systems chemistry" approach using reaction vessels ranging from microlitre (0.32 μL) to multi-millilitre (up to 20 mL) volumes, containing liquid formamide-water mixtures with controlled concentrations of Europan-relevant salts such as mirabilite ($Na_2SO_4 \cdot 10H_2O$) and epsomite ($MgSO_4 \cdot 7H_2O$). These solutions would be irradiated over timescales of tens of hours to a week using a range of lamp wavelengths (325-625 nm and broad-spectrum white light) in a photoreactor or similar system, with temperature stabilised using a water or coolant bath.

By varying vessel size, solute concentration, salt identity, irradiation wavelength, and temperature in a controlled manner, such experiments would map how each parameter influences the formation of complex chemical products. The central goal is to identify the conditions that yield the highest abundances of amino acids or other prebiotically relevant biomolecules and to determine which combinations of radiation type, temperature, and saline environment are most conducive to molecular complexity.

8.4.2 Mass-Spectrometric Identification of Radiolysis Products

A further priority is the use of GC-MS and LC-MS to directly analyse the molecular residues produced during both solid-state and aqueous irradiation experiments. While IR and VUV spectroscopy reveal broad chemical trends and major functional groups, they cannot unambiguously identify many of the small or transient photoproducts expected from formamide radiolysis, nor can they quantify trace-level species that fall below optical detection thresholds. Mass-spectrometric analysis of post-irradiation residues - both the solid films generated in the ion, electron, and VUV experiments and the aqueous products from brine irradiations - would allow precise identification of

individual molecules, including amino acids, carboxylic acids, nitriles, and other low-abundance organics. Quantifying product yields across irradiation regimes would also enable direct comparison of reaction efficiencies, constraining which pathways dominate under Europa-like conditions. Such datasets would provide a molecular-level bridge between laboratory chemistry and the species targeted by JUICE and Europa Clipper, linking experimentally verified reaction networks to mission-relevant observables.

8.4.3 Time- and Fluence-Dependent Reaction Network Modelling

A complementary direction for future work is the development of reaction network models capable of capturing the time- and fluence-dependent chemistry observed in this thesis. The radiolysis pathways identified here - fragmentation of formamide, formation of CO, CO_2, OCN^-, and radicals, and the interplay between recombination and secondary loss - provide a natural basis for constructing kinetic schemes in which the measured G-values act as initial rate constraints. Such models would enable extrapolation of product abundance evolution beyond the laboratory fluences explored here, offering insight into long-term behaviour under Europa-like radiation conditions. Although an entirely mechanistic description is beyond the scope of this work, both differential-equation networks and stochastic or Monte Carlo approaches could be employed to explore how competing pathways, radical lifetimes, and matrix effects control chemical evolution.

Once extended to aqueous systems, these models could predict the long-term evolution of more complex chemistry, including amino acid synthesis and other prebiotically relevant products, by incorporating reaction channels derived from GC-MS and LC-MS analyses. This approach would link short-duration laboratory irradiations to the long, slow processing regimes expected in Europa's ocean and near-surface brines.

8.4.4 Mission-Aligned Analogue Experiments

Another avenue for future work will involve refining laboratory analogues using compositional and environmental constraints returned by Europa Clipper and JUICE. In-

struments such as Europa Clipper's MISE and MASPEX, and JUICE's MAJIS and PEP, will provide unprecedented information on the distribution of salts, volatiles, and organic materials, regional energetic particle fluxes, and temperature gradients across Europa's surface. As these datasets become available, laboratory experiments can be updated to include more realistic brine compositions, mixed-volatile ices, hydrated salts, and irradiation conditions matched to observed ion and electron fluxes. Temperature regimes representative of polar, equatorial, and chaos terrains can also be replicated.

Such mission-aligned analogue studies will help translate spacecraft observations into chemical pathways. Combined with mass-spectrometric analysis of laboratory residues, they will allow mission detections of CO_2, OCN^-, and other key species to be connected back to experimentally derived reaction networks. This iterative approach will produce analogues that increasingly mirror Europa's true chemical environments.

8.4.5 Mixed and Sequential Radiation Experiments

Finally, future work should incorporate mixed and sequential irradiation experiments that reproduce the multi-component radiation environment on Europa. The present study isolates ions, electrons, and VUV photons to identify first-order behaviours, but real surfaces are simultaneously exposed to all three, and the resulting chemistry is unlikely to be a simple sum of the individual components. Sequential experiments - such as VUV followed by electrons, or electrons followed by ions - would reveal whether irradiation order alters chemical pathways, product yields, or matrix structure. For example, VUV-induced compaction may influence the penetration of subsequent electrons, while ion-induced lattice defects could modify the retention or reactivity of VUV-generated fragments. Electron-stimulated desorption may also deplete precursors before ion-driven radiolysis takes place.

A key limitation of the present approach is that individual ion, electron, or VUV irradiations are not fully representative of Europa's true radiation environment, where these agents act concurrently and may produce non-linear, synergistic effects. Mixed-irradiation setups, in which ions, electrons, and photons act concurrently or in con-

trolled ratios, offer a direct route to identifying such synergistic behaviours. These experiments would quantify how combined irradiation modifies the formation efficiencies of CO_2, OCN^-, CO, HNCO, and other products, and whether mixed regimes enhance or suppress the production of more complex organics. Such studies would provide a more realistic assessment of Europa's surface chemistry, where depth-dependent energy deposition produces strongly coupled chemical environments. Together, sequential and mixed-irradiation experiments would bridge the gap between idealised laboratory conditions and the complex radiation fields encountered across Jupiter's icy moons.

8.5 Final Conclusions

This thesis has investigated the radiolytic and photolytic processing of formamide-water ices under conditions relevant to Europa and other icy bodies, using ion, electron, and VUV irradiation to map how energy deposition mode, temperature, and substrate composition control chemical evolution. Across all regimes, formamide proved far more resilient than its simple molecular structure suggests: its core electronic signature persisted under VUV irradiation, its destruction followed characteristic fragmentation-recombination pathways, and its mean lifetime under Europa-like ion fluxes remained on the order of 10^5 years. High-LET ions drove efficient dense-track radiolysis in the near-surface bulk and produced stable residues such as CO_2 and OCN^-; electrons provided more diffuse, depth-extended processing while dominating near-surface depletion; and VUV photons reshaped only the optical skin, with chemistry strongly dependent on temperature. Substrate effects revealed that salt-rich terrains enhance destruction and favour oxidised products, whereas more inert or mineral-like surfaces promote preservation. Together, these results provide the first systematic dataset for mixed formamide-water ices processed by multiple radiation types and demonstrate that Europa's surface chemistry is vertically stratified, dynamically evolving, and governed by a competition between destruction and transformation rather than simple molecular loss.

More broadly, this work highlights that the detectability of prebiotic molecules on

Europa depends not only on their intrinsic stability but on the radiation environment, substrate composition, temperature regime, and geological context in which they reside. The findings presented here offer a framework for interpreting upcoming observations from JUICE and Europa Clipper, helping to constrain where organics are most likely to persist and how radiolysis signatures may manifest across Europa's diverse terrains. At the same time, they emphasise the need for future laboratory studies that incorporate realistic brine compositions, sequential and mixed irradiation, and mass-spectrometric product identification, ultimately linking laboratory chemistry to mission observables. While Europa remains a challenging environment for organic survival, this thesis shows that formamide and its derivatives can persist long enough - and transform sufficiently - to contribute meaningfully to prebiotic chemistry within the Jovian system. As new mission data refines our understanding of Europa's surface and interior, the groundwork laid here will help guide the next generation of analogue experiments and strengthen the chemical foundations of our search for life beyond Earth.

Appendix A

Determination of G-Values from Exponential Dose–Response Fits

A.1 Overview

The radiation chemical yields (G-values) reported in this work were derived from the initial destruction rates of formamide obtained from dose-response curves. The procedure combined experimental FTIR measurements, column density calculations, analytical fitting of the resulting dose-response curves, and linear regression of the initial low-dose regime. This approach is consistent with established practice in the laboratory ice irradiation literature, where G-values are conventionally determined from the initial, approximately linear region of the dose–response curve rather than from an analytical derivative of a fitted function; this ensures that the reported yields reflect the true early-stage radiochemical efficiency and remain directly comparable across different radiation types, ice compositions, and experimental conditions.

A.2 Determination of Column Density

Infrared spectra were collected throughout each ion irradiation experiment and manually baseline-corrected prior to analysis, following the procedure described in Section 4.2.1. The integrated absorbance of selected formamide absorption bands - at 1388 cm^{-1} and 1328 cm^{-1}, corresponding to the CH scissoring and CN stretching modes, respectively - was determined at each irradiation step.

Column densities were calculated from the integrated absorbance using literature band strengths according to:

$$N = \frac{\ln(10) \int A(\tilde{\nu})\, \mathrm{d}\tilde{\nu}}{A'} \tag{A.1}$$

where N is the column density (molecules cm^{-2}), $\int A(\tilde{\nu})\, \mathrm{d}\tilde{\nu}$ is the integrated absorbance (cm^{-1}), and A' is the literature band strength (cm molecule^{-1}). The factor of ln(10) arises from the conversion between the base-10 absorbance scale - as output by the FTIR spectrometer - and the natural logarithm convention adopted by the band strength literature, in which band strengths are defined in terms of optical depth. The band strengths used were those described in Section 3.3.3.

Column densities were calculated independently for both formamide absorption bands. Since both features arise from the same parent molecule, comparable destruction rates were expected; independent analysis of both bands therefore provided an internal consistency check on the derived G-values.

A.3 Construction of Dose–Response Curves

The calculated column densities were plotted as a function of cumulative absorbed energy. The absorbed energy per irradiation step was determined from the particle fluence and the energy deposited per incident ion, as described in Section 4.4.3, yielding a dose axis expressed in eV cm^{-2}. The resulting dose-response curves describe the evolution of molecular column density as a function of increasing radiation dose and form the basis of the subsequent G-value analysis.

A.4 Analytical Fitting of Dose-Response Curves

To minimise the influence of point-to-point spectral noise and provide a smooth representation of the overall destruction behaviour, each dose-response curve was fitted in Origin using a double-exponential decay function of the form:

$$N(E) = A_1\, e^{-E/t_1} + A_2\, e^{-E/t_2} + y_0 \tag{A.2}$$

where A_1 and A_2 are the amplitudes of the fast and slow decay components, t_1 and t_2

are the corresponding characteristic energy constants (eV cm^{-2}), and y_0 represents the residual column density approached at high dose. All five parameters were treated as free during the fit. The double-exponential form was adopted because the formamide bands typically exhibited an initial rapid decline followed by a slower secondary loss - multi-timescale behaviour consistent with compaction, radical trapping, and matrix restructuring at higher doses, as discussed in Section 3.3.3. The fitted function therefore serves as a smooth mathematical interpolant of the dose-response data rather than a mechanistic model of the underlying chemistry.

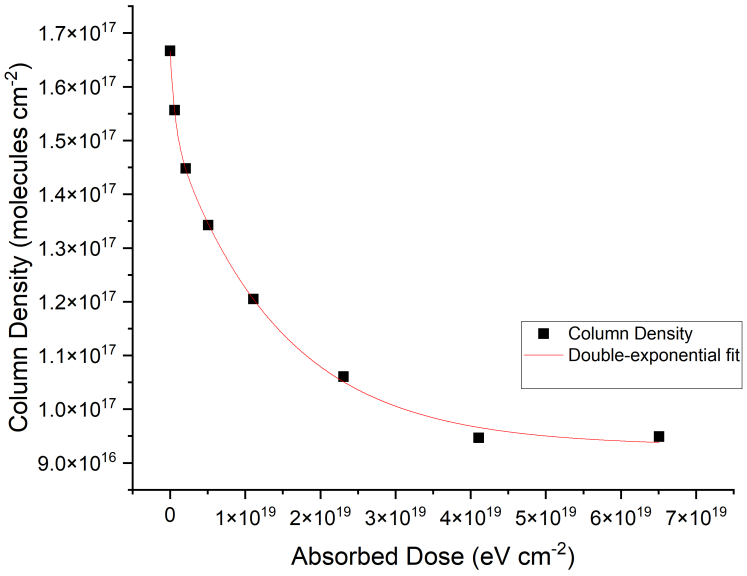


Figure A.1: Representative dose-response curve illustrating the G-value extraction procedure described in this appendix, shown here for the 1328 cm^{-1} formamide band under S^{5+} ion irradiation on a ZnSe substrate. Black squares represent experimental data points; the red curve shows the fitted double-exponential decay function (Equation A.2). This procedure was applied identically to all ion irradiation datasets.

The fitted parameters A_1, A_2, t_1, t_2, and y_0 were extracted from Origin and used as inputs to the subsequent Python analysis.

A.5 Determination of the Initial Destruction Rate

The fitted exponential function was evaluated numerically in Python to generate a smooth, densely sampled representation of the low-dose behaviour of the system. An upper energy limit, $E_{\max}$, was selected by visual inspection of the fitted curve as the

point beyond which the response deviated appreciably from linearity - that is, where curvature due to precursor depletion, secondary chemistry, or significant matrix restructuring became apparent. A set of evenly spaced points was generated between zero absorbed energy and $E_{\max}$, and a least-squares linear regression was applied to the initial subset of these points corresponding to the most linear portion of the response:

$$N(E) = mE + c \tag{A.3}$$

where m is the gradient (molecules eV^{-1}) and c is the intercept (molecules cm^{-2}). The fitted gradient corresponds to the initial destruction rate $\mathrm{d}N/\mathrm{d}E$, which approximates the instantaneous rate of molecular destruction in the limit of low dose, prior to the onset of non-linear effects.

A.6 Calculation of G-Values

The initial destruction rate was converted into a radiation chemical yield according to:

$$G(-M) = 100 \left| \frac{\mathrm{d}N}{\mathrm{d}E} \right| \tag{A.4}$$

where $G(-M)$ represents the number of parent molecules destroyed per 100 eV of absorbed energy, and the absolute value is taken to return a positive yield for a destruction process, following the sign convention described in Section 3.3.1. Uncertainties in the G-values were estimated by propagating the standard errors on the fitted exponential parameters (A_1, A_2, t_1, t_2) through their partial derivatives with respect to the evaluated function, and combining the contributions in quadrature. This provides a conservative estimate of the precision of the derived slope, reflecting the sensitivity of the initial linear regime to variations in the fitted parameters within their respective standard errors. Systematic uncertainties arising from band strengths, baseline placement, and ice thickness - which affect the absolute column density scale rather than the shape of the dose-response - are discussed separately in Section 3.3.4.

This procedure was applied independently to both formamide absorption bands

(1388 cm^{-1} and 1328 cm^{-1}), and the resulting G-values were compared as an internal consistency check on the derived destruction yields. The same procedure was applied to the product bands of CO (2135 cm^{-1}), CO_2 (2340 cm^{-1}), and OCN^- (2165 cm^{-1}), yielding formation G-values $G(+P)$ for each species. In these cases the dose-response curves were fitted with logarithmic or saturating growth functions rather than exponential decays, reflecting the fast initial rise and subsequent plateau characteristic of product accumulation as precursor availability decreases. The initial slope of the fitted function was extracted and converted to $G(+P)$ using the same linear regression procedure described above.